

UNIVERSITY OF OKLAHOMA
GRADUATE COLLEGE

NUMERICAL SIMULATIONS OF CYCLIC STORM BEHAVIOR:
MESOCYCLOGENESIS AND TORNADOGENESIS

A Dissertation

SUBMITTED TO THE GRADUATE FACULTY

in partial fulfillment of the requirements for the

degree of

Doctor of Philosophy

BY

EDWIN JEROME ADLERMAN

Norman, Oklahoma

2003

UMI Number: 3109067

INFORMATION TO USERS

The quality of this reproduction is dependent upon the quality of the copy submitted. Broken or indistinct print, colored or poor quality illustrations and photographs, print bleed-through, substandard margins, and improper alignment can adversely affect reproduction.

In the unlikely event that the author did not send a complete manuscript and there are missing pages, these will be noted. Also, if unauthorized copyright material had to be removed, a note will indicate the deletion.

UMI[®]

UMI Microform 3109067

Copyright 2004 by ProQuest Information and Learning Company.

All rights reserved. This microform edition is protected against unauthorized copying under Title 17, United States Code.

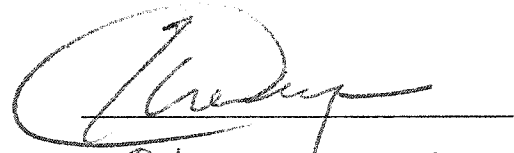
ProQuest Information and Learning Company
300 North Zeeb Road
P.O. Box 1346
Ann Arbor, MI 48106-1346

© Copyright by EDWIN JEROME ADLERMAN 2003
All Rights Reserved

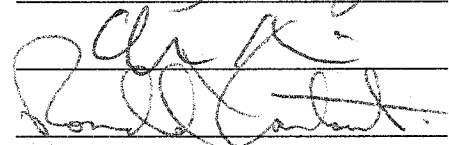
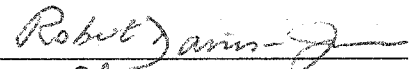
NUMERICAL SIMULATIONS OF CYCLIC STORM BEHAVIOR:
MESOCYCLOGENESIS AND TORNADOGENESIS

A Dissertation APPROVED FOR THE
SCHOOL OF METEOROLOGY

BY



Howard B. Bluestein



Donald

ACKNOWLEDGEMENTS

I am grateful to many people. First, I thank my advisor and committee chair, Dr. Kelvin Droegemeier, for his support, encouragement, and endless energy. I also thank the other members of my committee: Dr. Alan Shapiro, Dr. Howie Bluestein, Dr. Robert Davies-Jones, and Dr. Ron Kantowksi. Their comments and suggestions greatly improved the dissertation. I'd like to thank Dr. Dan Weber, Dr. Ming Xue, and Dr. Keith Brewster for answering numerous questions about ARPS and providing invaluable computer support. Computer support was also provided by Dr. Henry Neeman and Dr. Mark Laufersweiler. Dr. Lou Wicker, Dr. David Dowell, Don Burgess, and Mike Magsig have contributed to relevant discussions on cyclic storms and tornadogenesis. I am also grateful to both Dr. Josh Wurman for the field experience of the ROTATE-98 project, and to the organizers of the VORTEX-94 and VORTEX-95 projects.

Of course, I must thank all of the good friends, officemates, and colleagues who have crossed paths with me over the years, including, but not limited to: Amanda Autry, Randy Stevens, Dan Smith, everyone at $\Theta\Delta X$ -Theta Deuteron, Dr. John Mewes and Richelle, Mark O'Malley, Curtis Marshall, Scott Ellis, Clinton Wallace, J. J. Gourley, Karen Sonntag, Paul and Janelle Janish, Drs. Scott and Yvette Richardson, Dr. Mark and Amy Askelson, John Krause, Dr. Ernani Nascimento, Paul Robinson, Beth Clarke, Andy Worthington, Rob Hale, Drs. Evgeni Fedorovich and Petra Kastner-Klein, Drs. Jerry Straka and Kathy Kanak, Allison Silveira, and Mary 'Darling!' Young. A special thanks goes out to the Poker Crew, including J. J. Harris, Amy Buhl, James Rogers, Andy Reader, Scott Giagrande, Kristin Kuhlman, and Kyle Brooks. I also thank my mom, my sister, and my aunt for their full support over the years.

This research was supported by the National Science Foundation under Cooperative Agreement ATM91-20009 and Grants ATM-9222576 and ATM-9981130 to Professor Kelvin Droegemeier at the University of Oklahoma. The numerical simulations were performed at the Pittsburgh Supercomputing Center, the Oklahoma Supercomputing Center for Education and Research, and the Environmental Computing Applications System, the latter of which is funded by the National Science Foundation under Grant EAR95-12145. Some of the graphics were generated using the ZXPLLOT package developed by Ming Xue at the University of Oklahoma.

Finally, I must also thank Gil Gentry for *finally* bringing sushi to Norman, Tobin and Eric of Buchanan Bicycles for providing great service, and MOOTS for building perfect titanium works of art.

TABLE OF CONTENTS

<i>Chapter 1</i>	<i>Introduction</i>	1
<i>Chapter 2</i>	<i>Background</i>	7
2.1	Brief Historical Review	7
2.2	Cyclic Mesocyclogenesis and Tornadogenesis	13
2.3	Recent Work on Cyclic Mesocyclogenesis and Tornadogenesis	19
<i>Chapter 3</i>	<i>Sensitivity of Cyclic Mesocyclogenesis to Environmental Wind and Thermodynamic Structure</i>	26
3.1	Introduction	26
3.2	Methodology	26
3.3	Design of the Parameter Space	29
3.3.1	<i>Review of Past Parameter Space Studies</i>	29
3.3.2	<i>Design of the Parameter Space</i>	33
3.4	Simulation Overview and the Control Experiment	35
3.4.1	<i>Introduction</i>	35
3.4.2	<i>The Control Experiment</i>	37
3.4.3	<i>Overview of the Simulations</i>	45
3.5	Half-Circle Hodograph Simulations	49
3.5.1	<i>Uniform Shear Distribution Over 10 km</i>	49
3.5.2	<i>Variations in Shear Distribution Over 10 km</i>	54
3.5.3	<i>Uniform Shear Distribution Over 6 km</i>	61
3.5.4	<i>Variations in CAPE</i>	69
	3.5.4.1 Weisman and Klemp Sounding	69
	3.5.4.2 Del City Sounding	70
3.6	Quarter-Circle Simulations	71
3.6.1	<i>3 km Turning Depth</i>	71
3.6.2	<i>1 km Turning Depth</i>	82
3.7	Three-Quarter Circle Simulations	86
3.8	Full-Circle and Helical Hodograph Simulations	89
3.9	Straight-Hodograph Simulations	98
3.10	Summary and Discussion	99
<i>Chapter 4</i>	<i>The Numerical Simulation of Cyclic Tornadogenesis</i>	114
4.1	Introduction	114
4.2	Methodology	115

4.3	Simulation Overview	116
4.3.1	<i>General Structure</i>	116
4.3.2	<i>Time-height summaries</i>	122
4.4	Mesocyclogenesis and the transition between cycles	132
4.4.1	<i>Introduction</i>	132
4.4.2	<i>Occlusion Cycle "C"</i>	132
4.4.3	<i>Transitions in Other Occlusion Cycles</i>	149
4.5	Trajectory Results	157
4.5.1	<i>Introduction</i>	157
4.5.2	<i>Mesocyclogenesis Trajectories</i>	160
4.5.2	<i>Tornadogenesis Trajectories</i>	177
4.6	Summary and Discussion	188
<i>Chapter 5</i>	<i>Summary, Conclusions and Outlook</i>	194
<i>Bibliography</i>		200
<i>Appendix A</i>	Trajectory Code Description	214
<i>Appendix B</i>	Magnitude of the Numerical Diffusion Term in ARPS	216

ABSTRACT

Building upon previous work that examined the dynamics and model sensitivity of cyclic mesocyclogenesis, this study uses idealized numerical simulations to investigate the cyclic redevelopment of vertical vortices in supercell storms. The study is comprised of two parts. First, we examine the environmental parameter space that delineates between the timing and modes of mesocyclone occlusions. Second, we use a high-resolution numerical simulation to examine cyclic tornadogenesis.

For the parameter study, we examine variations in hodograph shape, shear magnitude, shear distribution, and CAPE. We simulate storms whose behavior ranges from steady-state to varying degrees of occluding cyclic mesocyclogenesis. However, we also demonstrate that a new mode of *non-occluding* cyclic mesocyclogenesis may occur in certain environments. The preferred mode of cycling is strongly related to both the hodograph shape and the strength of the shear.

Straight hodographs produce *only* non-occluding cyclic mesocyclogenesis. Introducing some curvature with the quarter-circle hodograph allows steady, non-occluding and occluding modes to be simulated. When a higher degree of curvature is introduced with half-circle and three-quarter circle hodographs, the tendency for non-occluding cyclic mesocyclogenesis is diminished. None of the full-circle hodographs exhibited cycling during the 4-hour simulation.

In the cyclic tornadogenesis study, we simulate a storm that undergoes six mesocyclone cycles during a five-hour simulation. Three of the mesocyclone cycles are tornadic, with one cycle containing two instances of tornadogenesis. The evolution of each mesocyclone occlusion is similar to that in the previous conceptual model, although the details of each transition period (from one cycle to the next) vary significantly.

Backward trajectories through the mesocyclone show that when development occurs in an area relatively free of influence from the previous cycle, parcels generally descend through the rear-flank downdraft (RFD) or

ascend from east and northeast of the gust front. However, when the mesocyclone of a new cycle develops in close proximity to that of an occlusion, some parcels are recycled through the occluding mesocyclone or the occlusion downdraft.

Backward trajectories through two of the simulated tornado cyclones demonstrate that parcels entering the strongest circulation travel near the ground through a baroclinic zone northwest of the mesocyclone. Parcels along the periphery of the tornadic mesocyclone have more varied histories depending on the details of a particular cycle. In general, they originate at higher levels, with some ascending through the updraft before descending in the occlusion downdraft.

CHAPTER 1

INTRODUCTION

During the last 35 years, our understanding of supercell thunderstorms has increased dramatically as a result of numerical simulations, surface and airborne observations, and theory. Notably, significant progress has been made in the understanding of both mid-level and near-ground mesocyclogenesis, i.e. the development of a 3-9 km diameter region of vertical vorticity greater than 0.01 s^{-1} with both height and time continuity. Recent numerical simulations have progressed further downscale to the study of tornadogenesis within a full cloud model.

An interesting and relatively unexplored aspect of supercell storms is the tendency for successive mesocyclone redevelopment within the same storm. Although all types of convection may exhibit periodic variations in updraft velocity, rainfall, or reflectivity, supercells are oftentimes distinguished by mesocyclones (with *or* without an accompanying tornado) that undergo cyclic redevelopment similar to the occlusion process of a midlatitude synoptic-scale cyclone. This behavior first was noted in observations of tornado families and was termed "cyclic tornadogenesis." It was later shown that each cyclic tornado usually is accompanied by a distinct updraft/mesocyclone, i.e., "cyclic mesocyclogenesis." Although a mesocyclone may undergo cyclic *variations in intensity* throughout the lifetime of storm, we reserve the term "cyclic mesocyclogenesis" for those storms in which a new near-ground mesocyclone clearly forms in a location spatially separated from its predecessor.

Because the cyclic occlusion process occurs on an average timescale of 45 min over distances of 25-40 km (given an average storm speed of approximately 10-15 m s⁻¹), dual-Doppler studies with sufficiently detailed spatial and temporal resolution have been rare until the recent use of mobile Doppler-radar platforms. In addition, little attention has been paid to the mesocyclone occlusion process in previous numerical simulations, possibly a result of the long integration times required and/or sensitivities to the spatial resolution and environmental sounding.

Recent simulations of supercell tornadogenesis have yielded interesting results that compare favorably with observations. However, detailed analyses of the results have been limited, with only two studies utilizing trajectory and/or circulation analyses to investigate the source of rotation within the tornado cyclone. In addition, each study simulated a different type of supercell, so only limited comparisons can be made between the two.

The simulation of multiple occlusions in a classic supercell thunderstorm by Adlerman et al. (1999) was a first step toward understanding the dynamics that underlie the occlusion process in cyclic mesocyclogenesis. As a prelude to examining the environmental conditions that control storm cycling, Adlerman and Droegemeier (2002) also studied the sensitivity of cyclic mesocyclogenesis to model parameters. [The latter study, which is part of the author's doctoral research, recently was published and is not included here other than in summary form.] *As an extension of these works, this study seeks to 1) explore the environmental parameter space that not only delineates cyclic from non-cyclic supercells, but also controls the timing and character of mesocyclone occlusions; and 2) understand the process of cyclic tornadogenesis in the context of a single high-resolution numerical simulation.*

With regard to the first topic, it has been shown previously that a systematic variation in shear for a single hodograph shape can cover a broad range of storm

morphologies, from supercells to single and multicells, as well as lines and bow echoes. It is reasonable to assume that a similar variation in shear might produce supercells that also span cyclic and non-cyclic behavior (i.e., from a steady-state storm, to one occlusion, to two occlusions, etc...). Therefore, we base our parameter study upon variations in vertical shear, with variations in CAPE playing a more limited role in order to keep the number of simulations reasonable. Given a specified hodograph (i.e. a single shape), we seek to determine whether changing the magnitude and/or distribution of vertical shear can induce transitions between cyclic and non-cyclic behavior. If this indeed occurs, can we use a parameter that characterizes the simulation's sounding (e.g., the bulk Richardson number or storm-relative helicity) to delineate between environments conducive to non-cyclic versus cyclic behavior? Similarly, can such parameters also discriminate between the number and length of the occlusion cycles?

Given the recent finding that the dynamics of straight and highly curved hodographs are fundamentally different (see Chapter 2), it is also reasonable to expect that hodograph shape may influence cyclic behavior. Therefore, we also examine a full range of hodograph topologies (straight, quarter-circles with and without tails, half-circles, three-quarter circles, and full-circles) in order to determine whether profound differences in cycling behavior are observed when measures of vertical shear are similar, yet the hodograph shape is not.

Because our parameter study attempts to relate changes in cyclic behavior to both hodograph shape and measures of the vertical shear, it is natural to ask what physical effects induce changes in mesocyclone cycling. For example, we have shown previously that changes in the strength of the cold outflow, the intensity of the near-ground mesocyclone, and the motion of the gust front dramatically affect mesocyclone cycling. Similarly, can variations in cycling within the parameter

study be directly related to the same effects, albeit induced via the influence of the environmental wind profile rather than model parameters?

The second part of this study focuses on the analysis of storm dynamics associated with cyclic tornadogenesis. Similar to recent simulations of tornadogenesis within a storm-scale model (see Chapter 2), we focus on the development of the "tornado cyclone" rather than the dynamics of the tornado vortex itself. We previously demonstrated that both the model configuration and environmental sounding influence the character and timing of the occlusion process. Therefore, it is reasonable to ask whether the introduction of higher-resolution also fundamentally changes the time and/or character of the occlusion process, or if the large-scale evolution remains similar to that previously simulated. Because some studies have shown that the correlation between updraft redevelopment and each tornado cycle may vary, it is also natural to study the relationship between the scales of the cyclic mesocyclone and associated tornado. For example, is the latter a fine-scale version of the former, or is the evolution more complex? Similarly, does each mesocyclone cycle correspond to a cycle of tornadogenesis?

We also have demonstrated that an occlusion sets the stage for subsequent near-ground mesocyclogenesis to proceed rapidly. It is natural to ask whether this also occurs within the context of cyclic "tornadogenesis." Therefore, we will explore the vorticity dynamics of each cycle of tornadogenesis and study how they are related to the processes that promote near-ground mesocyclogenesis. For example, do the parcel trajectories and vorticity dynamics of mesocyclogenesis differ from those of "tornadogenesis"? Do differences exist between cycles? Finally, do previous cycles also "set the stage" for subsequent tornadogenesis?

A final motivation for this study can be cast from the inevitable limitations of the observing systems. Despite recent advances that have led, for example, to a

radar-based climatology of mesocyclones, field projects such as VORTEX and high-resolution radar measurements of tornadoes, numerical simulation remains the most practical method of obtaining the densely-spaced four-dimensional information required for dynamical analyses of *near-ground* processes in thunderstorms. Although the numerical simulations presented in this study are somewhat limited by their idealized nature (e.g., a free-slip lower boundary, simple microphysics and initiation mechanism, etc...), they represent a first step toward a comprehensive understanding of the cyclic nature of supercell thunderstorms.

The dissertation is organized as follows. Chapter 2 presents a literature review of severe storm dynamics and cyclic mesocyclogenesis/tornadogenesis.

Building upon the material presented in Adlerman and Droegemeier (2002), Chapter 3 presents results of the environmental sensitivity study of cyclic mesocyclogenesis. Variations in hodograph shape, shear magnitude, shear distribution, and CAPE are examined, and corresponding trends in cycling behavior and general storm characteristics (e.g. updraft size, precipitation location) are demonstrated. Physical explanations for the simulated trends in cycling behavior are given as well as a comparison with the limiting case of an idealized Beltrami flow.

Chapter 4 presents a downscale extension of Adlerman et al. (1999), highlighting a high-resolution (105 m horizontal grid spacing) nested grid simulation of cyclic tornadogenesis. The simulated storm undergoes six cycles of mesocyclogenesis over a 5-hour simulation, three of which contain very strong near-ground vortices with wind speeds on the order of 50 m s^{-1} and pressure deficits greater than 20 mb. Trajectories are used to demonstrate the variations in mesocyclogenesis between cycles, to illuminate differences between the simulated evolution of mesocyclogenesis and "tornadogenesis", and to compare

mesocyclogenesis/tornadogenesis mechanisms with previous analyses of simulations.

Chapter 5 summarizes the results and discusses their implications for future research into cyclic storms.

CHAPTER 2

BACKGROUND

2.1 Brief Historical Review

Early in the history of severe storm research, it was recognized that updraft rotation, storm splitting, and storm motion deviant from the mean wind were often correlated with tornadoes, hail, and damaging winds (e.g., Byers 1942; Newton and Katz 1958; Newton and Newton 1959; Fujita 1958; Hirschfeld 1960). Continuing studies (e.g., Browning and Ludlam 1962; Browning and Landry 1963; Browning and Donaldson 1963) focused on the internal structure of convection, and recognized that especially long-lasting severe storms were organized to allow the storm's potentially buoyant inflow to remain undisrupted by the downdraft and associated precipitation. Browning (1964) extended this idea and proposed a flow pattern that took into account strong vertical shear, consistent with rightward propagation and the initiation of downdrafts at midlevels by evaporational cooling. These organized rotating storms were termed "supercells" (Browning 1962), and it was hypothesized that the inflow branch of such storms carried horizontal vorticity which could be tilted into the vertical and stretched, thereby accounting for observed updraft rotation (Browning and Landry 1963; Barnes 1968; Barnes 1970). Early attempts to explain the anomalous propagation of supercells include the obstacle flow analogy of Newton and Newton (1959) and the Kutta-Joukowski lift force (Kutta 1902; Joukowski 1910) mechanism of Fujita and Grandioso (1968).

The advent of three-dimensional non-hydrostatic models (e.g. Tapp and White 1976; Klemp and Wilhelmson 1978a) soon allowed the investigation of many aspects of severe storms including splitting, rotation, and propagation (e.g. Klemp

and Wilhelmson 1978b; Wilhelmson and Klemp 1978, 1981). Rotunno and Klemp (1982, 1985) explained the preferential enhancement of storms that propagate off the hodograph as a result of favorable vertical pressure gradients (i.e. “dynamic forcing”) generated by both the interaction between a thunderstorm updraft and the environmental wind and the rotation of the updraft itself. This work was verified in the results of Weisman and Klemp (1984), who extended an earlier study to include the effects of curved hodographs.

Rotunno and Klemp (1982, 1985) also partitioned the dynamic pressure forcings into linear (i.e. updraft-shear interaction) and nonlinear terms. They found that the linear terms could account for the bias of right (left) moving storms in clockwise (counterclockwise) turning hodographs, while the nonlinear terms were necessary to explain storm splitting, storm movement off a straight hodograph, and rotationally-induced storm propagation. However, their heuristic model (Rotunno and Klemp 1982) to diagnose the linear pressure perturbations is invalid at low-levels and gives an erroneous pressure distribution if applied throughout the *entire* depth of the troposphere (Davies-Jones 1985, 1996a, 2002, 2003; Davies-Jones et al. 2001). In addition, their decomposition of the pressure forcing into shear and extension terms (Rotunno and Klemp 1985) rather than “spin” and “splat” (Bradshaw and Koh 1981; Adrian 1982) has been called into question as these terms are not invariant to rotation of the coordinate axes (Davies-Jones 2002; Gaudet and Cotton 2003).

Early work on the origins of mid-level rotation (Rotunno 1981; Lilly 1982, 1983) suggested that environmental vortex lines were tilted into the vertical to form a vortex pair straddling the updraft. Based on these earlier studies, Davies-Jones (1984) used linear theory to show that the tilting of storm-relative environmental streamwise vorticity by an updraft can account for initial mid-level

mesocyclogenesis in any generalized wind profile. Both observational and numerical studies (e.g. Lilly 1982, 1983, 1986a,b; Rotunno and Klemp 1982; Weisman and Klemp 1982; Klemp and Rotunno 1983; Brandes 1984; Rotunno and Klemp 1985; Davies-Jones et al. 1990; Droegemeier et al. 1993; Davies-Jones 2002) still support this hypothesis.

The streamwise-vorticity perspective (Davies-Jones 1984) is limited in that it cannot explain storm splitting and nonlinear updraft propagation. It also has been criticized as incomplete (Weisman and Rotunno 2000) because it needs a given updraft motion to predict rotation. However, it has the advantage of allowing an analytic Beltrami flow to be interpreted as a natural paradigm for supercell dynamics (e.g., Davies-Jones 1985; Lilly 1986b).

Weisman and Rotunno (2000) argued that the rotationally-induced propagation theory of Rotunno and Klemp (1982, 1985) is more relevant than the streamwise-vorticity perspective because the dynamic processes of updraft generation and maintenance are essentially nonlinear, regardless of hodograph shape. In addition, they suggested that the idealized Beltrami flow does not adequately capture supercell dynamics. However, using nonlinear formulas for updraft motion in supercell storms and a formal solution for the nonhydrostatic vertical pressure-gradient force, Davies-Jones (2002, 2003) showed that the dynamics of supercell storms for straight and circular shear are different. Nonlinear rotationally-induced propagation was shown to be important for straight shear, while the importance of linear shear-induced propagation increased with hodograph curvature, eventually dominating in the limiting case of a Beltrami flow. Therefore, Davies-Jones (2002) concluded that a combination of both perspectives is necessary to understand the propagation of supercell updrafts in all shears. In all cases, the

tilting of storm-relative environmental streamwise vorticity explained the origin of mid-level rotation.

The development of *low-level* rotation in a homogeneous environment cannot proceed similarly to mid-level mesocyclogenesis because environmental streamlines and barotropic vortex lines cannot turn sharply upward near the ground (Davies-Jones 1982, 1996b, 2000a; Davies-Jones and Brooks 1993; Davies-Jones et al. 2001) in the absence of strong upward pressure-gradient forces. For example, in a simple “in, up, and out” circulation (Davies-Jones 1982) operating in a sheared environment and driven by positive buoyancy aloft, parcels have to rise well above the surface to gain appreciable vertical vorticity as a result of tilting. This vorticity cannot be transported back downward against the flow because the eddies are too weak, a result which has been demonstrated in several numerical simulations (Rotunno and Klemp 1985; Davies-Jones and Brooks 1993; Walko 1993). Strong upward pressure-gradient forces could be generated at the head of a gust-front (e.g., Simpson 1972), but the importance of this effect is unknown. However, as pointed out by Davies-Jones et al. (2001), numerical simulations not able to resolve such an effect still produce strong rotation at the ground.

Strong upward pressure-gradient forces could also be generated by the dynamic-pipe effect (Leslie 1971; Trapp and Davies-Jones 1997), which can build small-scale rotation to the ground in certain environments (e.g., Trapp 1999). Because the large-scale (compared to the scale of a tornado) mesocyclone circulation probably never attains cyclostrophic balance before tornadogenesis and therefore remains porous to radial parcel motions, it is unlikely that the dynamic-pipe effect is important for the *initial* development of rotation near the ground. Since cyclostrophic balance in a mesocyclone would prevent air from entering the sides of the circulation (assuming it is inertially stable), this would imply that trajectories

traveling through the updraft should rotate cyclonically. However, both radar observations and numerical simulations (e.g., Klemp et al. 1981) demonstrate that the trajectories turn *anticyclonically* with the stronger environmental wind, illustrating that the mesocyclone indeed remains quite porous during mesocyclogenesis. Even in a Beltrami flow, where the vortex lines and streamlines coincide, the trajectories turn anticyclonically (Lilly 1986b) and the flow is not cyclostrophic (Davies-Jones et al. 2001). However, Wakimoto et al. (2003) have recently demonstrated that when a tornado is *already present*, the low-level mesocyclone ($z = 400$ m, diameter ~ 4 km) may be in quasi-cyclostrophic balance.

Near-ground mesocyclogenesis in the cool air just behind the gust front therefore must evolve as a result of either (i) the reorientation of baroclinic vortex lines (generated by buoyancy gradients) by the updraft (Klemp and Rotunno 1983; Rotunno and Klemp 1985) and both the downdraft and updraft (Davies-Jones and Brooks 1993; Brooks et al. 1993; Brooks et al. 1994; Wicker and Wilhelmson 1995; Davies-Jones 1996b, 2000a; Adlerman et al. 1999; Davies-Jones et al. 2001), and/or (ii) the downward transport of angular momentum and barotropic vorticity (associated with a mid-level mesocyclone) by a downdraft which spirals into an updraft near the surface (Davies-Jones 2000b; Davies-Jones et al. 2001; Markowski et al. 2003).

Klemp and Rotunno (1983) first attempted the simulation of supercell tornadogenesis within a cloud-scale model, but coarse vertical resolution (500 m) and an extremely short integration time (6 min) limited their work. However, they did reproduce many of the observed features associated with intense near-ground mesocyclogenesis and the occlusion process, such as strong low-level convergent amplification of vertical vorticity and an occlusion downdraft driven by vertical pressure gradient forces (Adlerman et al. 1999). As noted by Wilhelmson and Wicker

(2001), this solution really represents an adjustment of the fine grid to coarse-grid initialization, rather than a true evolution of tornadogenesis.

Building upon a preliminary study limited by a short integration time (Wicker 1990), Wicker and Wilhelmson (1993,1995) simulated the development of tornadic vortices within a classic supercell thunderstorm using a two-way nested grid model. Using a fine grid of 15x15 km and 120 m horizontal grid spacing, two "tornadoes" associated with the same low-level mesocyclone were simulated, each with a lifespan of approximately 10 minutes. Both vortices appeared to develop after the initiation of updraft pulses that built upward with time. Wicker and Wilhelmson (1995) suggested that the pulses were driven by strong vertical pressure gradients induced by a sudden increase in midlevel mesocyclone rotation. However, this hypothesis leads to a somewhat circular argument as to cause and effect. Trajectory analyses revealed that cyclonic vorticity in the mesocyclone was generated mainly from inflow air, and the downdrafts introduced primarily negative vorticity in to the mesocyclone. In addition, they demonstrated that the vorticity dynamics of parcels entering the tornado were substantially different from those entering the mesocyclone, with most of the tornado's vorticity generated along nearly horizontal trajectories that travel through the baroclinic zone near the ground.

A similar study by Grasso and Cotton (1995) also simulated a tornadic vortex within a classic supercell, albeit on a much smaller fine grid of 4x4 km with 100 m horizontal grid spacing. Although a detailed analysis was not undertaken, the vortex built down from the subcloud layer to the surface, continually feeding on low-level vorticity that possibly was produced in the rear-flank downdraft.

More recently, Finley et al. (1998a, 2001, 2002) simulated tornadogenesis within a high-precipitation (HP) supercell. Using a two-way nested grid model with a fine grid of 20x20 km and 100 m horizontal grid spacing, two short lived (45-225 s)

tornadic vortices were simulated. Unlike the simulations of Wicker and Wilhelmson (1995) and Grasso and Cotton (1995), the vortices developed upward along the flanking line of the supercell and were not associated with the main mesocyclone. The first tornado appeared to be associated with increased convergence accompanying a cell merger, while the second tornado apparently was induced by a shearing instability along the gust front.

2.2 Cyclic Mesocyclogenesis and Tornadogenesis

Although our understanding of mesocyclone dynamics has advanced significantly in the last fifteen years, the corresponding process whereby one supercell can produce a periodic succession of low level mesocyclones and tornadoes, i.e. "cyclic mesocyclogenesis/tornadogenesis" has until recently remained relatively uninvestigated.

The phenomenon of cyclic tornadogenesis was first observed well before the dynamics of severe storms became quantified through numerical modeling and theory. Darkow and Roos (1970) studied Missouri tornadoes and observed that approximately 20% of the associated thunderstorms produced multiple tornadoes at intervals ranging from 20 min to 2 h, with a mean period of approximately 45 min. Observations (Fig. 2.2.1) from the Palm Sunday tornado outbreak of 11 April 1965 (Fujita et al. 1970) and the 3 April 1974 "Superoutbreak" (Fujita 1975; Forbes 1975, 1977) emphasized the dominance of cyclic-type supercells in certain environments. Early explanations (Fig. 2.2.2) of this phenomenon included the presence of multiple tornadoes rotating around a single mesocyclone (Snow and Agee 1975; Agee et al. 1976), thereby producing the familiar cycloidal damage paths associated with tornado families (e.g. Forbes 1975).

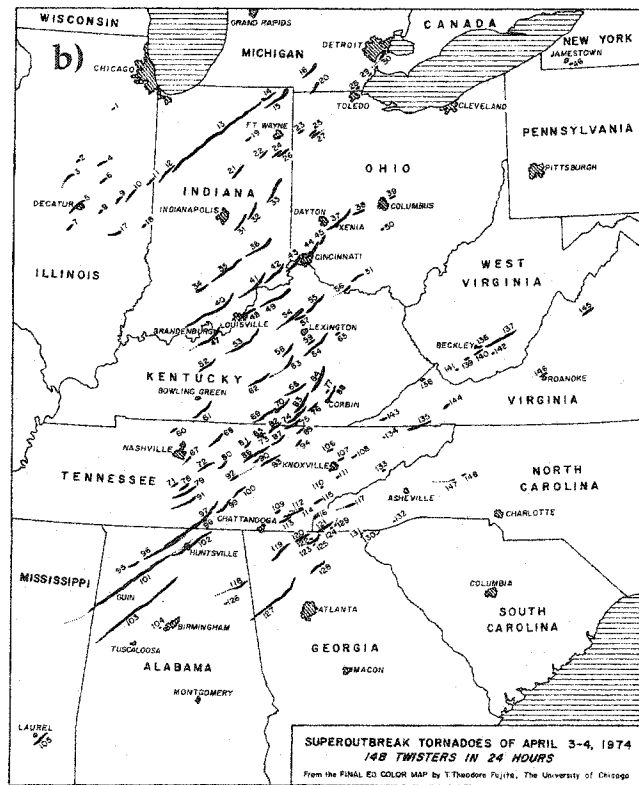
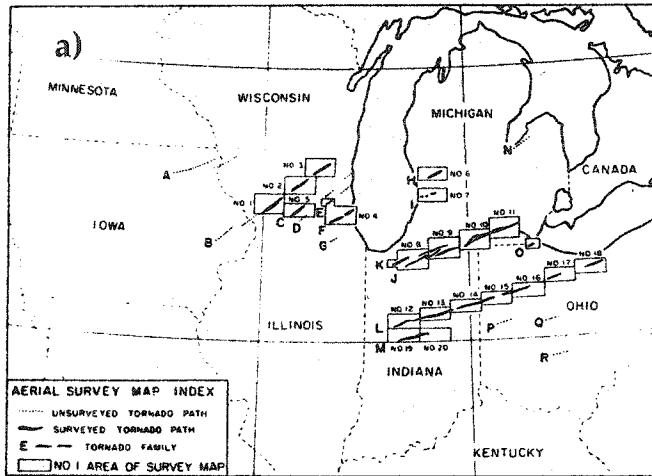


Figure 2.2.1: Tornado paths from a) the 11 April 1965 Palm Sunday tornado outbreak (Fujita et al. 1970) and b) the 3-4 April 1974 "Superoutbreak" (Fujita 1975).

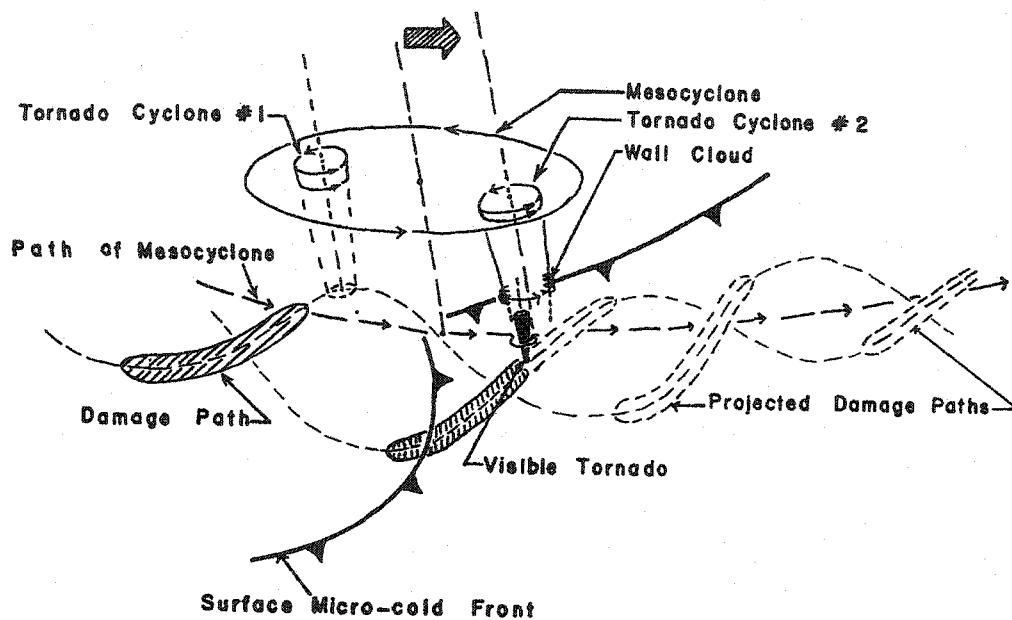


Figure 2.2.2: Schematic from Snow and Agee (1975) [also see Agee et al. 1976] of a mesocyclone containing two tornado cyclones and the accompanying tornado damage paths. Tornado families were theorized to arise from a single long-lived mesocyclone.

Lemon and Doswell (1979) used radar, aircraft, and visual observations to develop a conceptual model of mesocyclone/updraft evolution. They suggested that cyclic tornadogenesis results from the development of a new updraft/mesocyclone following the occlusion of the initial updraft/mesocyclone. This hypothesis later was supported by both field observations (Fig 2.2.3) (e.g. Rasmussen et al. 1982; Jensen et al. 1983) and by a comprehensive survey conducted by Burgess et al. (1982) of National Severe Storms Laboratory (NSSL) single-Doppler radar archives from 1971-1977. The latter study observed that most (76%) mesocyclones consist of a single core during their lifetime (a core being defined as an area of solid-body rotation approximately 4-6 km in diameter within a broader region of cyclonic motion on the order of 20 km in diameter). The remaining cases consisted of multiple cores, forming and dissipating, through a cyclic occlusion process with a period of approximately 40 minutes (Fig. 2.2.4).

Moller et al. (1994) observed that most major tornado outbreaks are composed of classic supercells. However, it is important to note that recent research suggests a continuum of severe storm types which extend not only through the low-precipitation (LP) to high-precipitation (HP) spectrum (Moller and Doswell 1988; Doswell and Burgess 1993; Moller et al. 1994), but also includes such phenomenon as hybrid storms (Foote and Frank 1983; Nelson 1987), transitional storms (Vasiloff et al. 1986; Richardson and Droegemeier 1996, 1998; Richardson 1999), and shallow-topped supercells in hurricane (Novlan and Gray 1974; McCaul 1987, 1991, 1993; McCaul and Weisman 1996) and other environments (Burgess and Davies-Jones 1979; Davies 1993; Kennedy et al. 1993; Foster et al. 1994; Monteverdi and Quadros 1994; Wicker and Cantrell 1996). Consequently, it is likely that a continuum of cyclic-type supercells also exists. For example, Kulie and Lin (1998) simulated a

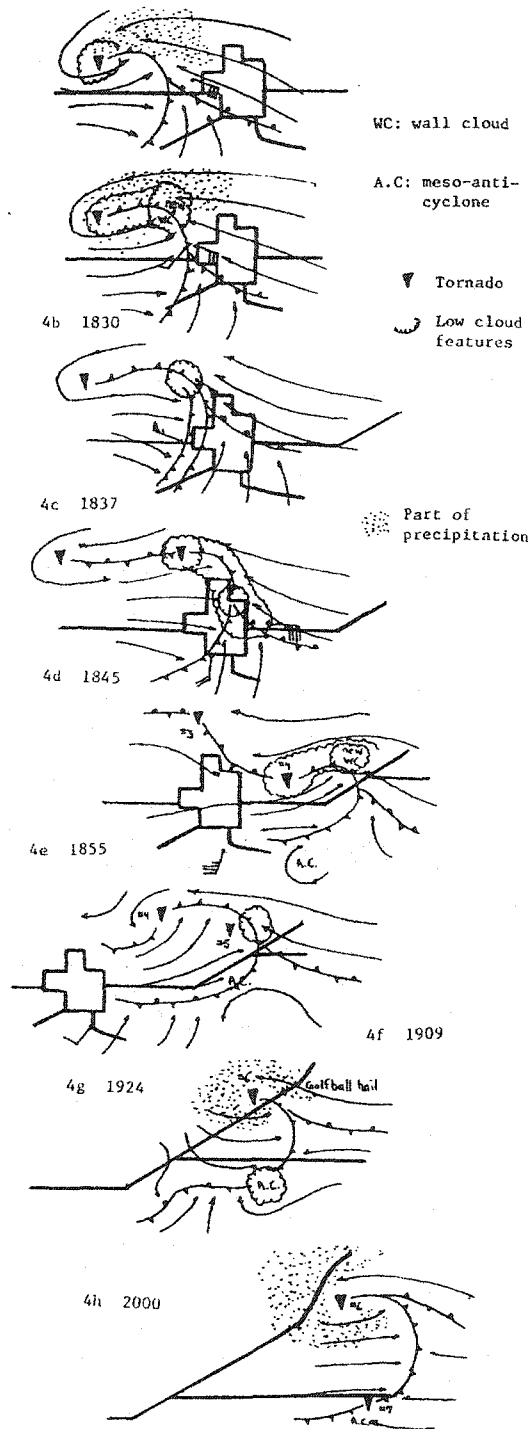


Figure 2.2.3: Schematic from Jensen et al. (1983) showing the evolution of the 19 May 1982 Pampa tornado family.

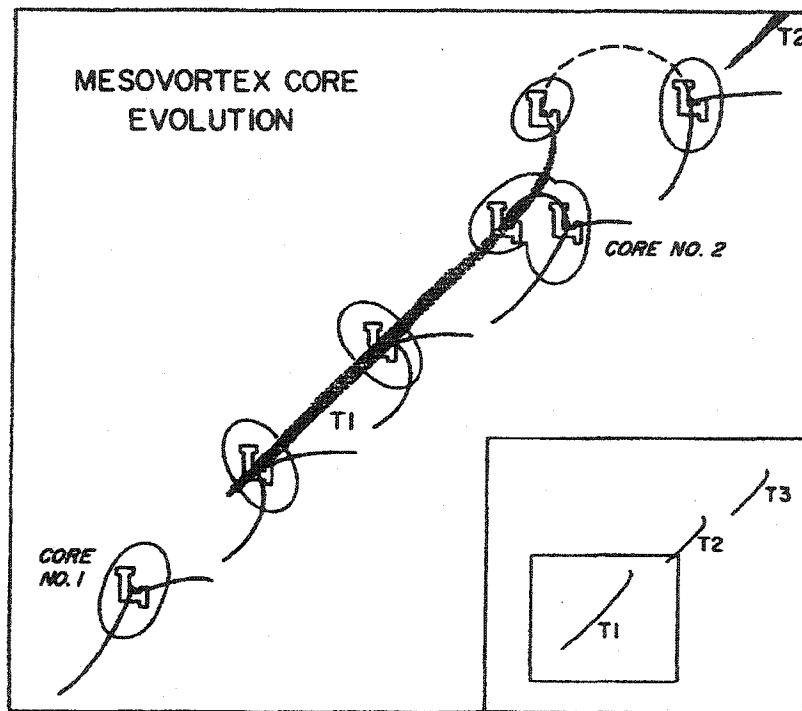


Figure 2.2.4: Conceptual model of mesocyclone core evolution as proposed by Burgess et al. (1982). Dark shaded lines indicate tornado tracks, and thin lines represent low-level wind discontinuities (i.e., rear and forward-flank gust fronts).

unique mode of cyclic low-level mesocyclogenesis in a hybrid HP tornadic supercell that lacked a mid-level mesocyclone throughout its lifetime.

2.3 Recent Work on Cyclic Mesocyclogenesis and Tornadogenesis

Brandes (1993) pointed out that the entire dual-Doppler archive of well-sampled supercell thunderstorms is limited to only approximately 10 cases. Comprehensive dual-Doppler observations of cyclic mesocyclogenesis/tornadogenesis are even more limited (Dowell et al. 1997). Although Johnson et al. (1987) presented limited dual-Doppler observations of cyclic tornadogenesis, Dowell and Bluestein (2002a,b) only recently presented the first high-quality dual-Doppler case study focused on the process of cyclic tornadogenesis. In light of these observational limitations, Adlerman et al. (1999) set out to investigate the process of cyclic mesocyclogenesis in a “classic” supercell thunderstorm through the use of an idealized three-dimensional storm-scale numerical simulation. Their investigation focused primarily on 1) the physical mechanisms responsible for initial mesocyclogenesis, 2) the evolution of the occlusion process and the importance of the rear flank downdraft (RFD), and 3) the process of updraft redevelopment and mesocyclogenesis associated with subsequent cycles.

Using the Advanced Regional Prediction System, ARPS (Xue et al. 1995, 2000, 2001, 2003), Adlerman et al. (1999) simulated a cyclic supercell thunderstorm which underwent two distinct occlusions during a four-hour period, with the beginning of a third indicated near the end of the simulation. The occlusion process exhibited a period of approximately 60 minutes and was qualitatively similar in each case, following the paradigm established by Burgess et al. (1982). The entire cyclic process was logically summarized in a five-stage conceptual model (Fig. 2.3.1). A

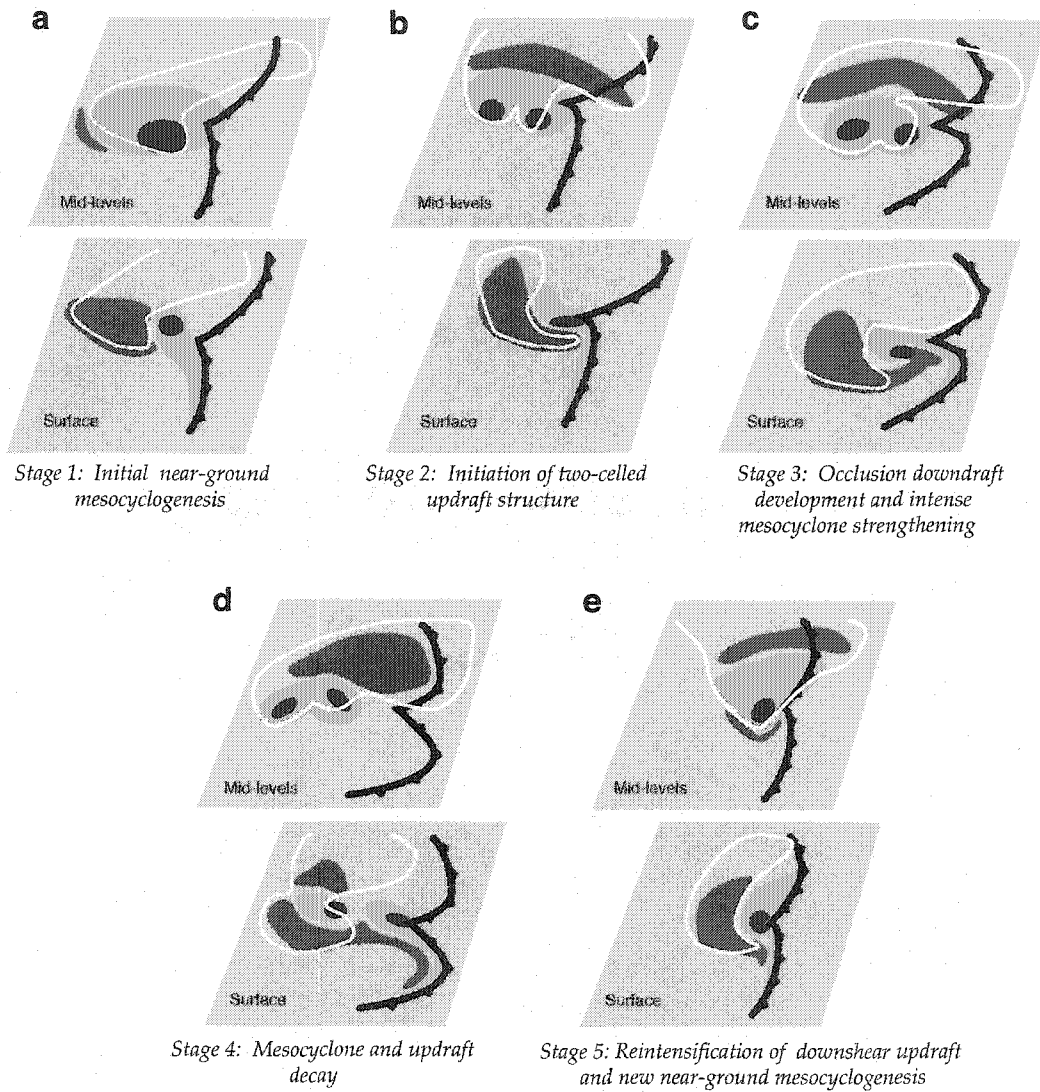


Figure 2.3.1: Schematic diagram of the five-part conceptual model for a single occlusion cycle, as described in Adlerman et al. (1999). Scalloped black line indicates the surface cold-pool boundary. Red indicates areas of vorticity maximum. Light blue indicates updraft areas and dark blue indicates downdraft areas. Single yellow contour indicates the boundary of the rain area.

trajectory analysis in semi-natural coordinates showed that the rapid intensification of an occluding low-level mesocyclone results from the tilting and stretching of streamwise vorticity produced by baroclinic generation, crosswise exchange, and streamwise stretching along descending parcel trajectories in the RFD. This mechanism was consistent with the scenario proposed by Davies-Jones and Brooks (1993) and suggested in the simulations of Grasso and Cotton (1995). Furthermore, although the process of low-level mesocyclogenesis was similar in each cycle, the second and third occlusion occurred more quickly, consistent with previous observational studies (e.g. Rasmussen et al. 1982). This was shown to result from the initial occlusion process itself, as low-level equivalent potential temperature/buoyancy contours are fortuitously oriented such that streamwise baroclinic generation can proceed without delay following the first occlusion.

Based upon an observational study of the 8 June 1995 VORTEX case, Dowell and Bluestein (2000) proposed a hierarchical classification of cyclic tornadogenesis modes. Characterizing the Adlerman et al. (1999) simulation as an 'outflow-dominated mode', the classification progresses to the 'balanced' and 'inflow-dominated' modes, depending on the relative motions of the main updraft and the low-level vorticity centers (Fig 2.3.2). Dowell and Bluestein (2002a,b) elaborated further upon this conceptual model, demonstrating the correlation between the updraft's relative motion and the transitions between modes of cyclic behavior during a single storm's lifetime (Fig 2.3.3). They also concluded that the cyclic modes simulated previously (Klemp 1987; Adlerman et al. 1999) are fundamentally different from their observations, since new vortices in their observations tended to form on the east side of the same updraft rather than from new updrafts along the gust front. However, as pointed out by Adlerman and Droegemeier (2000), this distinction may be more a reflection of the separation between the old and new

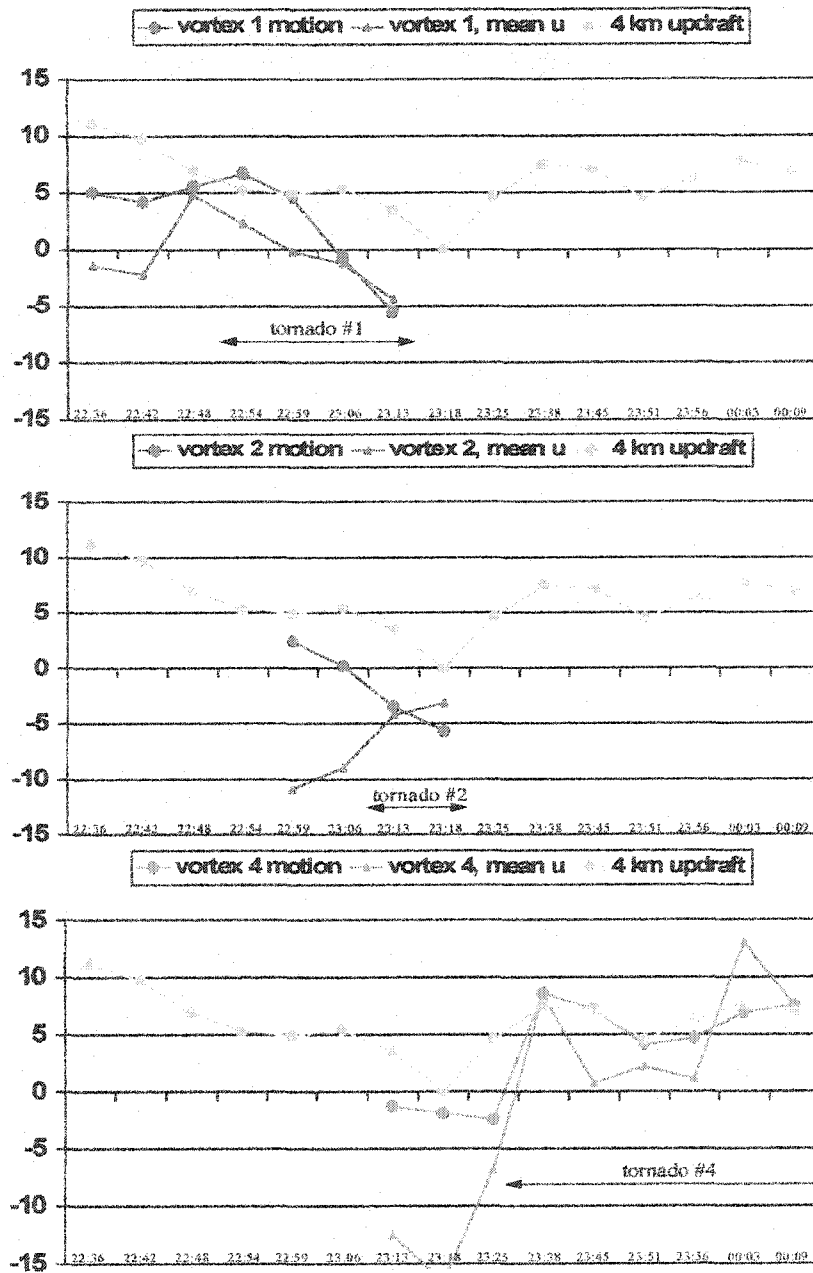


Figure 2.3.2: Comparison of the eastward motion of a tornadic updraft with the motion of the vorticity maxima, as described in Dowell (2000). Purple circles indicate the u-component of motion for the updraft center at 4 km AGL. Red, blue, and green circles indicate the observed values of u of the vorticity maxima corresponding to tornadoes #1, #2, and #4, respectively, at 500 m AGL. The time intervals when the vortices are tornadic are indicated. Triangles indicate the local mean value of u at z = 500 m within circles of diameter 5 km around the vorticity maxima.

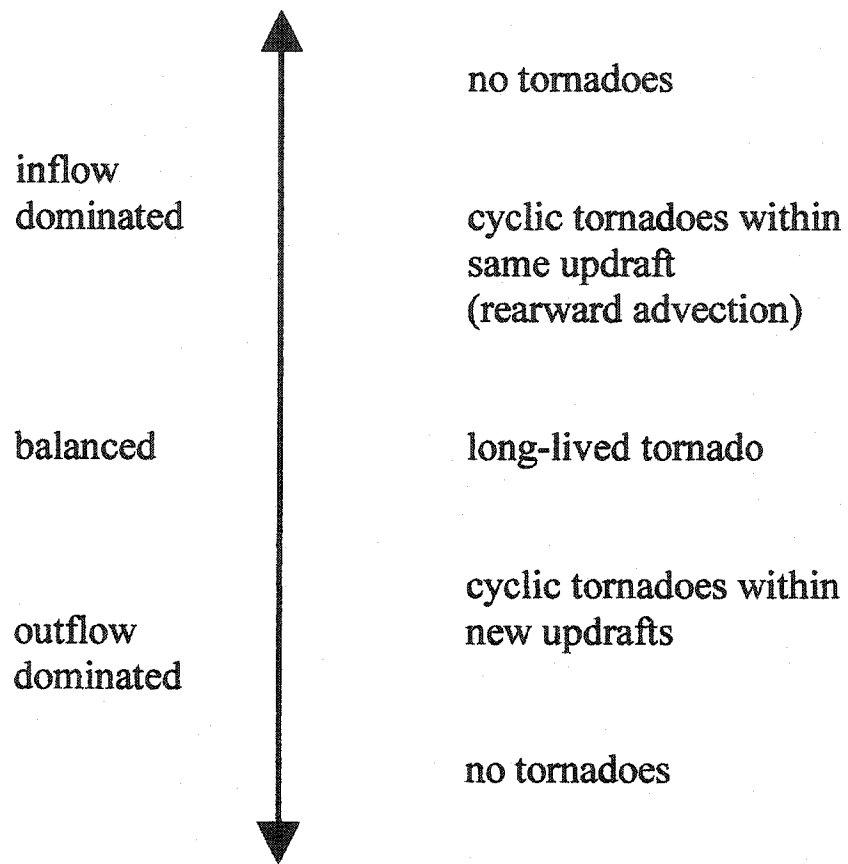


Figure 2.3.3: Characterization of supercell behavior according to inflow and outflow strength (from Dowell 2000).

tornado cyclones. As the separation distance decreases, there exists a regular progression from a nearly discrete updraft, to a dual updraft, to a unicellular updraft with smaller maxima embedded within.

As a first step toward identifying and understanding the conditions necessary to produce cyclic redevelopments within supercell updrafts, Adlerman and Droegemeier (2002) examined the effects of variations in model physical and computational parameters upon the cycling process. [Although this study is a part of this dissertation, it already has been published and is described only briefly here.] Changes in grid spacing, numerical diffusion, microphysics, and the coefficient of surface friction were found to alter the number and duration of simulated mesocyclone cycles (Fig 2.3.4). A decrease from 2.0 km to 0.5 km in horizontal grid spacing transformed a nearly perfectly steady, non-cycling supercell into one that exhibited three distinct mesocyclone cycles during the same time period. Decreasing the minimum vertical grid spacing at the ground tended to speed up the cycling process, while increasing it had the opposite effect. Ice microphysics was shown to cut short the initial cycling, while both simple surface friction and increased numerical diffusion tended to slow it down. Combining competing effects (i.e. ice microphysics with friction) tended to bring the simulation back to the evolution found in the control case. In summary, it was shown that the configuration of a numerical model could influence all of the important dynamics of cyclic regeneration to a degree that overwhelmed any intrinsic cyclic behavior.

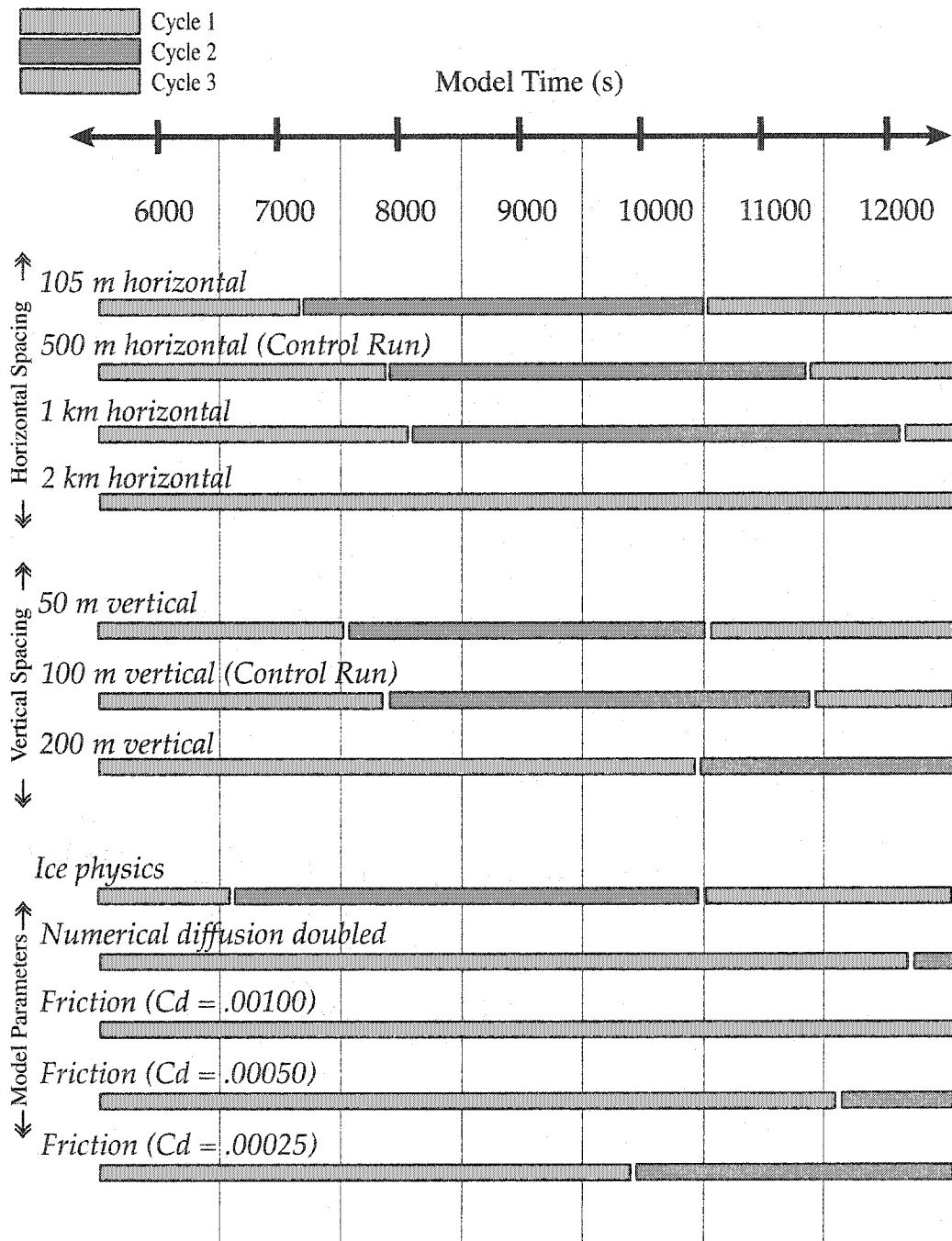


Figure 2.3.4: Variations in the timing and length of each mesocyclone cycle for changes in the horizontal grid spacing, changes in the vertical grid spacing, and changes in model physics and parameters. These simulations are described in Adlerman and Droegemeier (2002).

CHAPTER 3

SENSITIVITY OF CYCLIC MESOCYCLOGENESIS TO ENVIRONMENTAL WIND AND THERMODYNAMIC STRUCTURE

3.1 Introduction

Because numerical simulations (e.g., Weisman and Klemp 1982, 1984; Brooks et al. 1993; 1994), observations (e.g., Rasmussen and Straka 1998), and theory (e.g., Davies-Jones 2002) suggest that both hodograph shape and the magnitude of vertical environmental shear influence storm morphology, this part of the study examines the influence of variations in the environmental wind profile on cyclic mesocyclogenesis. Although thermodynamic parameters also have a profound influence upon supercell character (e.g., Davies 2002), only limited variations in CAPE are examined in order to keep the number of simulations reasonable. Therefore, multiple variations in hodograph shape, shear magnitude, shear distribution, and CAPE are examined with the intent of identifying corresponding trends in cycling behavior and explaining their cause.

3.2 Methodology

The simulation experiments are conducted using Version 5.0 of the Advanced Regional Prediction System (ARPS), a three-dimensional, nonhydrostatic model developed for storm scale numerical weather prediction (Xue et al. 2000, 2001, 2003). Similar to Adlerman et al. (1999) and Adlerman and Droegemeier (2002), the simulations are conducted using a horizontally homogeneous environment that is perturbed with an ellipsoidal thermal bubble. The computational grid has uniform horizontal spacing of 0.5 km within a 100 x 100 x 16 km domain, with 43 levels in the vertical. The vertical grid spacing varies smoothly from 100 m at the ground to 700

m near the top of the domain. This results in the lowest scalar grid point located at a height of 50 m, the level that we will interchangeably describe as “surface” or “near-ground.” Fourth-order advection is used in all directions for both scalar and vector fields. Cloud microphysics is treated using the Kessler warm-rain parameterization scheme, while subgrid-scale turbulent mixing is represented using a 1.5-order turbulent kinetic-energy closure. We have neglected ice physics in these simulations because we wanted to establish a control run that was as close as possible to that used in Adlerman and Droegemeier (2002). The Coriolis force, surface friction, surface physics, and terrain are not included. The model is integrated for four hours, and history files are saved every five minutes after 3300 s. A summary of model parameters is shown in Table 3.1.

At a horizontal grid spacing of 500 m, we note that it is unlikely that our solution is numerically converged (Adlerman and Droegemeier 2002). Since numerical convergence and the correct representation of an inertial subrange do not probably occur until horizontal grid spacings are less than 100 m (Bryan et al. 2003), it would be computationally unfeasible to conduct a large parameter study within such constraints. Although varying the grid spacing between 105 m and 1 km in Adlerman and Droegemeier (2002) did change the speed of cycling, *it did not fundamentally change the storm morphology or the mode of cycling*. Only when the grid spacing approached a size at which the mesocyclone was no longer well resolved (i.e., 2 km), was there a fundamental shift in behavior. Since the purpose of this study is to classify *general* trends in cycling based upon shear and hodograph shape, changes in grid resolution would not necessarily invalidate any of the results. More likely, they would merely shift the parameter space, analogous to the effect of changing CAPE (Sec. 3.5.4). Similarly, sensitivities to microphysics, numerical

Parameter	Symbol	Value
Horizontal resolution	$\Delta x, \Delta y$	500 m
Vertical resolution	Δz	$100 \text{ m} \leq \Delta z \leq 700 \text{ m}$
Large time step	Δt	2.5 s
Small time step	$\Delta \tau$	0.5 s
Coriolis parameter	f	0.0 s^{-1}
Nondimensional surface drag coefficient	C_d	0.0
Fourth-order horizontal mixing coefficient	K_4	$1.25 \times 10^8 \text{ m}^4 \text{ s}^{-1}$
Second-order vertical mixing coefficient	K_2	$16 \leq K_2 \leq 784 \text{ m}^2 \text{ s}^{-1}$
Divergence damping coefficient	a	0.05
Initial thermal perturbation:		
Magnitude	$\Delta \Theta$	4.0 K
Horizontal Radius	x_r, y_r	9 km
Vertical Radius	z_r	1.5 km
Height of center above ground	z_c	1.5 km
Microphysics	Kessler warm-rain parameterization	
Lateral boundary conditions	Radiation	
Top boundary condition	Rigid with Rayleigh sponge layer	
Grid stretching function	Hyperbolic tangent	
Horizontal and vertical advection	Fourth-order	
Turbulence parameterization	Anisotropic 1.5-order TKE closure	

Table 3.1: Physical and computational parameters used in the control simulation

diffusion, and surface friction would also shift the parameter space, but leave the general findings valid.

3.3 Design of the Parameter Space

3.3.1 *Review of past parameter space studies*

In order to perform an environmental sensitivity study, we are faced with the challenge of constructing a parameter space that is broad enough to cover what we believe to be the full range of cyclic behavior, yet narrow enough to keep the number of simulations reasonable. It is thus appropriate to briefly review some of the methodologies that have been used in past parametric studies. We focus only on the setup of the numerical experiments rather than their results.

Weisman and Klemp (1982) utilized a well-known analytic moisture profile (i.e., now known as the “Weisman-Klemp” sounding) in their study of numerically-simulated storm structure. A straight hodograph (i.e., unidirectional shear) was used, but the shear was non-uniform with height and specified by a hyperbolic tangent function. The hodograph length ranged from 0-45 m s^{-1} , with most of the shear located below 6 km. CAPE was varied from approximately 1000-3000 J kg^{-1} .

A follow-up study by Weisman and Klemp (1984) used the same moisture profile, but with a half-circle hodograph of uniform vertical shear. The depth of turning was held constant at 5 km, with constant winds above. Hodograph radii varied from 3.2-15.9 m s^{-1} and the soundings’ CAPE was constant at approximately 2200 J kg^{-1} .

Klemp and Weisman (1983) and Weisman and Klemp (1986) described a broader set of simulations using seven different wind profiles that covered a range of storm morphologies including multicells, supercells, and squall lines. The sounding again was the Weisman and Klemp (1982; 1984) analytic profile with the

CAPE held constant at 2200 J kg^{-1} . The hodographs' geometries used were straight, quarter-circle, quarter-circle with a tail (rectilinear shear), and half-circle.

Brooks and Wilhelmson (1993) studied the effects of hodograph curvature upon simulated storm intensity. The thermodynamic profile used was similar to that of Weisman and Klemp (1982; 1984), except with slightly drier midlevels. CAPE was held constant at approximately 2100 J kg^{-1} . Varying levels of hodograph curvature from 0-3 km were combined with several rectilinear shear profiles from either 3-7 km or 3-11 km. The curvature ranged from a nearly straight profile to one that approached a half-circle. The low-level shear was non-uniform, with the curvature profile specified by a linear increase with height of both the wind speed and change in wind direction. A smaller subset of these soundings was used by Brooks et al. (1993; 1994) to investigate the necessary conditions for the development and maintenance of low-level mesocyclones.

Droegemeier et al. (1993) investigated the influence of 0-3 km storm-relative environmental helicity (hereafter SRH₃) on simulated storm structure. The Weisman and Klemp (1982; 1984) thermodynamic profile was used, with a constant CAPE of approximately 2500 J kg^{-1} . Four sets of hodographs were used: quarter-circles, half-circles, three-quarter circles, and full-circles. The depth of turning varied from 2-4 km for the quarter-circle hodographs, and from 2-8 km for all other cases, with constant winds above the turning layer. The hodographs were constructed such that all had the same mean shear of $7.85 \times 10^{-3} \text{ s}^{-1}$.

Jahn (1995) investigated simulated storm environments in which the 0-6 km bulk Richardson number shear (hereafter BRNsh₆) and SRH₃ might predict different storm morphologies. The thermodynamic profile used was that of Weisman and Klemp (1982; 1984), with CAPE held constant at approximately 2500 J kg^{-1} . The hodographs were constructed with varying low-level shears below 4 km, rectilinear

shear between 4-12 km, and constant winds above 12 km. All of the low-level hodographs (0-4 km) consisted of a circular arc with uniform shear. The radii ranged from 6.5-38.3 m s⁻¹ with turning angles varying from 40-300 degrees.

Gilmore and Wicker (1998) conducted simulations to study the role of downdraft CAPE (DCAPE) in supercells. They used the 20 May 1977 Del City sounding, but with the wind profile replaced by a straight hodograph with most of the vertical shear confined below 6.7 km (similar to that used by Rotunno and Klemp 1985). Using constant vertical shear and CAPE, they changed DCAPE by varying moisture above the surface layer.

Weisman and Rotunno (2000) conducted a set of simulations to compare several theories of storm dynamics, i.e. those based upon updraft-shear interaction, SRH₃, and Beltrami flow. They employed the Weisman and Klemp (1982; 1984) thermodynamic profile and used four different hodographs: straight, quarter-circle with tail (i.e., rectilinear shear above 2 km), half-circle, and full-circle. The first three had a constant length of 35 m s⁻¹ with winds constant above 6 km, while the full-circle extended the half-circle hodograph to 12 km. The shear was uniformly distributed with height in all cases.

McCaul and Weisman (2001) studied the effects on storm structure of altering the shapes of the thermodynamic and wind profiles. They developed a new method of creating analytic soundings that allowed for independent specification of the CAPE, lifting condensation level (LCL), level of free convection (LFC), and the profiles of moisture, buoyancy, and shear. For this study, they constructed analytic thermodynamic profiles with a constant LCL of 454 m and equal to the LFC. For CAPE values set at 800 and 2000 J kg⁻¹, the level of maximum buoyancy was varied between 2.53-5.5 km and 4.1-7.1 km, respectively. Both straight and approximate half-circle hodographs also were constructed using a similar analytic technique. The

shear was distributed non-uniformly with height, with the amount of low-level shear increased (decreased) by essentially shifting the hodograph height points upward (downward).

McCaul and Cohen (2002) extended the work of McCaul and Weisman (2001) to study the influence of mixed layer and moist layer depths on storm structure. The mixed layer depth was represented by the height of the LCL, while the moist layer depth above was represented by the height of the LFC. Soundings were constructed as in McCaul and Weisman (2001), with approximate half-circle hodographs and CAPE values set at 800 and 2000 J kg⁻¹. In the first set of simulations, the LCL was set equal to the LFC and was varied from 0.5-2.0 km in 0.5 km increments. A second pair of simulations was also conducted, with the LFC set at 1.6 km, and the LCL set to 0.5 km.

In summary, a wide range of shear structures and hodograph shapes have been used in past studies. However, only a handful of authors (Klemp and Weisman 1983; Weisman and Klemp 1986; Droegemeier et al 1993) have examined a full range of hodograph shapes and shear magnitudes in the context of a single study. In addition, the thermodynamic differences between soundings have been very limited until the recent work of McCaul and Weisman (2001) and McCaul and Cohen (2002). Almost all previous parameter studies have been based upon an analytic sounding similar to that of Weisman and Klemp (1982), which contains an almost tropical moisture profile. [This profile was originally used to help counteract the model's tendency to mix out shallow low-level moisture. This problem is sometimes still evident when trying to initialize an observed sounding case with a warm bubble, but this is more likely a limitation of the simple initialization technique and coarse horizontal resolution, rather than the result of the microphysics and turbulence schemes.]

3.3.2 Design of the parameter space

The conceptual model of cyclic mesocyclogenesis presented in Adlerman et al. (1999) emphasized the relative motion of the gust front and storm updraft as a key component of the occlusion process. This implies that the magnitude and location of the storm's precipitation are critically important, as is the magnitude of the storm-relative inflow. Brooks et al. (1994) noted that variations in the 3-7 km (i.e. mid-level) shear could alter the distribution of precipitation within a storm and thereby influence the characteristics of the low-level mesocyclone. Jahn (1995) found that $BRNsh_6$ appeared to be the best discriminant for predicting mesocyclone intensity as a result of its correlation with storm-relative surface inflow. However, a more recent climatology by Rasmussen and Straka (1998) suggested that the storm-relative flow at 9-10 km was most closely correlated with the classification of storm type via precipitation distribution (i.e., LP, Classic, and HP) as a result of variations in the amount of hydrometeors that are reingested into the updraft after being transported away in the anvil. They suggested that a so-called "deep" BRN shear (hereafter $BRNsh_9$), measured between the boundary layer and 9 km, may be the best discriminant of storm type. If one assumes that the delineation between cyclic and non-cyclic storms may also be a function of precipitation and surface inflow, a deep BRN might be similarly useful.

When it comes to discriminating between tornadic and non-tornadic supercells, recent observational work suggests that somewhat different quantities may be important. Davies (2002) noted that given an environment supportive of supercells, lower CIN, lower LFC heights, and higher 0-3 km CAPE favored tornadic storms. Craven et al. (2002) found that tornadic storms were favored when the 0-1 km shear (magnitude of the vector difference) was large and when the 100 mb mean

layer LCL (MLLCL) was low. These findings were confirmed and extended in Brooks and Craven (2002). Rasmussen (2003), updating a prior study by Rasmussen and Blanchard (1998) (also see Markowski et al. 1998), also found that tornadic storms were favored by lower LCL heights, higher 0-3 km CAPE, higher 0-1 km SRH (hereafter SRH_1), and a higher energy-helicity index (EHI, Hart and Korotky 1991) modified to use SRH_1 . Many of these findings were supported by previous analyses of RUC-2 forecast soundings by Edwards and Thompson (2000) and Thompson et al. (2002a,b).

Beyond traditional measures used to classify environments supportive of supercells (e.g. the BRN or the EHI), it appears that different parameters may differentiate between the type of supercell (i.e. LP, HP, or classic) versus its tornadic potential. It is not obvious which set of indices might be better related to storm cycling, particularly because one might argue that a tornadic storm is much more likely to undergo an occlusion process than a nontornadic one as a result of stronger near-ground rotationally-induced downdrafts. However, it is equally probable that a non-tornadic outflow-dominant supercell (or possibly an HP supercell) might be more likely to occlude as a result of stronger surges in gust front motion. This situation is further complicated because our simulations cannot accurately resolve the difference between a tornadic and non-tornadic simulated storm, so it is questionable how applicable a particular index might be.

Rather than basing our parameter space upon a specific index and constructing hodographs that cover a limited range of that parameter, we instead utilize the full range of hodograph shapes for this study and use only those which produce sustainable supercell storms. We base our control run upon the half-circle hodograph because it represents an idealization of our previous simulations and has been used extensively in previous parameter studies. We then extend the study to

include straight, quarter-circle (with and without additional rectilinear shear), three-quarter circle, and full-circle hodographs. Variations in CAPE are limited to a few cases.

3.4 Simulation Overview and the Control Experiment

3.4.1 Introduction

Before we begin our description of the simulations, several clarifications are in order. First, we define the moment of “occlusion” as the time when a near-ground mesocyclone becomes detached from the gust-front and wraps downdraft air completely around itself (Fig. 3.4.1). This is consistent with the descriptions in Adlerman et al. (1999) and Adlerman and Droegemeier (2002). By definition, an occlusion separates two cycles of a storm undergoing occluding cyclic mesocyclogenesis (OCM). Therefore, e.g., if a storm undergoes four cycles it must occlude three times. During a particular cycle, the storm’s near-ground mesocyclone may undergo strengthening and weakening with both periodic and/or pulsating behavior. As long as the mesocyclone does not completely disappear and reform in a different location, such behavior would still be classified as one cycle.

We define *non-occluding* cyclic mesocyclogenesis (NOCM) as the repeated development of near-ground mesocyclones which do not go through an occlusion process as part of their weakening and dissipation phase. Oftentimes, this process occurs when near-ground mesocyclones move down the gust front away from the main updraft, rather than wrapping back into the precipitation core. They become separated from the main updraft, and a new mesocyclone will form farther northward, near the forward-flank precipitation boundary (Fig 3.4.1).

Both occluding and non-occluding cyclic mesocyclogenesis may occur during a storm’s lifetime. In order to avoid confusion between OCM and NOCM, all

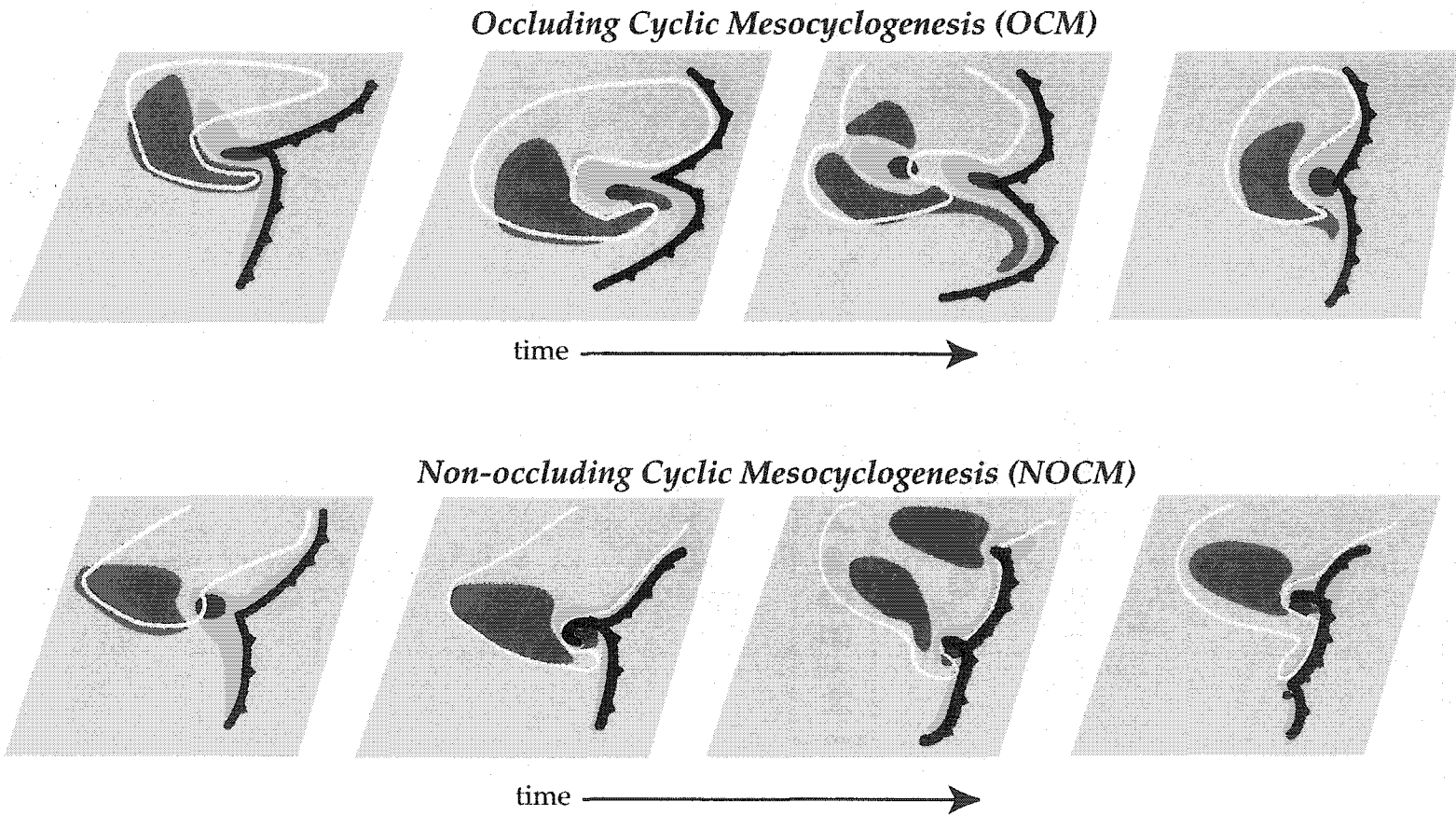


Figure 3.4.1: Schematic of the approximate surface patterns for occluding and non-occluding cyclic mesocyclogenesis. Scalloped black line indicates the surface cold-pool boundary. Red indicates area of vorticity maxima. Light blue indicates updraft areas and dark blue indicates downdraft areas. Single yellow contour indicates the boundary of the rain area.

references to “occlusions” will refer to the occluding mode of cyclic mesocyclogenesis. References to “cycles” will be clarified as OCM cycles (i.e., “occlusion cycles”) or NOCM cycles. In addition, all cycling schematics will use different representations for OCM and NOCM, with NOCM cycles notated as “Meso 1”, “Meso 2”, etc...

3.4.2 *The Control Experiment*

In our previous simulations (Adlerman et al. 1999; Adlerman and Droegemeier 2002), the horizontally homogeneous base state was initialized using a composited sounding (Fig 3.4.2) associated with the well documented 20 May 1977 Del City, Oklahoma Storm (e.g. Ray et al. 1981, Johnson et al. 1987). This sounding has a CAPE of 2673 J kg^{-1} , calculated using the virtual temperature correction and accounting for water-loading (i.e., using the adiabatic liquid water content in the virtual temperature calculation, similar to the “density temperature” as defined by Emanuel 1994, p113). When calculated without these modifications, the CAPE is 3777 J kg^{-1} . In all further discussions, the uncorrected method of calculation will be used because it is consistent with the definition of the bulk Richardson number (Weisman and Klemp 1982).

In order to establish a control sounding in which the vertical shear can be modified easily, it is useful to develop an idealization of the Del City wind profile. After rotating the original Del City hodograph by 15 degrees, re-centering, and estimating its termination point at 10 km, the Del City hodograph is approximated by a half-circle hodograph of radius 19 m s^{-1} (Fig. 3.4.3), with uniform shear throughout the depth of turning (0-10 km). This yields a BRNsh_c (BRNsh_o) of approximately 13.4 (17.5) m s^{-1} compared to 12.3 (15.5) m s^{-1} for the original Del City sounding. A listing of sounding parameters is shown in Table 3.2.

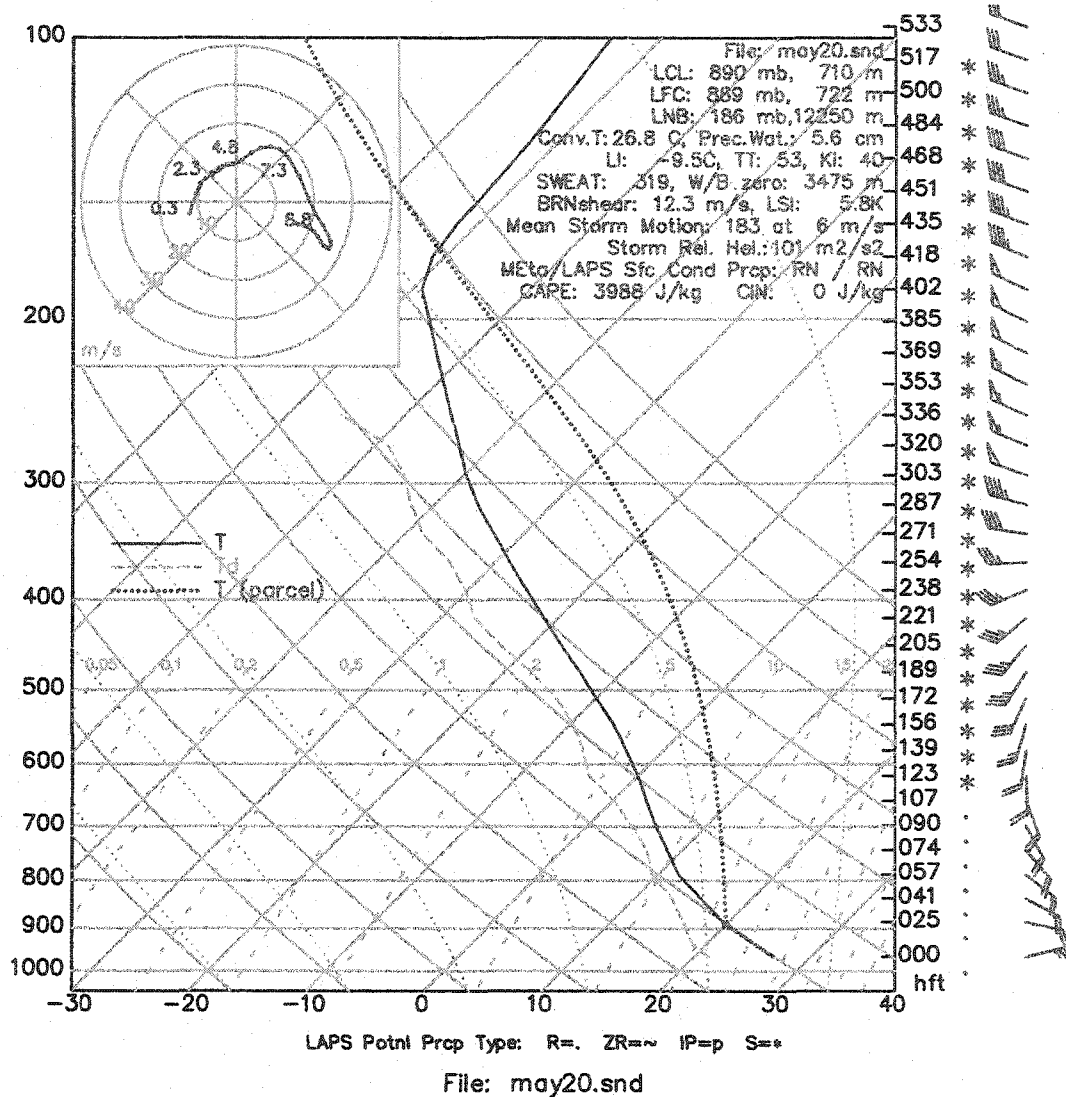


Figure 3.4.2: Sounding and hodograph from the 20 May 1977 Del City, Oklahoma, storm. Both are composited from the 1500 UTC Fort Sill, Oklahoma, and 1620 UTC Elmore City, Oklahoma, soundings, as described in Ray et al. (1981).

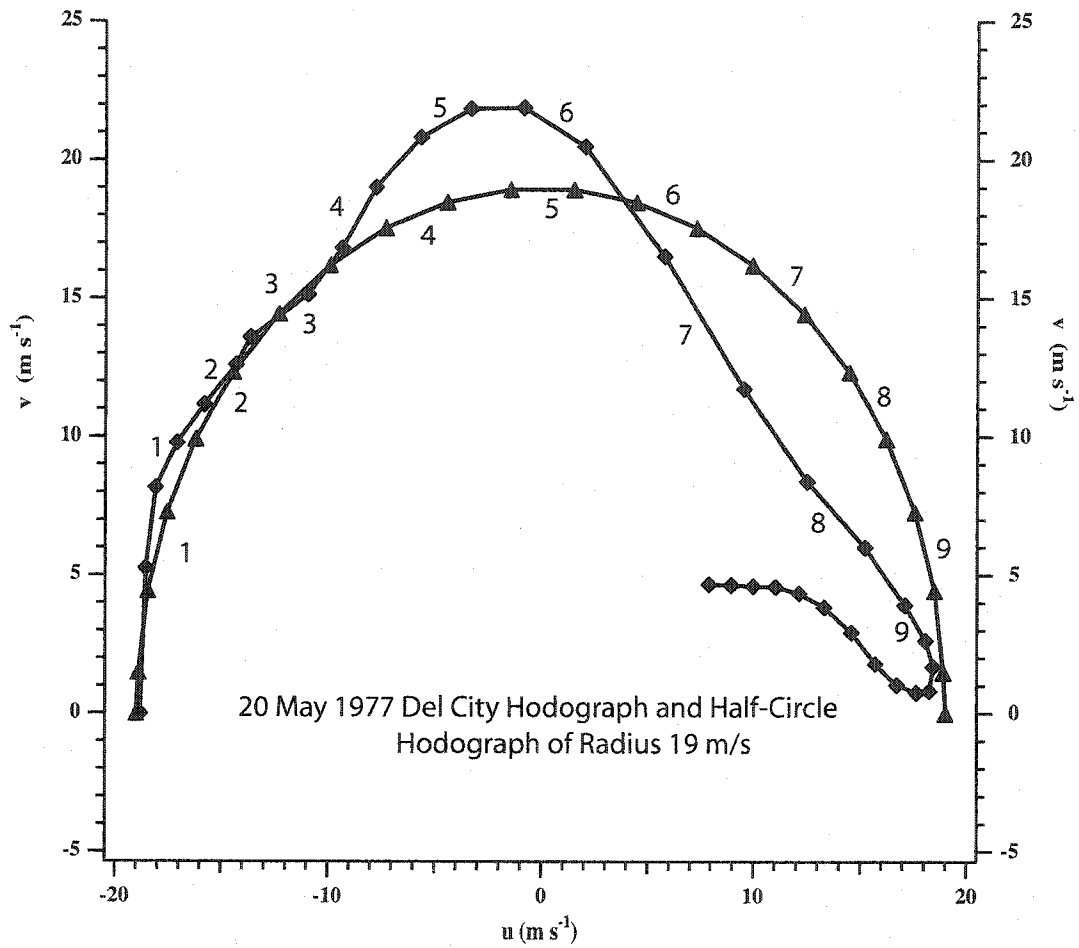


Figure 3.4.3: Hodograph from the original 20 May 1977 Del City case (diamond points, Ray et al. 1981) and the idealized half-circle hodograph (triangle points) with a radius of 19 m s⁻¹ and a turning depth of 10 km.

<i>Simulation Name and Abbreviation</i>	<i>Description</i>	<i>CAPE (J kg⁻¹)</i>	<i>BRN shear (m s⁻¹)</i>	<i>BRN</i>	<i>Deep BRN shear (ms⁻¹)</i>	<i>Deep BRN</i>	<i>SRH 0-1km (m²s⁻²)</i>	<i>SRH 0-3km (m²s⁻²)</i>	<i>SR Sfc. Inflow (ms⁻¹)</i>
Control	Half circle, $r = 19 \text{ m s}^{-1}$ from 0-10 km, $qv_{\text{sfc}} = 16.4 \text{ g kg}^{-1}$	3777	13.4	42	17.5	25	87 (73)	244 (166)	16.2
Half_r15	Half circle, $r = 15 \text{ m s}^{-1}$ from 0-10 km	3777	10.6	67	13.8	40	55 (50)	155 (116)	12.9
Half_r25	Half circle, $r = 25 \text{ m s}^{-1}$ from 0-10 km	3777	17.7	24	23.0	14	153 (114)	431 (251)	21.4
Half_r30	Half circle, $r = 30 \text{ m s}^{-1}$ from 0-10 km	3777	21.2	17	27.7	10	201 (164)	570 (361)	23.7
Half_r35	Half circle, $r = 35 \text{ m s}^{-1}$ from 0-10 km	3777	24.7	12	32.3	7	250 (223)	700 (490)	37.6
Half6_r9	Half circle, $r = 9 \text{ m s}^{-1}$ from 0-6 km	3777	9.0	92	10.7	66	46 (44)	120 (103)	10.6
Half6_r11	Half circle, $r = 11 \text{ m s}^{-1}$ from 0-6 km	3777	11.4	58	13.5	41	67 (70)	185 (166)	12.0
Half6_r15	Half circle, $r = 15 \text{ m s}^{-1}$ from 0-6 km	3777	15.0	33	17.8	24	123 (120)	372 (281)	15.5
Half6_r18	Half circle, $r = 18 \text{ m s}^{-1}$ from 0-6 km	3777	18.0	23	21.4	17	173 (170)	517 (394)	18.5
Half6_r21	Half circle, $r = 21 \text{ m s}^{-1}$ from 0-6 km	3777	21.0	17	25.0	12	261 (227)	785 (521)	23.6
Ctrl_c2233	Control, but with qv_{sfc} lowered to 13.8 g kg^{-1}	2233	13.4	25	17.5	15	87 (73)	244 (166)	16.2
Ctrl_c2991	Control, but with qv_{sfc} lowered to 15.4 g kg^{-1}	2991	13.4	33	17.5	20	87 (73)	244 (166)	16.2
Ctrl_c4353	Control, but with qv_{sfc} increased to 17.3 g kg^{-1}	4353	13.4	48	17.5	28	87 (73)	244 (166)	16.2
Ctrl_c5086	Control, but with qv_{sfc} increased to 18.5	5086	13.4	57	17.5	33	87 (73)	244 (166)	16.2

Table 3.2: Summary of the model soundings and their derived parameters

	g kg ⁻¹								
Shift_L1	Control, with shear shifted downward	3777	19.2	20	22.1	15	369(382)	547 (478)	20.6
Shift_L2	Control, with shear shifted downward	3777	18.2	23	21.7	16	201 (183)	459 (335)	20.0
Shift_L3	Control, with shear shifted downward	3777	16.8	27	20.4	18	147 (136)	381 (277)	18.1
Shift_L4	Control, with shear shifted downward	3777	14.8	34	18.8	22	108 (94)	292 (207)	17.5
Shift_U1a	Control, with shear shifted upward, conducted to test the sensitivity of Shift_U1	3777	12.5	48	16.7	27	72 (61)	208 (142)	15.1
Shift_U1	Control, with shear shifted upward	3777	11.7	54	15.9	30	67 (53)	192 (122)	15.1
Shift_U1b	Control, with shear shifted upward, conducted to test the sensitivity of Shift_U1	3777	11.0	62.5	15.2	33	62 (45)	179 (107)	15.1
Shift_U2	Control, with shear shifted upward	3777	10.3	71	14.5	36	49 (39)	141 (93)	13.8
Shift_U3	Control, with shear shifted upward	3777	9.1	91	13.1	44	41 (31)	118 (73)	12.7
Shift_U4	Control, with shear shifted upward	3777	7.4	139	10.8	65	25 (20)	72 (50)	10.3
Qtr3_1000	Quarter-circle, $r = 10 \text{ m s}^{-1}$ from 0-3 km	3777	8.9	68	9.9	54	43 (46)	111 (94)	9.5
Qtr3_1010	Quarter-circle, $r = 10 \text{ m s}^{-1}$ from 0-3 km, tail length 10 m s^{-1} from 3-9 km	3777	9.6	82	11.8	54	50 (47)	127 (106)	10.9
Qtr3_1020	Quarter-circle, $r = 10 \text{ m s}^{-1}$ from 0-3 km, tail length 20 m s^{-1} from 3-9 km	3777	10.4	70	13.9	39	58 (54)	144 (118)	12.4
Qtr3_1020_rotCL	Qtr_1020, with tail rotated 45° clockwise	3777	9.0	92	11.1	61	49 (50)	139 (113)	9.6
Qtr3_1020_rotCC	Qtr_1020, with tail rotated 45° counter- clockwise	3777	10.9	63	14.9	34	65 (52)	145 (105)	14.9
Qtr3_1040	Quarter-circle, $r = 10 \text{ m s}^{-1}$ from 0-3	3777	12.0	52	18.5	22	84 (61)	207 (141)	17.1

Table 3.2, continued

	km, tail length 40 m s ⁻¹ from 3-9 km								
Qtr3_1060	Quarter-circle, r = 10 m s ⁻¹ from 0-3 km, tail length 60 m s ⁻¹ from 3-9 km	3777	13.8	40	23.2	14	92 (69)	227 (164)	18.6
Qtr3_1500	Quarter-circle, r = 15 m s ⁻¹ from 0-3 km	3777	13.3	42	14.8	34	97 (95)	236 (189)	15.2
Qtr3_1505	Quarter-circle, r = 15 m s ⁻¹ from 0-3 km, tail length 5 m s ⁻¹ from 3-9 km, conducted to test the sensitivity of Qtr_1510	3777	13.7	41	15.7	30	113 (98)	278 (199)	16.8
Qtr3_1510	Quarter-circle, r = 15 m s ⁻¹ from 0-3 km, tail length 10 m s ⁻¹ from 3-9 km	3777	14.0	38	16.7	27	113 (102)	279 (208)	16.8
Qtr3_1515	Quarter-circle, r = 15 m s ⁻¹ from 0-3 km, tail length 15 m s ⁻¹ from 3-9 km, conducted to test the sensitivity of Qtr_1510	3777	14.4	36	17.7	24	113 (105)	280 (217)	16.8
Qtr3_1520	Quarter-circle, r = 15 m s ⁻¹ from 0-3 km, tail length 20 m s ⁻¹ from 3-9 km	3777	14.8	35	18.7	22	119 (109)	285 (227)	18.0
Qtr3_1520_c5086	Qtr_1520, but with qv _{stc} increased to 18.5 g kg ⁻¹	5086	14.8	47	18.7	29	119 (109)	285 (227)	18.0
Qtr3_1520_c2233	Qtr_1520, but with qv _{stc} lowered to 13.8 g kg ⁻¹	2233	14.8	20	18.7	13	119 (109)	285 (227)	18.0
Qtr3_1520_rotCL	Qtr_1520, with tail rotated 45° clockwise	3777	13.4	42	15.6	31	116 (105)	296 (228)	16.5
Qtr3_1520_rotCC	Qtr_1520, with tail rotated 45° counter-clockwise	3777	15.3	32	19.9	19	113 (104)	242 (202)	19.2
Qtr3_1540	Quarter-circle, r = 15 m s ⁻¹ from 0-3 km, tail length 40 m s ⁻¹ from 3-9 km	3777	16.4	28	23.1	14	162 (121)	408 (264)	22.2
Qtr3_1560	Quarter-circle, r = 15 m s ⁻¹ from 0-3	3777	18.0	23	27.7	10	179	458 (299)	24.1

Table 3.2, continued

	km, tail length 60 m s ⁻¹ from 3-9 km						(134)		
Qtr3_2000	Quarter-circle, r = 20 m s ⁻¹ from 0-3 km	3777	17.7	24	19.8	19	159 (153)	415 (294)	18.2
Qtr3_2010	Quarter-circle, r = 20 m s ⁻¹ from 0-3 km, tail length 10 m s ⁻¹ from 3-9 km	3777	18.5	22	21.6	16	193 (164)	506 (322)	20.6
Qtr3_2020	Quarter-circle, r = 20 m s ⁻¹ from 0-3 km, tail length 20 m s ⁻¹ from 3-9 km	3777	19.2	21	23.6	14	221 (174)	563 (348)	23.3
Qtr3_2040	Quarter-circle, r = 20 m s ⁻¹ from 0-3 km, tail length 40 m s ⁻¹ from 3-9 km	3777	20.7	18	27.8	10	252(193)	634 (401)	26.5
Qtr3_2060	Quarter-circle, r = 20 m s ⁻¹ from 0-3 km, tail length 60 m s ⁻¹ from 3-9 km	3777	22.3	15	32.3	7	272 (211)	690 (451)	28.0
Qtr1_1020	Quarter-circle, r = 10 m s ⁻¹ from 0-1 km, tail length 20 m s ⁻¹ from 1-9 km	3777	13.2	43	16.1	29	158 (144)	205 (179)	15.8
Qtr1_1040	Quarter-circle, r = 10 m s ⁻¹ from 0-1 km, tail length 20 m s ⁻¹ from 1-9 km	3777	17.4	25	23.0	14	240 (186)	368 (261)	20.0
Qtr1_1060	Quarter-circle, r = 10 m s ⁻¹ from 0-1 km, tail length 20 m s ⁻¹ from 1-9 km	3777	21.8	16	30.1	8	306 (229)	507 (346)	25.6
Qtr1_1520	Quarter-circle, r = 15 m s ⁻¹ from 0-1 km, tail length 20 m s ⁻¹ from 1-9 km	3777	17.8	24	20.8	17	295 (272)	373 (317)	20.1
Qtr1_1540	Quarter-circle, r = 15 m s ⁻¹ from 0-1 km, tail length 40 m s ⁻¹ from 1-9 km	3777	21.9	16	27.6	10	420 (335)	605 (422)	23.8
Qtr1_1560	Quarter-circle, r = 15 m s ⁻¹ from 0-1 km, tail length 60 m s ⁻¹ from 1-9 km	3777	26.1	11	34.5	6	533 (395)	824 (527)	29.6
Qtr1_2020	Quarter-circle, r = 15 m s ⁻¹ from 0-1 km, tail length 20 m s ⁻¹ from 1-9 km	3777	22.4	15	25.5	12	482 (411)	595 (462)	25.2
Qtr1_2040	Quarter-circle, r = 15 m s ⁻¹ from 0-1 km, tail length 40 m s ⁻¹ from 1-9 km	3777	26.4	11	32.2	7	650 (497)	887 (590)	28.9

Table 3.2, continued

Qtr1_2060	Quarter-circle, $r = 15 \text{ m s}^{-1}$ from 0-1 km, tail length 60 m s^{-1} from 1-9 km	3777	30.6	8	39.0	5	804 (588)	1147 (732)	35.5
3qtr_r15	3/4-circle, $r = 15 \text{ m s}^{-1}$ from 0-10 km	3777	14.2	38	16.1	29	97 (102)	288 (235)	14.0
3qtr_r19	3/4-circle, $r = 19 \text{ m s}^{-1}$ from 0-10 km	3777	18.0	23	20.4	18	155 (157)	463 (360)	17.8
3qtr_r25	3/4-circle, $r = 25 \text{ m s}^{-1}$ from 0-10 km	3777	23.7	14	26.9	10	261 (257)	773 (573)	22.9
3qtr_r30	3/4-circle, $r = 30 \text{ m s}^{-1}$ from 0-10 km	3777	28.4	9	32.2	7	295 (355)	863 (783)	23.6
360_r15	Full-circle, $r = 15 \text{ m s}^{-1}$ from 0-10 km	3777	16.1	29	15.3	32	135 (155)	411 (373)	14.5
360_r19	Full-circle, $r = 19 \text{ m s}^{-1}$ from 0-10 km	3777	20.4	18	19.3	20	207 (246)	643 (589)	17.5
360_r25	Full-circle, $r = 25 \text{ m s}^{-1}$ from 0-10 km	3777	26.9	10	25.4	12	322 (418)	1054 (989)	20.5
720_r15	Two full-circles, $r = 15 \text{ m s}^{-1}$ from 0-15 km	3777	16.4	28	13.4	42	155 (193)	487 (494)	13.5
720_r19	Two full-circles, $r = 19 \text{ m s}^{-1}$ from 0-15 km	3777	20.7	18	17.0	26	248 (310)	801 (792)	16.8
Straight_47	Straight hodograph, length = 47 m s^{-1} from 0-10 km	3777	11.6	56	16.9	27	25 (21)	76 (65)	13.8
Straight_60	Straight hodograph, length = 60 m s^{-1} from 0-10 km	3777	14.7	35	21.4	17	40 (31)	120 (94)	17.2
Straight_79	Straight hodograph, length = 79 m s^{-1} from 0-10 km	3777	19.3	20	28.1	10	60 (46)	181 (138)	24.7
Straight_94	Straight hodograph, length = 94 m s^{-1} from 0-10 km	3777	23.1	14	33.7	7	76 (66)	226 (198)	30.0

Table 3.2, continued

When this idealized hodograph is used to initialize the model (the sounding's thermodynamic quantities remains the same), it produces a control simulation (Fig 3.4.4) that is remarkably similar, though not perfectly identical to that reported in Adlerman and Droegemeier (2002). The principal storm develops into a mature supercell by 3600 s, with a pronounced hook and strong near-ground mesocyclone by 4200 s. The first occlusion cycle begins after 6600 s, with the development of a dual updraft structure and an occluded surface gust front. Near-ground vorticity peaks at 7200 s, and the first occlusion occurs shortly thereafter, with the development of a new near-ground mesocyclone by 7800 s.

The second occlusion cycle proceeds similarly to the first. Near-ground vorticity peaks in the occluding mesocyclone at 11400 s and the occlusion occurs at approximately 12000 s. A new mesocyclone develops once again to the east, and the storm continues without another occlusion evident through the end of the simulation (14400 s).

3.4.3 Overview of the Simulations

A description of all of the soundings used in the parameter study is shown in Table 3.2. Most conventional idealized hodograph shapes are simulated, including a full-circle, a three-quarter circle, a half-circle, a quarter-circle (with and without rectilinear shear), and finally a straight hodograph. Varying both the hodograph shape and the total magnitude and distribution of the shear produces three modes of behavior in the simulated storms: non-occluding cyclic mesocyclogenesis, occluding cyclic mesocyclogenesis, and steady non-cycling. Although the transitions among the modes of storm behavior are not always simple or regular, we can make several generalizations based upon our results.

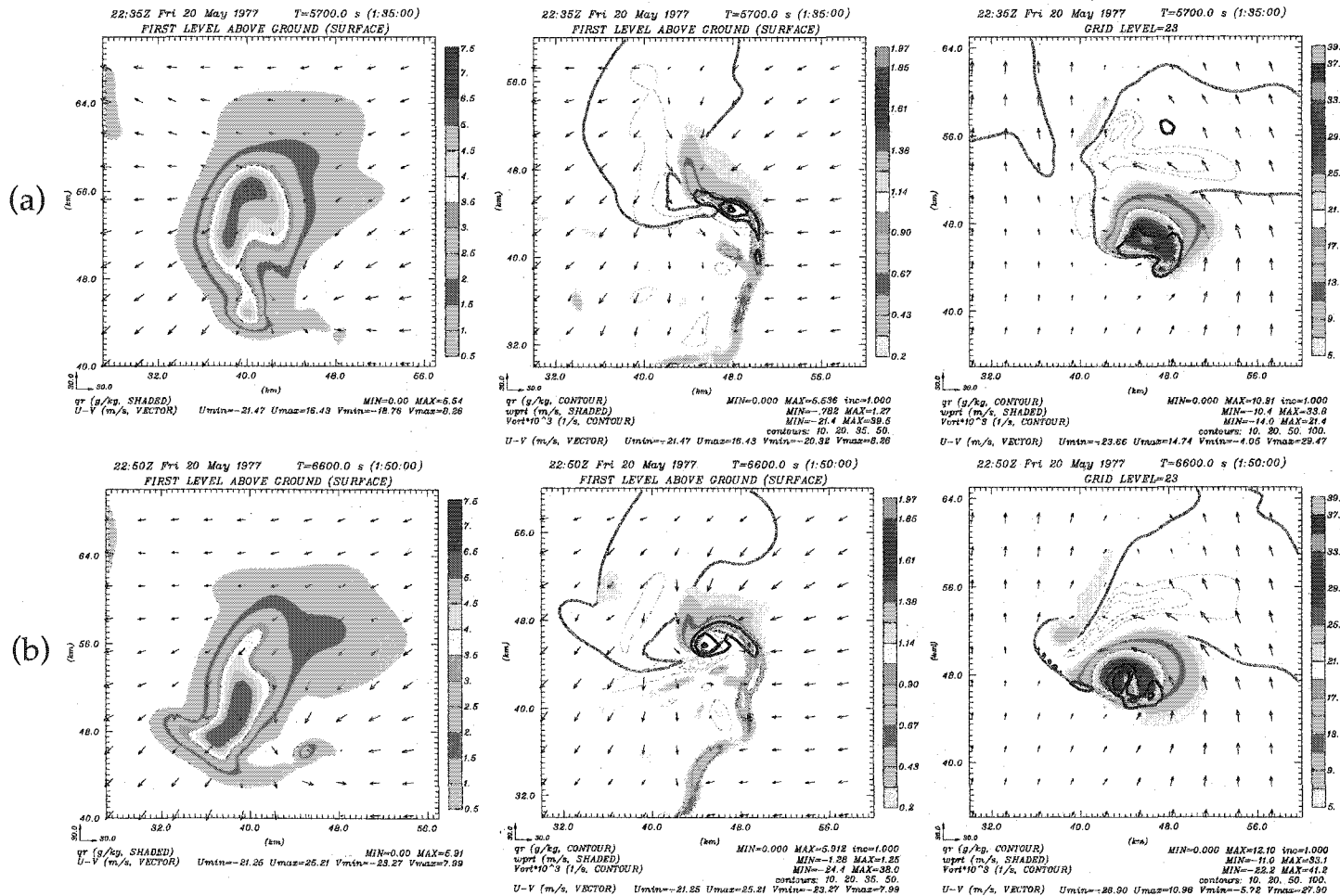


Figure 3.4.4: Plots of rainwater mixing ratio (left) and vertical velocity at $z = 50$ m (center) and $z = 4.5$ km (right) for the Control run at $t = 5700$ s (a) and 6600 s (b). Negative vertical velocity contoured in light blue at an interval of 0.3 (center) and 5.0 $m\ s^{-1}$ (right). Vertical vorticity contoured in black at irregular intervals $0.01, 0.02, 0.035,$ and 0.05 s^{-1} . Single dark blue contour indicates 1 $g\ kg^{-1}$ rainwater mixing ratio.

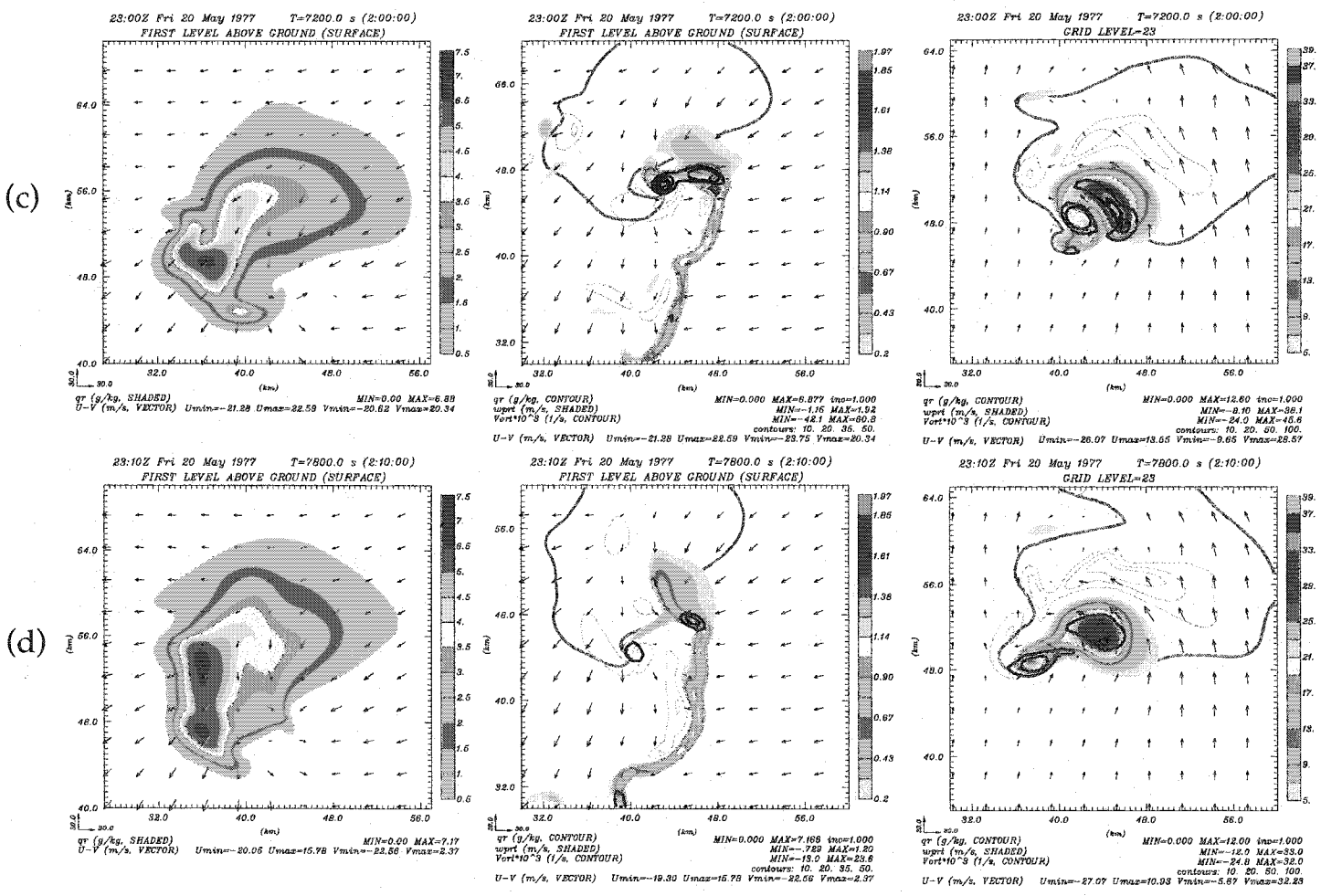


Figure 3.4.4, continued: As in (a) and (b), except for t= 7200 s (c) and 7800 s (d).

(e)

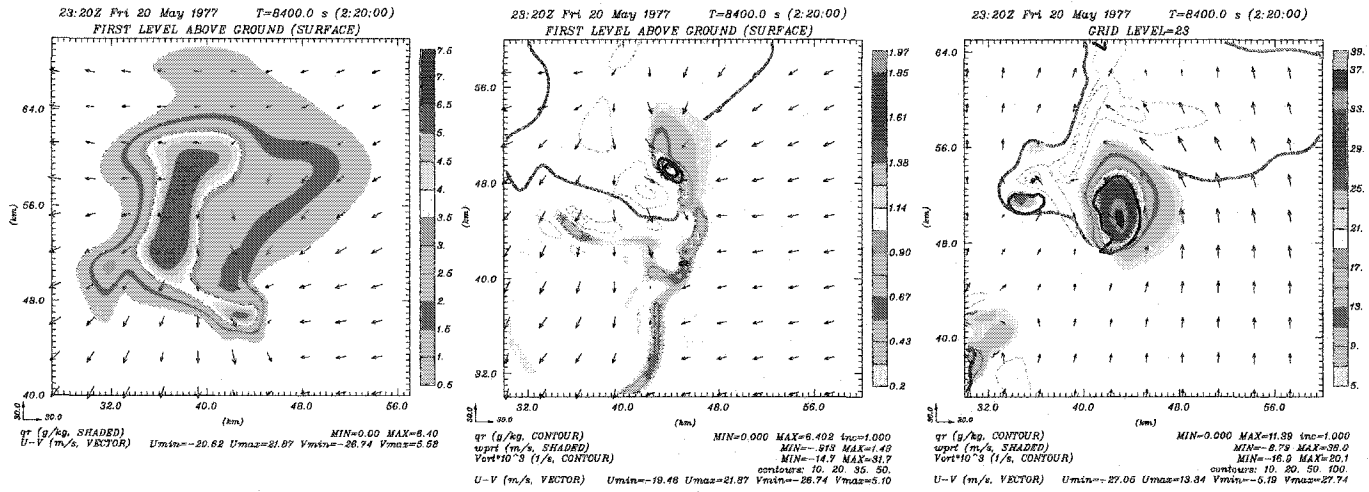


Figure 3.4.4, continued: As in (a) and (b), except for t= 8400 s (e).

First, straight hodographs always produce storms that undergo non-occluding cyclic mesocyclogenesis. When some curvature is added to the hodograph, i.e., a quarter-circle with rectilinear shear, all three modes of behavior emerge. At very low-shears, the storms tend to be steady or exhibit occluding cyclic mesocyclogenesis. At intermediate and higher shears, they tend to exhibit non-occluding cyclic behavior. However, a tendency toward non-occluding behavior is induced when the curved shear is confined to a shallower layer.

As we extend the simulations to half-circle hodographs, the tendency for non-occluding cyclic behavior is diminished, except at very high shears in shallower depths of turning. For most half-circle hodographs, steady behavior is observed at very low shears and at high shears, with occluding behavior in between. This trend continues for the three-quarter circle hodographs, with steady behavior again observed at higher shears. Finally, for the full-circle hodographs no cycling is observed during the control simulation period. We now proceed to describe in detail the behavior of each.

3.5 Half-Circle Hodograph Simulations

3.5.1 Uniform Shear Distribution over 10 km

As a first step in examining variations of the environmental wind profile, we begin with a half-circle hodograph over a depth of 10 km in order to maintain similarity with the control simulation. Four experiments are conducted, with shear uniformly distributed over the turning depth. Radii of 15, 25, 30, and 35 m s^{-1} are used, and the simulations are designated Half_r15, Half_r25, Half_r30, and Half_r35, respectively. A radius of 10 m s^{-1} did not produce a sustainable storm, a result of 0-3 km storm-relative inflow less than 10 m s^{-1} (Droegemeier et al. 1993). The control simulation has a radius of 19 m s^{-1} , thereby placing it between Half_r15 and

Half_r25. As mentioned previously, all of the simulations described produce supercell storms. [For our criteria, we have assumed that a supercell 1) remains relatively isolated and distinct throughout the length of the simulation, i.e. not multicellular, embedded in lines, or interacting with other convective elements and 2) contains a mesocyclone with time and height continuity from at least mid-levels (around 4 km) and above. All storms which met these criteria also possessed some form of hook, although there were large variations in size and shape.]

The hodographs (Fig. 3.5.1) cover a range of mean shears (Rasmussen and Wilhelmson 1983) from $4.7 \times 10^{-3} \text{ s}^{-1}$ to $11 \times 10^{-3} \text{ s}^{-1}$, and a range of BRNsh₆ (BRNsh₉) from 10.6-24.7 (13.8-32.3) m s^{-1} (Table 3.2). SRH₃ (SRH₁), computed from the average domain speed used to keep the storm of interest nearly stationary, vary over a range of 155-700 (55-250) $\text{m}^2 \text{ s}^{-2}$ (Table 3.2). These values are up to 71% larger than those (Table 3.2) computed from storm motions estimated via the method of Davies and Johns (1993). A complete summary of the differences between the estimated and actual SRH for all of the model simulations is shown in Figure 3.5.2.

The effects of hodograph radii changes are quite varied, but *they clearly suggest that increasing shear throughout the same depth of turning tends to slow down and eventually terminate the cycling process.* A summary of cycling characteristics is shown in Figure 3.5.3. Half_r15 produces a small supercell that appears to be a miniature version of the one in the control run. It produces three full OCM cycles, with the first and second occlusions delayed by approximately 300 s. Half_r25 produces a storm that appears very similar to the control run, except that it has a stronger near-ground mesocyclone and occludes only once (at 9600 s).

Half_r30 and Half_r35 both produce supercell storms that are much larger in areal extent than in the control run and do not cycle throughout the entire simulation period (Fig 3.5.3). Differences in the sizes of the updraft and rainwater

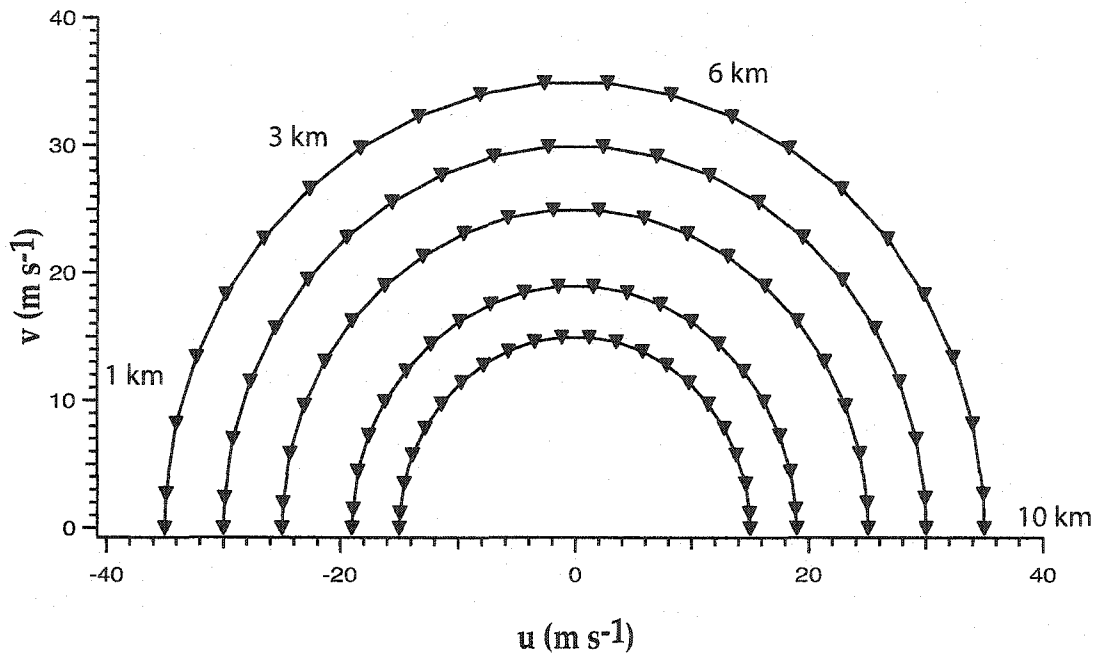


Figure 3.5.1: Hodographs for simulations Half_r15, Control, Half_r25, Half_r30, and Half_r35.

Half-circle Hodographs Over 10 km

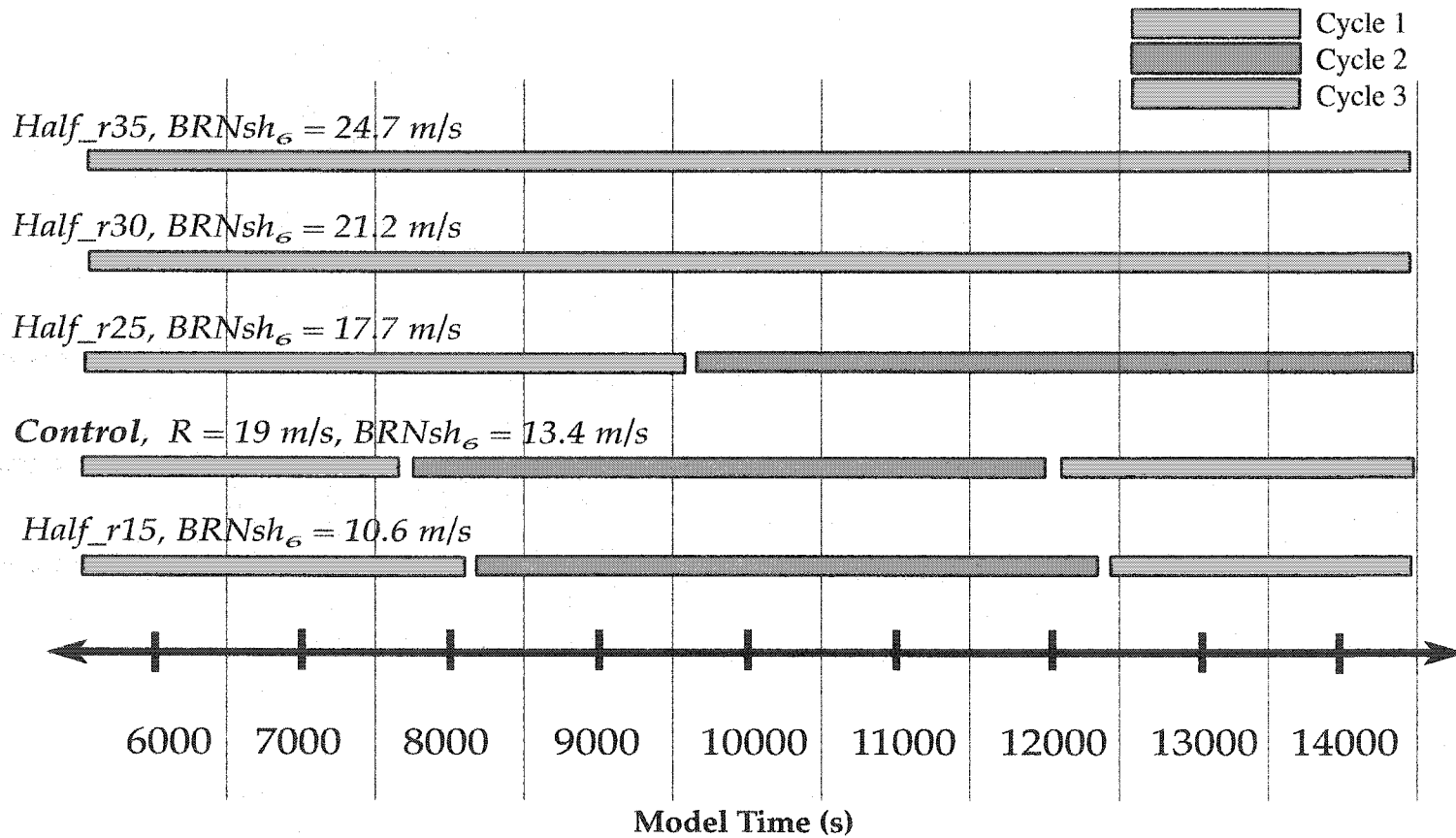


Figure 3.5.3: Schematic of cycling behavior for the Control and Half simulations. Duration of each OCM cycle indicated by the colored bars. Each gap between bars represents an occlusion.

areas between the lowest and highest shear cases (Half_r15 and Half_r35) are quite striking (Fig. 3.5.4). The areal extent of rainwater at $z = 50$ m increases from approximately 120 to 840 km², while the areal extent of the updraft at $z = 4.5$ km increases from approximately 60 to 360 km². These effects may result from inhibited turbulence dissipation in the most helical flows (Lilly 1986b; Andre and LeSieur 1977; Kraichnan 1973).

Half_r30 and Half_r35 exhibit quite different supercell structures toward the end of the simulation. Similar to the other hodograph cases, Half_r35 remains quite 'classic' throughout its lifetime. In contrast, Half_r30 becomes less 'classic' and takes on features characteristic of a 'high-precipitation' (HP) storm (Moller and Doswell 1988), with increasing amounts of rain wrapping around the upshear side of the mesocyclone. By 12300 s, its updraft and gust-front begin to stretch out into a nearly north-south orientation and the storm appears to be transitioning toward a more outflow-dominated mode (Fig 3.5.5).

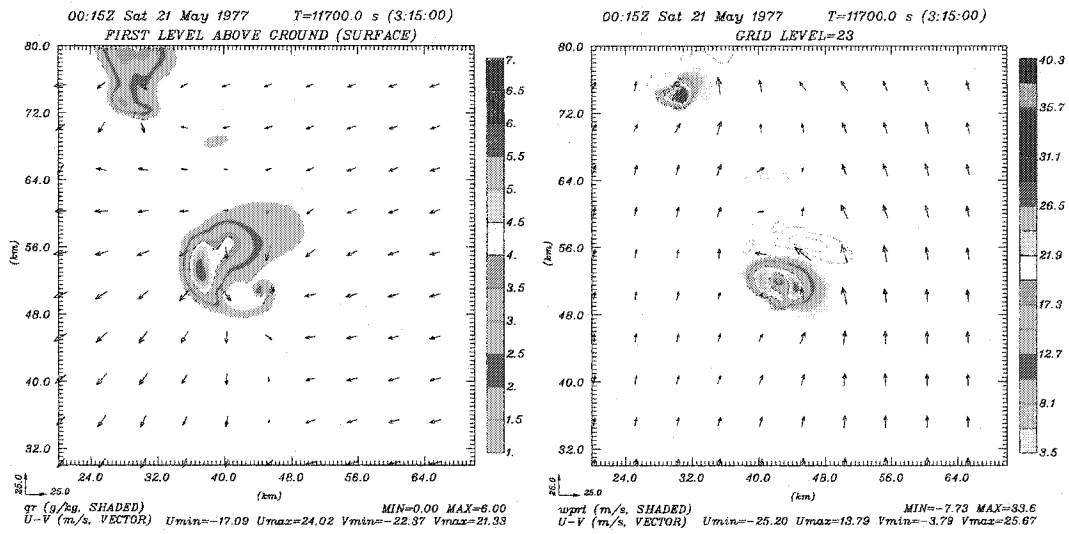
In summary, simply changing the radius of the control run hodograph over a fixed depth results in a relatively orderly progression of the cyclic behavior. As the radius and overall shear increase, the OCM cycles decreases in number and are delayed. At high enough shear the storm transitions to a non-cycling supercell.

3.5.2 Variations in Shear Distribution over 10 km

In order to explore the effects of changes in the vertical distribution of vertical shear, we systematically shift the location of height points along the arc of the control case hodograph. Using a hyperbolic tangent function that also is used for vertical grid stretching (Eqn. 3.1) in the ARPS (Xue et al. 1995; Adlerman and

$$\Delta z(i) = \Delta z_{av} + \frac{\Delta z_{min} - \Delta z_{av}}{\tanh(2\alpha)} \tanh\left[\frac{2\alpha}{1-a}(i-a)\right] \quad \text{for } i = 1, 2, 3, \dots, (nz - 3) \quad (3.1)$$

Simulation Half_r15



Simulation Half_r35

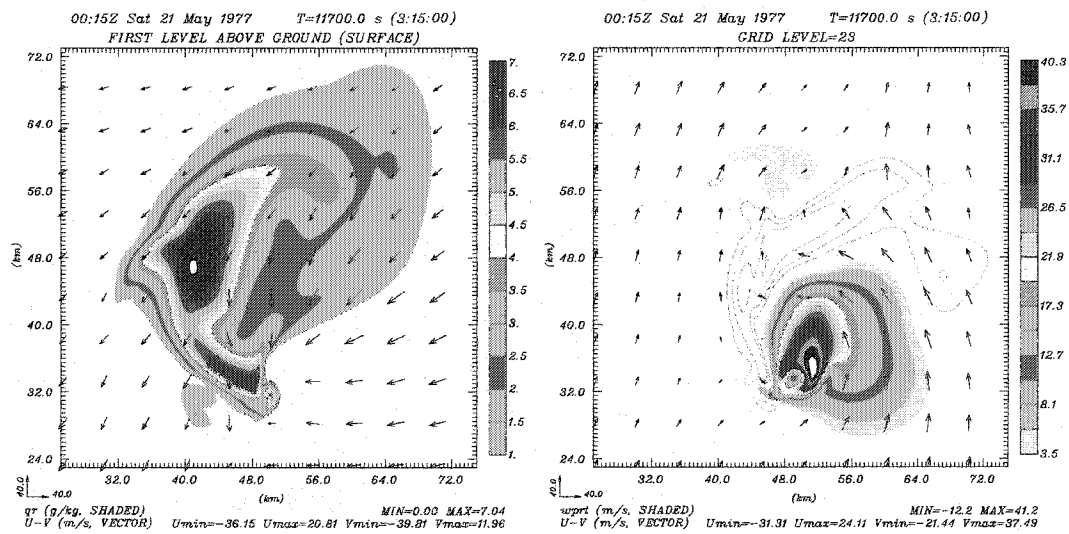


Figure 3.5.4: Plots of rainwater mixing ratio at $z = 50$ m (left) and vertical velocity at $z = 4.5$ km (right, color-filled) for simulations Half_r15 (top) and Half_r35 (bottom) at $t = 11700$ s. Negative vertical velocity contoured in light blue at an interval of 3 m s^{-1} .

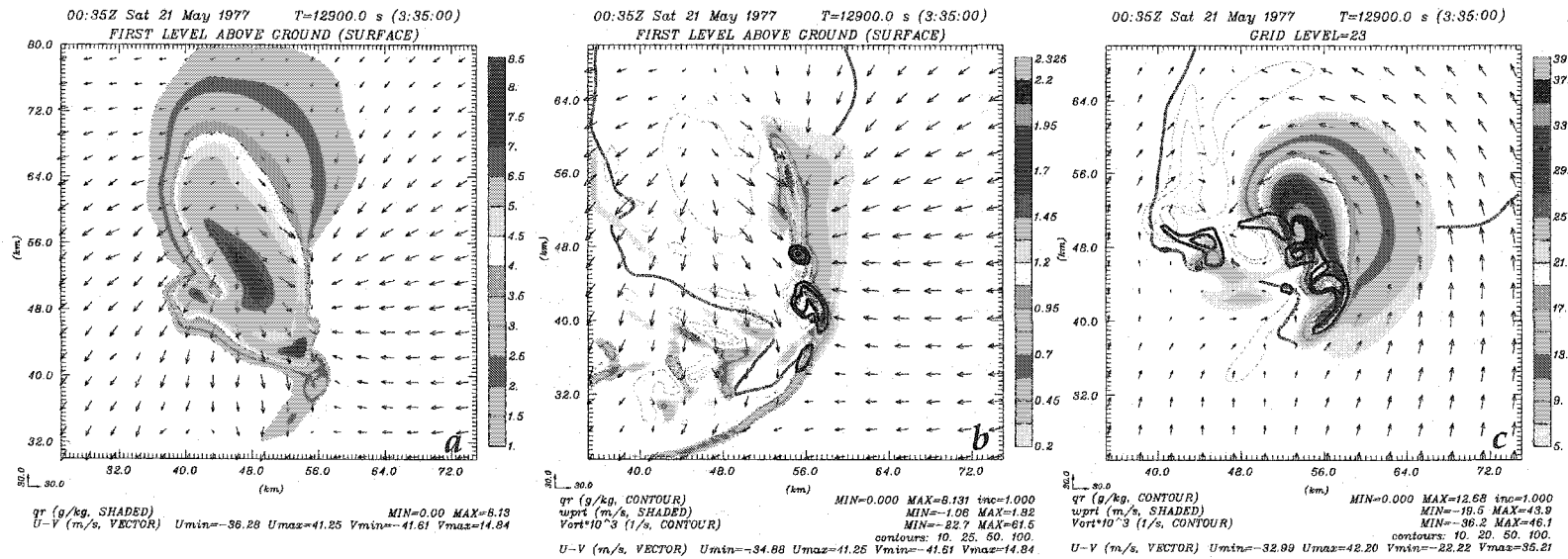


Figure 3.5.5: Plots of (a) rainwater mixing ratio, (b) vertical velocity (color-filled) at $z = 50$ m, and (c) vertical velocity (color-filled) at $z = 4.5$ km for simulation Half_r30 at $t = 12900$ s. In (b) and (c): negative vertical velocity contoured in light blue at an interval of 0.3 and 5.0 $m\ s^{-1}$ respectively; vertical vorticity contoured in black at irregular intervals of 0.01 , 0.02 , 0.05 , and 0.1 s^{-1} ; single dark blue contour indicates $1\ g\ kg^{-1}$ rainwater mixing ratio.

Droegemeier 2002), we transform the uniform vertical distribution of environmental wind data points both downward and upward, which increases (decreases) upper (lower) level shear or decreases (increases) upper (lower) level shear. This method thus preserves the shape of the hodograph and the mean shear ($6 \times 10^{-3} \text{ s}^{-1}$), i.e. the length of the hodograph divided by the depth of turning (Rasmussen and Wilhelmson 1983).

Eight simulations were conducted, four in which the *low-level shear* was increased (simulations Shift_L1, Shift_L2, Shift_L3, and Shift_L4) and four in which the *upper-level shear* was increased (simulations Shift_U1, Shift_U2, Shift_U3, and Shift_U4). Shift_L1 has the strongest low-level shear and Shift_U4 has the weakest (Fig. 3.5.6). As shown in Table 3.2, these hodographs cover a wide range of shears and helicities, with BRNsh_6 (BRNsh_9) values ranging from 7.4-19.2 (10.8-22.1) m s^{-1} and SRH_3 (SRH_1) values ranging from 72-547 (25-369) $\text{m}^2 \text{ s}^{-2}$. Despite some values of SRH_3 and BRN_6 that would usually suggest multi-cellular convection (e.g. Shift_U4), all simulations display clear supercell characteristics.

A summary of the cycling characteristics is shown in Figure 3.5.7. As the low-level shear is increased, the OCM cycling process slows significantly for simulations Shift_L3 and Shift_L2, eventually ceasing entirely in the highest low-level shear simulation, Shift_L1. Compared to the control run, the first and second occlusions are delayed 2100 s for Shift_L3. In Shift_L2, the first occlusion is delayed by 4500 s, and no second OCM cycle is observed.

For Shift_U2 through Shift_U4, an opposite progression in the timing of the OCM cycles is observed, with the mesocyclone cycling slowing as the low-level shear weakens and the upper-level shear increases, eventually ceasing for Shift_U4 (Fig. 3.5.7). However, Shift_U1 exhibits no cycling, with the storm becoming “stuck” in an occluded position for the duration of the simulation (Fig. 3.5.8). Since this

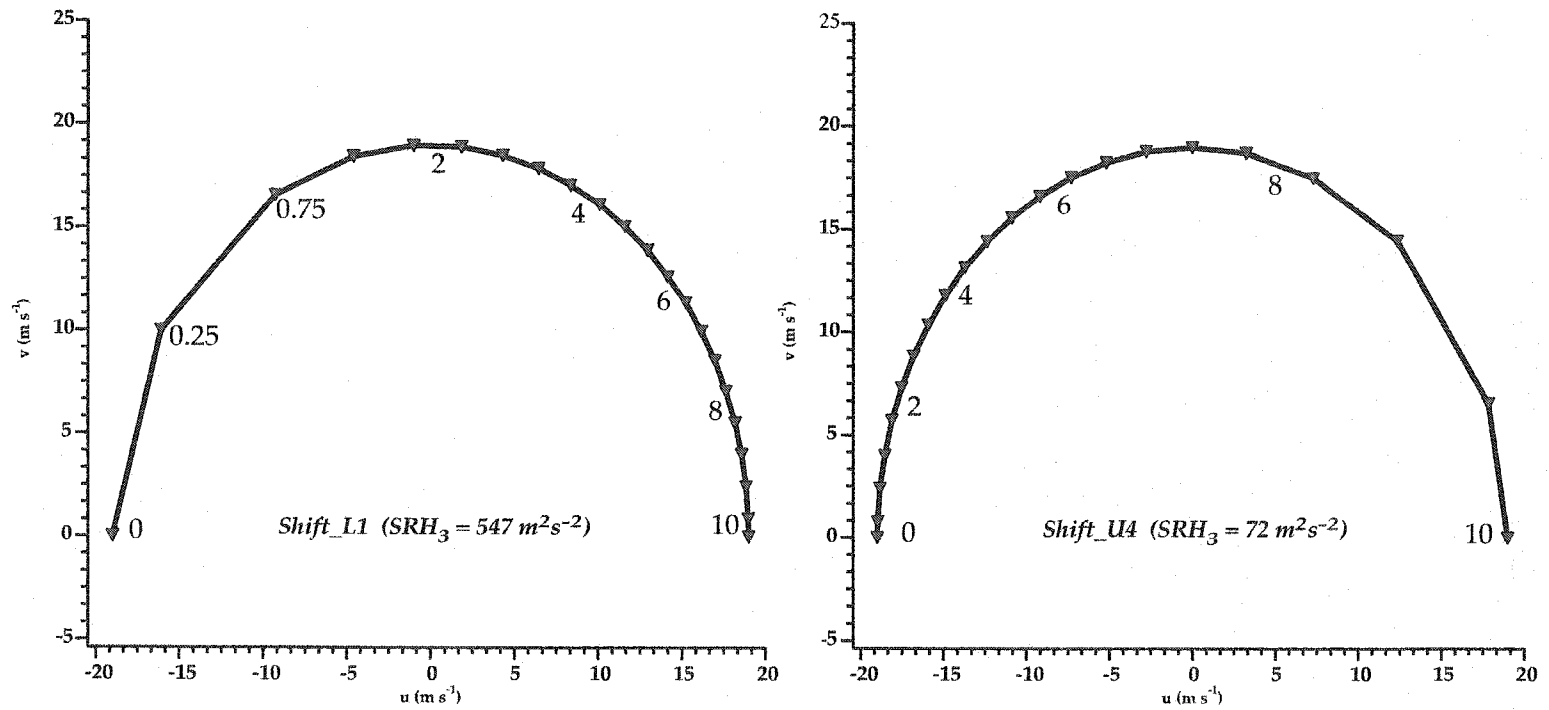


Figure 3.5.6: Hodographs for simulations Shift_L1 (left) and Shift_U4 (right).

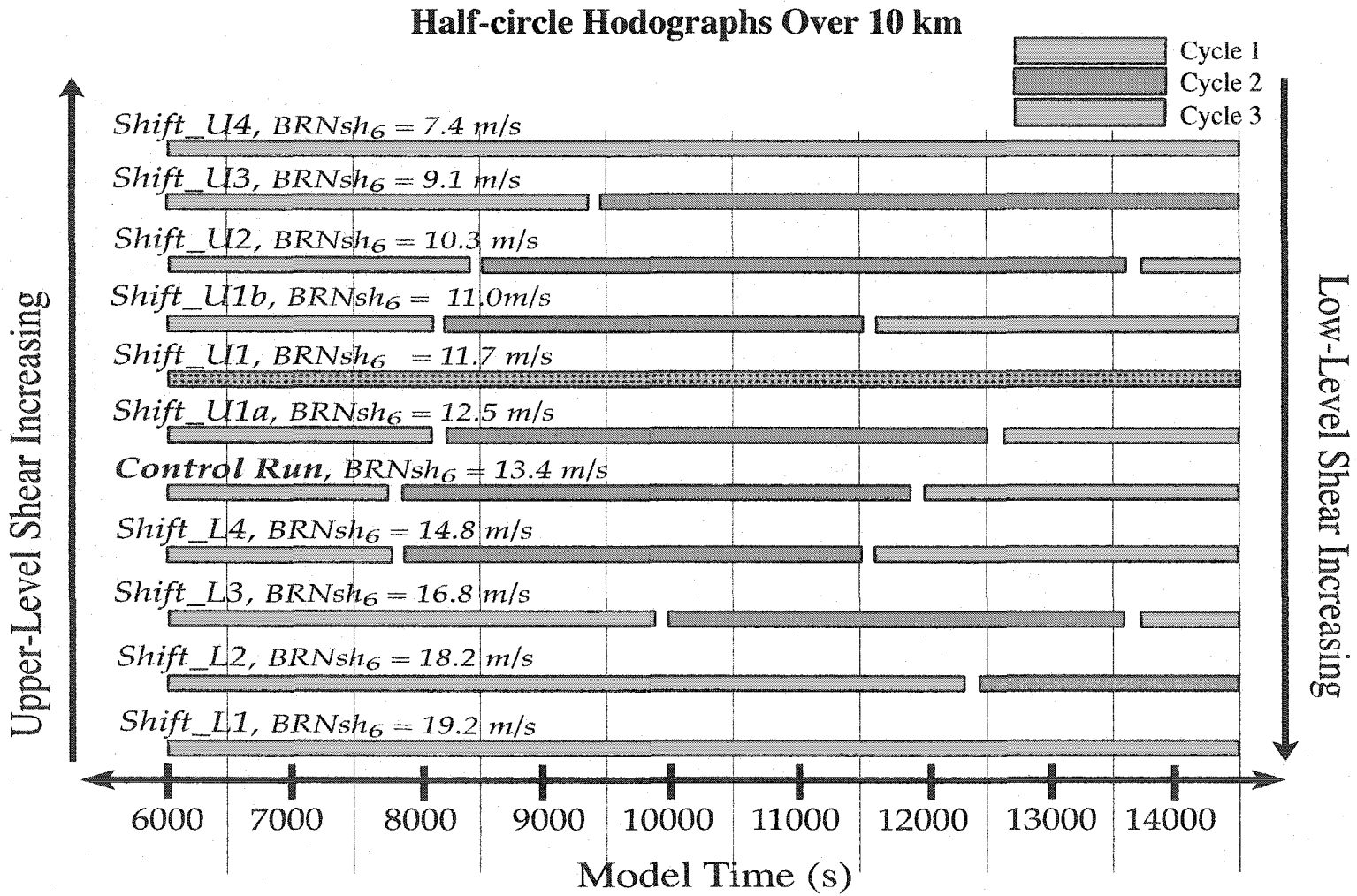


Figure 3.5.7: Schematic of cycling behavior for the Shift simulations. Dotted bar indicates the anomalous Shift_U1 run.

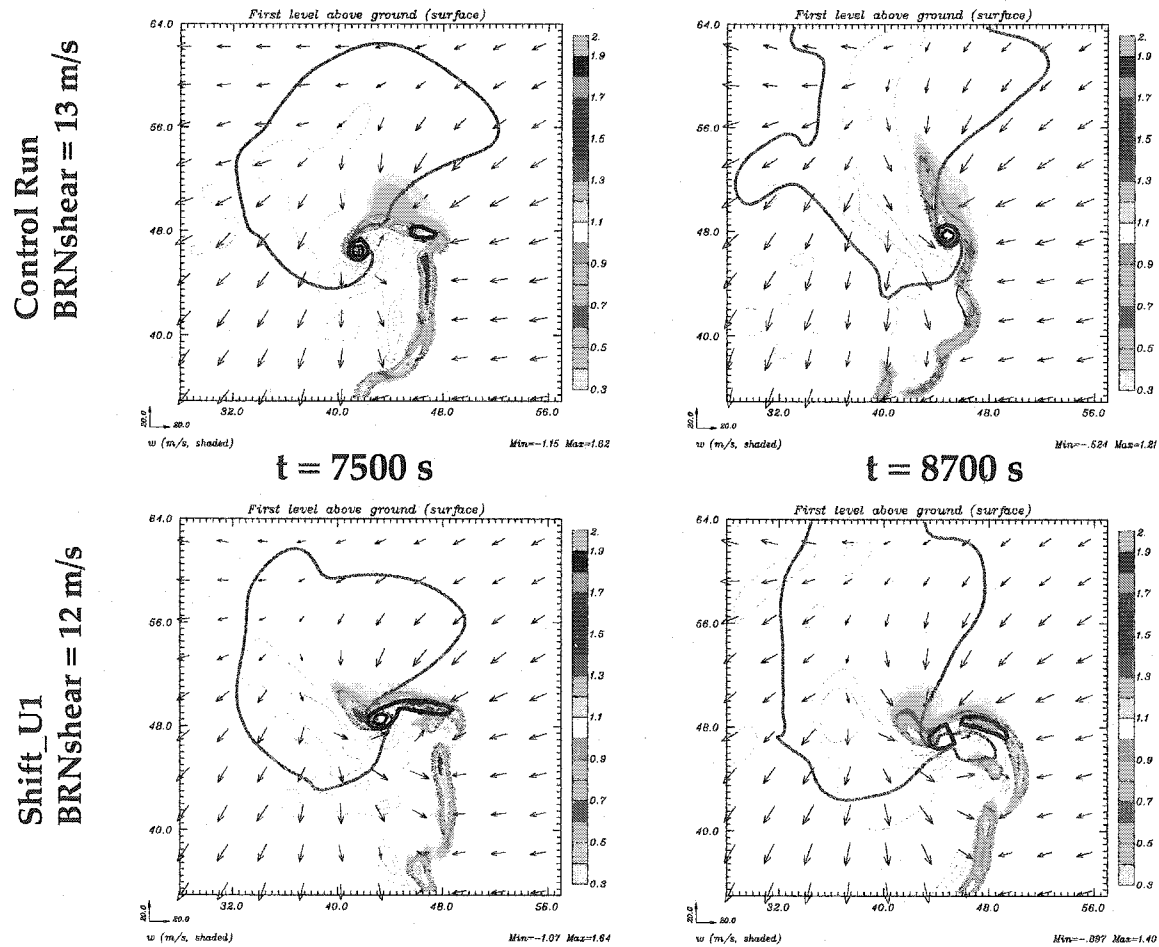


Figure 3.5.8: Comparison of vertical velocity for the control run (top) and Shift_U1 (bottom) at $t=7500$ s (left) and $t=8500$ s (right). Light blue contour indicates negative vertical velocity, contoured at an interval of 0.2 m s^{-1} . Dark blue contour indicates 1 g kg^{-1} rainwater mixing ratio. Vertical vorticity contoured in black at an interval of 0.02 s^{-1} .

seems unusual, two additional hodographs were constructed, Shift_U1a and Shift_U1b, each varying only slightly from Shift_U1 (Table 3.2). The differences in $BRNsh_6$ and SRH_3 are less than 0.8 m s^{-1} and $16 \text{ m}^2 \text{ s}^{-2}$, respectively. The storms in these two additional simulations do cycle slightly more slowly than those in the control run, thus fitting well into the pattern of cycling variations displayed in Figure 3.5.7. Because the storm structures are all quite similar, this sensitivity is puzzling but not surprising given previously demonstrated sensitivities (Adlerman and Droegemeier 2002). However, it does suggest that comparable sensitivities in the context of actual prediction could be remedied by an ensemble approach (e.g., Hou et al. 2001). Although an ensemble mean for convective storms would be of little value (Levit et al. 2004), conditional probabilities would still be useful.

In summary, either increasing the low-level shear while reducing the upper-level shear or increasing the upper-level shear while reducing the low-level shear has the same effect of reducing the number of occlusion cycles and delaying their timing. Between these two extremes, there exists a fairly orderly progression of occlusion behavior which regresses back toward the control run, although some anomalous sensitivities are observed.

3.5.3 Uniform Shear Distribution over 6 km

In order to examine the effect of confining the turning layer to a shallower depth (6 km), five additional half-circle hodograph simulations are conducted with the shear still uniformly distributed within this layer. The radii are chosen such that each simulation has the same corresponding mean shear as the previous half-circle runs (i.e., Half_r15 through Half_r35, including the control run), giving respective radii of 9, 11, 15, 18, and 21 m s^{-1} (Fig. 3.5.9). The simulations are

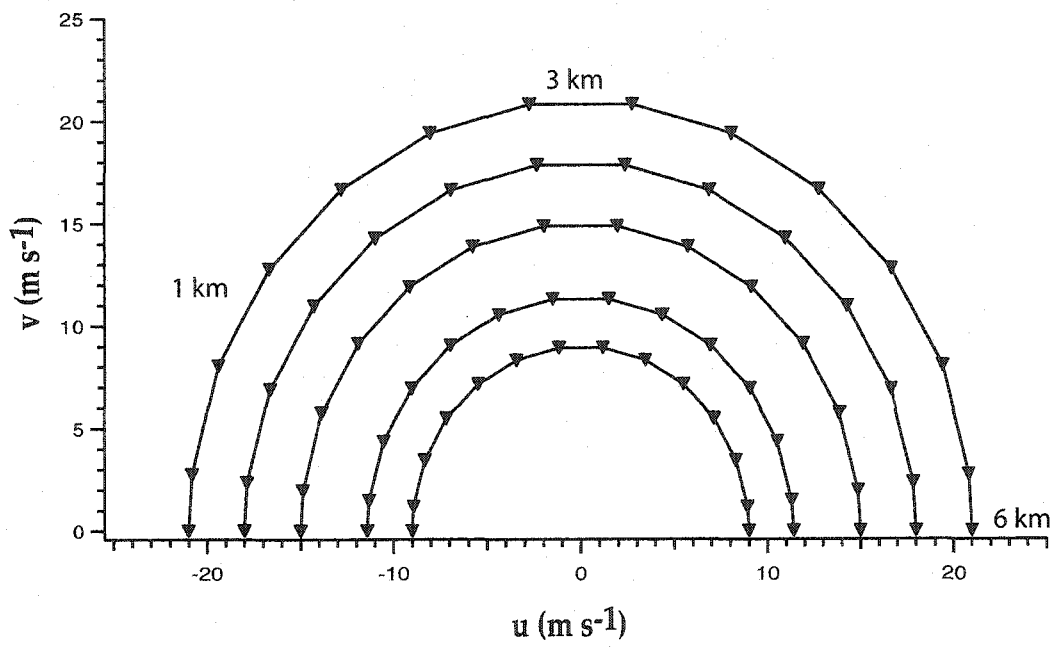


Figure 3.5.9: Hodographs for simulations Half6_r9, Half6_r11, Half6_r15, Half6_r18, and Half6_r21.

designated Half6_r9, Half6_r11, Half6_r15, Half6_r18, and Half6_r21, respectively. As shown in Table 3.2, these hodographs again cover a wide range of shears and helicities, with BRNsh₆ (BRNsh₉) values ranging from 9.0-21.0 (10.7-25.0) m s⁻¹ and SRH₃ (SRH₁) values ranging from 120-785 (46-261) m² s⁻².

Similar to Half_r15 (Fig. 3.5.4), Half6_r9 produces supercell quite small in areal extent (e.g., the updraft at 4.5 km covers approximately 42 km²). However, it does not cycle throughout the duration of the simulation (Fig. 3.5.10), and its near-ground mesocyclone remains relatively weak when compared to that in the control run.

Simulations Half6_r11 and Half6_r15 produce OCM cyclic supercells that qualitatively resemble those in the control case but cycle more slowly (Fig. 3.5.10). Compared to the control run, the first occlusions for Half6_r11 and Half6_r15 are delayed by 1200 s and 3000 s, respectively. The second occlusions are delayed by 2400 s and 2100 s, respectively.

Simulation Half6_r18 also produces an OCM cyclic supercell, but similar to Half_r30, it takes on a more HP character toward the end of the run. It undergoes its first occlusion at approximately the same time as the control run (7800 s), but its second occlusion is delayed to 14400 s, or 2400 s later than the control (Fig. 3.5.10).

In the highest shear simulation, Half6_r21, the process of cyclic mesocyclogenesis occurs in an unusual *non-occluding* mode (NOCM) that is not evident in any of the other half-circle hodograph simulations. The first mesocyclone and associated hook (Figs. 3.5.11a-c) form as in the control run, with a strong vorticity maximum (A) extending from the surface upward through 4 km altitude at 7800 s. However, because the surface winds behind the gust front remain mostly northerly (Figs. 3.5.11b,e) the near-ground mesocyclone does not occlude, but travels southward down the gust front. As the mid-level updraft also develops farther

Half-circle Hodographs Over 6 km

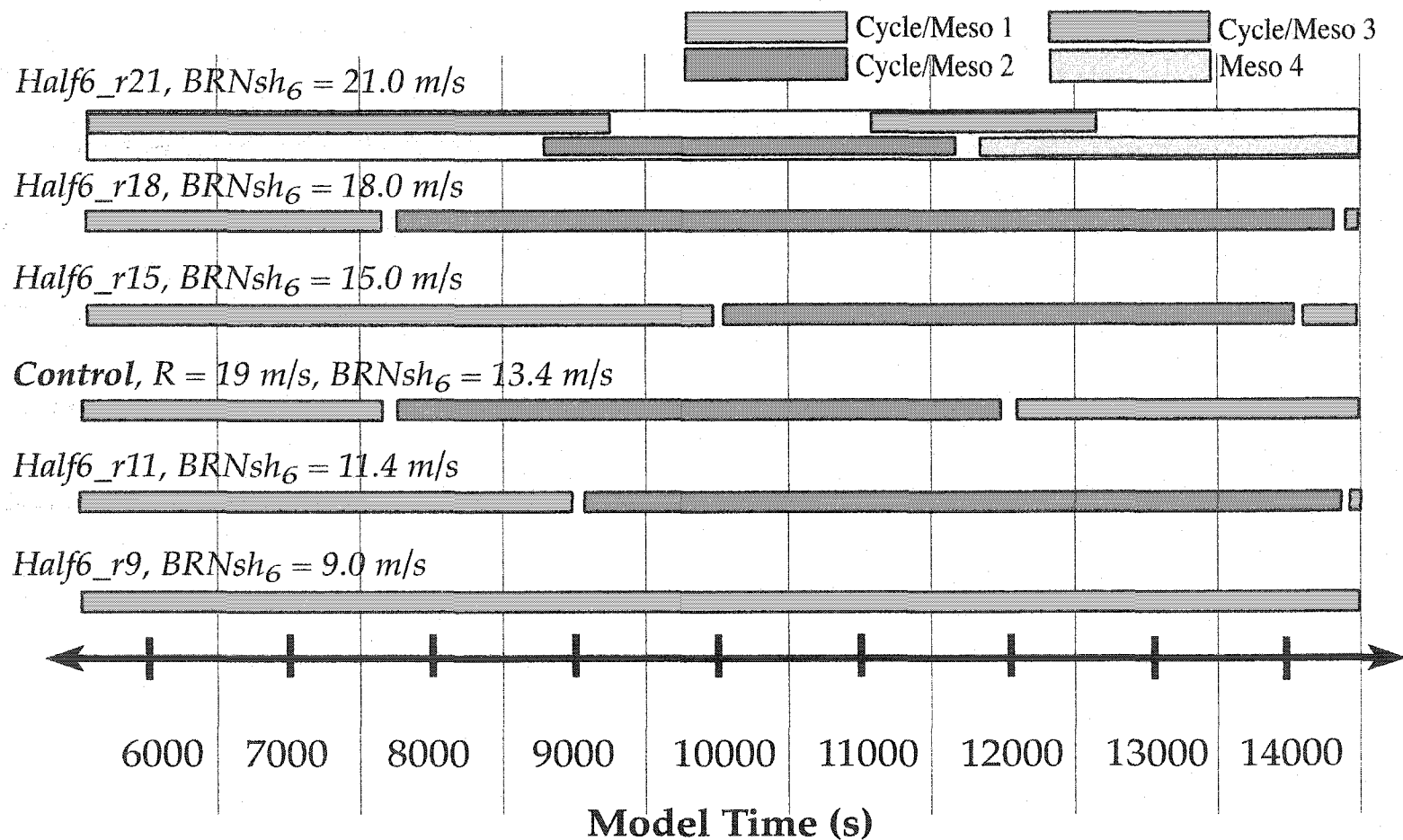


Figure 3.5.10: Schematic of cycling behavior for the Half6 simulations. Simulations in which NOCM occurs are indicated by the shaded background bar, with colored bars indicating the lifetime of each surface mesocyclone.

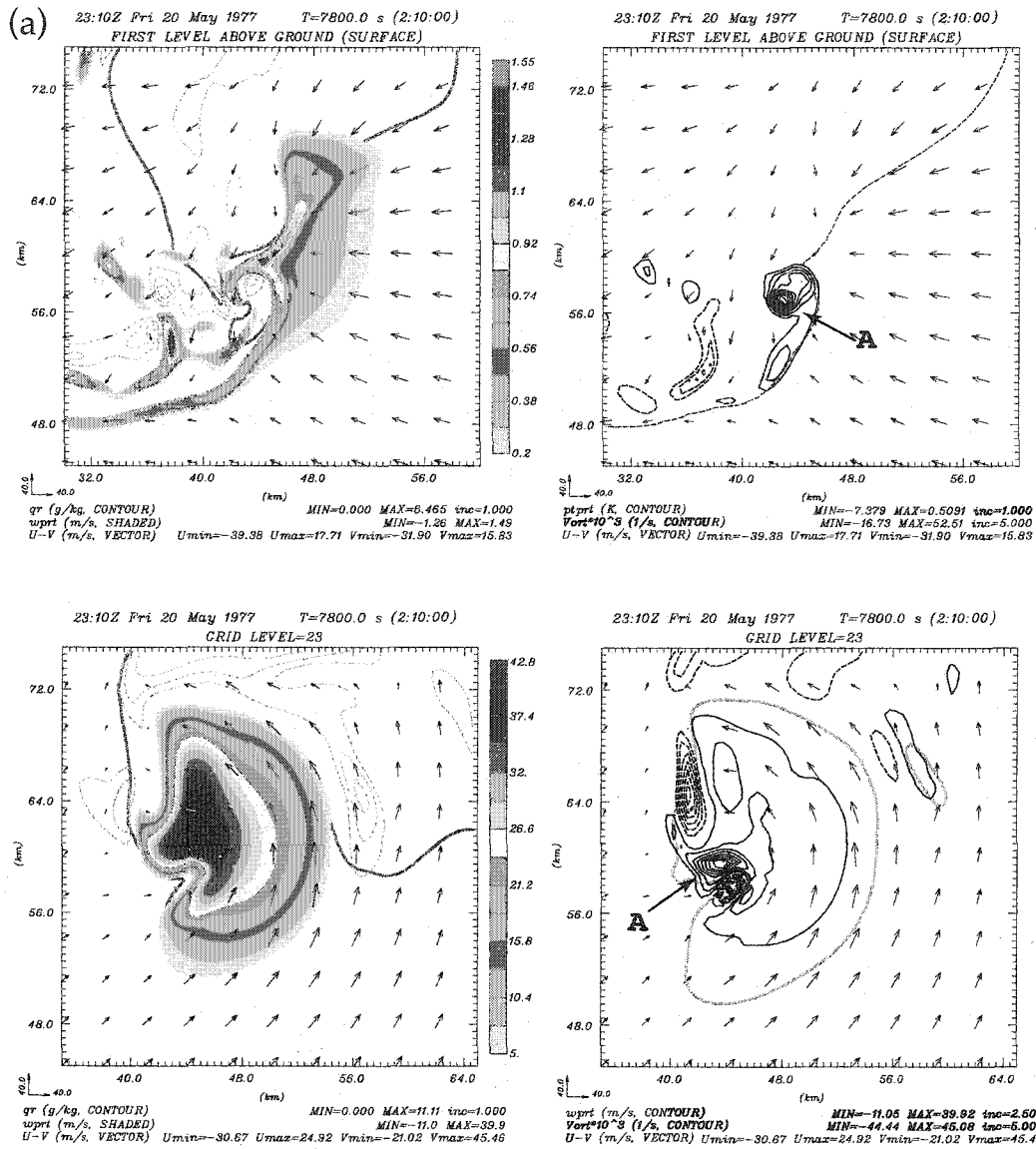


Figure 3.5.11: a) Plots of vertical velocity (left, color-filled) and vertical vorticity (right) at $z = 50$ m (top) and $z = 4.5$ km (bottom) for simulation Half6_r21 at $t = 7800$ s. Negative vertical velocity contoured in light blue at an interval of 0.3 m/s (top) and 3.0 m/s (bottom). Vertical vorticity contoured at an interval of 0.005 s^{-1} . Dark blue contour indicates 1 $g\ kg^{-1}$ rainwater mixing ratio. Purple contour indicates -1 degree K perturbation potential temperature. Light green contour indicates 2.5 m/s vertical velocity. Successive mesocyclones indicated by "A" and "B".

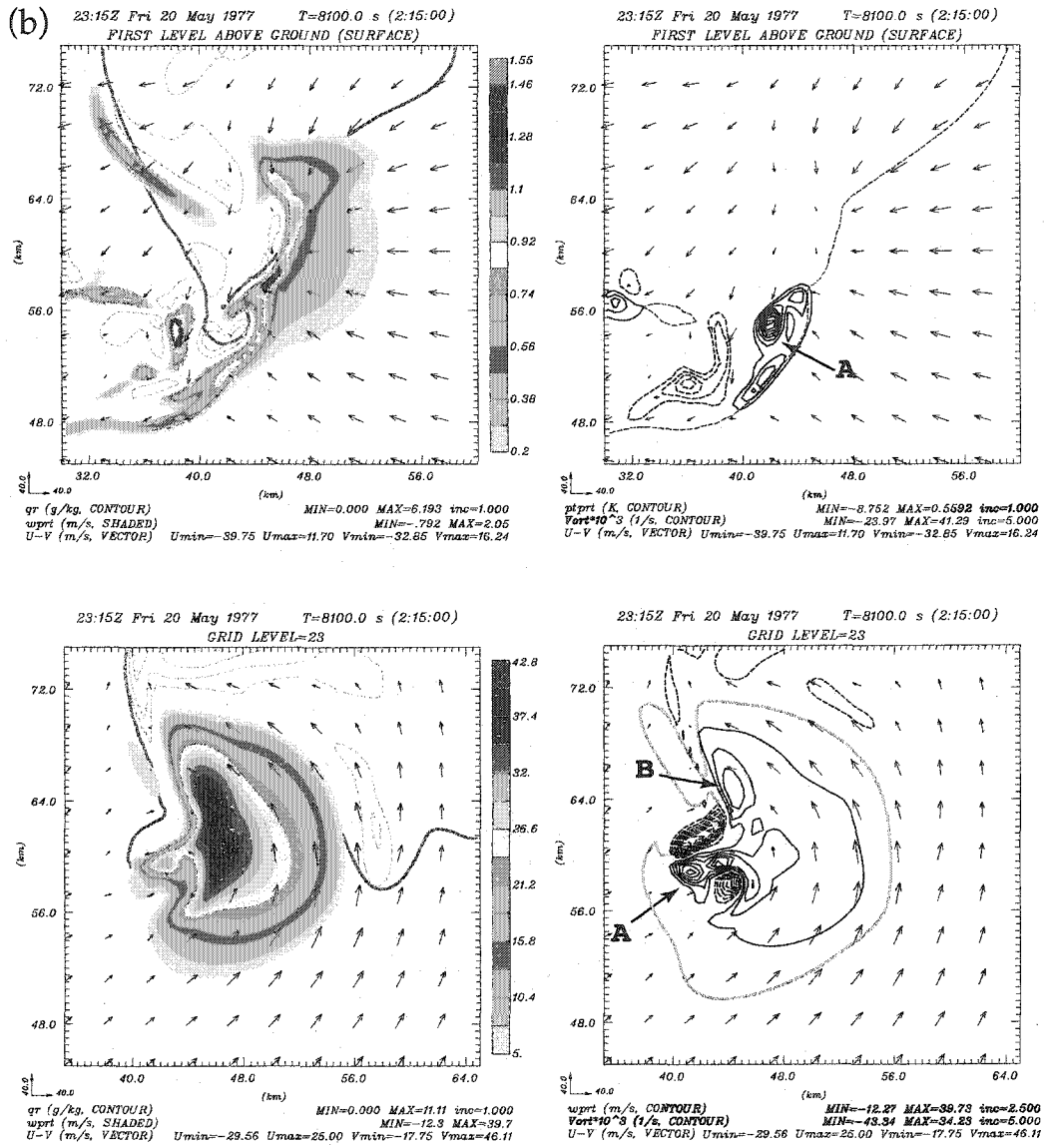


Figure 3.5.11, continued: b) Same as in (a), except at $t = 8100$ s.

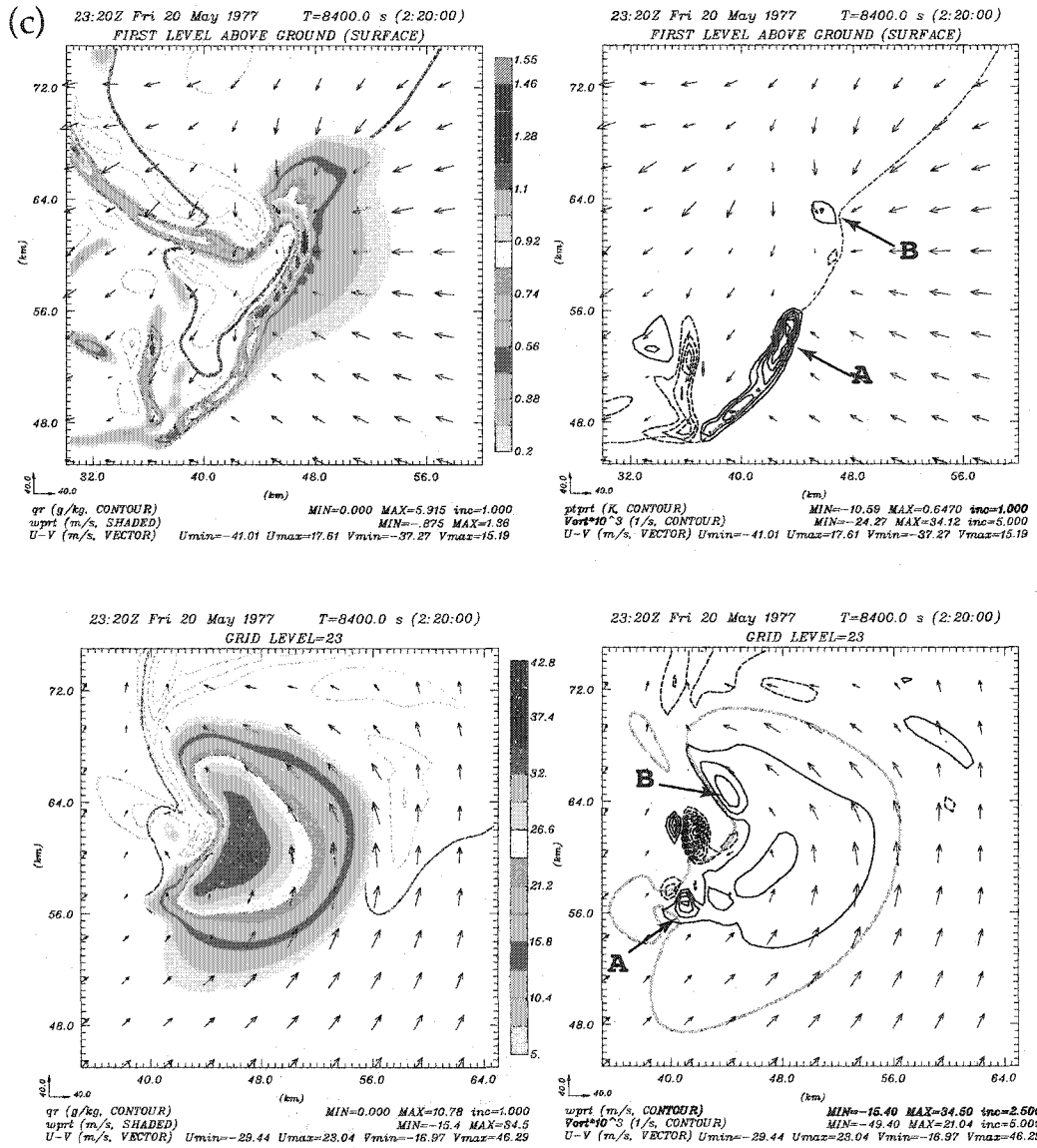


Figure 3.5.11, continued: c) Same as in (a), except at t = 8400 s.

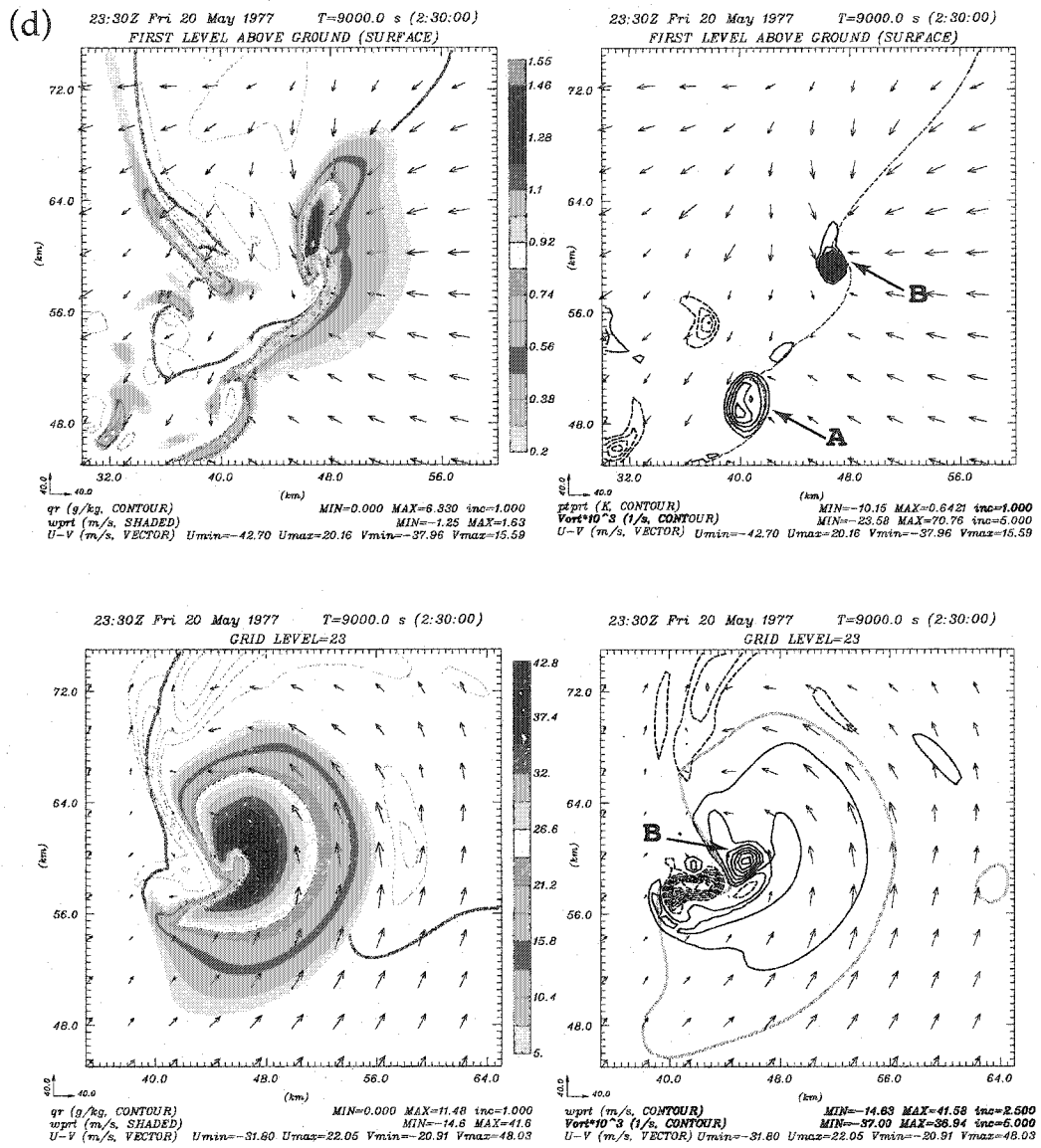


Figure 3.5.11, continued: d) Same as in (a), except at $t = 9000$ s.

southward (Fig. 3.5.11f), the mesocyclone center at 4 km remains well correlated with the near-ground mesocyclone. At the same time, however, a new near-ground mesocyclone develops farther *north* along the gust front, with a new mid-level mesocyclone (B) also apparent (Figs. 3.5.11d-f). As this new near-ground and mid-level mesocyclone move farther south (Figs. 3.5.11g-i), the old one dissipates. The remaining near-ground vorticity moves southwestward and can be seen as a cyclonic flare in the rainwater contour (Figs. 3.5.11d,g). Throughout this transition the updraft never takes on a dual-maxima appearance (Adlerman and Droegemeier 1999), but remains unicellular, with the maxima shifting northward with time. This type of NOCM cyclic regeneration, occurs again at 11100 s and 11700 s (Fig. 3.5.10), after which the storm takes on HP characteristics.

In summary, *when we confine the shear to a shallower depth in our half-circle hodograph simulations, the behavior becomes slightly less regular than in our previous results.* Similar to the Shift simulations, at the lowest shear the storm no longer occludes. At intermediate shears, occluding cyclic mesocyclogenesis (OCM) occurs but without any clear trends in timing. At the highest shear, the storm behavior transitions to non-occluding cyclic mesocyclogenesis (NOCM).

3.5.4 Variations in CAPE

3.5.4.1 Weisman and Klemp Sounding

As a preliminary step toward investigating the role of CAPE in cyclic regeneration, we repeated the control case but with the base state thermodynamics replaced by the Weisman and Klemp (1982) analytic sounding (the hodograph is still the half-circle of Fig. 3.4.3). Low-level mixing ratios of 12-18 g kg⁻¹ were used, covering a range of CAPE from 937-4105 J kg⁻¹. As might be expected, these simulations were quite different from the control case. Soundings in which the

CAPE was comparable to that of the Del City experiment (i.e. mixing ratios $> 15 \text{ g kg}^{-1}$) tended to produce storms having features more toward the HP end of the supercell spectrum than the control case, most likely a result of the higher water content in the analytic profile. In addition, the larger rain areas in these simulations initiated convection throughout the domain after 7200 s, which oftentimes interacted with the storm of interest and complicated any further conclusions from the simulation. Some simulations did exhibit a degree of regeneration, but none clearly underwent a cyclic occlusion process. Therefore, because these experiments lacked a single case that would be comparable to our control run, no clear conclusions about the role of CAPE in cyclic regeneration could be made from this set of experiments. In order to obtain results that are less ambiguous and more easily interpreted, a systematic variation of the Del City thermodynamics is undertaken. We note that these results suggest that the vertical distribution of CAPE has a strong influence upon storm cycling, as might be inferred from other studies (e.g., McCaul and Weisman 2001).

3.5.4.2 *Del City Sounding*

Because replacing the Del City thermodynamics with those of the Weisman and Klemp analytic sounding produced ambiguous results, we therefore vary the low-level moisture of the original control sounding in order to manipulate the CAPE. Four soundings are produced, Ctrl_c2233, Ctrl_c2991, Ctrl_c4353, and Ctrl_c5086, with respective CAPE's of 2233, 2991, 4353, and 5086 J kg^{-1} (Table 3.2). For each, the relative humidity of the control sounding from 0-250 m is altered, resulting in surface mixing ratios of 13.8, 15.1, 17.3, and 18.5 g kg^{-1} , versus 16.0 g kg^{-1} for the control case. It is important to note that varying the CAPE in this manner also varies the LCL and LFC heights, which can strongly influence storm

characteristics (McCaul and Cohen 2002). Although the control sounding has an LCL (LFC) height 710 (722) m, the modified soundings extend the range of LCL (LFC) values from 467-1044 (474-1217) m.

A summary of the resultant cycling characteristics is shown in Figure 3.5.12. In all cases, storm shape, structure, and behavior are very similar to the control run, i.e., supercells undergoing OCM. For the lowest CAPE simulation, Ctrl_c2233, no cycling is observed. Ctrl_c2991 produces two OCM cycles, with the first occlusion slowed by approximately 3600 s from the control run. For the higher CAPE simulations, the cycling characteristics appear to converge, with the first and second occlusions hastened by 300 s or less. Although this represents a very limited sampling of the parameter space, *the effects of the CAPE changes clearly suggest that increasing (decreasing) the CAPE tends to speed up (slow down) the OCM cycling process.*

3.6 Quarter-Circle Simulations

3.6.1 3km Turning Depth

The quarter-circle hodograph is unique for two reasons. First, it represents the best approximation to the average observed supercell sounding (e.g., Chisholm and Renick 1972; Doswell and Evans 2003), although Davies-Jones (2003) has recently criticized this finding because the curvature of a mean hodograph does not necessarily equal the mean of the individual curvatures. Second, the quarter-circle hodograph easily allows for independent analytic variations in the amount of upper and lower level shear. With this in mind, three sets of quarter-circle hodograph simulations are conducted, with radii of 10, 15, and 20 m s^{-1} . In this section, the depth of turning is kept constant at 3 km, with levels of westerly rectilinear shear from 0-60 m s^{-1} distributed from 3-9 km. Sixteen hodographs of this type are used, each named according to the convention Qtr3_RRSS, where RR is the radius and SS

Half-circle Hodographs Over 10 km

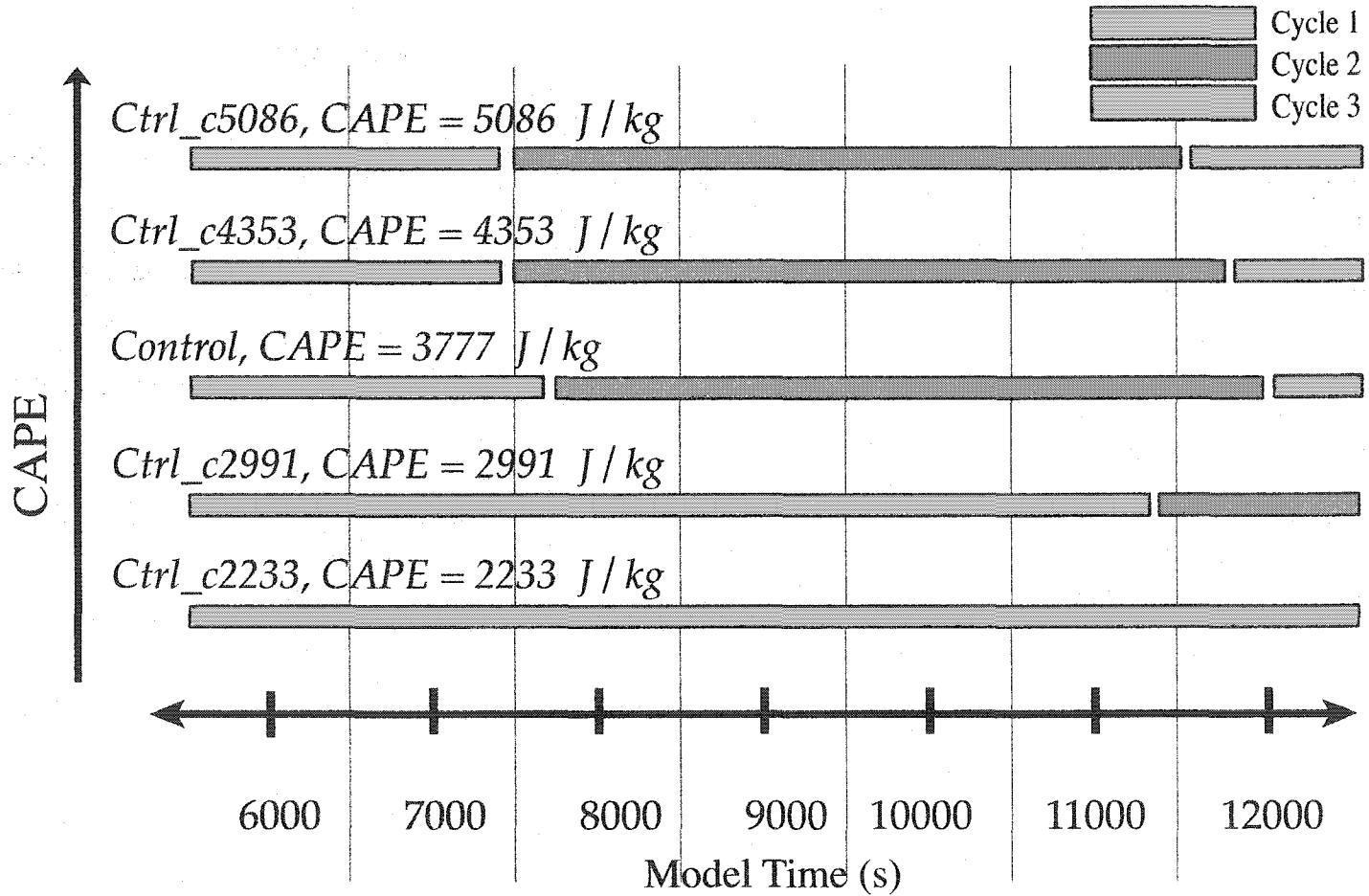


Figure 3.5.12: Schematic of cycling behavior for the Ctrl_c simulations.

is the “magnitude” (hodograph length in m s^{-1}) of the rectilinear shear (Table 3.2). In order to examine the effect of relocating falling precipitation, four additional simulations (Qtr3_RRSSrot) are conducted with the westerly rectilinear shear rotated $\pm 45^\circ$. Finally, one pair of simulations (Qtr3_RRSS_cCAPE) is conducted to assess whether the influence of CAPE variations is similar to that previously described (Section 3.5.4). The complete set of soundings is described in Table 3.2 and the corresponding hodographs are shown in Figs. 3.6.1a-c. As in previous simulations, these hodographs again cover a wide range of shears and helicities, with BRNsh_0 (BRNsh_0) values ranging from 8.9-20.7 (9.9-27.8) m s^{-1} and SRH_3 (SRH_1) values ranging from 111-634 (43-252) $\text{m}^2 \text{s}^{-2}$.

A summary of the cycling characteristics for the quarter-circle simulations of radius 10 m s^{-1} (Qtr3_10, Table 3.2) is shown in Figure 3.6.2. For the lowest shear case, Qtr3_1000, the simulation produces a very small (i.e., the areal extents of the updraft at 4.5 km and q_r at 35 m are only 24 km^2 and 128 km^2 , respectively) non-cycling supercell despite values of BRN and SRH that might suggest a multicellular storm. However, its mesocyclone remains fairly weak throughout the run, with near-ground vorticity never exceeding 0.03 s^{-1} . As the rectilinear shear is increased (i.e., above 3 km), the simulated storms begin to cycle (OCM). In Qtr3_1010, two OCM cycles occur with an occlusion at approximately 11400 s (Fig 3.6.2). When the rectilinear shear is increased to 20 m s^{-1} in Qtr3_1020, three OCM cycles are observed, with the first occlusion occurring approximately 3600 s earlier than in Qtr3_1010 (Fig 3.6.2). When the rectilinear shear is increased further for Qtr3_1040, mesocyclone cycling slows and only one occlusion is observed at 12000 s.

A transition in the mode of cycling occurs when the rectilinear shear is increased to its highest value of 60 m s^{-1} (higher than what might realistically be observed in a severe storm situation) for Qtr3_1060. Although a classic occlusion

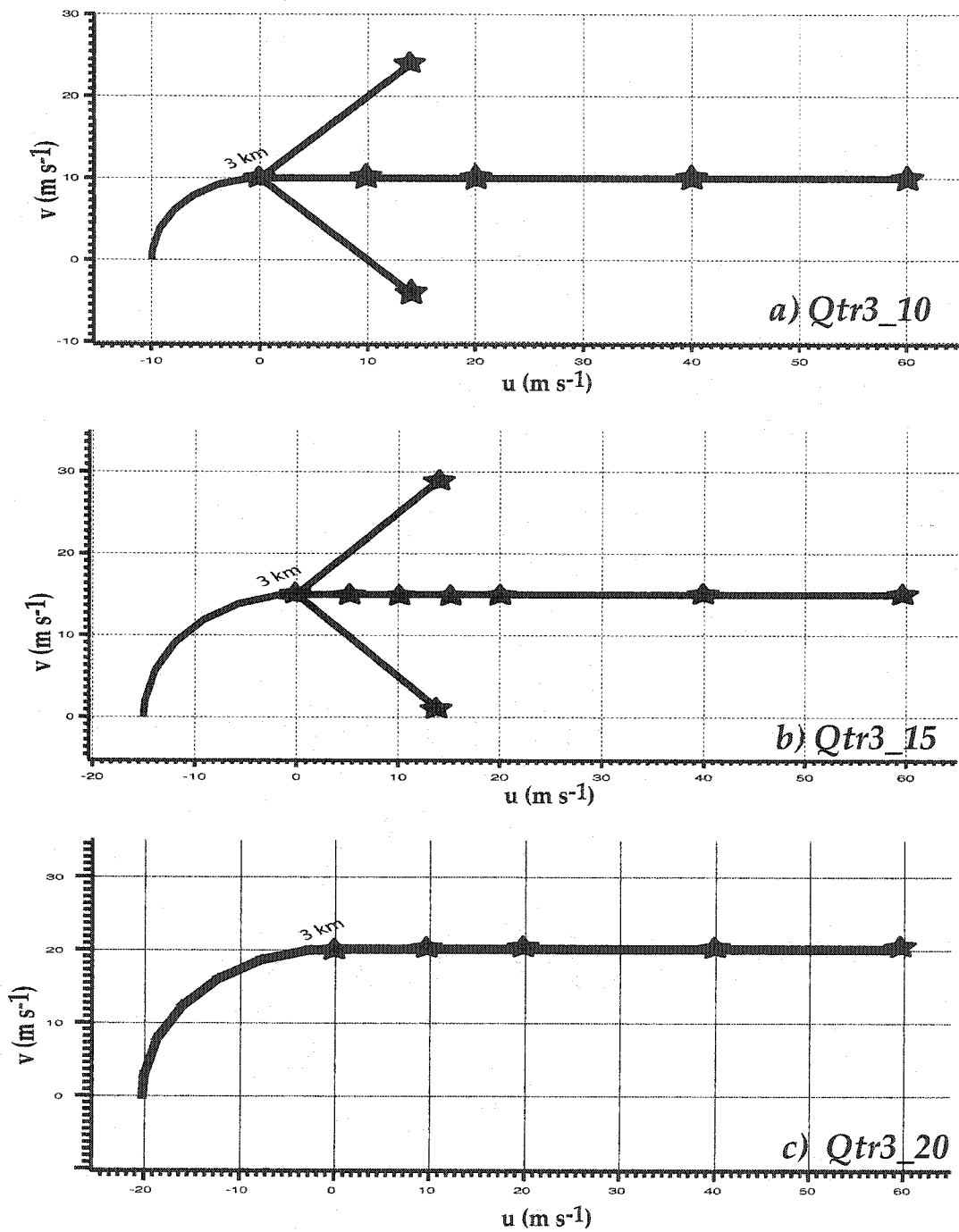


Figure 3.6.1: Hodographs for simulations a) Qtr3_10, b) Qtr3_15, and c) Qtr3_20. Stars indicate the termination point of the rectilinear shear for each of the simulations, as described in Table 3.2.

Quarter-circle Hodographs Over 3 km with Radii of 10 m/s

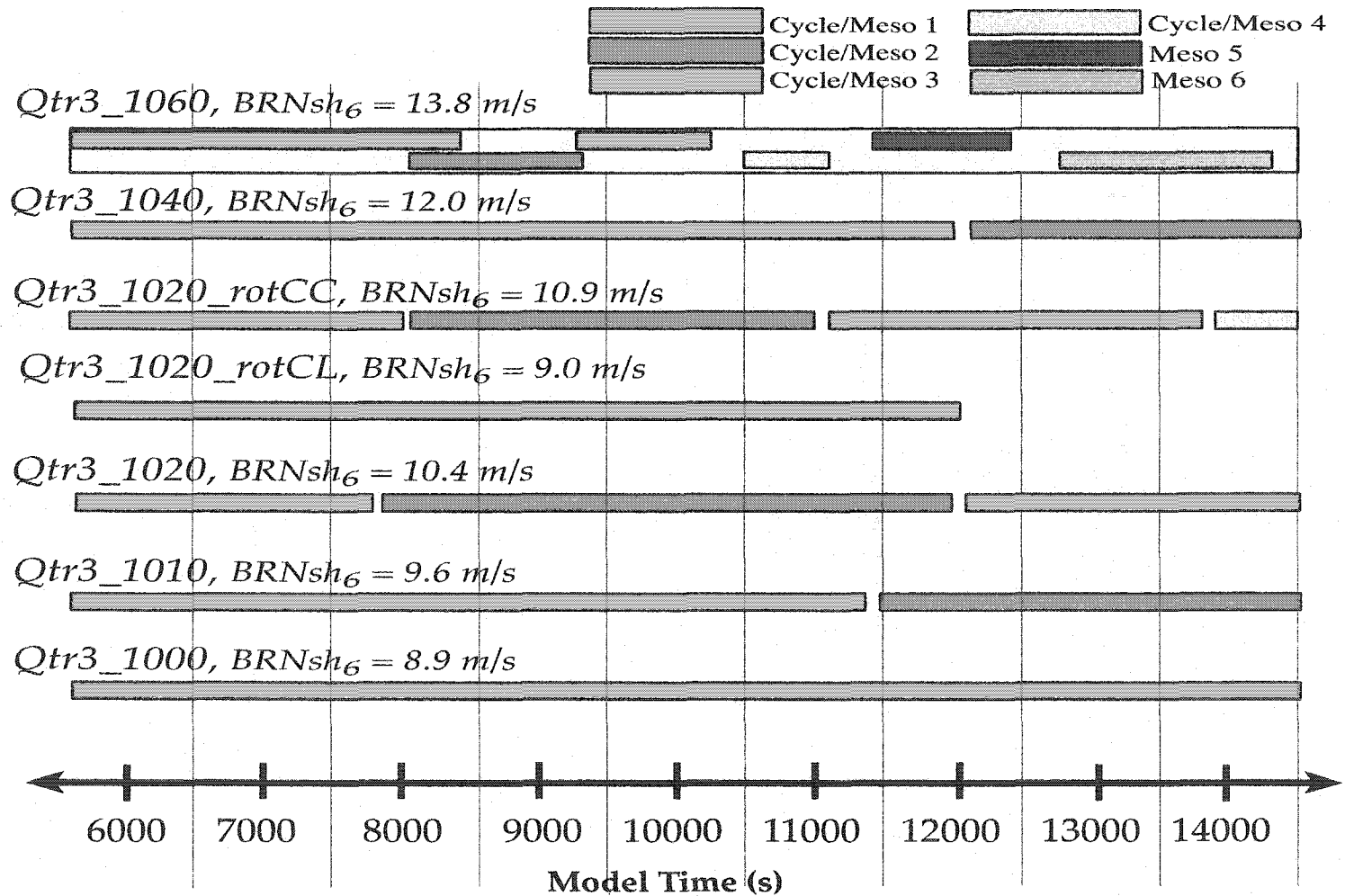


Figure 3.6.2: Schematic of cycling behavior for the Qtr3_10 simulations.

occurs at 8100 s, during the rest of its lifetime the storm undergoes the non-occluding mode of cyclic mesocyclogenesis (NOCM), with near-ground mesocyclones repeatedly forming farther north along the gust. This is similar to the behavior of Half6_r21 (Sec. 3.5.3; Fig. 3.5.11) except that in Qtr3_1060, the cyclic behavior is more rapid, with a somewhat remarkable six near-ground mesocyclones observed during the four hour simulation (Fig. 3.6.2).

Overall, the pattern of cycling behavior for the Qtr3_10 simulations is similar to that of the Half6 simulations (Sec. 3.5.3; Fig. 3.5.10). At very low shear, we observe no cycling. As the shear increases, OCM cycling commences. Then, at high shear, the storm transitions to non-occluding cyclic mesocyclogenesis.

When we increase the radius of the quarter-circle to 15 m s^{-1} (simulations Qtr3_15, Table 3.2), cycling behavior becomes more varied (Fig. 3.6.3). In the lowest shear simulation, Qtr3_1500, two OCM cycles occur, with the occlusion taking place at approximately 8100 s. When the rectilinear shear is increased to 20 m s^{-1} in Qtr3_1520, the storm undergoes two occlusions, the first approximately 1200 s later than in Qtr3_1500. However, when the rectilinear shear is only 10 m s^{-1} , the storm changes cycling modes and undergoes non-occluding cyclic mesocyclogenesis after 10800 s. Because this behavior is anomalous compared to surrounding simulations in the parameter space, two additional simulations are conducted with rectilinear shear of 5 and 15 m s^{-1} . Similar to Qtr3_1500, both Qtr3_1515 and Qtr3_1505 undergo two OCM cycles, with the first occlusion occurring from 300 to 900 s later than in Qtr3_1520 (Fig 3.6.3). Therefore, this sensitivity seems to be an isolated event, similar to that encountered in Shift_U1 (Sec. 3.5.2). As before, similar sensitivities in the context of actual prediction might be remedied by an ensemble approach utilizing conditional probabilities (e.g., Levit et al. 2004).

Quarter-circle Hodographs Over 3 km with Radii of 15 m/s

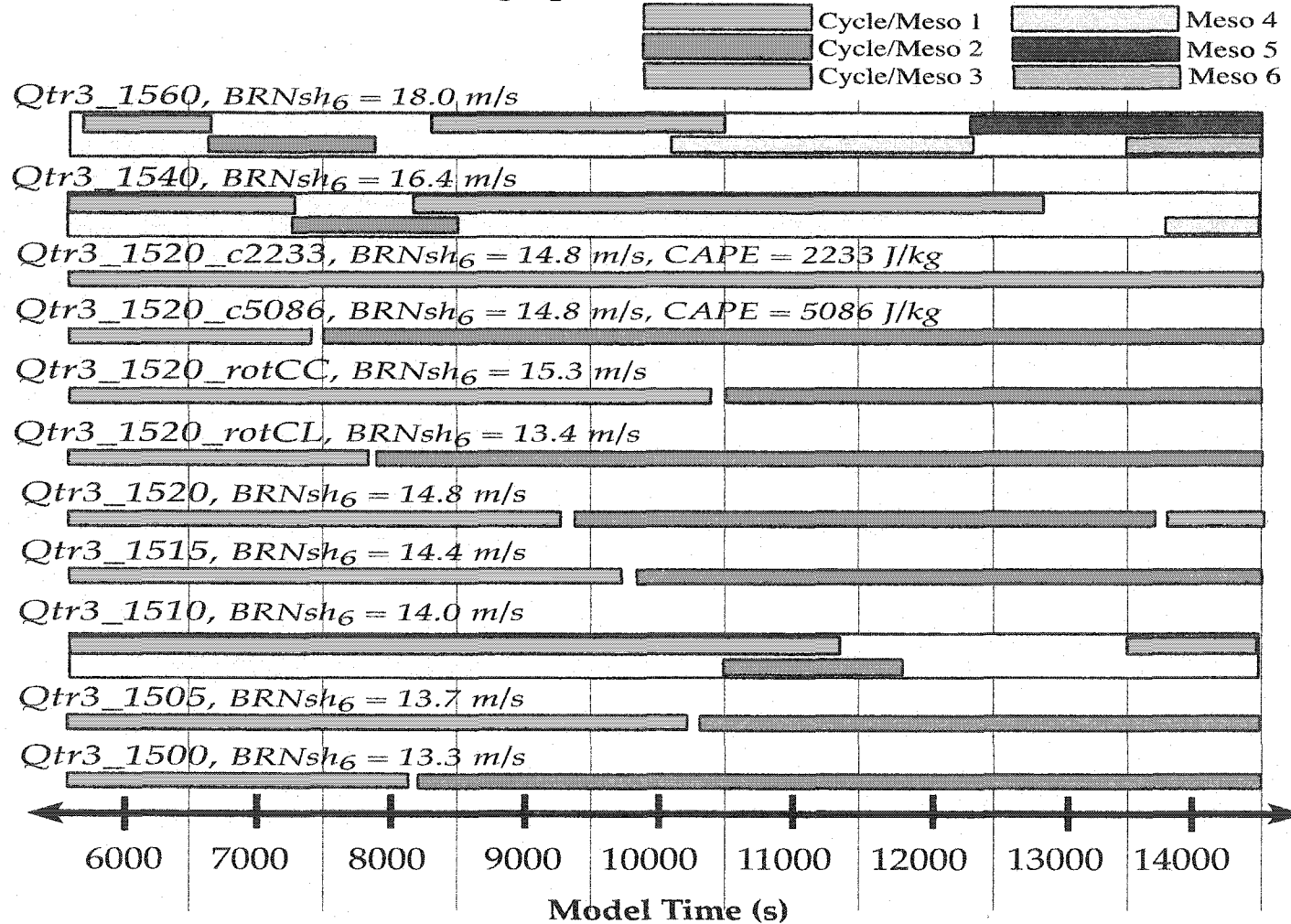


Figure 3.6.3: Schematic of cycling behavior for the Qtr3_15 simulations.

When the rectilinear shear is increased to 40 and 60 m s⁻¹ in Qtr3_1540 and Qtr3_1560 (Fig 3.6.3), the simulated storms again transition to a rapid mode of non-occluding cyclic mesocyclogenesis, similar to that simulated in Qtr3_1060. Four mesocyclones occur in Qtr3_1540 while six develop in Qtr3_1560. There appears to be a tendency for more rapid NOCM cycling with increasing shear in this case, a trend that is opposite to that simulated in many of the OCM cyclic cases (e.g., Sec. 3.5).

When we increase the radius of the quarter-circle hodograph to 20 m s⁻¹ (simulations Qtr3_20, Table 3.2) the mode of cycling transitions to almost entirely NOCM. A summary of these cycling characteristics is shown in Figure 3.6.4. Three mesocyclones are produced in Qtr3_2000, while Qtr3_2010 yields six. As the rectilinear shear is further increased (Qtr3_2020 through Qtr3_2060, Fig. 3.6.4), the number of simulated mesocyclones decrease and the initial and subsequent mesocyclones are delayed. This behavior is similar to that found in many of our other simulations (e.g., Sec. 3.5, 3.7). Unlike the Qtr3_15 cases, there does not appear to be a trend for more rapid NOCM cycling with increasing shear (or else the trend is confined to the Qtr3_2000-Qtr3_2010 simulations).

In order to briefly examine the role of CAPE upon mesocyclone cycling (OCM) for a hodograph other than the control run (Sec. 3.5.4), two additional soundings are constructed based on Qtr3_1520. CAPE is increased in Qtr3_1520_c5086 to 5086 J kg⁻¹ and decreased in Qtr3_1520_c2233 to 2233 J kg⁻¹. The thermodynamic profiles correspond to simulations Ctrl_c5086 and Ctrl_c2233 (Table 3.2; Sec. 3.5.4.2), respectively. When the CAPE is increased, Qtr3_1520_c5086 undergoes one occlusion, approximately 1800 s earlier than in Qtr3_1520 (Fig 3.6.5). When the CAPE is reduced, Qtr3_1520_c2233 undergoes no occlusions during the entire simulation (Fig. 3.6.3). Although this again represents a very limited sampling

Quarter-circle Hodographs Over 3 km with Radii of 20 m/s

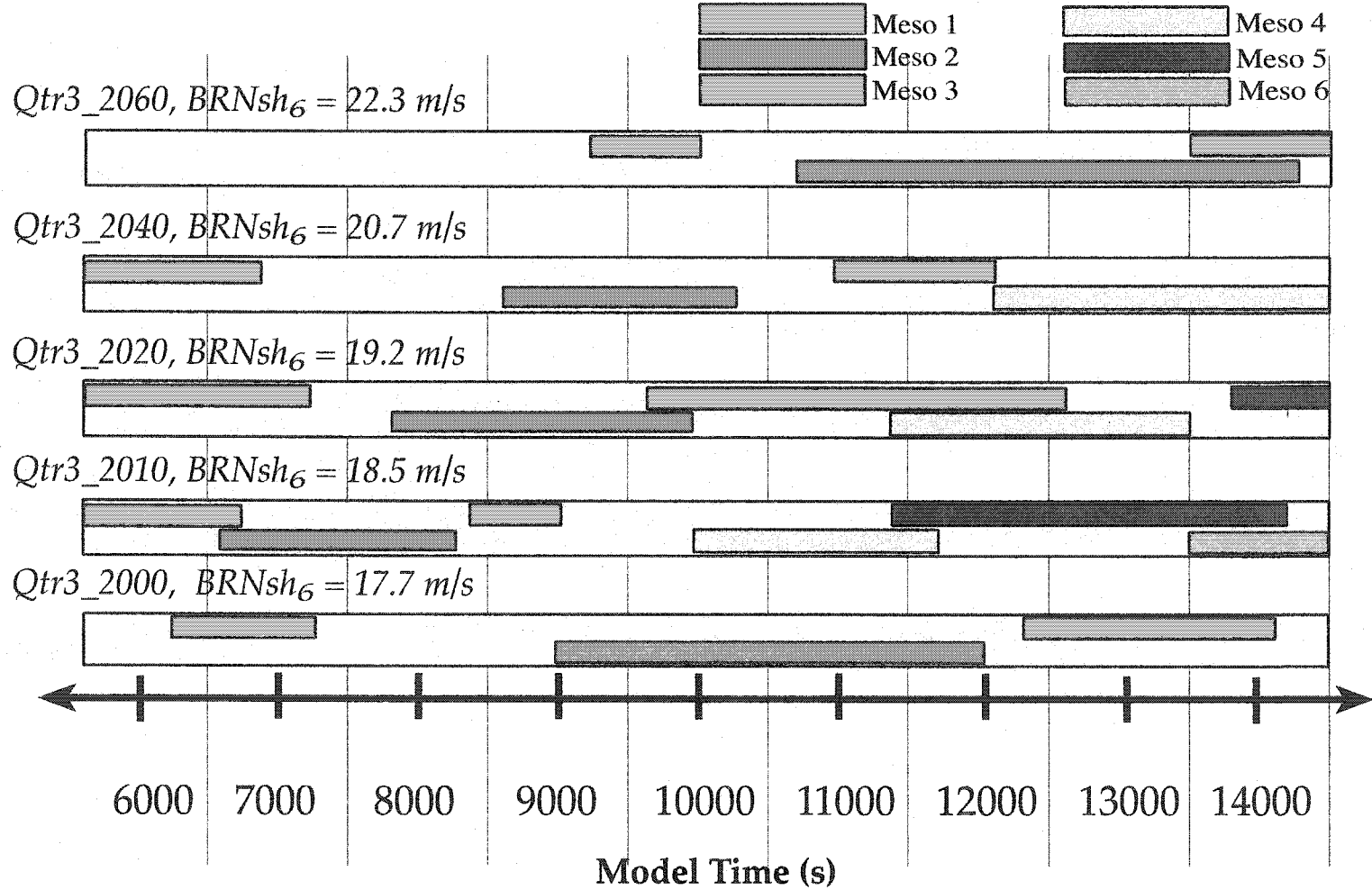


Figure 3.6.4: Schematic of cycling behavior for the Qtr3_20 simulations.

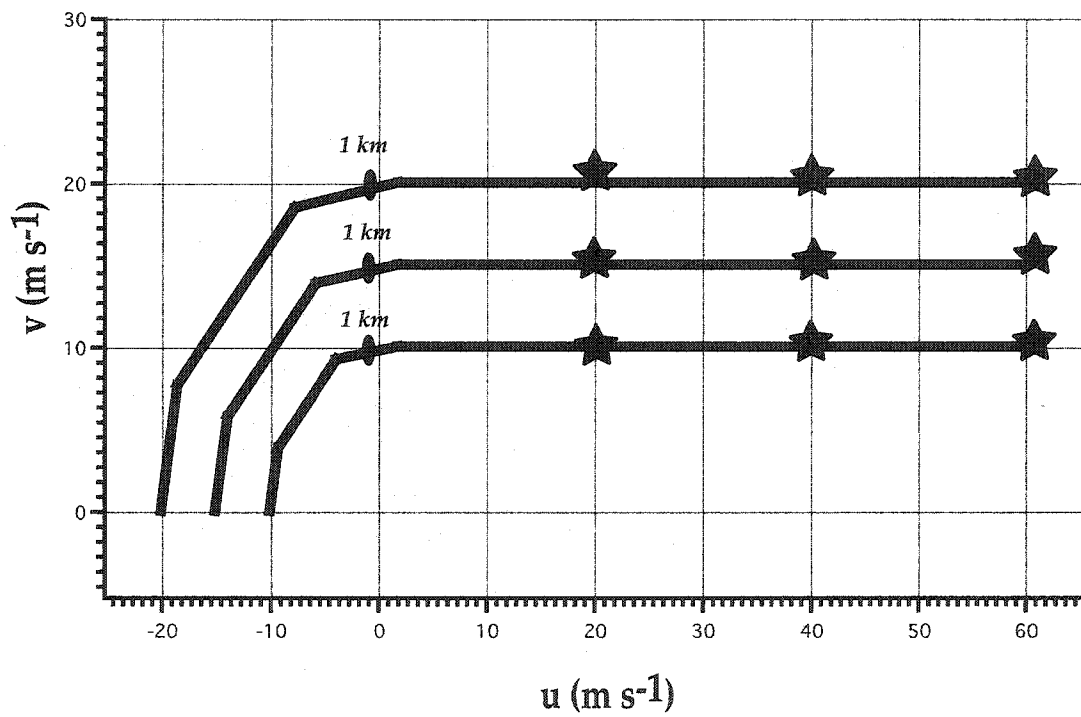


Figure 3.6.5: Hodographs for simulations Qtr1_10, Qtr1_15, Qtr1_20. Stars indicate the termination point of the rectilinear shear for each of the simulations, as described in Table 3.2.

of the parameter space, the effects of the CAPE changes suggest that increasing (decreasing) the CAPE tends to speed up (slow down) the OCM cycling process. This result is consistent with those simulations using the control run hodograph (Sec. 3.5.4) and suggests that higher CAPE results in a storm that is unsteadier.

Four additional simulations are conducted to examine the role of surface precipitation location by varying the angle of the 3-9 km rectilinear shear $\pm 45^\circ$. When the hodograph tail is rotated clockwise, the hodograph becomes somewhat similar in shape to a half-circle. Therefore, we might expect more regular OCM behavior, as in Section 3.5.1. However, this configuration also might force more precipitation into the inflow area, possibly delaying or stopping cycling altogether (e.g., Sec. 3.8). Rotating the hodograph tail counterclockwise produces a wind profile that is similar to that of a straight hodograph. This might move precipitation farther away from the incipient near-ground mesocyclone, slowing initial mesocyclogenesis. It also might induce a transition to more rapid NOCM cycling, as in Section 3.9.

Using Qtr3_1020 and Qtr3_1520 as our reference runs, we construct hodographs (Figs. 3.6.1a-b; Table 3.2) Qtr3_1020_rotCL (Qtr3_1020_rotCC) and Qtr3_1520_rotCL (Qtr3_1520_rotCC) in which the rectilinear shear is rotated 45° clockwise (counterclockwise). These alterations have fairly small effects upon parameters such as SRH and BRN (Table 3.2). However, the effects upon OCM cycling are quite varied, with somewhat opposite trends observed between the corresponding runs. Qtr3_1020 occludes twice during the simulation, at approximately 7800 and 12000 s (Fig 3.6.2). With the rectilinear shear rotated clockwise in Qtr3_1020_rotCL, the storm does not cycle and dissipates at approximately 12000 s (Fig. 3.6.2). When the rectilinear shear is rotated counterclockwise in Qtr3_1020_rotCC, the storm occludes three times (rather than

two), and the OCM cycling process appears to be hastened after the first two cycles (Fig 3.6.2).

The opposite trend is observed in the Qtr3_1520 simulations. Qtr3_1520 undergoes three OCM cycles (Fig. 3.6.3), with the first occlusion at approximately 9300 s. When the rectilinear shear is rotated clockwise in Qtr3_1520_rotCL, only two OCM cycles are evident, but the first occlusion occurs 1500 s earlier than Qtr3_1520. When the rectilinear shear is rotated counterclockwise in Qtr3_1520_rotCC, the storm undergoes two OCM cycles, with the first occlusion 1200 s later than Qtr3_1520.

In summary, these quarter-circle hodographs produce relatively *irregular* cycling behavior, with both occluding and non-occluding modes occurring. However, *the results do suggest that both very low and very high shears tend to inhibit cycling except in cases where the storm transitions to non-occluding cyclic mesocyclogenesis at high shear.* When NOCM becomes the dominant mode, initial and subsequent mesocyclones appear to be delayed with increasing shear, similar to OCM. Lastly, CAPE changes again suggest that increasing (decreasing) the CAPE tends to speed up (slow down) the OCM cycling process.

3.6.2 1 km Turning Depth

As discussed in Section 3.3.2, recent studies (Craven et al. 2002; Brooks and Craven 2002; Rasmussen 2003) suggest that the 0-1 km shear and/or SRH is important in differentiating between environments which support tornadic versus non-tornadic supercells. In order to briefly examine the effects of confining the quarter-circle shear to this smaller depth, a second set of simulations is undertaken. Three additional sets of quarter-circle hodograph simulations are conducted, again with turning radii of 10, 15, and 20 m s⁻¹ (Table 3.2; Figure 3.6.5). However, the

depth of turning is kept constant at 1 km, with levels of westerly rectilinear shear from 20-60 m s⁻¹ distributed from 1-9 km. Similar to the previous runs, each simulation is named according to the convention Qtr1_RRSS, where RR is the radius and SS is the length of the rectilinear shear. Unlike many of our other hodographs, this configuration confines most of the SRH to the 0-1 km layer, as evidenced by the range of SRH₁ (SRH₃) from 158-804 (205-1147) m² s⁻². We note that our range of SRH₁ extends well beyond what might usually be observed in the atmosphere, i.e., usually less than 400 m² s⁻² (e.g., Rasmussen 2003).

Figure 3.6.6 summarizes the cycling characteristics of the Qtr1 simulations. Simulation Qtr1_1020 maintains a weak near-ground mesocyclone throughout much of the simulation until it undergoes an occlusion at approximately 14100 s. In Qtr1_1040, the non-occluding mode of cyclic mesocyclogenesis occurs between 8100-8400 s, followed by an occlusion at 12600 s. However, after this occlusion the storm remains disorganized with no near-ground mesocyclone. Qtr1_1020 and Qtr1_1040 are the only Qtr1 simulations that produce occluding cyclic mesocyclogenesis. Qtr1_1060 generates storms exhibiting non-occluding cyclic mesocyclogenesis between 6600 and 7200 s, after which it remains quasi-steady, i.e., possessing a single strong near-ground mesocyclone which fluctuates in intensity.

Simulation Qtr1_1520 remains fairly weak and disorganized throughout the simulation, with only two near-ground mesocyclones developing during the entire simulation. Qtr1_1540 and Qtr1_1560 behave similarly to Qtr1_1060, with 1-2 NOCM cycles followed by a transition to a quasi-steady supercell with a strong near-ground mesocyclone.

Simulations Qtr1_2020, Qtr1_2040, and Qtr1_2060 behave similarly, with no near-ground mesocyclone development until after two hours of simulation time (although a single dominant storm is present). Once the near-ground mesocyclone

Quarter-circle Hodographs Over 1 km with Radii of 10-20 m/s

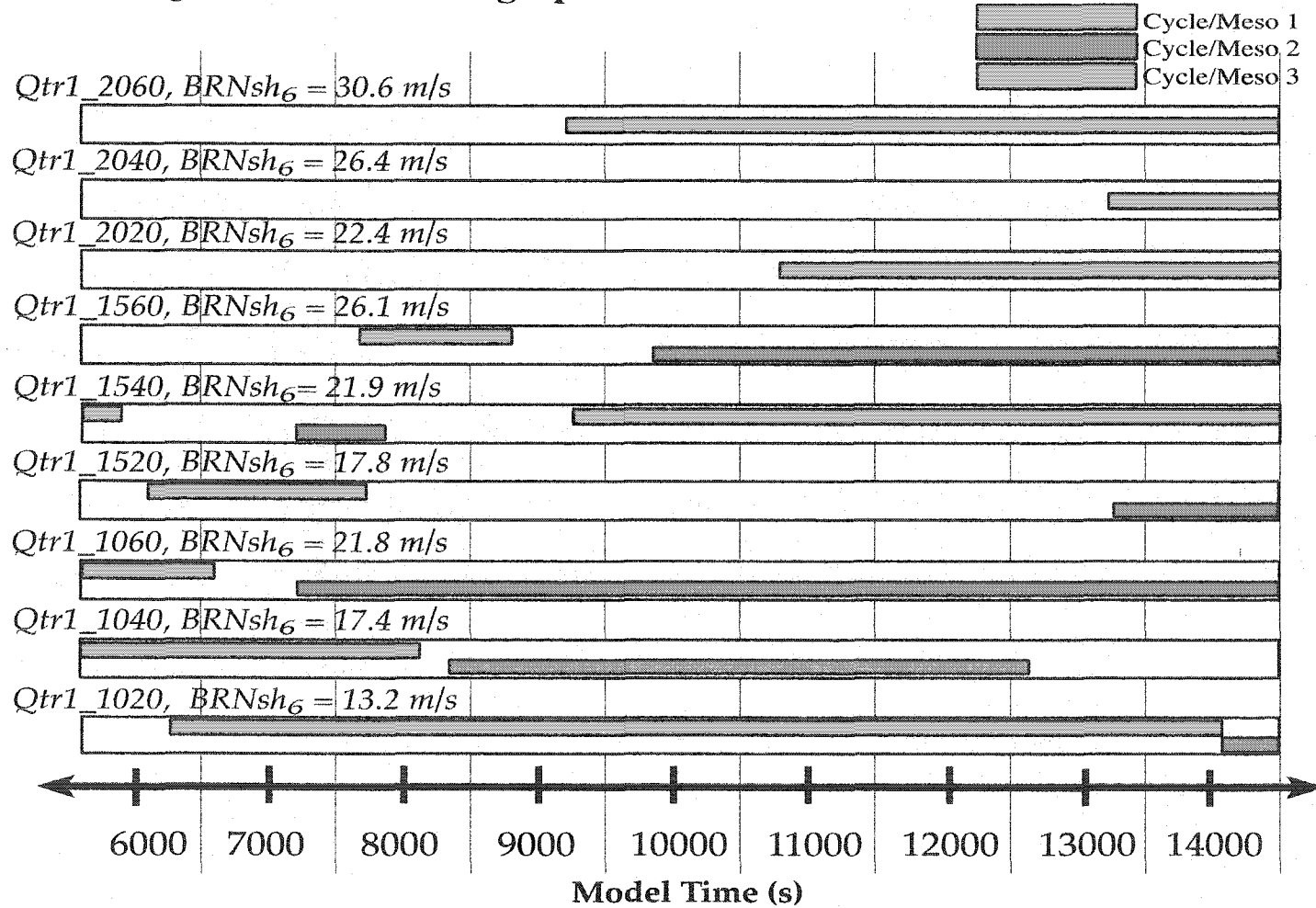


Figure 3.6.6: Schematic of cycling behavior for the Qtr1 simulations.

develops, it remains present until the end of the simulation with no cycling or occlusions. This appears to result from the extremely strong low-level shear present in this set of hodographs, consistent with the simulations in Section 3.5.2.

It is of interest to note that the Qtr1 simulations produce the strongest near-ground mesocyclones of all the runs shown in Table 3.2, consistent with their large values of SRH_1 and streamwise vorticity in the lowest 1 km. Indeed, the big (small) time step in the Qtr1 runs was lowered to 1.5 (0.3) s from 2.5 (0.5) s in order to keep the simulations stable. During their final cycles, simulations Qtr1_1040, Qtr1_1060, Qtr1_1540, Qtr1_1560, Qtr1_2040, and Qtr1_2060 all contain near-ground vorticity maxima in excess of $140 \times 10^{-3} \text{ s}^{-1}$, with approximate storm-relative winds in excess of 60 m s^{-1} surrounding the near-ground mesocyclone. Qtr1_2060 produces a near-ground mesocyclone that is in approximate cyclostrophic balance, with a 58 mb pressure drop across 5 km and surface winds of 71 m s^{-1} . The unusual strength of these simulated storms is consistent with observational evidence that higher SRH_1 values correlate well with stronger tornado-producing supercells (e.g., Rasmussen 2003). [We note that this is the author's only simulation of an *entire* near-ground mesocyclone that appears to be approximately cyclostrophic. However, since the horizontal grid spacing is a relatively coarse 500 m, it is not obvious that such a feature would maintain the same spatial scale in a higher resolution simulation. Since the tangential winds are high and the swirl ratio is large, tornadogenesis might occur on the periphery of the mesocyclone's strongest winds (Rotunno 1984; 1986).]

In summary, when the shear is confined to a shallower depth of 1 km, the quarter-circle hodographs again produce relatively irregular cycling behavior, with both occluding and non-occluding modes occurring. Because the rectilinear shear now extends over a greater depth, those simulations with the smallest amount of rectilinear shear appear to be negatively influenced by the smaller magnitude of

storm-relative winds. Those with larger amounts of rectilinear shear produce extremely strong near-ground mesocyclones, consistent with trends observed in observations of supercell environments (Craven et al. 2002; Brooks and Craven 2002; Rasmussen 2003). Similar to our results in the previous section, when non-occluding cyclic mesocyclogenesis becomes the dominant mode, initial and subsequent mesocyclones appear to be delayed with increasing shear.

3.7 Three-Quarter Circle Simulations

Three-quarter circle hodographs have been used only occasionally in storm simulations (e.g. Droegemeier et al. 1993) and represent the approximate upper limit of what might be observed in an environment supportive of supercells (e.g., McCaul's 1993 close-proximity hurricane supercell hodograph is closer to a three-quarter circle rather than a full circle). As a result of problems associated with the precipitation distribution produced by a full-circle hodograph (see section 3.8), three-quarter circle hodographs also are probably the most realistic approximation to a Beltrami flow that can be achieved while still retaining classic supercell structure.

Four sets of three-quarter circle hodograph simulations are conducted, 3qtr3_r15, 3qtr_r19, 3qtr_r25, and 3qtr_r30, with respective radii of 15, 19, 25, and 30 m s^{-1} (Fig. 3.7.1). In all cases, the depth of turning is set to 10 km, similar to that of the half-circle simulations. Given the large amount of curvature, these hodographs cover a higher range of shears than some of the other runs, with BRNsh_6 (BRNsh_9) values ranging from 14.2-28.4 (16.1-32.3) m s^{-1} and SRH_3 (SRH_1) values ranging from 288-863 (97-295) $\text{m}^2 \text{s}^{-2}$.

A summary of the simulations is shown in Figure 3.7.2. 3qtr_r15 produces a supercell that occludes twice, at 9900 and 14400 s. A similar evolution occurs for

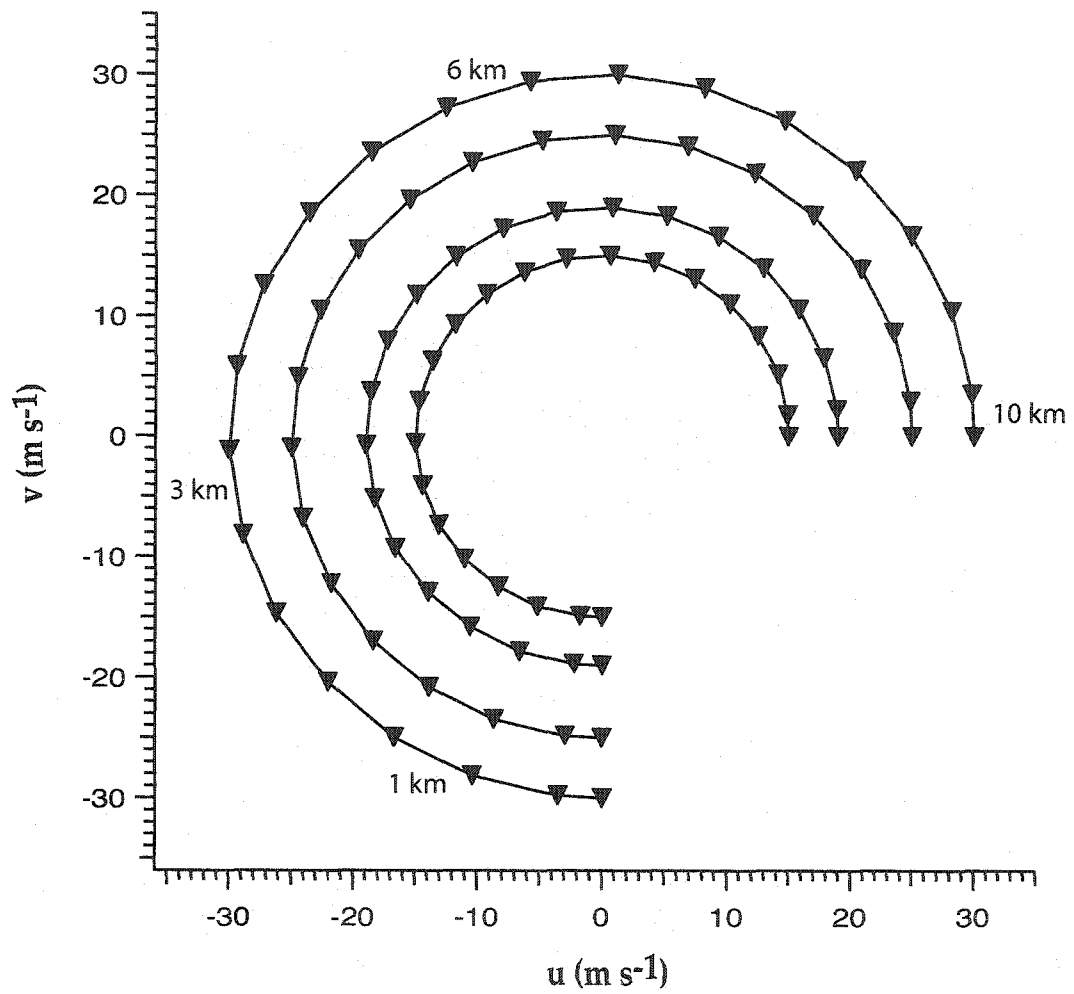


Figure 3.7.1: Hodographs for simulations 3qt_r15, 3qtr_r19, 3qtr_r25, and 3qtr_r30.

Three-quarter circle Hodographs Over 10 km

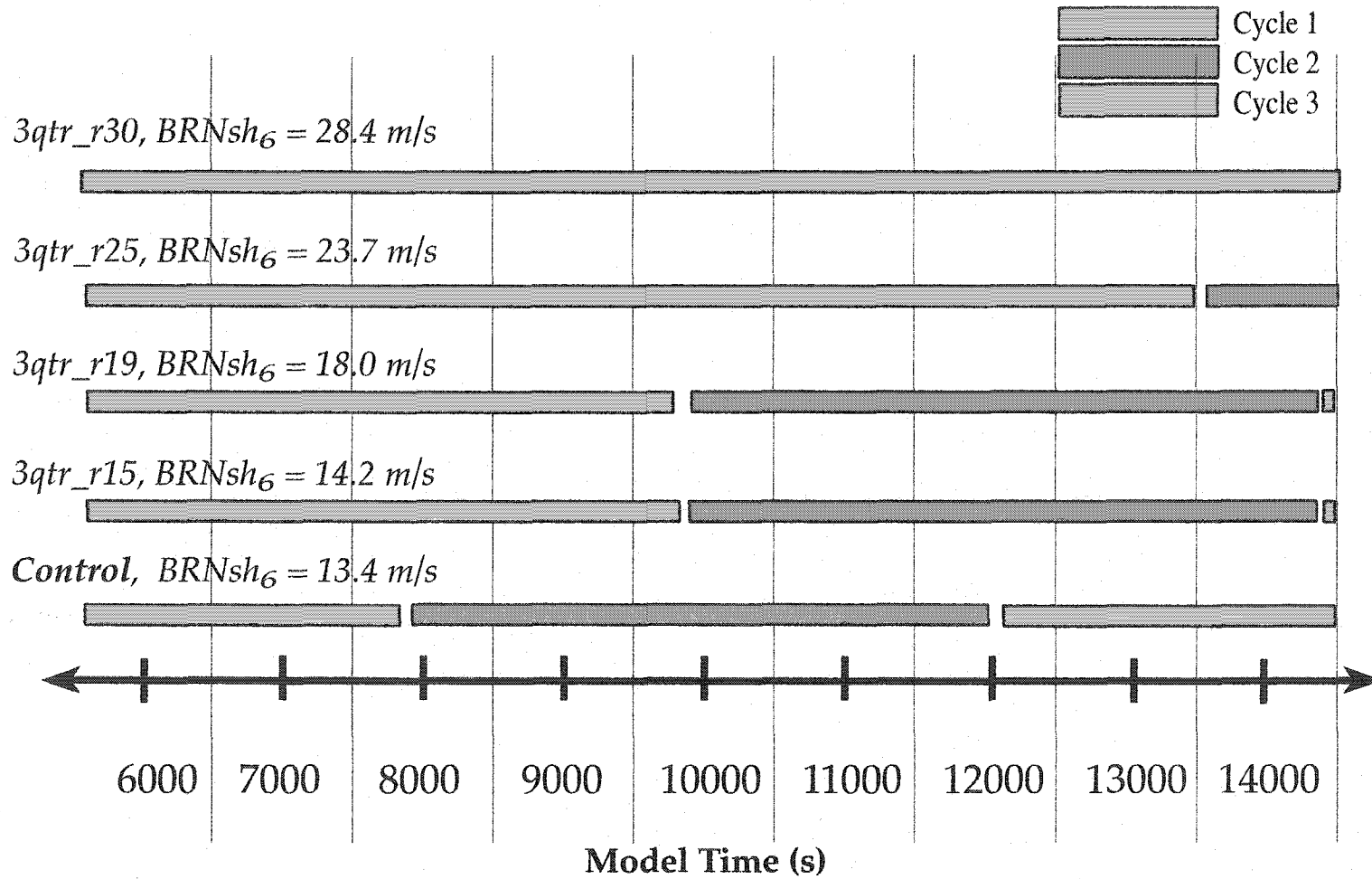


Figure 3.7.2: Schematic of cycling behavior for the 3qtr simulations.

3qtr_r19, with two occlusions occurring at approximately the same times. The occlusion process begins to slow down with higher shear, with 3qtr_r25 occluding only once at 13500 s. Finally, the highest shear simulation, 3qtr_r30, undergoes no cycling and appears to be “over-sheared” (e.g. Brooks et al. 1993), with no low-level mesocyclone development throughout the simulation.

The morphologies of the three-quarter circle simulations remain qualitatively similar to the control run. Similar to the half-circle simulations (Section 3.5 and Fig. 3.5.4), there is a noticeable increase in areal updraft size with increasing shear, with an approximate 200-300% increase from simulation 3qtr_r15 to 3qtr_r30. Unlike some of the half-circle simulations, the storm structure does not suddenly become more HP near the end of the higher shear simulations. However, in the runs which do cycle, the simulated storms display a unique characteristic in which the occluding mesocyclone wraps very deep into the precipitation core of the storm (Fig. 3.7.3) where it progresses backward (relative to the location of the new mesocyclone) and decays.

In summary, the three-quarter circle simulations show cycling trends similar to those of the half-circle simulations, and *they again clearly suggest that increasing shear throughout the same depth of turning tends to slow down and eventually terminate the OCM cycling process.*

3.8 Full-Circle and Helical Hodograph Simulations

The full-circle hodograph represents an extreme case in which the environmental vorticity is almost purely streamwise at all heights within the turning depth. In the limit of vanishing CAPE, a steady-state updraft in circular shear can be *analytically* represented as a Beltrami flow (Davies-Jones 1985; Lilly 1986b), an

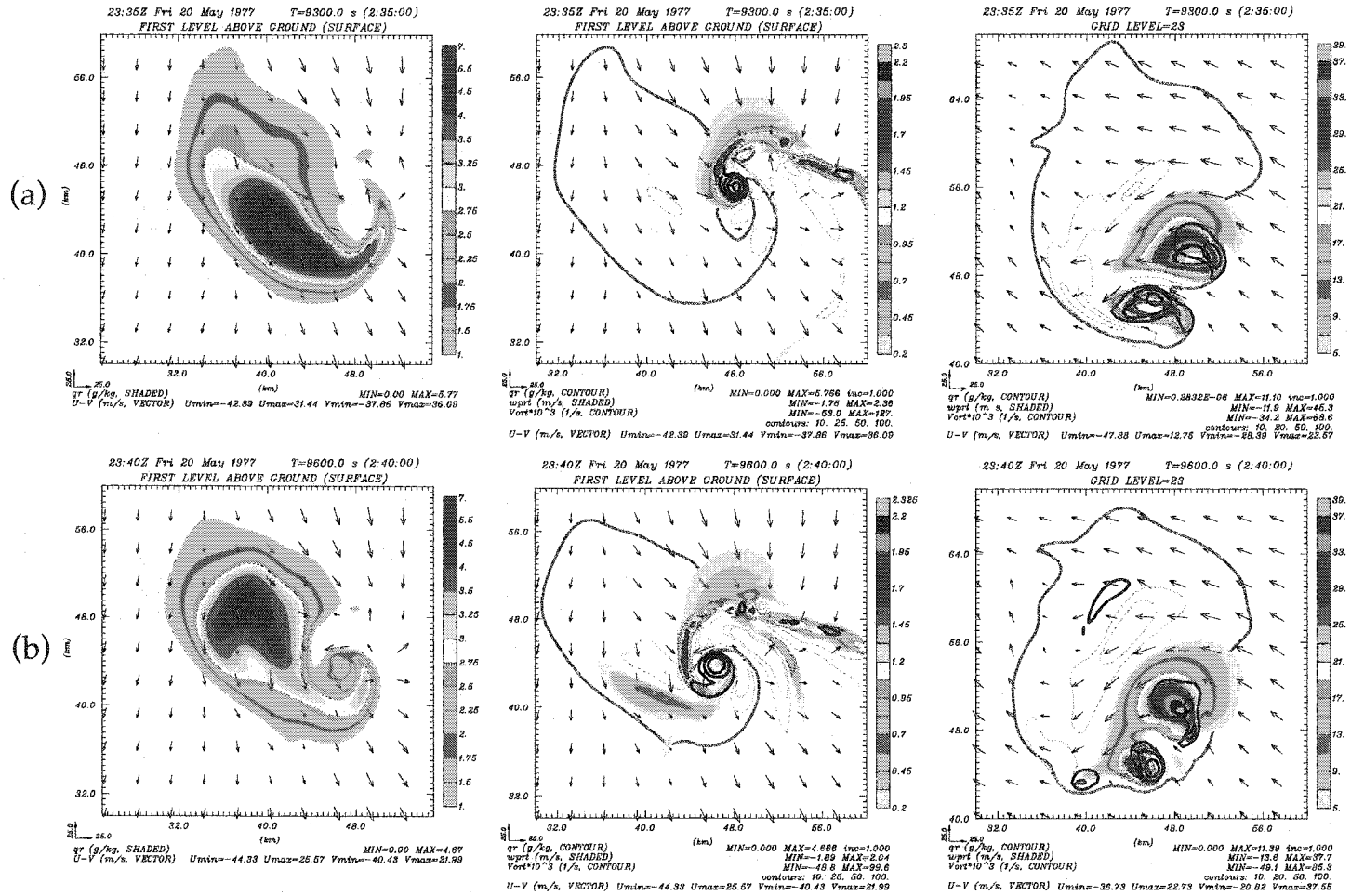


Figure 3.7.3: Plots of rainwater mixing ratio (left) and vertical velocity at $z = 50$ m (center) and $z = 4.5$ km (right) for 3qtr_r19 at $t = 9300$ s (a) and 9600 s (b). Negative vertical velocity contoured in light blue at an interval of 0.3 (center) and 5.0 s^{-1} (right). Vertical vorticity contoured in black at irregular intervals $0.01, 0.02, 0.05,$ and 0.1 s^{-1} . Single dark blue contour indicates 1 g kg^{-1} rainwater mixing ratio.

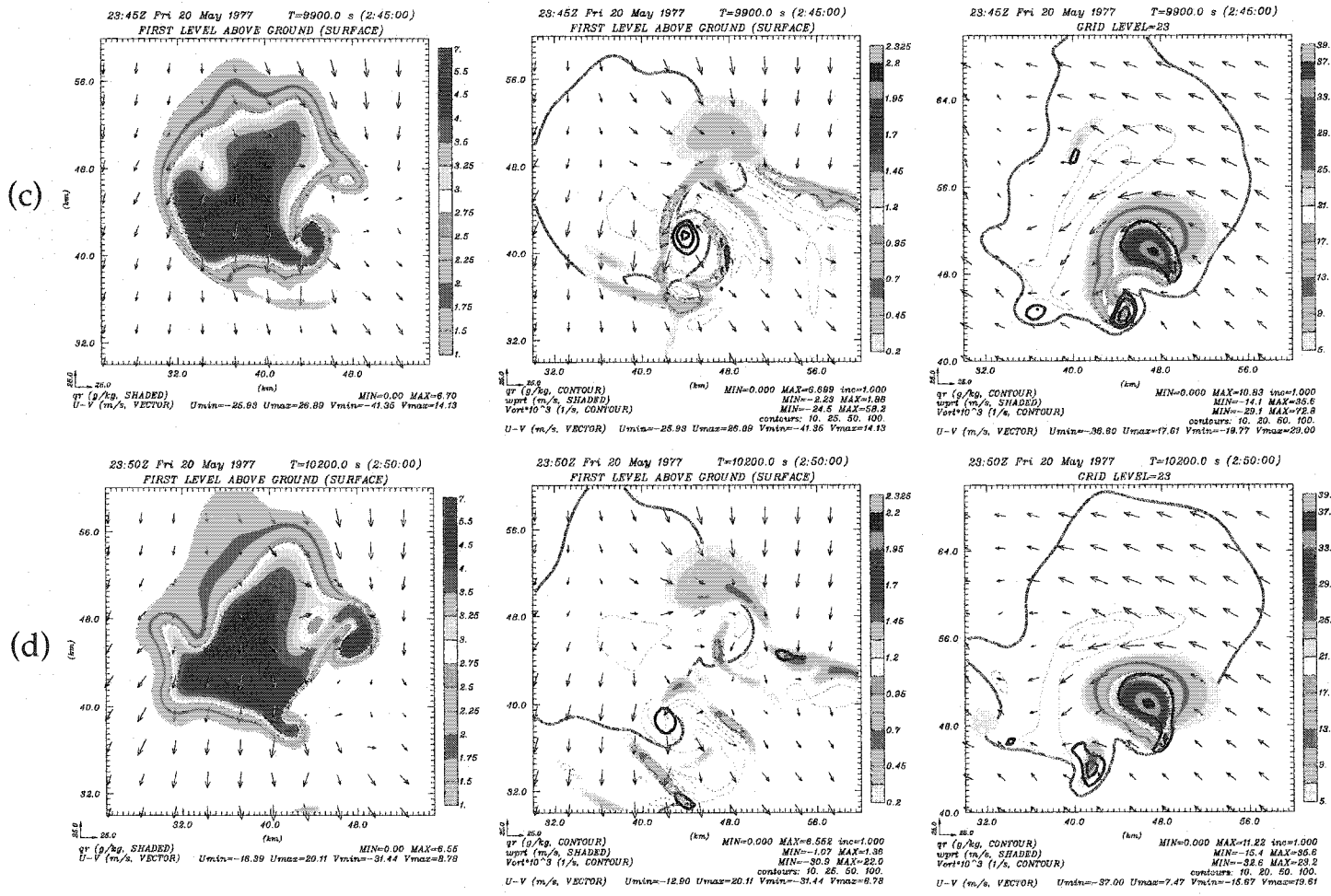


Figure 3.7.3, continued: As in (a) and (b), except for $t=9900$ s (c) and 10200 s (d).

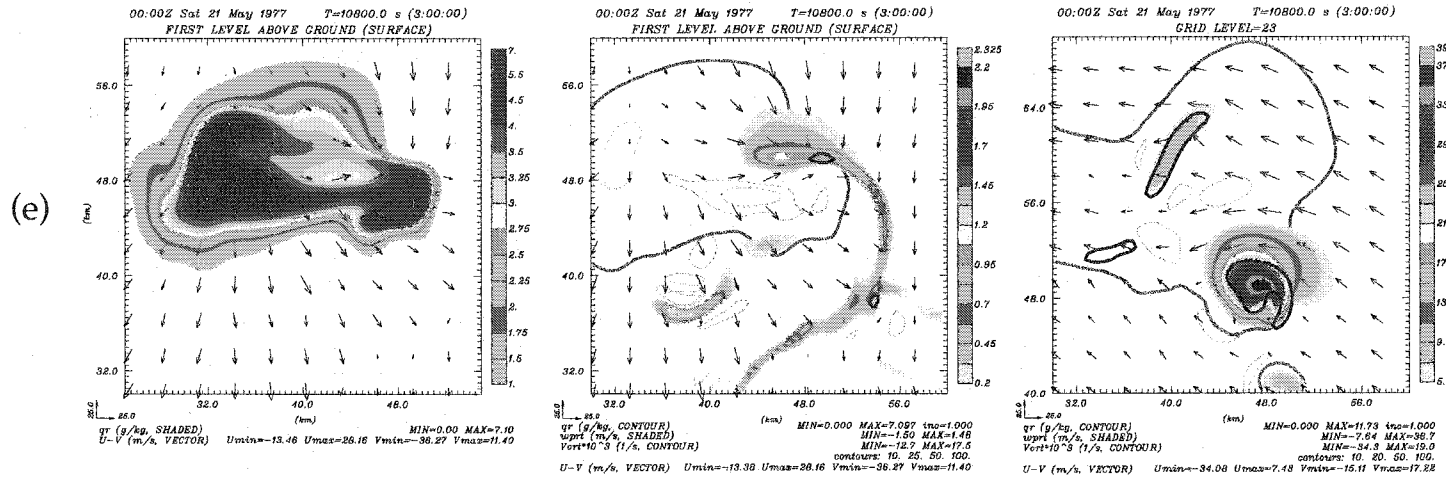


Figure 3.7.3, continued: As in (a) and (b), except for $t=10800$ s (e).

extreme in which nonlinear propagation ceases (Davies-Jones 2002). However, even in the presence of buoyancy, Davies-Jones (2002) demonstrated that a simulated storm in circular shear has characteristics qualitatively similar to a Beltrami updraft.

Three full-circle (360° of turning) hodograph simulations are conducted. In each, the depth of turning is kept constant at 10 km, with radii of 15, 19, and 25 m s^{-1} (Fig. 3.8.1). The simulations are designated 360_r15, 360_r19, and 360_r25, respectively. As shown in Table 3.2, these hodographs also cover a higher range of shears than some of the other runs, with BRNsh_6 (BRNsh_9) values ranging from 16.1-26.9 (15.3-25.4) m s^{-1} and SRH_3 (SRH_1) values ranging from 411-1054 (135-322) $\text{m}^2 \text{s}^{-2}$. A simulation with a radius of 10 m s^{-1} also was attempted, but the simulated storm failed to survive more than 90 minutes. This result is consistent with the circular shear simulations of Weisman and Rotunno (2000), although it is not clear why they failed to use a slightly larger radius. Davies-Jones (2002) speculates on why their supercell decayed after an hour.

In addition to the full-circle hodograph simulations, two helical (720° of turning) hodograph simulations also are conducted, with radii of 15 and 19 m s^{-1} . Although these hodographs are obviously unrealistic, they are included for completeness. The simulations are designated 720_r15 and 720_r19, respectively. The turning depth is set to 15 km because 10 km produces too much shear to sustain a supercell storm. As in the full-circle cases, these hodographs also cover a higher range of shears than some of the other runs, with BRNsh_6 (BRNsh_9) values ranging from 16.4-20.7 (13.4-17.0) m s^{-1} and SRH_3 (SRH_1) values ranging from 487-801 (155-248) $\text{m}^2 \text{s}^{-2}$.

Neither the full-circle nor the helical hodograph simulations produce occluding storms during the 4-hour simulation period. Despite the high values of SRH and BRNsh, it appears that circular shear has a detrimental effect upon the

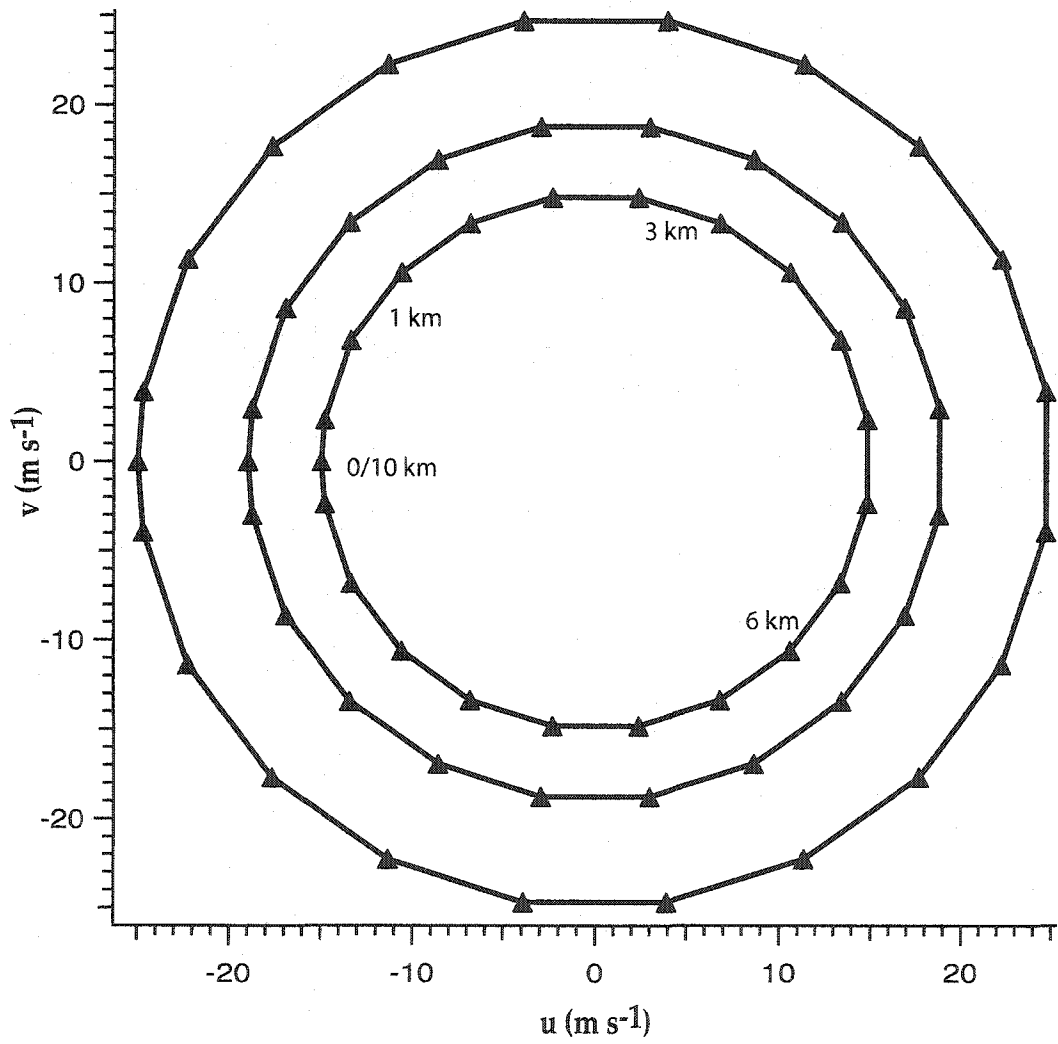


Figure 3.8.1: Hodographs for simulations 360_r15, 360_r19, and 360_r25.

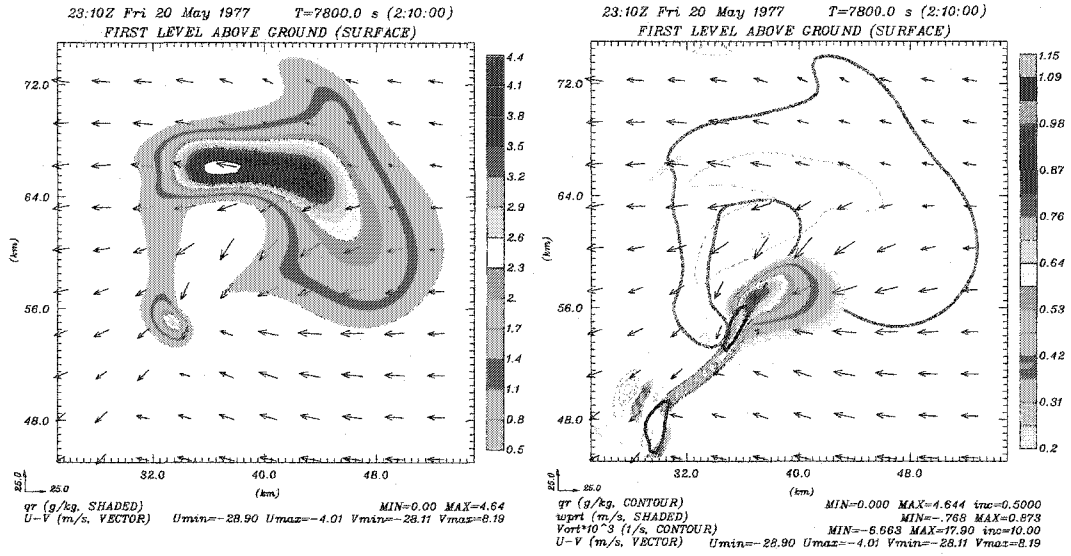
simulated storms. This effect most likely results from the unnatural redistribution of precipitation that causes the storms to rain into their inflow (Fig. 3.8.2). The storms do have some basic similarities to a Beltrami flow (Davies-Jones 2002), especially in the higher shear simulation 360_r25. For example, the circular mid-level mesocyclone is nearly coincident with the updraft and is surrounded by a semi-circular area of anticyclonic vorticity, approximately coincident with the downdraft (Fig 3.8.3).

Both the helical simulations and 360_r25 have relatively weak low-level mesocyclones throughout the simulation. In the case of 360_r25, it appears that the storm is overwhelmed by the magnitude of the shear. Only 360_r15 and 360_r19 are able to develop low-level mesocyclones near the end of the simulation which are moderately strong with respect to our other cases (vertical vorticity of $53\text{-}68 \times 10^{-3} \text{ s}^{-1}$). Unlike the other circular shear simulations, 360_r15 appears to begin an occlusion process at 14400 s. When this simulation is extended to 16200 s, the storm does in fact occlude at 15300 s, although the low-level mesocyclone is still fairly weak (vertical vorticity of $33 \times 10^{-3} \text{ s}^{-1}$). When this is taken into account, the full-circle simulations appear to follow the pattern demonstrated in some of the previous hodograph shapes, with higher shears inducing a more steady-state storm with OCM cycling either slowing or stopping.

The helical hodograph simulations show no such pattern and appear to exhibit more unsteady behavior than their full-circle counterparts, with rapid development, decay, and splitting of multiple updraft maxima associated with the main storm of interest. Interestingly, this behavior is more pronounced in the higher-shear simulation, 720_r19.

In summary, the storms produced in the circular shear simulations appear to be negatively impacted by the lack of a mechanism to keep precipitation away from

Simulation 360_r19



Simulation 720_r15

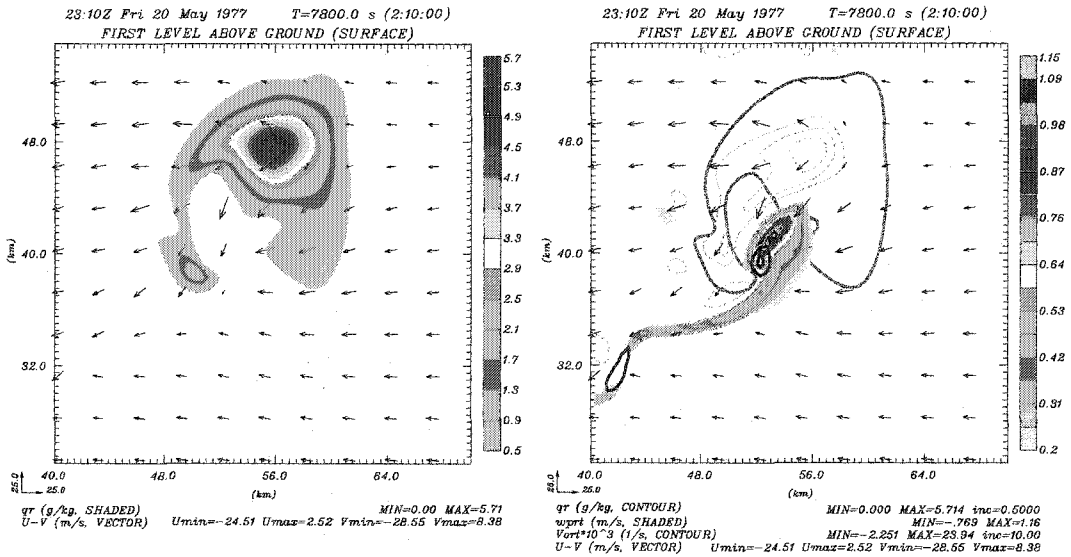


Figure 3.8.2: Plots of rainwater mixing ratio (left) and vertical velocity (right, color-filled) at $z = 50$ m for simulations 360_r19 (top) and 720_r15 (bottom) at $t = 7800$ s. Negative vertical velocity contoured in light blue at an interval of 0.2 m s^{-1} . Vertical vorticity contoured in black at an interval of 0.01 s^{-1} . Dark blue contour indicates 1 g kg^{-1} rainwater mixing ratio.

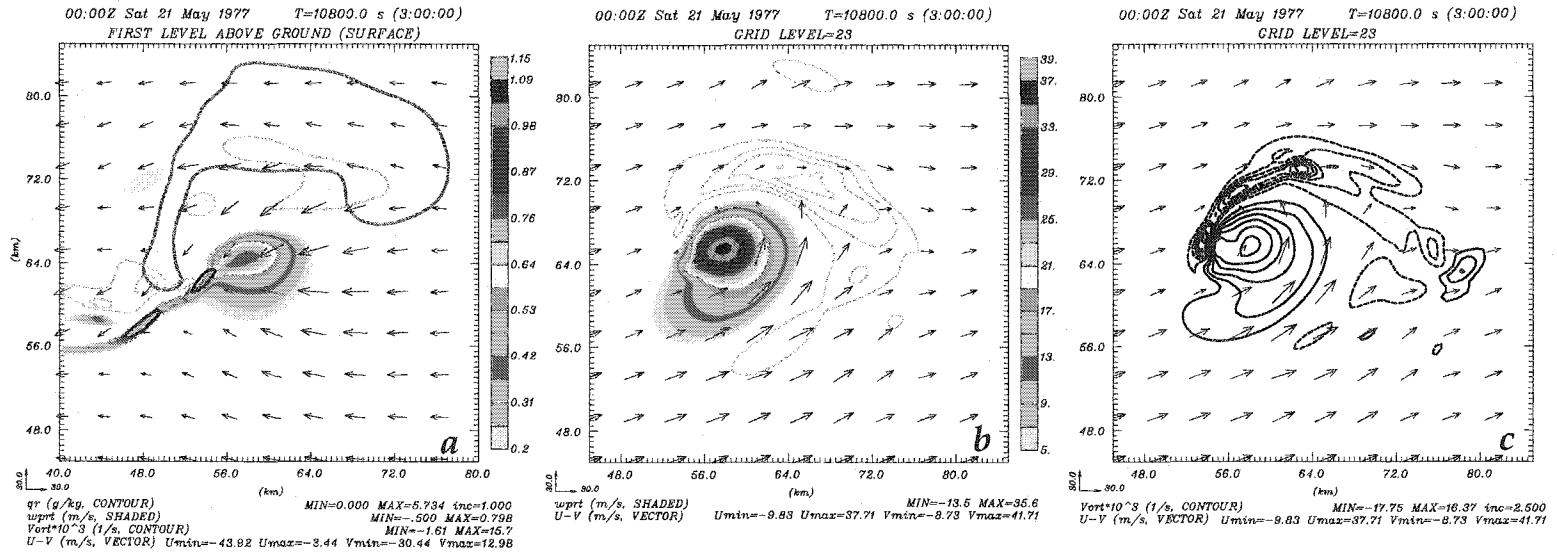


Figure 3.8.3: Plots of vertical velocity (color-filled) at $z = 50$ m (a) and $z = 4.5$ km (b), and vertical vorticity at $z = 4.5$ km (c) for simulation 360_r25 at $t = 10800$. In (a) and (b): negative vertical velocity contoured in light blue at an interval of 0.3 and 5.0 m s^{-1} , respectively. In (a): vertical vorticity contoured in black at an interval of 0.1 s^{-1} ; single dark blue contour indicates 1 g kg^{-1} rainwater mixing ratio.

the storm inflow. This problem is exacerbated in the helical hodograph simulations, which produce weaker storms that are unsteadier than those in their full-circle counterparts. While none of the helical hodograph simulations exhibit cycling, extension of the full-circle simulations out for another half-hour shows *that increasing shear throughout the same depth of turning tends to slow down and eventually terminate the OCM cycling process.*

3.9 Straight-Hodograph Simulations

The straight hodograph represents the other extreme of shear structure. Because linear shear-induced propagation cannot move an updraft off a straight hodograph, nonlinear rotationally-induced propagation must dominate. Storm splitting is required, and mirror-image updrafts propagate away from one another.

Four straight-hodograph simulations are conducted. The shear is linearly distributed from 0-10 km, and the lengths of the hodographs are chosen such that they have the same mean shear as simulations Half_r15 through Half_r30. This results in hodograph lengths of 47, 60, 79, and 94 m s⁻¹, and the simulations are designated Straight_47, Straight_60, Straight_79, and Straight_94, respectively. As shown in Table 3.2, these hodographs cover a wider range of shears than helicities, with BRNsh₆ (BRNsh₉) values ranging from 11.6-23.1 (16.9-33.7) m s⁻¹ and SRH₃ (SRH₁) values ranging from 76-226 (25-76) m² s⁻². Simulations Straight_79 and Straight_94 would fall under the category of “severely-sheared storms” as described by Marwitz (1972).

None of the straight-hodograph simulations occlude during the 4-hour simulation time. However, *all* of the simulations do undergo the same type of non-occluding cyclic mesocyclogenesis (NOCM) evident in Half6_r21 (Section 3.5.3), Qtr3_1510, Qtr3_1540, Qtr3_1560, Qtr3_1060, the Qtr3_20 simulations, and the Qtr1

simulations (Section 3.6). This occurrence is unique, as it is the only set of simulations in which every run displays this characteristic behavior, an example of which is shown in Figure 3.9.1 for Straight_47. Storm morphology is qualitatively similar to the behavior displayed in Half6_r21 (Fig. 3.5.11).

Figure 3.9.2 displays the entire lifecycle of each moderately strong (near-ground vertical vorticity $> 0.02 \text{ s}^{-1}$) near-ground mesocyclone during the straight-hodograph simulations. There is little discernible regularity to the pattern of cycling for these non-occluding cases. However, two general trends are apparent. *First, it appears that the lifetime of each mesocyclone decreases as the shear increases.* This is quite opposite to the trend demonstrated previously, namely that increasing shear tended to slow OCM cycling. *Second, similar to most of our previous results, the time of initial mesocyclone cycling is slowed with increasing shear.*

3.10 Summary and Discussion

As shown in the previous sections, the mode and character of mesocyclone cycling depends upon the shape of the hodograph, the distribution and magnitude of the vertical shear, and the buoyancy profile. Although the behavior seems quite complex and irregular, we generalize some of our findings in the schematic of Figure 3.10.1. Here, we plot the mode of storm behavior (steady, occluding cyclic, or non-occluding cyclic) as a function of hodograph shape and a generalized measure of vertical shear. Because we have shown that the distribution and location of vertical wind shear within a hodograph can radically alter storm morphology, we assume this generalized shear to be some average quantification of shear throughout the lower- to upper- troposphere, e.g. the product of BRNsh, (DBRNsh) and SRH₁. Overlapping boundaries in the parameter space indicate locations where multiple modes of cycling were simulated. However, because we have shown there exist

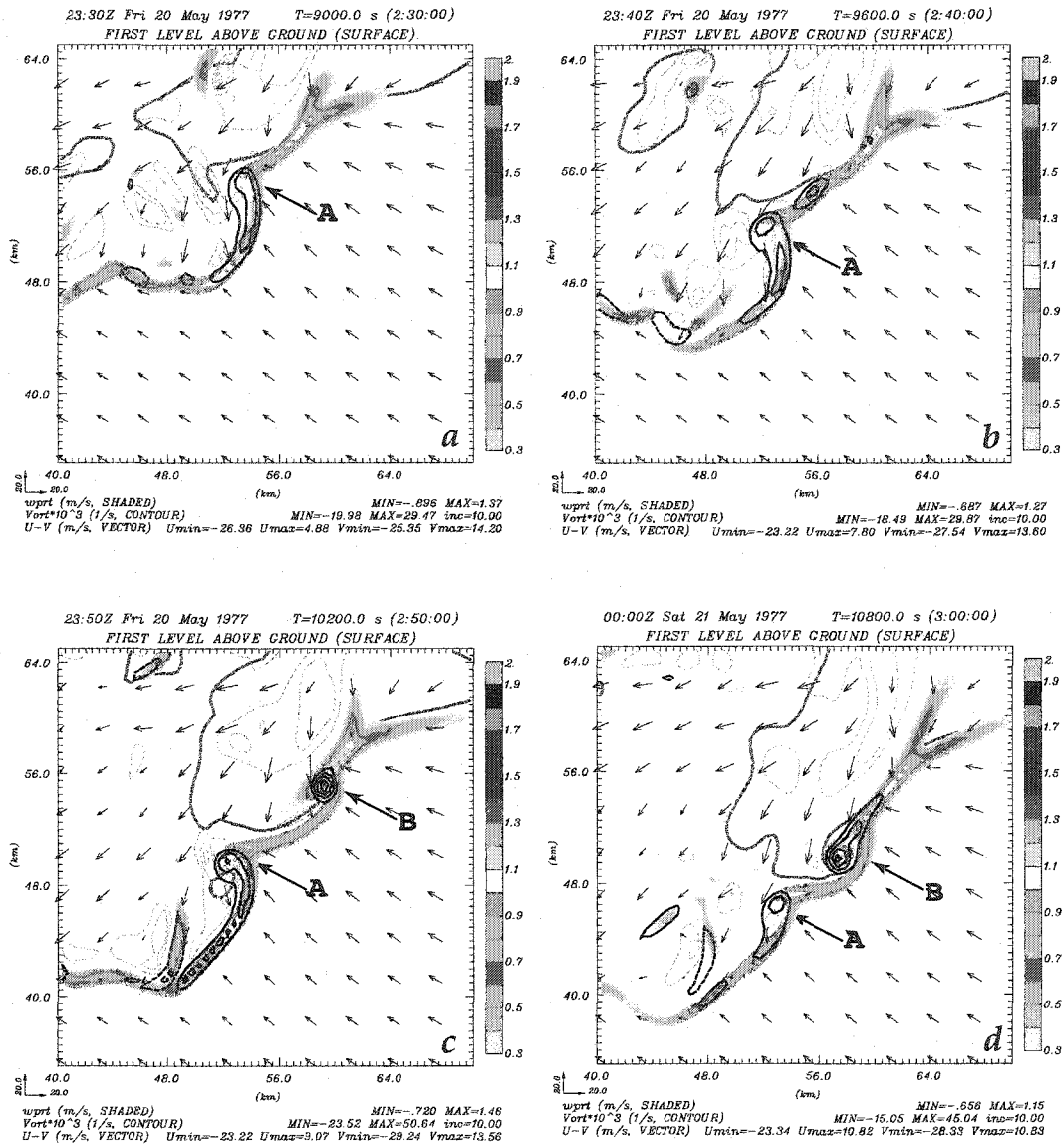


Figure 3.9.1: Plots of vertical velocity (color-filled) at $z = 50$ m for simulation Straight_47 at a) 9000 s, b) 9600 s, c) 10200 s, and d) 10800 s. Negative vertical velocity contoured in light blue at an interval of 0.2 m s^{-1} . Vertical vorticity contoured in black at an interval of 0.01 s^{-1} . Dark blue contour indicates 1 g kg^{-1} rainwater mixing ratio. Successive mesocyclones indicated by "A" and "B".

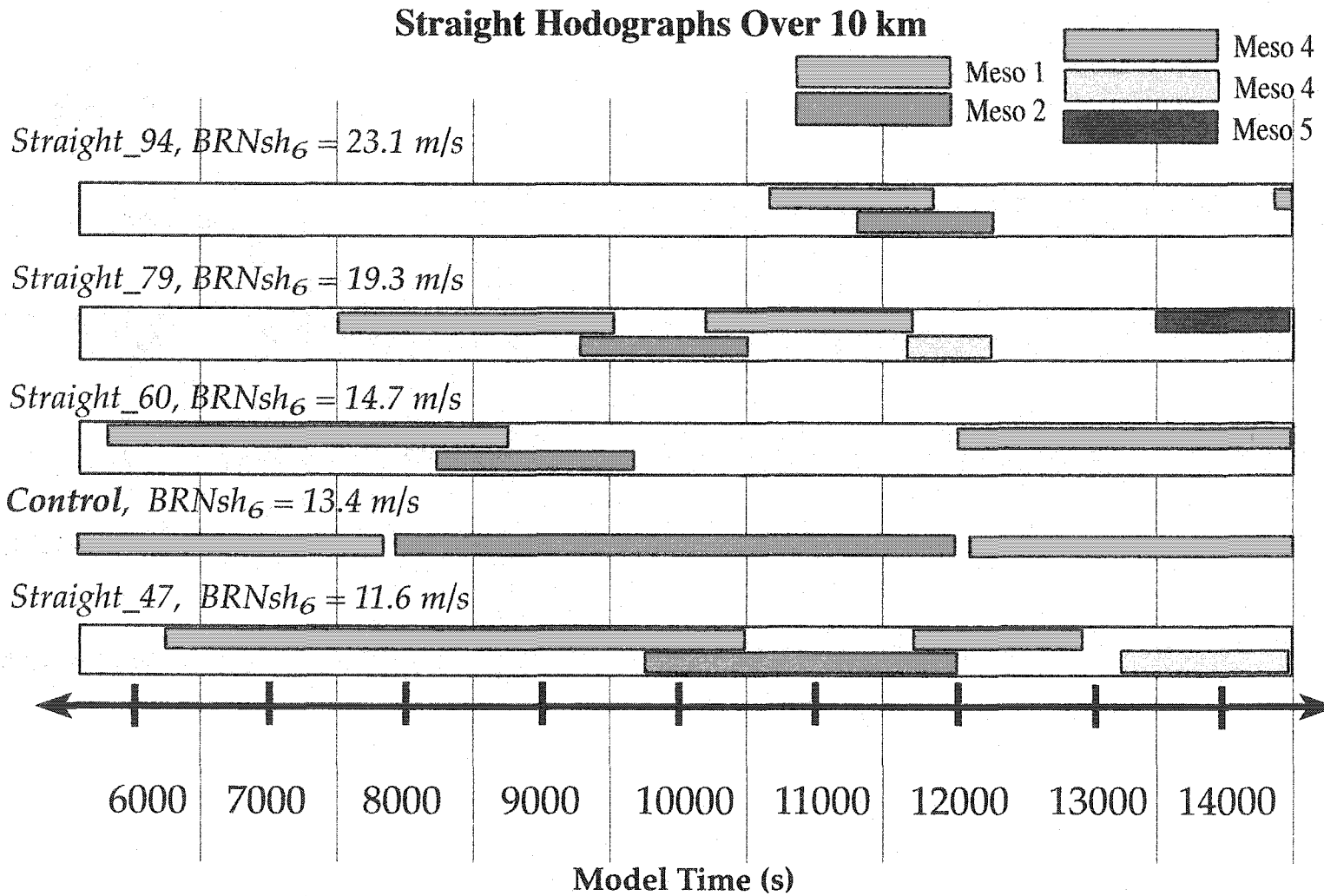


Figure 3.9.2: Schematic of cycling behavior for the Straight simulations.

significant sensitivities to the environmental sounding, the boundaries between regions should be regarded as an average result rather than a fixed transition between cycling modes.

Figure 3.10.1 shows that our straight hodograph simulations always produce storms that undergo non-occluding cyclic mesocyclogenesis. When we introduce a quarter-circle hodograph with rectilinear shear, we observe all three modes of behavior. At very low-shears, the storms tend to be steady or exhibit occluding cyclic mesocyclogenesis. At intermediate and higher shears, they tend to exhibit non-occluding cyclic behavior.

When we extend the simulations to half-circle hodographs, the tendency for non-occluding cyclic behavior is diminished. For most half-circle hodographs, steady behavior is observed at very low shears and at high shears, with occluding behavior in between. This trend continues for the three-quarter circle hodographs, with steady behavior again observed at higher shears. Finally, the full-circle hodographs exhibit non-cycling behavior during the control period.

This schematic does not include several of our additional findings. For example, in cases of occluding cyclic mesocyclogenesis, we showed that higher CAPE speeded up the cycling process and lower CAPE inhibited it. Therefore, holding the range of shear constant, this CAPE influence would shift the schematic to the left (right) for lower (higher) CAPE. We also demonstrated that extremes of shear confined to either the lowest or highest elevations tended to slow down cycling in the simulated storms, except when they transitioned to non-occluding behavior. Assuming that the measure of shear in the diagram contains an average value through the troposphere, the schematic then remains approximately correct. In cases in which both occluding and non-occluding cyclic behavior were simulated,

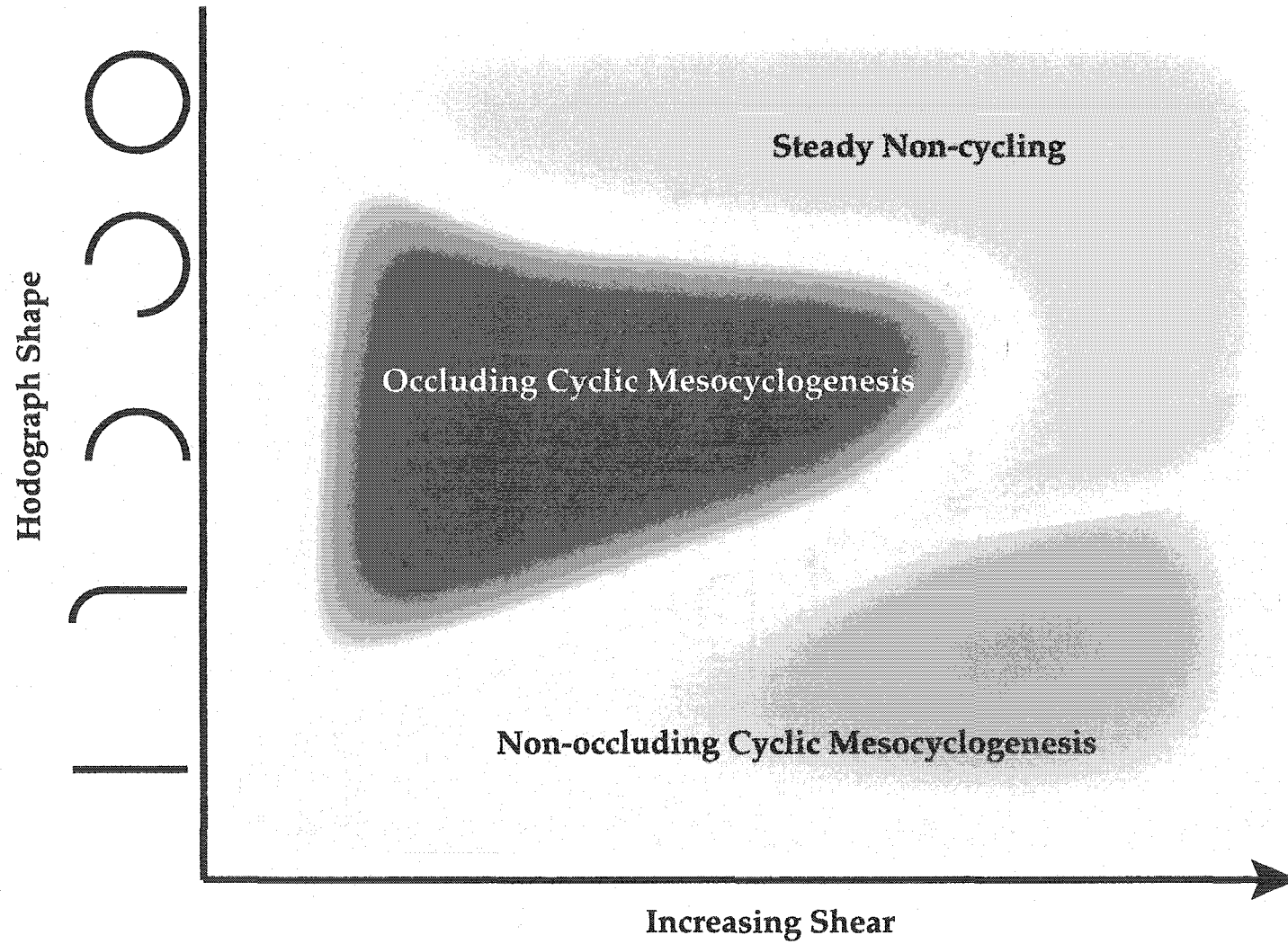


Figure 3.10.1: Summary of cycling behavior for average shear versus hodograph shape .

confining the low-level hodograph curvature (and majority of the helicity) to a shallower depth favored the non-occluding mode of cycling.

The non-occluding cyclic simulations also demonstrated some trends which are not included in the schematic. Initial and subsequent mesocyclones appear to be delayed with increasing rectilinear shear, similar to the occluding mode. At higher shears, there was some evidence that the non-occluding cycles became shorter, a trend opposite to that observed in the occluding mode.

A natural question to ask is whether the timing of the occlusion cycles (for the occluding cyclic storms) can be correlated with any of the indices that characterize the initial environmental sounding. Figures 3.10.2a-e display scatter plots of the time of the first mesocyclone occlusion versus BRN_6 , BRN_9 , SRH_1 , SRH_3 , and storm-relative surface inflow (SRIN), respectively. [Alternatively, the total number of occlusion cycles could also be plotted, but this is much less informative because the values range only from 1-4 and a significant inverse correlation exists with the initial occlusion times, i.e., a linear correlation coefficient of -0.84]. Simulations which did not occlude during the 4-hour period are shown with an occlusion time indicated as "Indeterminate." In all of the plots, there exists a significant clustering of values around the fastest initial occlusions, with the non-occluding examples tending to be more widely dispersed. One can also see the trend of occlusion slowing with higher shears, especially in the plots of BRN_6 and BRN_9 (Figs. 3.10.2a-b). However, no index is clearly superior in discriminating among occlusion timings.

A more significant difference in indices is found between our occluding and non-occluding cyclic cases. Figures 3.10.3.a-b display a comparison of box and whisker plots of SRH_1 , SRH_3 , BRN_6 , BRN_9 , and SRIN for the occluding and non-occluding simulations. In addition, Figure 3.10.3c displays a box and whiskers plot of the ratios of the actual and estimated values of SRH_1 and SRH_3 for the same

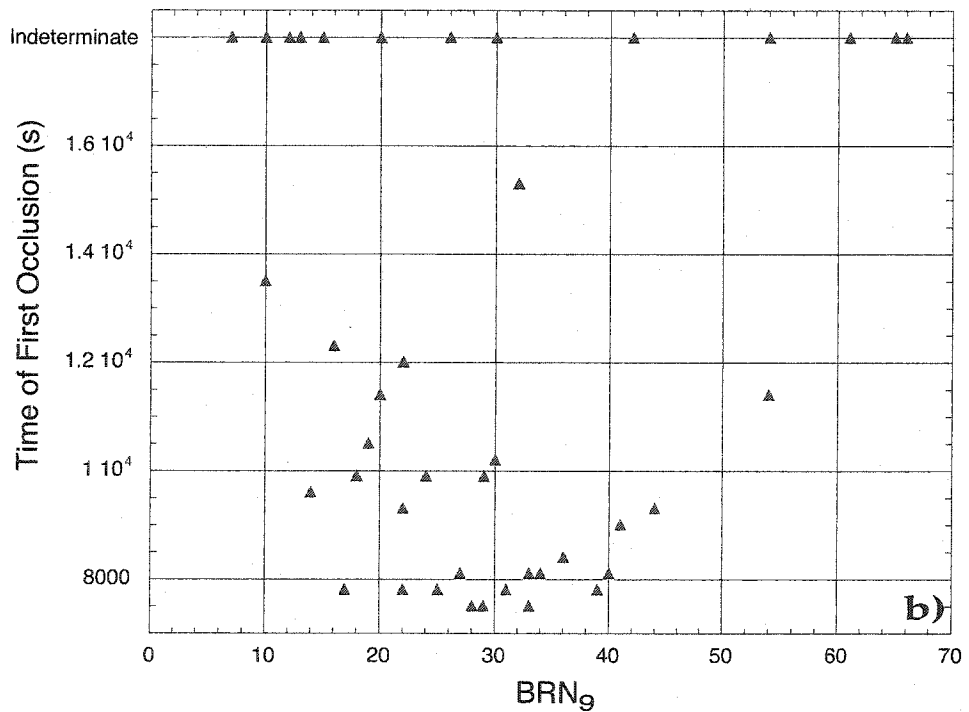
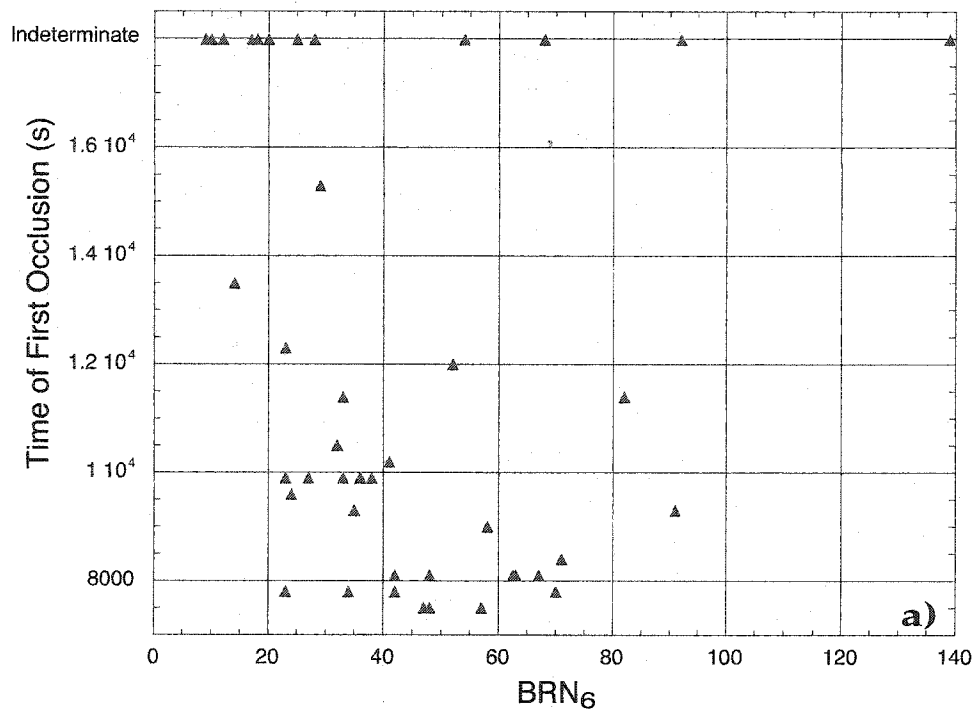


Figure 3.10.2: a) Time of first occlusion versus 0-6 km BRN. Only non-NOCM runs are displayed. Simulations which did not occlude are at the top of the graph as "indeterminate". b) Same as a), except for 0-9 km BRN.

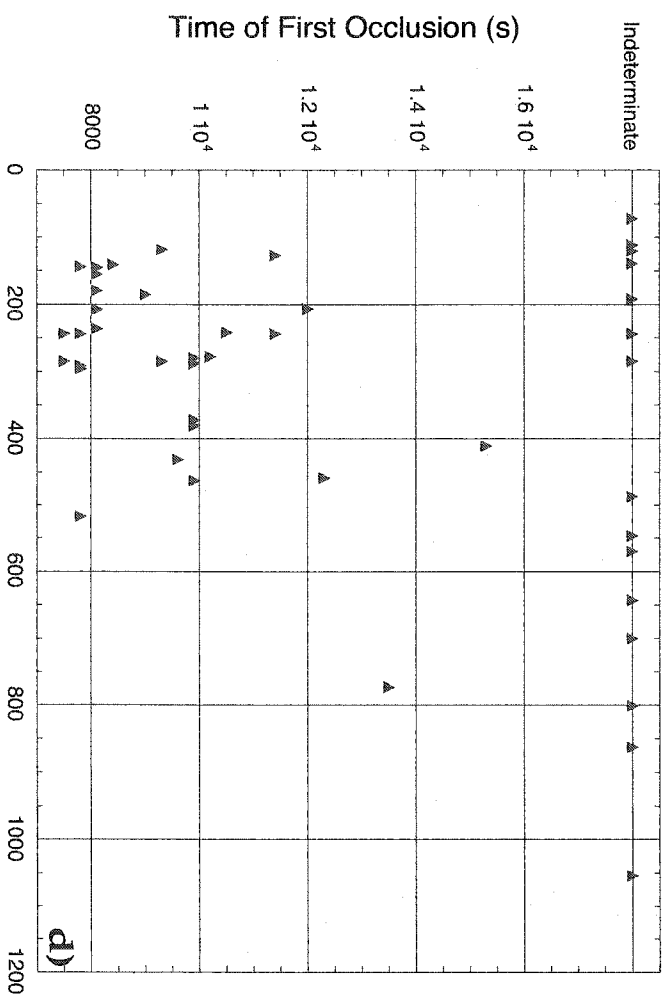
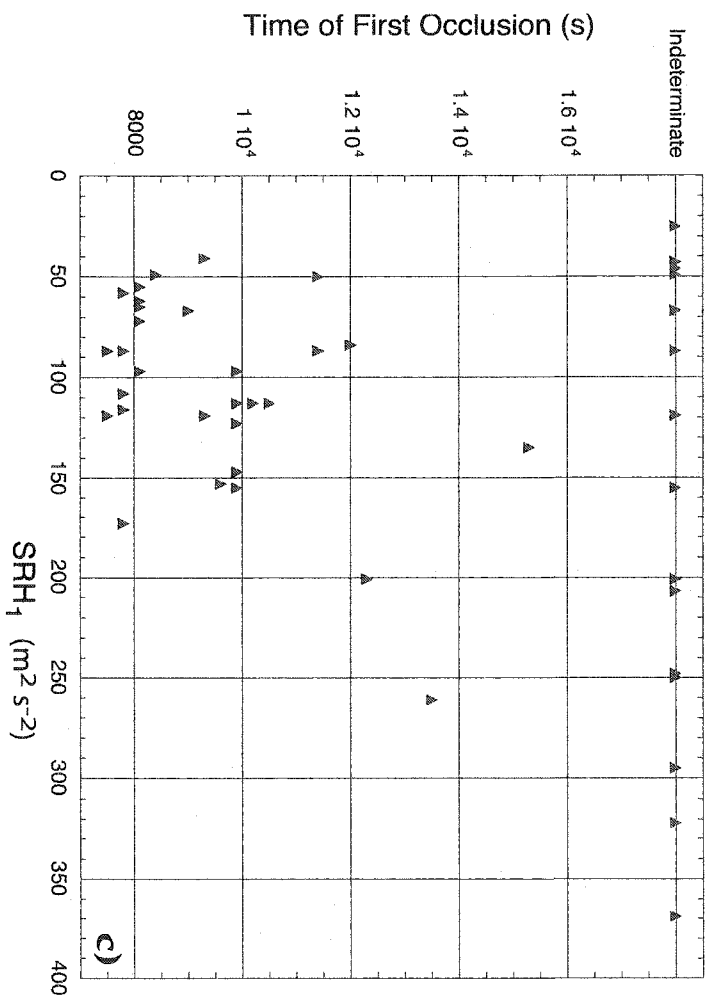


Figure 3.102, continued: c) Same as a), except for 0-3 km SRH. d) Same as a), except for 0-3 km SRH.

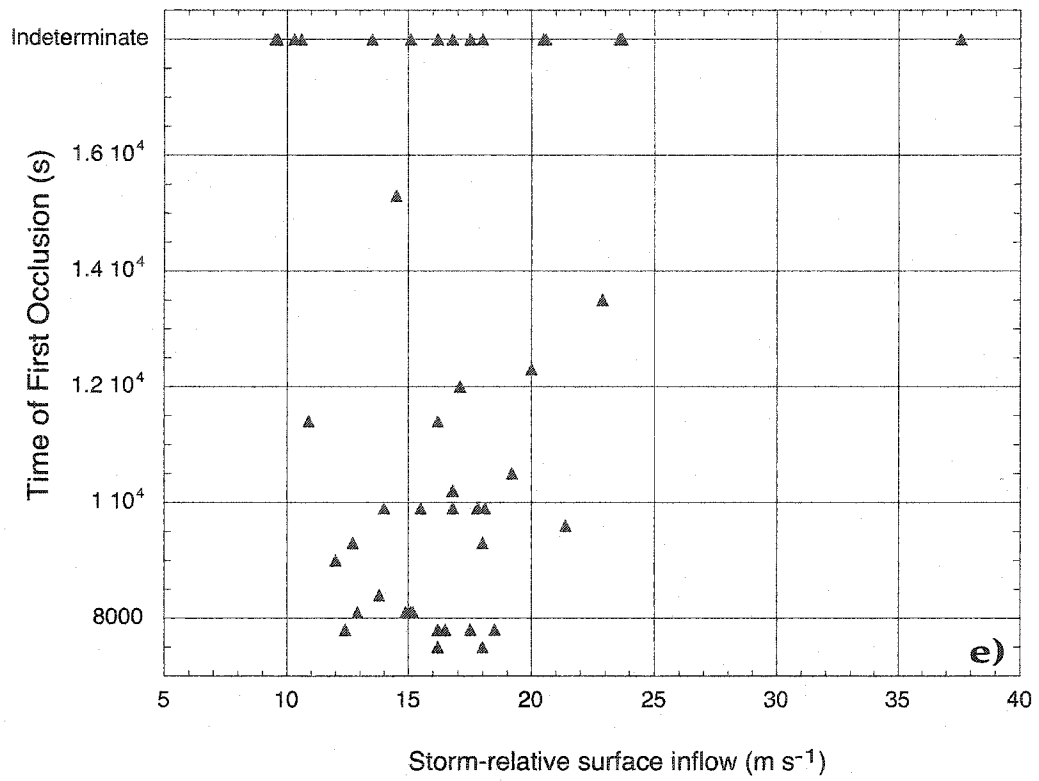


Figure 3.10.2, continued: e) Same as a), except for storm-relative surface inflow, calculated using the average domain speed of each simulation.

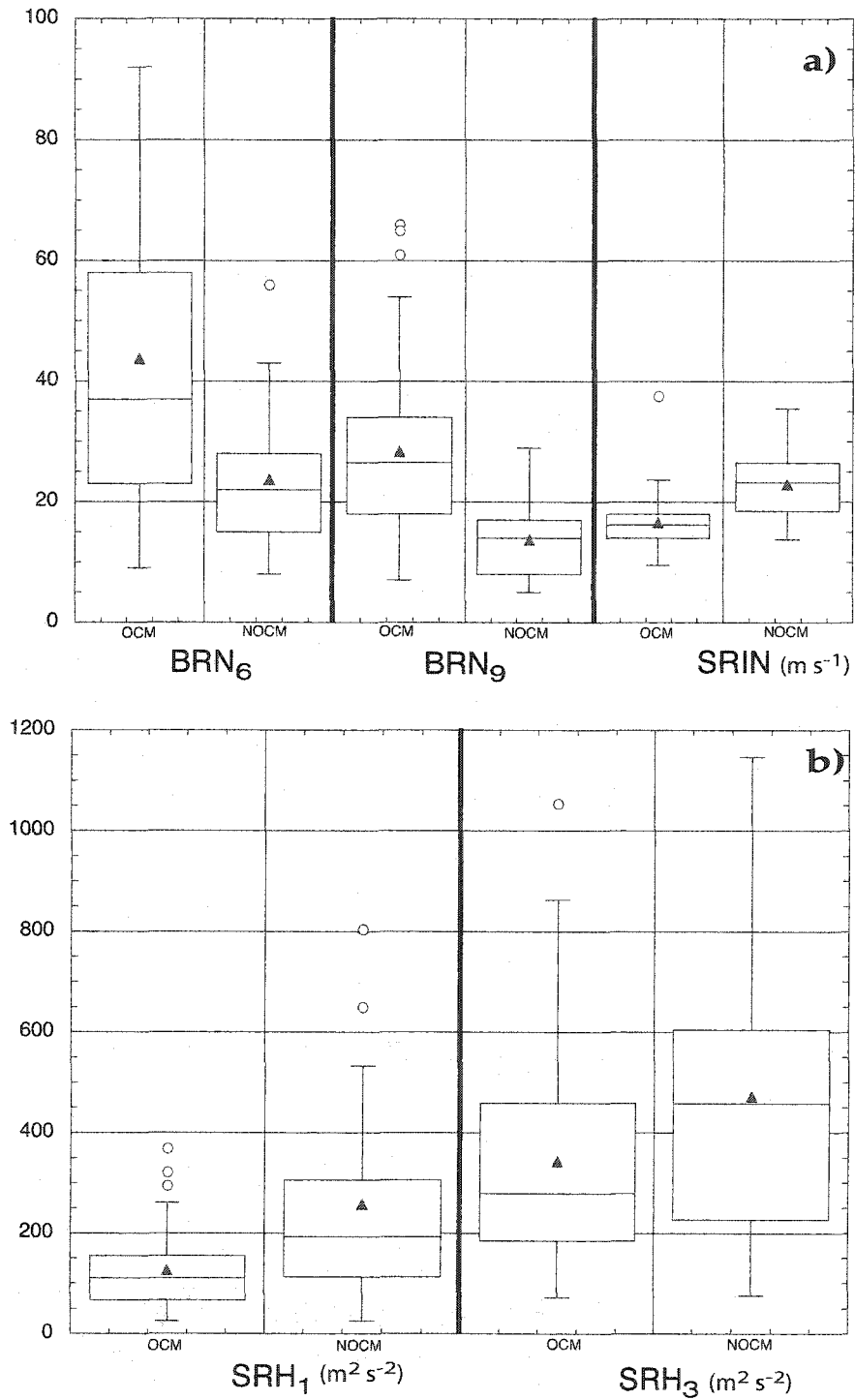


Figure 3.10.3 a) Box and whiskers plots of 0-6 km BRN, 0-9 km BRN, and storm-relative surface inflow for the OCM and NOCM simulations. Mean value indicated by the red triangle. Outliers indicated by the hollow circles. b) As in a), except for 0-1 km SRH and 0-3 km SRH.

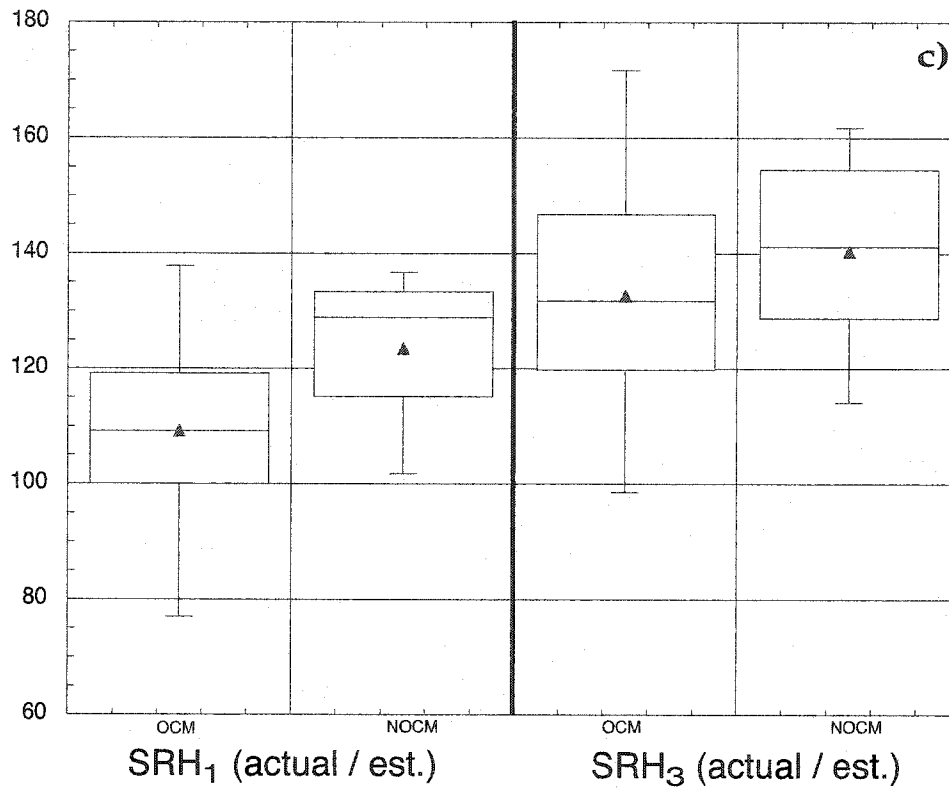


Figure 3.10.3 , continued: c) As in a), except for the ratios of actual to estimated values of 0-1 km and 0-3 km SRH (multiplied by 100). The actual SRH is calculated from average domain speed, while the estimated SRH is calculated from the method of Davies and Johns (1993).

simulations. It is clearly evident from these that non-occluding cyclic behavior tends to dominate when the initial sounding has a higher SRH, lower BRN, and a larger storm-relative inflow.

Lastly, since there is no obviously superior sounding index that discriminates among the first occlusion timings (Fig. 3.10.2), in Figure 3.10.4 we contour the same timings as a function of two sounding indices. When we plot the first occlusion as a function of SRH versus BRN (Figs. 3.10.4a-d), we obtain fairly similar results. Although the use of BRN_6 seems to produce a more orderly correlation, the triangular (rather than square) shape of the contours emphasizes the fact that the BRN and SRH are not really independent of one another in our soundings. We can artificially expand our parameter space by combining indices. For example, Figure 3.10.4e displays an index of shallow shear (SRH_1) versus a combined index of deeper shear ($BRN_9 * SRH_3$). This method produces a more robust plot, with a relatively orderly and bounded region in which cycling occurs.

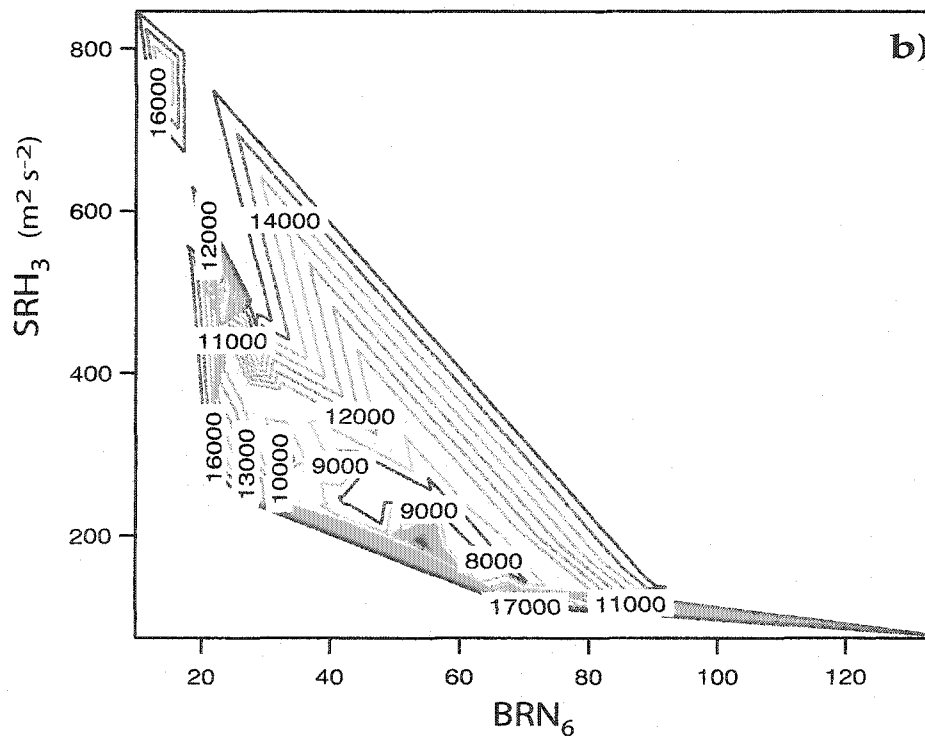
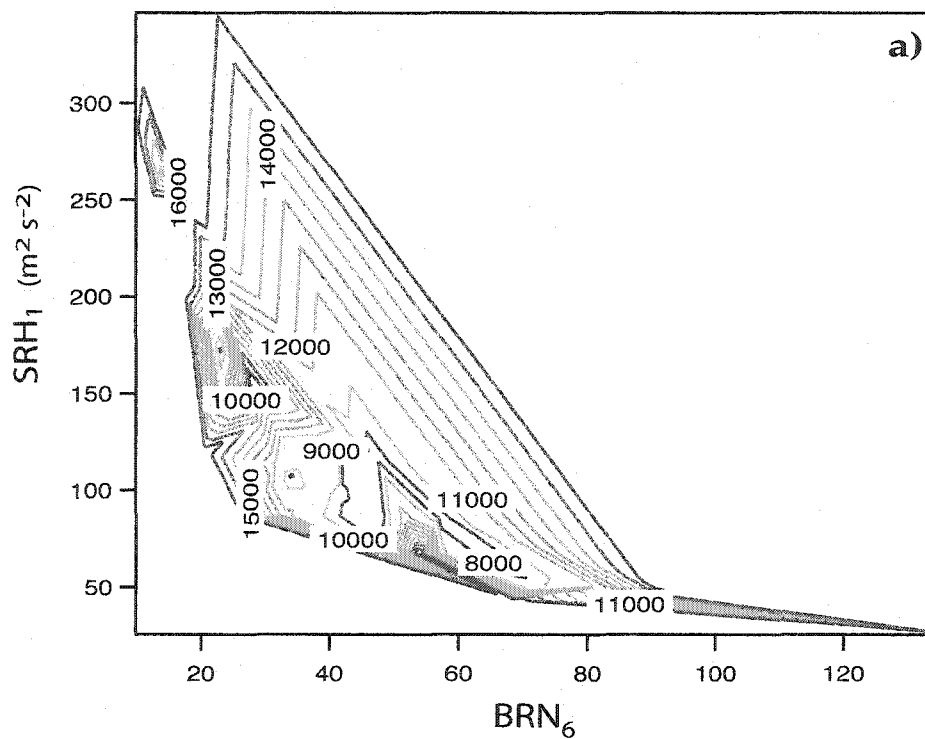


Figure 3.10.4: a) Contour plot of the time of first occlusion versus 0-6 km BRN and 0-3 km SRH. b) Same as in a), except for 0-6 km BRN and 0-1 km SRH.

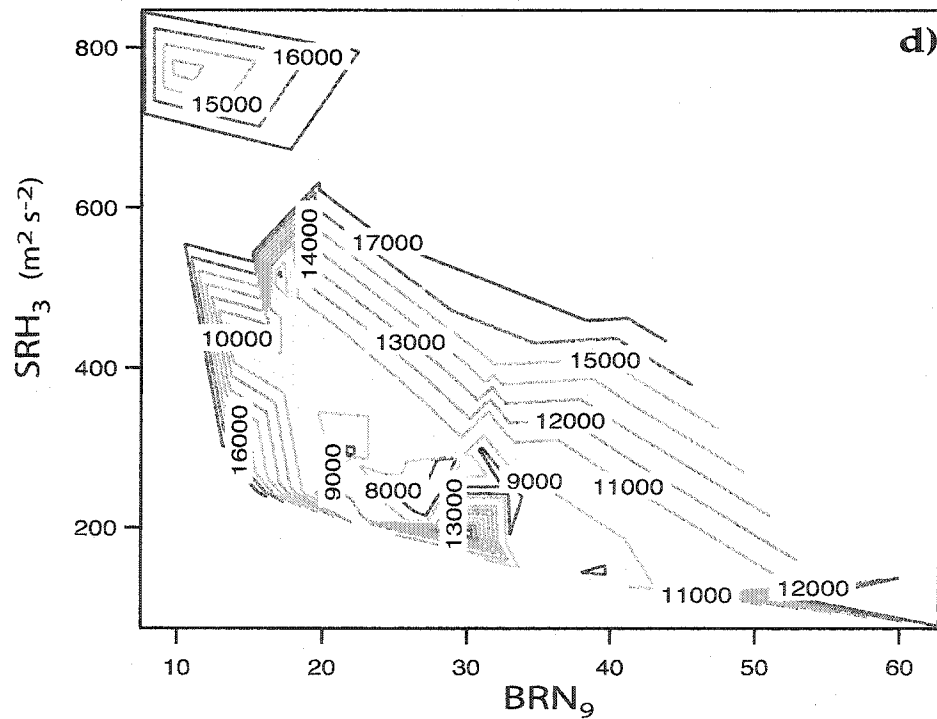
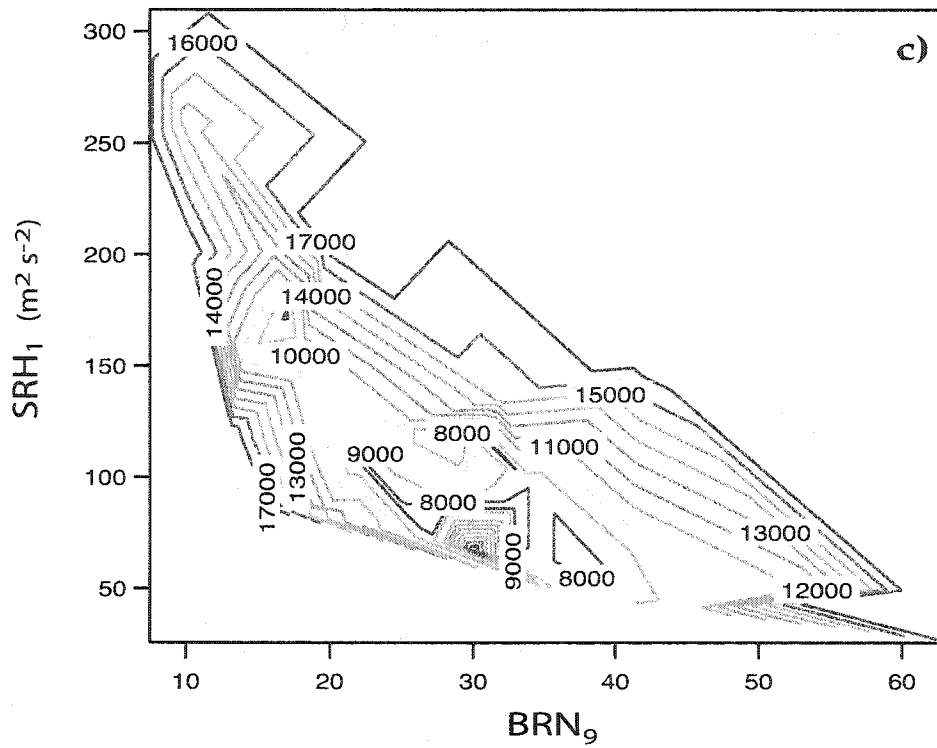


Figure 3.10.4, continued: c) Same as in a), except for 0-9 km BRN and 0-1 km SRH. d) Same as in a), except for 0-9 km BRN and 0-3 km SRH.

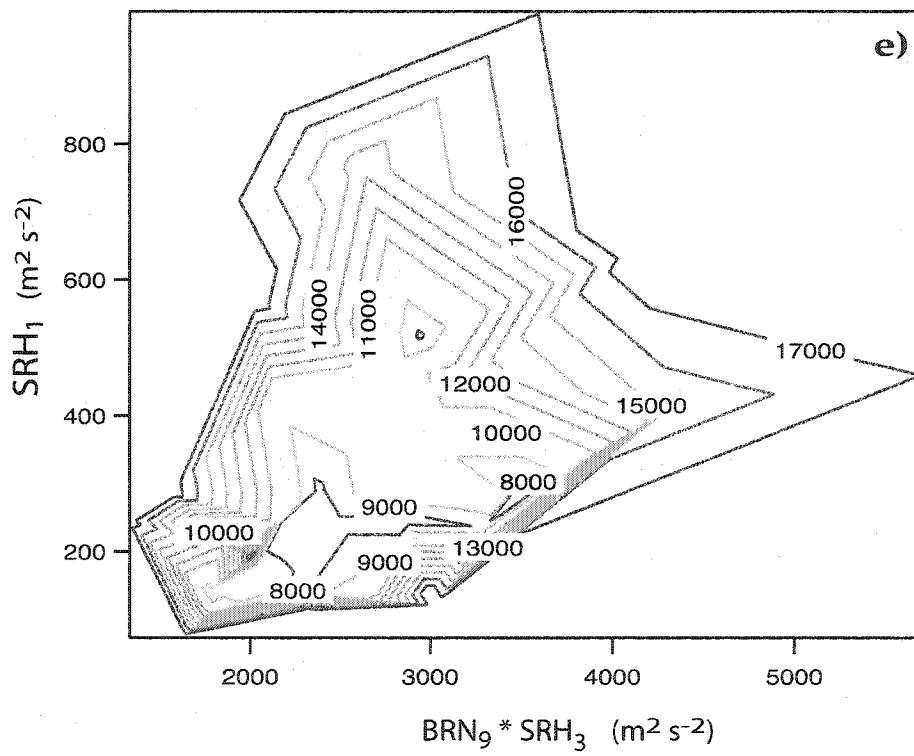


Figure 3.10.4, continued: e) Same as in a), except for 0-1 km SRH and the product of 0-3 km SRH and 0-9 km BRN.

CHAPTER 4

A NUMERICAL SIMULATION OF CYCLIC TORNADOGENESIS

4.1 Introduction

Having investigated the effects of both model parameters and the environmental sounding upon mesocyclone cycling, we now focus on a downscale extension of a previous numerical simulation in order to investigate the relationship between cyclic mesocyclogenesis and cyclic tornadogenesis. We seek to understand whether the introduction of higher-resolution fundamentally changes the timing and character of the occlusion process and whether the vorticity dynamics of cyclic mesocyclogenesis differ from those of cyclic tornadogenesis.

Although we describe our results as a simulation of "cyclic tornadogenesis", the horizontal grid spacing of 105 m precludes the explicit resolution of all but the largest tornado vortices. However, because the main focus of this study is on the development of the tornado cyclone and its relationship to the cycles of mesocyclogenesis, we emphasize that this grid resolution is sufficient to represent the relevant dynamical processes, including the beginnings of an inertial subrange (Bryan et al. 2003). Therefore, we take an approach similar to that of previous studies of tornadoes modeled with their parent storm (Grasso and Cotton 1995; Wicker and Wilhelmson 1995; Finley et al. 2001) and leave the detailed dynamics of the tornado vortex itself to simulations made in the absence of the parent storm (e.g. Fiedler 1995; Lewellen et al. 1997).

4.2 Methodology

The simulation experiments are conducted using Version 4.4 of the Advanced Regional Prediction System, ARPS (Xue et al. 2000, 2001, 2003). The ARPS includes the two-way nested grid interface system, developed by Berger and Olinger (1984) and applied to meteorological models by Skamarock and Klemp (1993), that allows placement of an arbitrary number of fine grids within a coarse grid simulation. These grids usually have a horizontal spacing that is 1/3rd to 1/5th that of the next higher level. Multiple levels of grid nesting are allowed, as are overlapping and rotated grids. The interface system controls the grid and data structure, coordinates the time integration of the grids, and handles the exchange of information between different grid levels.

The strategy for grid placement within this simulation is as follows. The outer grid covers an area 70.3 x 70.3 km² and has a horizontal spacing of 525 m. This grid is used mainly to provide lateral boundary conditions for the fine grid, and no detailed analysis is carried out on it. The fine grid covers an area 22.6 x 22.6 km² and has a horizontal spacing of 105 m. *This grid is oriented so that it contains the entire updraft and downdraft of the storm throughout the length of the simulation from t=0 s.* This avoids all transient effects and removes the possibility of spurious behavior and numerical noise that can be created when updrafts/downdrafts travel through grids of different horizontal resolution. In the vertical, 45 levels are used on both grids over a depth of 16 km. The grid spacing stretches smoothly from 70 m at the surface to 700 m at the top of the domain. This results in the lowest scalar grid point located at a height of 35 m, a level that we will interchangeably describe as “surface” or “near-ground.”

Similar to Adlerman et al. (1999) and Adlerman and Droegemeier (2002), the numerical simulation is conducted using a horizontally homogeneous environment,

and convection is initialized by an ellipsoidal thermal bubble at $t=0$ s. The base state environment is described by the sounding (Figs. 3.4.2 and 3.4.3) from the well-documented 20 May 1977 Del City, Oklahoma Storm (Ray et al. 1981, Johnson et al. 1987). Fourth-order advection is used for both scalar and vector fields. Cloud microphysics is treated using the Kessler (1969) warm-rain parameterization scheme, while subgrid-scale turbulent mixing is represented using 1.5-order turbulent kinetic-energy closure. The Coriolis force, surface friction, surface physics, and terrain are not used. The model is integrated for five hours, and after 3300 s history files are saved every 30 seconds on both grids. This results in 491 fine-grid files of size 44.2 megabytes and 491 coarse-grid files of size 18 megabytes. The files are in GRIB format, which makes them approximately 3 times smaller than the corresponding uncompressed binary data file. We discard most of the coarse-grid files, saving them only every 300 s. This results in a total dataset size of approximately 22.5 gigabytes. A summary of the model parameters is shown in Table 4.1.

Several other model configurations were tried initially, including the use of ice physics and simple surface friction. Strong sensitivities to both (detailed in Adlerman and Droegemeier 2002) precluded their use in this study since only a small number of preliminary runs could be performed due to available computational resources.

4.3 Simulation Overview

4.3.1 General structure

Although the large-scale evolution of the simulated supercell storm is quite similar to that described in Adlerman et al. (1999) and Adlerman and Droegemeier (2002), there exist several significant differences in the timing and character of the

Parameter	Symbol	Value
Gridpoint dimensions of outer (inner) grid	$n_x \times n_y \times n_z$	137*137*45 (218*218*45)
Horizontal grid spacing, outer (inner) grid	$\Delta x, \Delta y$	525 (105) m
Vertical grid spacing (both grids)	Δz	$70 \text{ m} \leq \Delta z \leq 692 \text{ m}$
Large time step, outer (inner) grid	Δt	2.5 (0.5) s
Small time step, outer (inner) grid	$\Delta \tau$	0.75 (0.15) s
Coriolis parameter	f	0.0 s^{-1}
Nondimensional surface drag coefficient	C_d	0.0
Fourth-order horizontal mixing coefficient	K_4	$2.65 \times 10^8 \text{ m}^4 \text{ s}^{-1}$
Second-order vertical mixing coefficient	K_2	$5.9 \leq K_2 \leq 575 \text{ m}^2 \text{ s}^{-1}$
Divergence damping coefficient	a	0.05
Initial thermal perturbation:		
Magnitude	$\Delta \Theta$	4.0 K
Horizontal Radius	x_r, y_r	9 km
Vertical Radius	z_r	1.5 km
Height of center above ground	z_c	1.5 km
Microphysics	Kessler warm-rain parameterization	
Lateral boundary conditions (outer grid)	Radiation	
Top boundary condition	Rigid with Rayleigh sponge layer	
Grid stretching function	Hyperbolic tangent	
Horizontal and vertical advection	Fourth-order	
Turbulence parameterization	Anisotropic 1.5-order TKE closure	

Table 4.1: Physical and computational parameters used in the nested-grid simulation

occlusion process at high-resolution. A summary of the entire simulation during its period of cycling (approximately 5700-15000 s) is shown in Figure 4.3.1.

After initialization, the right-moving storm rapidly evolves into a supercell by 3600 s, with a strong mesocyclone and hook apparent by 5100 s (Fig. 4.3.1a). During the remainder of the simulation, six mesocyclone cycles occur (labeled A-F), accompanied by five distinct occlusions. All of the occlusions fall into the category of OCM discussed in Chapter 3. Three of the cycles ("B", "C", and "E") contain intense short-lived (i.e., several minutes) near-ground vortices that we classify as tornadic, occurring at approximately 7380, 8400, 10620, and 13600 s.

The first occlusion, during the transition from cycle "A" to "B", occurs at approximately 6300 s, roughly 1000 s earlier than an identical non-nested simulation that used a horizontal grid-spacing of 500 m (Adlerman and Droegemeier 2002). This occlusion is the weakest and most ill-defined of the series (Fig. 4.3.1a).

The second cycle, "B", continues until the next occlusion at approximately 9000 s. The transition from mesocyclone cycle "B" to "C" is the most spatially separate of all the occlusions (Fig. 4.3.1b, 9300 s). In contrast with the transition between cycle "B" and "C", the remaining occlusions at 11100 s (from cycle "C" to "D", Fig. 4.3.1b), 12900 s (from cycle "D" to "E", Fig. 4.3.1c) and 14400 s (from cycle "E" to "F", Fig. 4.3.1c) occur with the new and old mesocyclones forming and dissipating relatively close together.

Considering those mesocyclone cycles which are tornadic ("B", "C", "E") versus those which are non-tornadic ("A", "D", "F"), the rainwater (or corresponding reflectivity) field does not provide any strongly distinguishing characteristics. Although the tornadic vortices at 7380 and 10620 s occur on the tip of a strongly wrapped hook (Figs. 4.3.1a,b), similar features at 12000 and 15000 s (Figs. 4.3.1b,c) are not tornadic. In contrast, the tornadic vortex at 8400 s forms

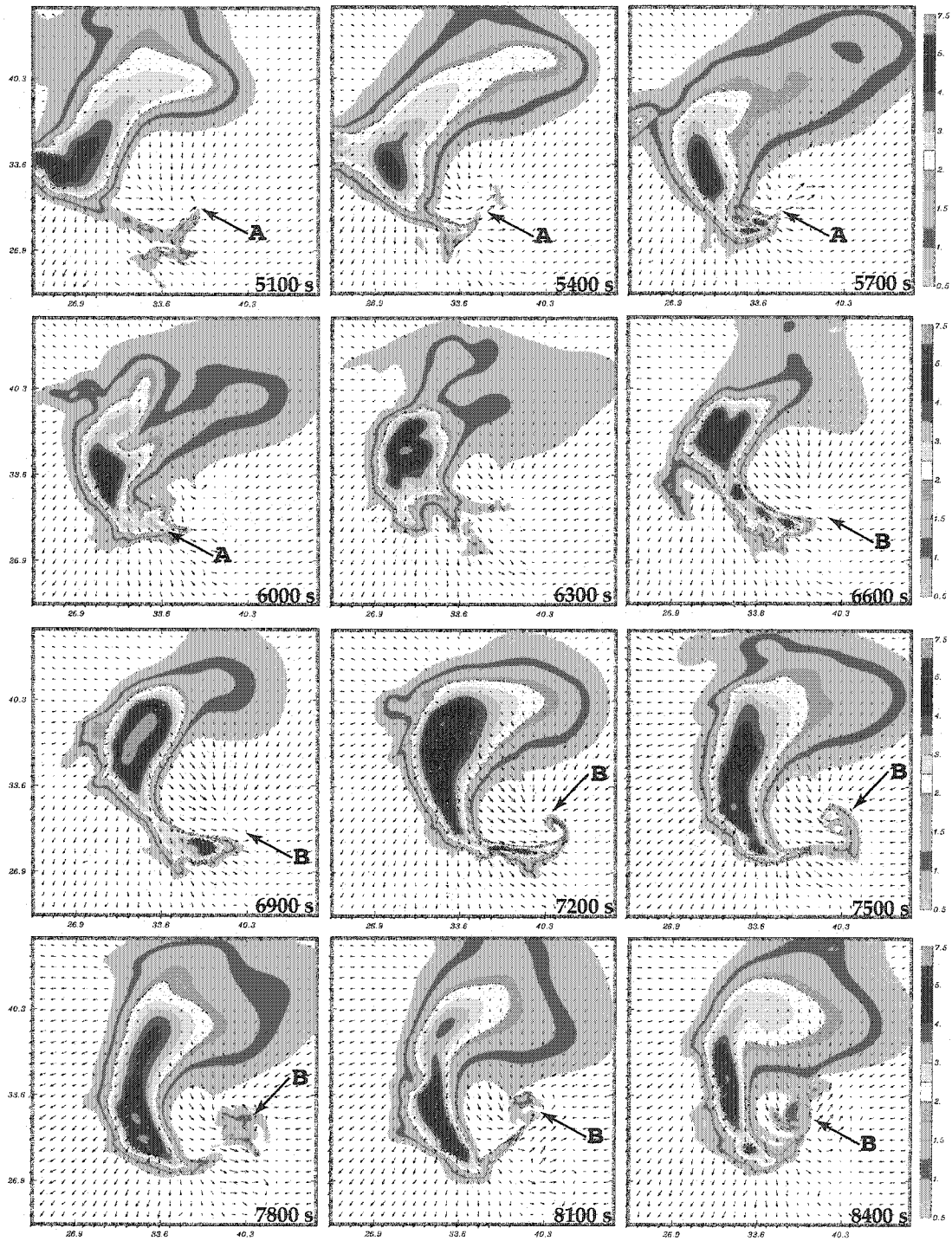


Figure 4.3.1a: Plots of rainwater mixing ratio, q_r (g kg^{-1}) for the cyclic tornadogenesis simulation. Entire fine-grid domain is shown. Successive mesocyclones are indicated by "A", "B", etc. Model time is indicated on each plot, from $t = 5100$ to 8400 s.

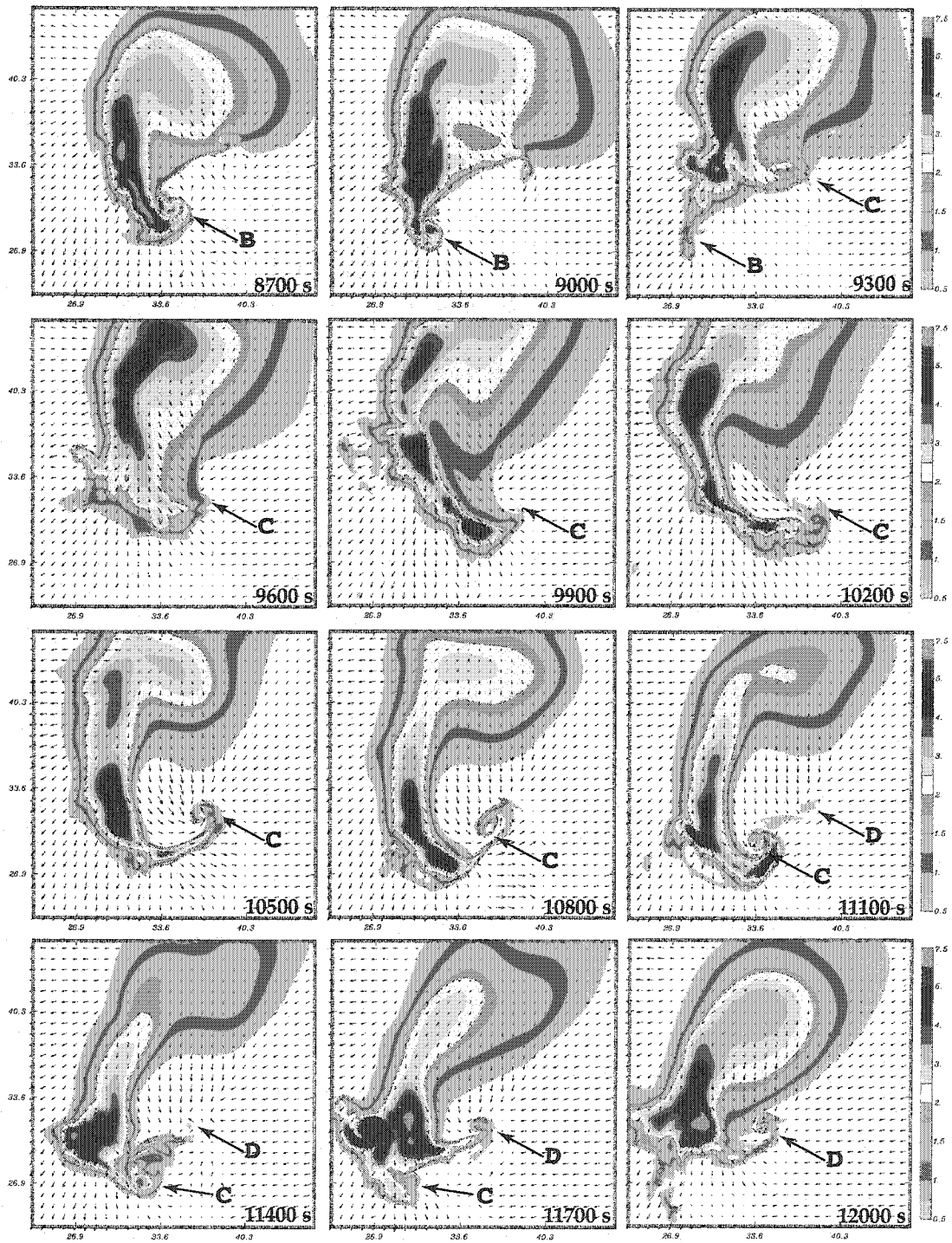


Figure 4.3.1b: As in Fig. 4.3.1a, except for $t = 8700$ to 12000 s.

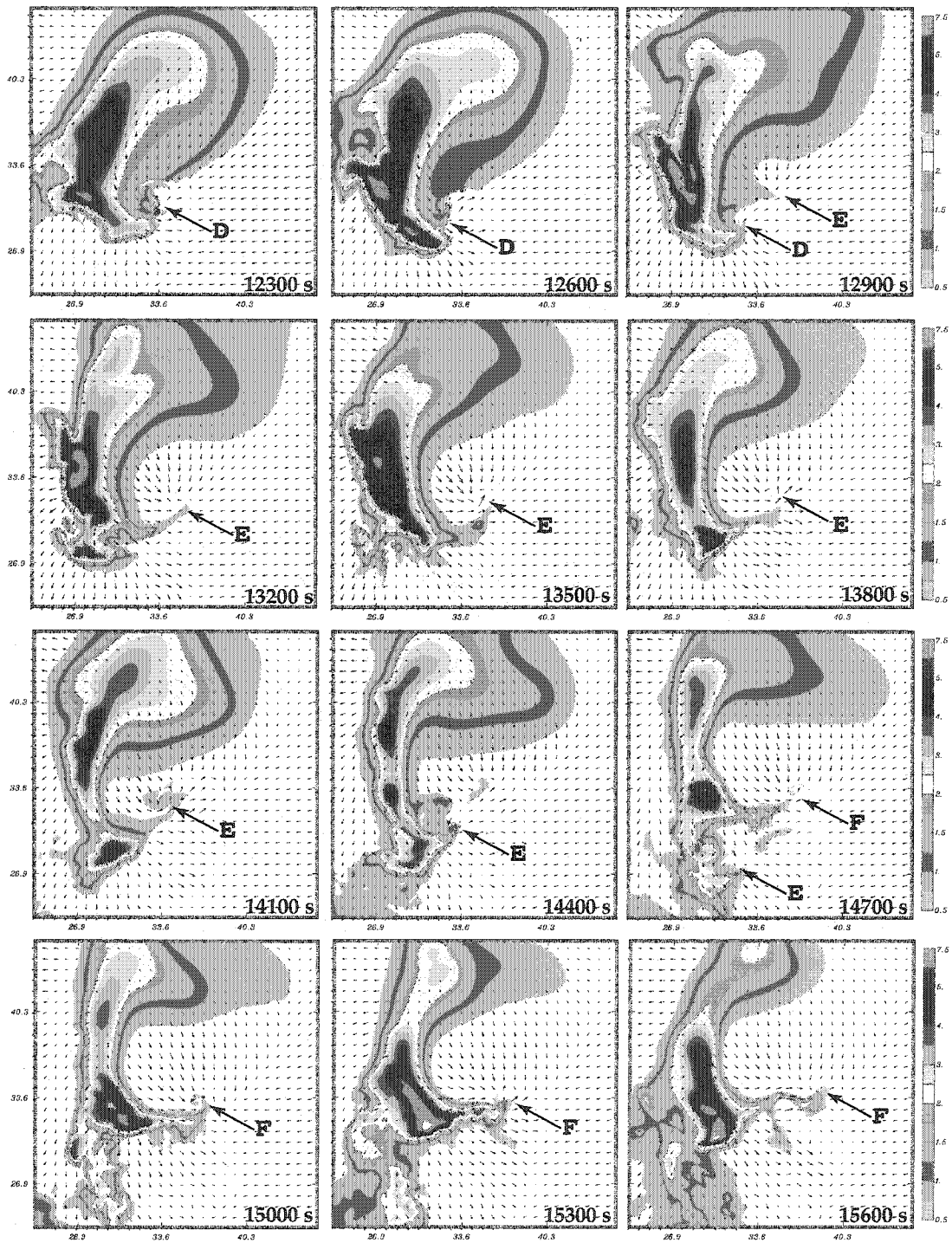


Figure 4.3.1c: As in Fig. 4.3.1a, except for $t = 12300$ to 15600 s.

toward the end of cycle "B" as echo is very occluded and fairly diffuse (Fig. 4.3.1a), while the tornadic vortex at 13600 s forms in association with the weakest hook signature (Fig. 4.3.1c). This lack of correlation between the hook and a tornadic vortex is similar to that discussed in the review by Markowski (2002).

Although cycle "B" lasts 2700 s, cycle "C" lasts only 2100 s. A trend of progressively shorter mesocyclone cycles is observed, with cycle "D" lasting 1800 s and cycle "E" lasting 1500 s. However, after the transition to cycle "F" at approximately 14400 s, the supercell begins to take on a more elongated shape (Fig 4.3.1c) with convection forming farther south in the domain. No further cycling occurs through the end of the simulation at 18000 s.

4.3.2 Time-height summaries

Domain-wide fine-grid time-height plots of maximum updraft (Fig. 4.3.2), maximum downdraft (Fig 4.3.3), minimum perturbation pressure (Fig. 4.3.4), and maximum vertical vorticity (Fig 4.3.5) reveal several characteristics common to each storm cycle. All of these plots are unsmoothed and use output saved at 30 s intervals. Because the fine-grid domain contains only our storm of interest, domain-wide plots give the same result as if we had used a reduced maxima/minima search region within a conventional single-grid domain, as in the time-height plots of Adlerman et al. (1999) and Adlerman and Droegemeier (2002).

The first and most obvious result from the time-height plots is that each cycle is associated with multiple non-periodic updraft pulses (Fig. 4.3.2) which tend to peak just before the occlusion process begins. As the occlusion occurs and the storm begins to reorganize, a temporary weakening is evident. This cycling pattern also was described in Adlerman et al. (1999, see Fig. 6) and is more apparent during the longer cycles. It can be seen in the transitions between the first and second cycles at

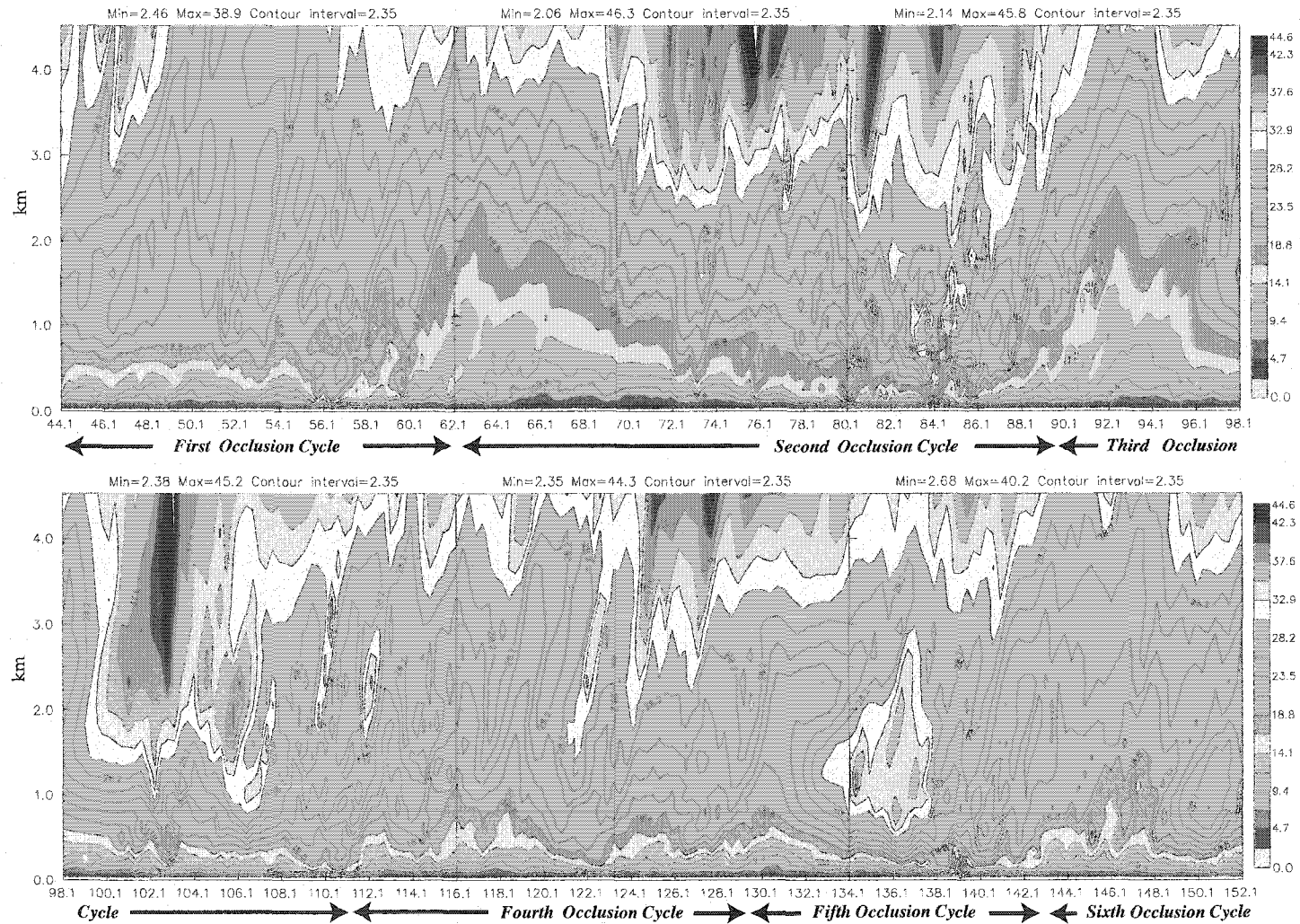


Figure 4.3.2: Time-height plot of fine-grid domain-wide maxima in vertical velocity (m s^{-1}). Height in km indicated on left axis. Model time $\times 10^2$ s indicated on the lower axis. Maximum and minimum of each 1800 s segment indicated on the top of the plot.

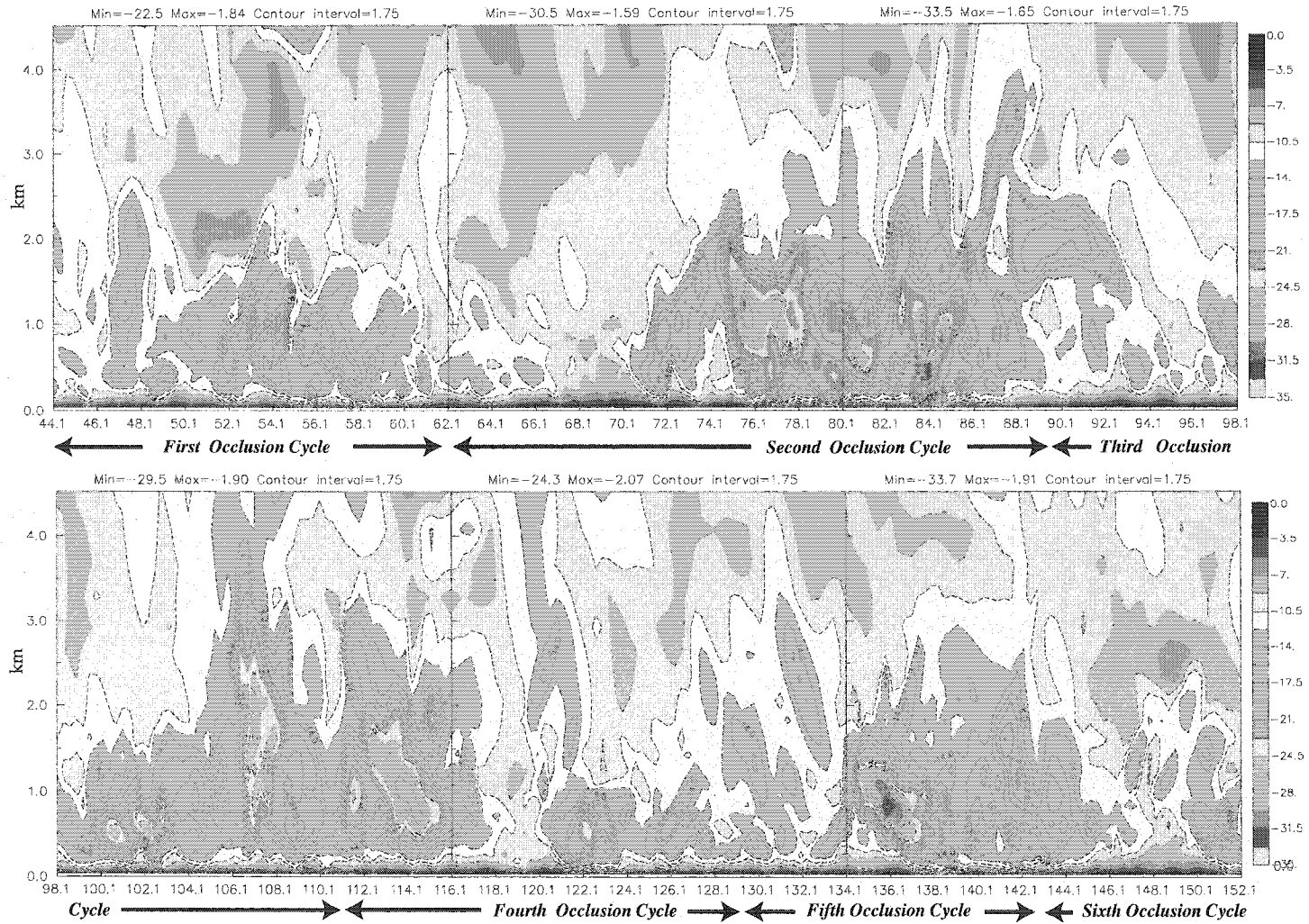


Figure 4.3.3: Time-height plot of fine-grid domain-wide minima in vertical velocity (m s^{-1}). Height in km indicated on left axis. Model time $\times 10^2$ s indicated on the lower axis. Maximum and minimum of each 1800 s segment indicated on the top of the plot.

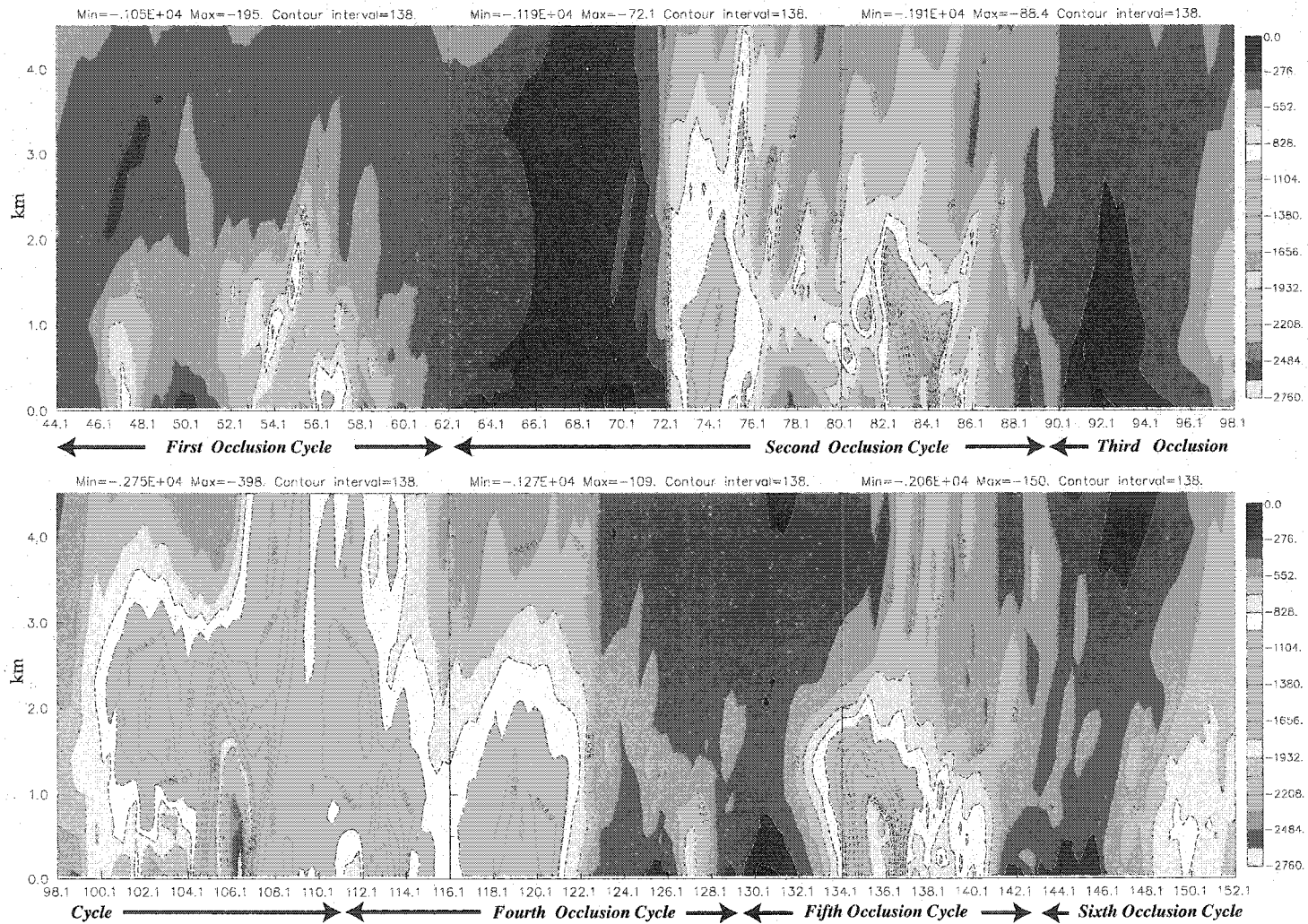


Figure 4.3.4: Time-height plot of fine-grid domain-wide minima in perturbation pressure (Pa). Height in km indicated on left axis. Model time $\times 10^2$ s indicated on the lower axis. Maximum and minimum of each 1800 s segment indicated on the top of the plot.

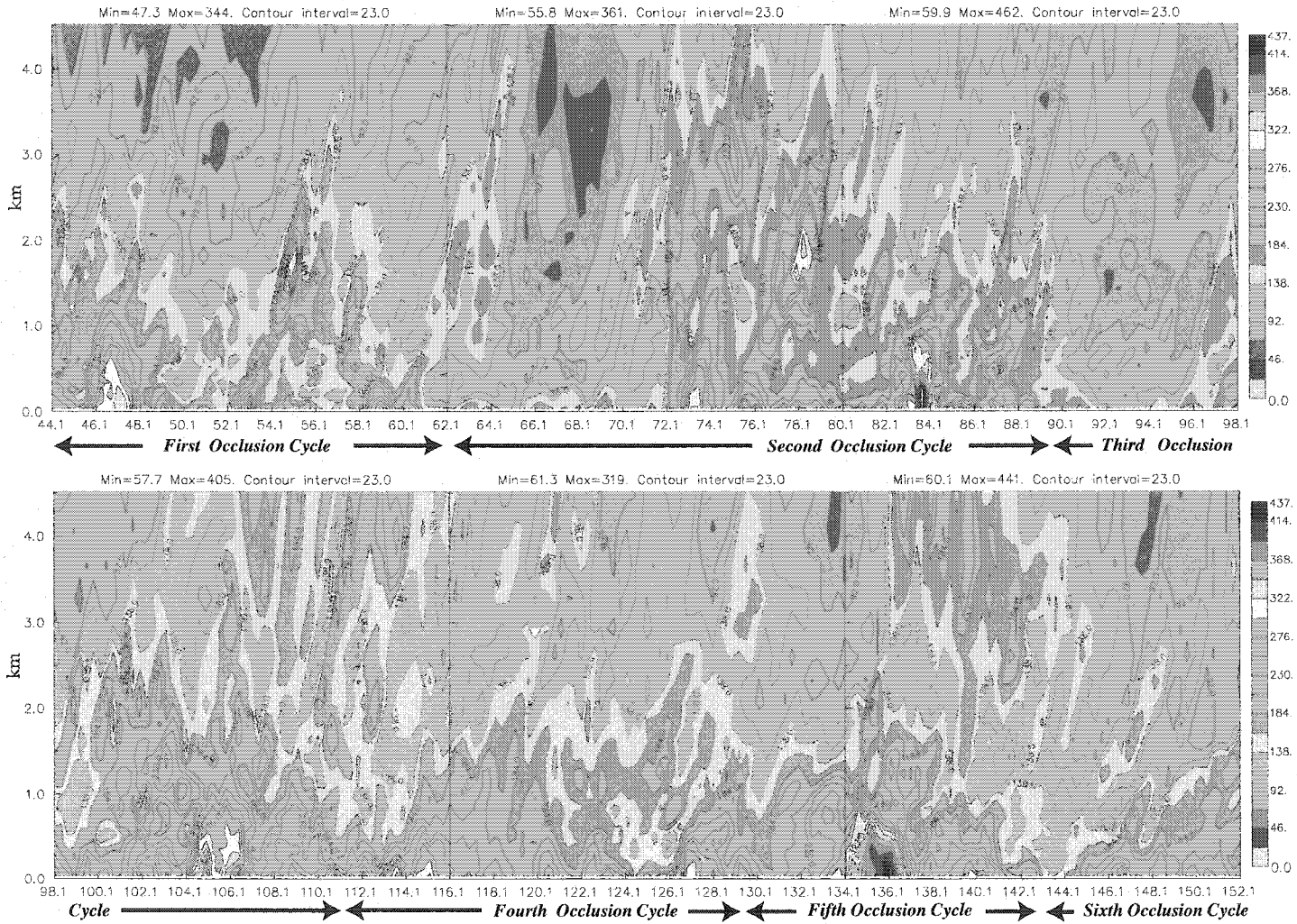


Figure 4.3.5: Time-height plot of fine-grid domain-wide maxima in vertical vorticity (s^{-1}). Height in km indicated on left axis. Model time $\times 10^2$ s indicated on the lower axis. Maximum and minimum of each 1800 s segment indicated on the top of the plot.

6200 s and between the second and third cycles at 9200 s. For the faster cycles, in which the old and new mesocyclones are located closer together, the weakening is briefer and less pronounced (e.g. at 11210, 13010 and 14410 s).

Considering the minimum perturbation pressure (Fig. 4.3.4) and maximum vorticity (Fig. 4.3.5), there exists considerable variation in the intensity of the strongest vortices during each cycle (assuming that the simulated pressure deficits at low-levels are mostly dynamically induced by rotation). Indeed, only the second, third, and fifth cycles contain strong near-ground vortices that might reasonably be viewed as "tornadoes", i.e., those vortices that have time and height continuity, are located in the 'correct' position relative to other features, and go through the occlusion process. The vortex at 10620 s is the most intense, with a surface pressure deficit of 27.5 mb and ground-relative winds of 49 m s^{-1} . The other strong near-ground "tornadic" vortices occur at 7380, 8400, and 13600 s, with respective pressure deficits of 12, 19 and 20 mb, and peak ground-relative winds of 41, 53, and 44 m s^{-1} .

Comparing the downdraft maxima (Fig. 4.3.2) with the updraft (Fig. 4.3.1) and vertical vorticity maxima (Fig. 4.3.5), the most intense phases of each mesocyclone cycle are accompanied by low-level ($< 2 \text{ km}$) downdrafts exceeding 15 m s^{-1} . They usually represent precipitation induced rear-flank downdraft development. However, during and immediately after several of the near-ground vortex intensifications (7600, 8400, 10700, 11400, and 13600 s), downward-developing downdrafts in excess of 25 m s^{-1} penetrate to very low levels (200-600 m). These appear to be forced by rotationally-induced downward vertical pressure gradients because the downdrafts correlate well with the minima in pressure perturbations (Fig. 4.3.4).

Comparing the vorticity maxima (Fig 4.3.5) and pressure minima (Fig. 4.3.4), vertical vorticity does not seem to be a very good indicator of the degree of

organization of a particular mesocyclone and/or tornado cyclone. [We define the tornado cyclone as the 400-500 m diameter area of intense vorticity ($> 0.1 \text{ s}^{-1}$) at the lowest grid level, coincident with the center of rotation and the largest perturbation pressure deficit] For example, the intensification at 10620 s is accompanied by the strongest vertical velocities (Fig. 4.3.2) and the strongest and most vertically continuous pressure deficit (Fig. 4.3.4), yet its vorticity profile is not well distinguished from those at other times during the simulation (Fig. 4.3.5). This appears to be a result of scaling issues associated with the grid spacing. The maximum vertical vorticity for a simulated storm will be proportional to the horizontal resolution (Adlerman and Droegemeier 2002). However, because we are using a horizontal grid spacing much smaller than the horizontal scale of a supercell storm, the maximum vertical vorticity at a particular vertical level will be most closely related to the scale of the storm's features at that level. Near the free-slip lower boundary where the vertical grid spacing is smallest, convergence is maximized and boundaries such as the gust front collapse to only a few grid points in width. Therefore, uniform upward development of vertical vorticity is not evident as in coarser-grid simulations (Adlerman et al. 1999, Fig. 7). Instead, updrafts exhibit maxima that still decrease upward in height, similar to the results of Wicker and Wilhelmson (1995, Fig. 10).

The use of a relatively crude measure of circulation, calculated around a square centered on the minimum in perturbation pressure (usually centered near the maximum in vertical velocity and vorticity), gives a better depiction of the vertical development of rotation associated with variations in mesocyclone strength. [In the next section we will show a similar plot, but centered on the maximum in vertical vorticity]. Figures 4.3.6-4.3.8 depict several time-heights of circulation measured this way, using respective circuits of diameter 0.5, 1.0, and 2.0 km. Although these

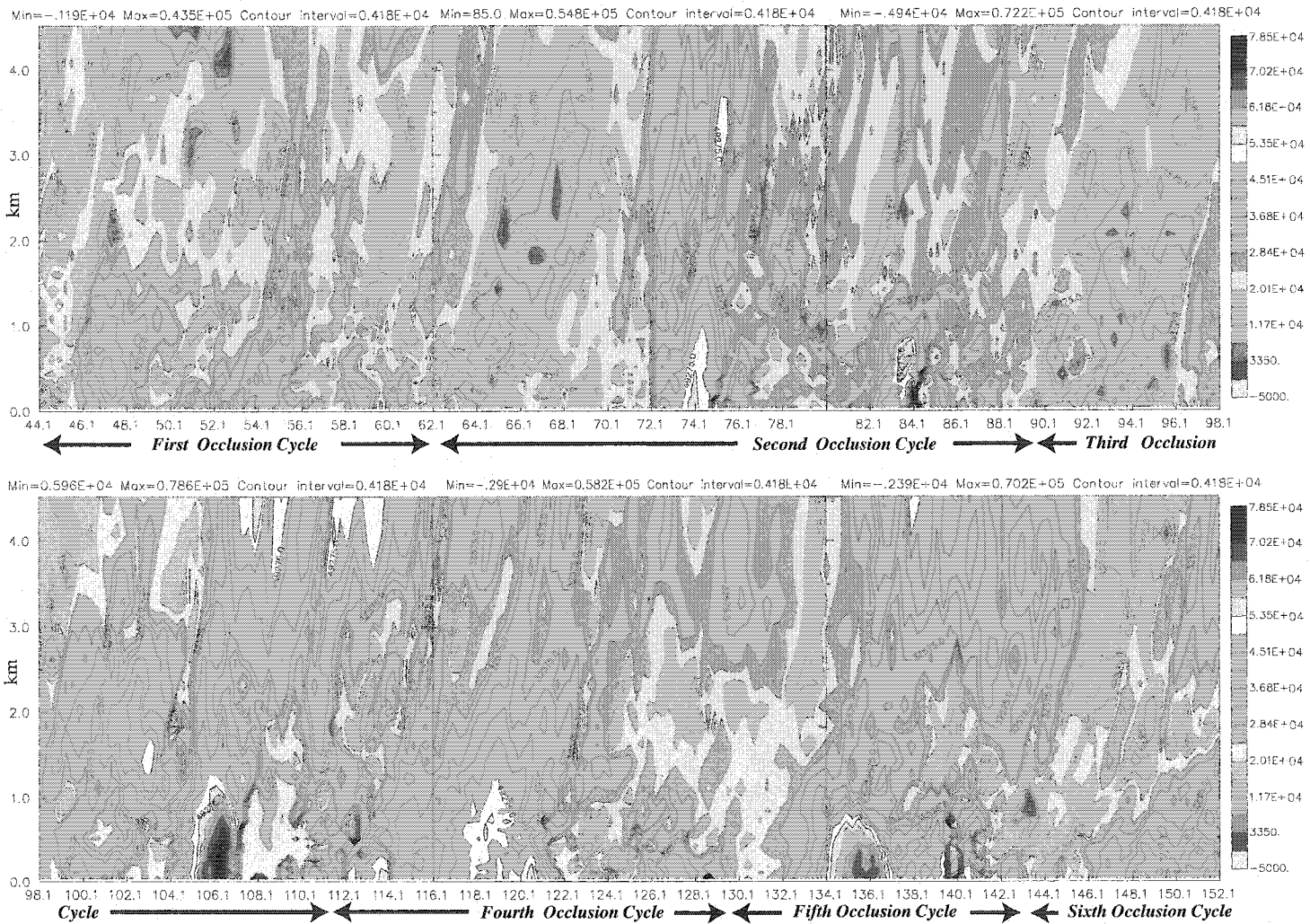


Figure 4.3.6: Time-height plot of fine-grid domain-wide maxima in circulation ($m^2 s^{-1}$). Circulation is calculated around a box with sides of 500m, centered on the minima in pressure perturbation at each level. Model time $\times 10^2$ s indicated on the lower axis. Maximum and minimum of each 1800 s segment indicated at top.

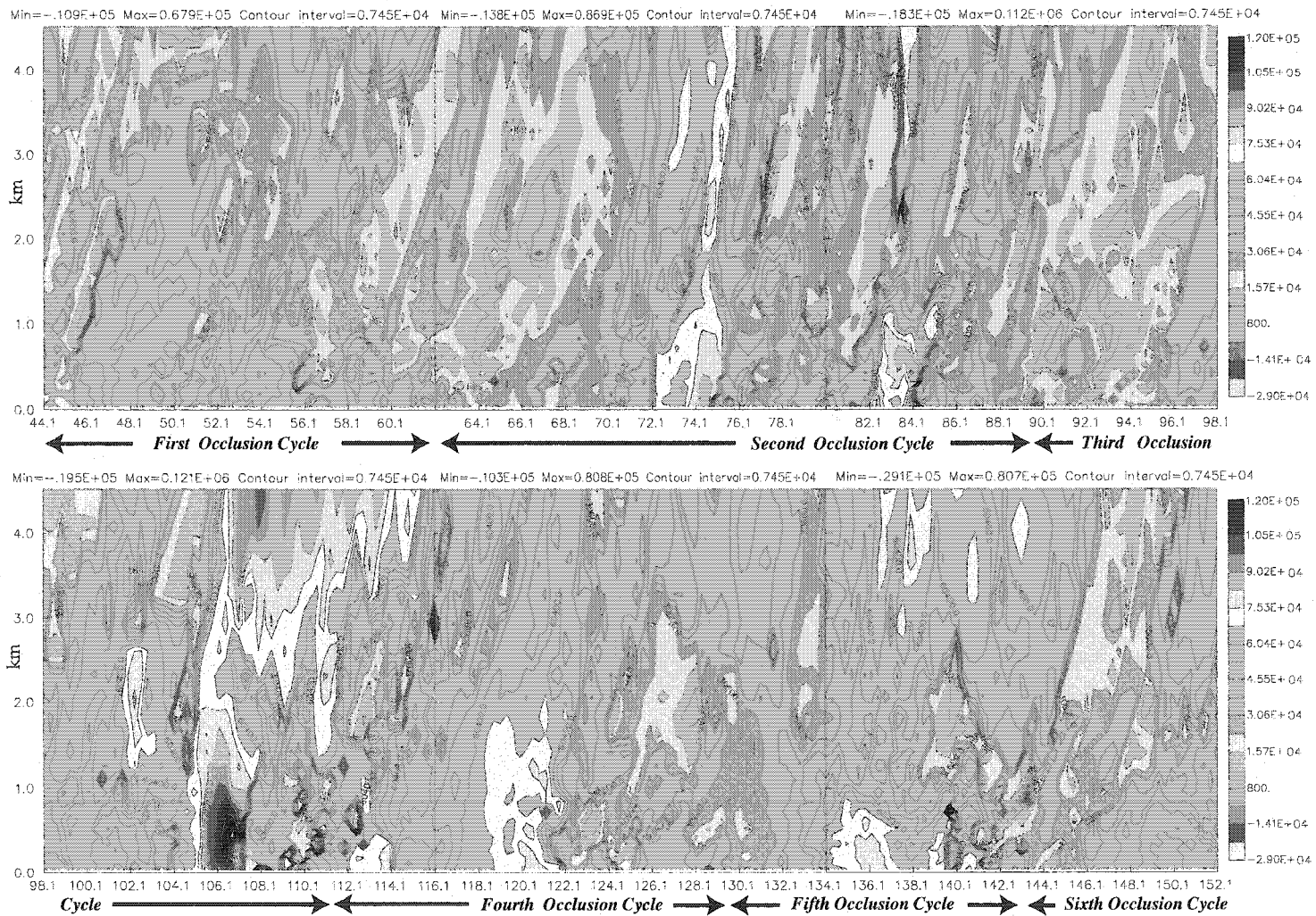


Figure 4.3.7: Time-height plot of fine-grid domain-wide maxima in circulation ($m^2 s^{-1}$). Circulation is calculated around a box with sides of 1 km, centered on the minima in perturbation pressure at each level. Model time $\times 10^2$ s indicated on the lower axis. Maximum and minimum of each 1800 s segment indicated at top.

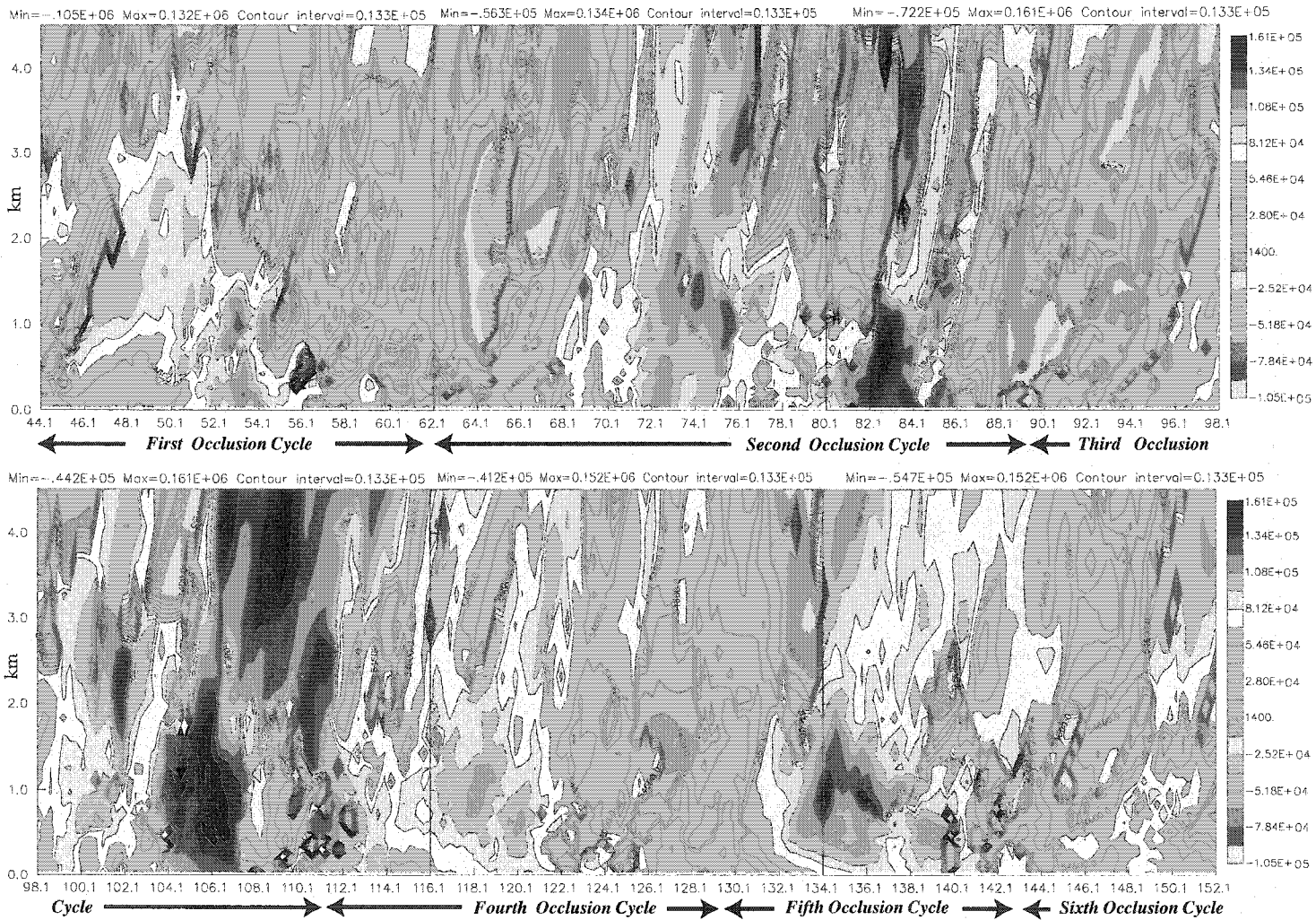


Figure 4.3.8: Time-height plot of fine-grid domain-wide maxima in circulation ($m^2 s^{-1}$). Circulation is calculated around a box with sides of 2 km, centered on the minima in perturbation pressure at each level. Model time $\times 10^2$ s indicated on the lower axis. Maximum and minimum of each 1800 s segment indicated at top.

circulation values may not be perfectly correlated vertically, especially during weaker mesocyclone phases, the use of the larger box sizes should offset these errors. In all of the plots (Figs. 4.3.6-4.3.8), vertical features which more closely parallel the maxima in vertical velocity (Fig. 4.3.2) are clearly evident as are the minima in perturbation pressure (Fig. 4.3.4). The intensification during cycle three (10620 s) clearly stands out as the strongest phase during the supercell's evolution (Figs. 4.3.7 and 4.3.8).

4.4 Mesocyclogenesis and the transitions between cycles

4.4.1 Introduction

Adlerman et al. (1999) identified 5 stages in their conceptual model (Fig. 2.3.1) of a "typical" mesocyclone occlusion cycle: 1) initial near-ground mesocyclogenesis, 2) initiation of the dual updraft structure, 3) occlusion downdraft development and intense mesocyclone strengthening, 4) mesocyclone/updraft decay, and 5) reintensification and new near-ground mesocyclogenesis. In this section we examine the most intense tornadic occlusion cycle ("C") in the context of this conceptual model, and then briefly compare the transition of this cycle (from "C" to "D") with the four other transitions. A more detailed analysis of the mesocyclogenesis/tornadogenesis dynamics will be left to the next section.

4.4.2 Occlusion Cycle "C"

Figure 4.4.1 displays various horizontal cross-sections through the storm at 9810 s, corresponding approximately to Stage 1, initial near-ground mesocyclogenesis. At this point, cycle "C" has just begun and updrafts are beginning to increase (Fig. 4.3.2) after the temporary weakening following the termination of cycle "B." A strong single-cell updraft is apparent (Fig. 4.4.1a,b),

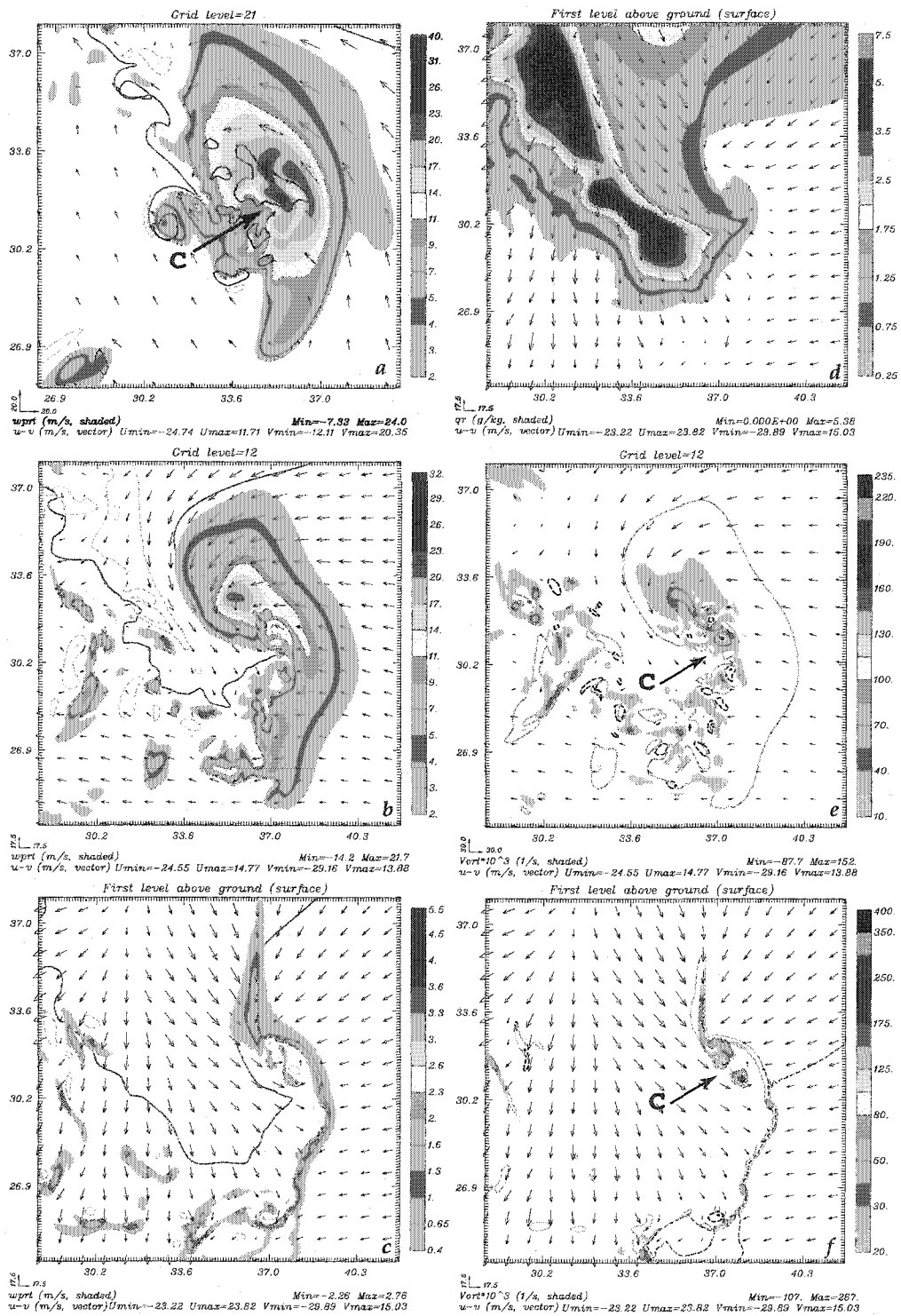


Figure 4.4.1: Horizontal cross-sections at $t = 9810$ s of: vertical velocity at (a) $z = 3$ km, (b) $z = 1$ km, and (c) $z = 35$ m; (d) rainwater mixing ratio, q_r , at $z = 35$ m; and vertical vorticity at (e) $z = 1$ km and (f) $z = 35$ m. Single black contour in (a) indicates vorticity isoline of 0.02 s^{-1} . Single blue contours in (a-c) indicate q_r isoline of 1 g kg^{-1} . Single green contours in (e) and (f) indicate vertical velocity isolines of 1 and 2.5 m s^{-1} , respectively. Single red contour in (f) indicates -1.0 K isoline of perturbation potential temperature. Dashed contours in (a-c) indicate negative vertical velocity contours of 5 , 5 , and 1 m s^{-1} , respectively. Dashed contours in (e) and (f) indicate negative vertical vorticity contours of 0.04 and 0.05 s^{-1} .

along with a developing hook (Fig. 4.4.1d). At the surface, a gust front extends north-south (Fig. 4.4.1c,f), with the southern section beginning to move eastward with the developing cold pool and rear-flank downdraft (RFD). At 1 km, the RFD located with the highest rainwater values (Fig. 4.4.1b,d) is evident in the center of the incipient hook, suggesting that it is mostly due to evaporative cooling and water loading.

One of the more striking characteristics of this simulation is the amount of smaller-scale structure present in the vertical velocity and vorticity fields. Although this is obviously expected, it presents somewhat of a dilemma when compared with traditional coarser-resolution simulations and radar analyses. In particular, objectively defining a single mesocyclone based upon a value of vorticity is no longer possible. Above the surface (Fig. 4.4.1a,b), a broad mesocyclonic circulation is present. However, even the single-celled updraft has well-resolved embedded maxima approximately 500 m in diameter. The corresponding vorticity field aloft (Fig. 4.4.1a,e) contains similar small-scale structures embedded in the overall circulation. When viewed in animations, these small-scale maxima/minima evolve rapidly (on the order of 60 s), but an overall single center of circulation and vorticity maximum can usually be identified and followed. This is what we identify as mesocyclone "C" in these figures.

At the surface (Fig. 4.4.1f), the vertical vorticity field contains a maximum at the head of gust front, i.e., where the north/south oriented portion intersects the northwest/southeast oriented eastward-moving section. However, multiple small-scale vortices are also apparent to the southeast. A broad mesocyclonic circulation encompasses this entire area.

The small intense vortices evolve rapidly in this early stage of the occlusion process and appear to be shed from the head of the gust front as the hook and rear-

flank downdraft wrap around it, forced by the broader mesocyclone circulation aloft. In essence, the gust-front acts as a vortex sheet, shedding vortices under forcing from the evaporatively-driven outflow. Although these vortices are shallow (1 km or less), they contain pressure deficits at the surface of up to 5 mb, strong enough to drive small occlusion downdrafts as they evolve (Fig. 4.4.1c). Wicker and Wilhelmson (1995) simulated similar vortex sheet instability along the gust-front, but in our case the vortices separate fully from the updraft associated with the gust-front (compare Fig. 4.3.2 with Wicker and Wilhelmson's Fig. 5; also see Finley et al. 2002). Comparable small-scale vortex behavior has recently been observed by Bluestein et al. (2003).

Figure 4.4.2 displays horizontal cross-sections through the storm at 10290 s, a point in time that is comparable to Stage 2 of the conceptual model. At $z = 3$ km (Fig. 4.4.2a), the updraft has taken on a dual-maxima structure, with vertical velocity maxima strengthening rapidly from 24 to 44 m s^{-1} . The western maximum contains what could be considered the original mesocyclone "C" and its associated updraft, while the eastern maximum is what will become the dominant updraft of the next cycle.

At the surface (Fig. 4.4.2c,d,f) a strong surge in the rear-flank downdraft (RFD) has bowed the gust-front outward to the east, and even formed a secondary gust-front structure approximately 1.5 km west of the original one. A corresponding downward and eastward advection of rainwater has extended and narrowed the hook (Fig. 4.4.2d). In addition to the developing cyclonic flare in the hook associated with the near-ground mesocyclone, an anticyclonic flare also is briefly noted on the southern side of the hook. This flare develops because the horizontal vorticity vector on the southern edge of the hook points to the west-southwest, a consequence of the baroclinic effect of the north-south precipitation gradient (westward-pointing

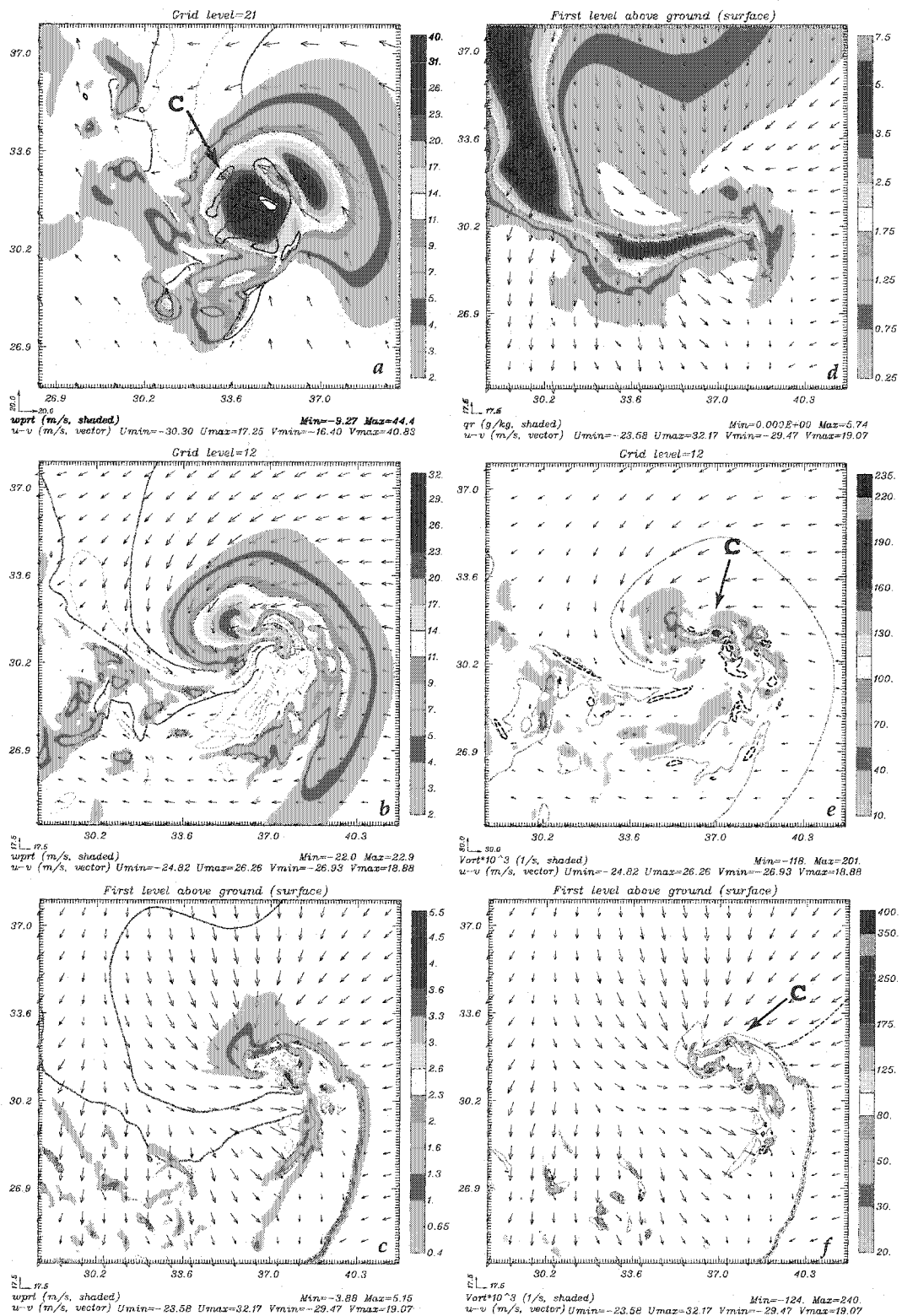


Figure 4.4.2: Same as in Fig. 4.4.1, except for $t = 10290$ s.

horizontal vorticity) plus the local effect of the shear caused by the RFD (30 m s⁻¹ east/southeast surface winds overlaid by weaker flow, south/southwestward-pointing horizontal vorticity). When this vorticity is tilted upward in the secondary gust front, it is mostly anti-streamwise, creating some areas of negative vertical vorticity (approximately -0.10 s⁻¹) correlated with positive vertical velocity (Fig. 4.4.2e,f). These vortices only last for a couple of minutes before they are pushed away from the main updraft and decay.

The strong surface convergence associated with the RFD, along with strong upward vertical pressure gradients (Fig. 4.4.3), results in a large increase in vertical velocity at the surface (Fig. 4.4.2c), with maxima at $z = 35$ m increasing from 2.8 to 5.2 m s⁻¹ at this time. This increase also is evident in the time-height plot of updraft (Fig. 4.4.3) as two maxima: the first just before 10210 s, which builds upward (i.e., driven by surface convergence) and the second just after 10210 s, which builds downward. At 1 km, the maximum upward pressure gradient force is centered just to the west of vorticity maximum (Fig 4.4.2e), accompanied by a downward pressure gradient just to the east of the same maximum. This couplet results from the slight westward tilt with height of the mesocyclone center (Fig. 4.4.2a,e,f) and its associated pressure deficit.

Maximum downdrafts also increase dramatically by 10290 s, especially between the surface and 1.5 km (Fig. 4.4.4, Fig. 4.4.2b,c). At 1 km (Fig 4.4.2b), this increase occurs in two locations: immediately adjacent to the maximum in updraft and vorticity, i.e. a developing occlusion downdraft, and immediately adjacent to the southern part of the hook. This occlusion-type downdraft is mainly driven by strong downward vertical pressure gradients of up to -1.3 m s⁻² at $z = 1$ km, centered on the eastern half of the mesocyclone. The other strong downdraft along the hook at this height (which can be considered part of the RFD) is driven by negative

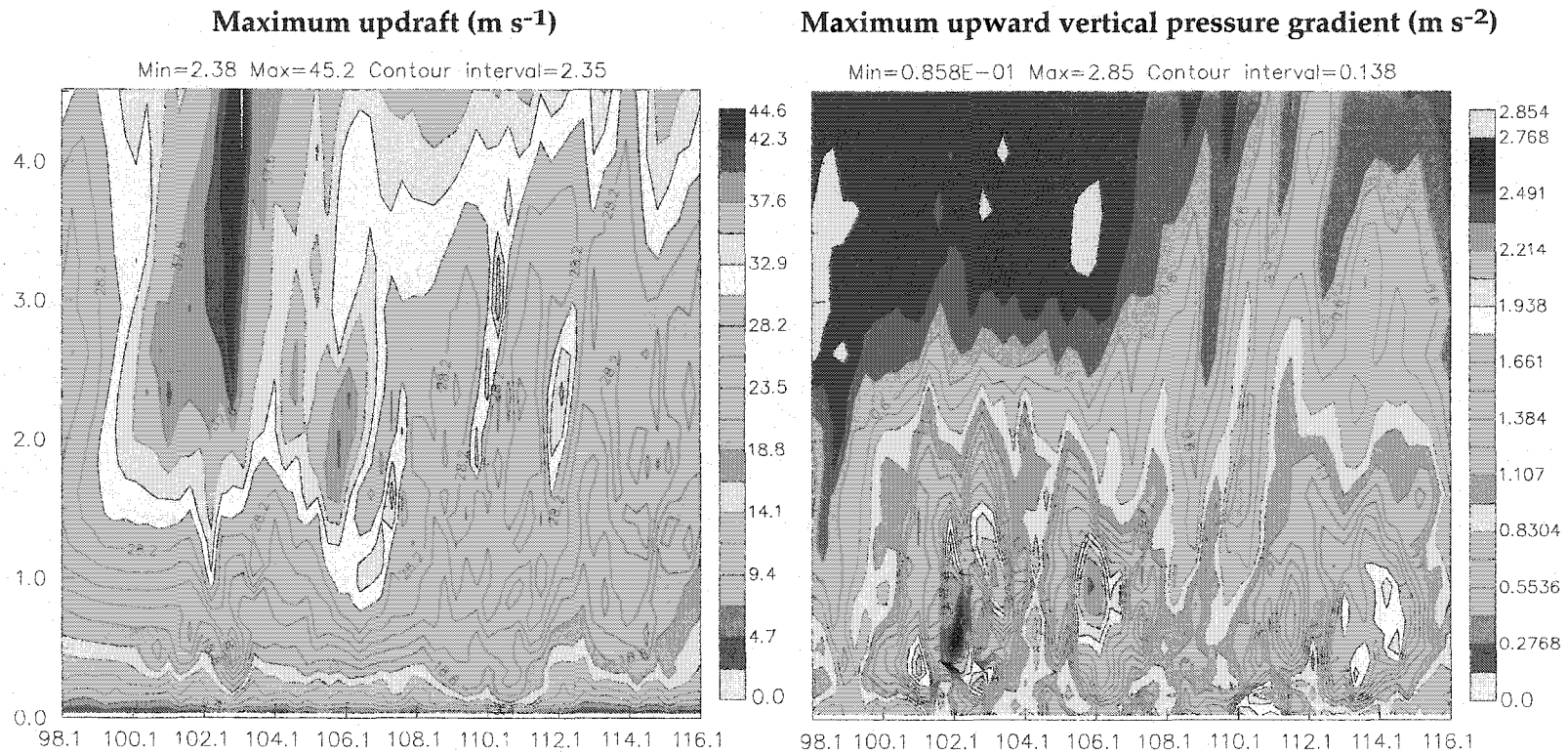


Figure 4.4.3: Time-height plots of maximum vertical velocity (m s^{-1}) and maximum upward vertical pressure gradient force (m s^{-2}) between 9810 and 11610 s (labeled $\times 10^2\text{s}$). Vertical axis is in km.

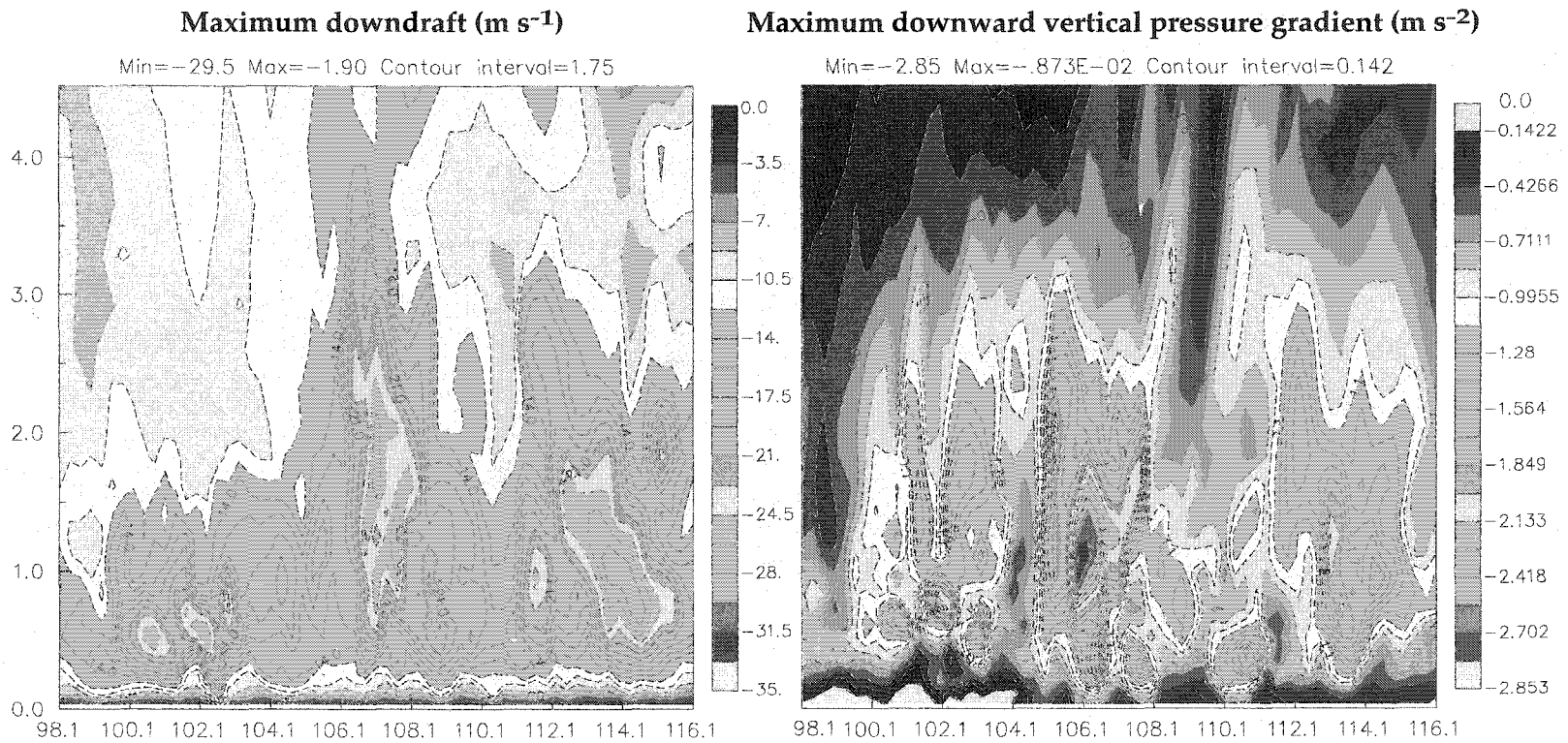


Figure 4.4.4: Time-height plots of minimum vertical velocity (m s^{-1}) and maximum downward vertical pressure gradient force (m s^{-2}) between 9810 and 11610 s (labeled $\times 10^2$ s). Vertical axis is in km.

buoyancy of -0.12 m s^{-2} immediately along the precipitation gradient, and downward vertical pressure gradient forces of -0.10 m s^{-2} further southeast in the warmer air. This might be akin to development of the “clear slot” (e.g., Markowski 2002) that sometimes precedes near-ground mesocyclone strengthening and tornadogenesis.

Near the surface, the vertical velocity and vertical vorticity remain somewhat disorganized, with small-scale cyclonic vortices rotating around a broader mesocyclonic circulation. Parts of both downdrafts at 1 km also have penetrated down toward the surface, near the center of the circulation (Fig. 4.4.2c).

By 10620 s (Fig. 4.4.5), the near-ground mesocyclone has rapidly intensified and a tornadic vortex has formed. The storm is at a point corresponding approximately to stage 3 of the conceptual model. At 1 km (Fig. 4.4.5a), the RFD and occlusion downdraft join together and form one nearly continuous downdraft along the hook. These downdrafts penetrate upward through 3 km and have nearly separated the dual updraft structure. This upward development is evident between 10410 and 10620 s on the time-height plot (Fig. 4.4.4).

A strong mesocyclone circulation exists at 1 and 3 km, straddling the updraft/downdraft interface (Fig. 4.4.5a,b). Although the maximum updraft at 3 km has weakened somewhat from 44.4 m s^{-1} to 32.6 m s^{-1} , at 1 km it has increased from 22.9 m s^{-1} to 31.0 m s^{-1} , forced by strong upward vertical pressure gradients (Fig. 4.4.3). Although not apparent in the vorticity maxima, a time-height plot (Fig. 4.4.6) suggests that the circulation initially increases aloft, between 0.5 and 2.5 km, prior to 10410 s. [In this case the circulation calculation was centered on the maximum in *vertical vorticity*, which gives similar, but not identical results to that centered on the minimum in perturbation pressure]. Between 10410 and 10620 s, there is a near-instantaneous increase in circulation through a deep layer that precedes the transformation from a

near-ground mesocyclone to a tornado. During the same time period, a descending maximum (from 2.5 to 1 km) in vertical velocity is present (Fig. 4.4.3). The time-height of pressure minima (Fig. 4.3.4) also supports the pattern seen in the evolution of circulation.

At the surface, three of the individual vortices described earlier (Fig. 4.4.2f, those west of $x = 37.2$ km) have rotated around one another and merged (Lee and Wilhelmson 1997a,b; Wicker and Wilhelmson 1995) to form a single intense tornadic vortex (Fig. 4.4.7). If we define the moment of tornadogenesis as when the individual vortices and accompanying surface pressure deficits rapidly congeal into a single maximum, the approximate time of tornadogenesis is 10500 s. Between 10440 and 10500 s, the surface pressure deficit increases by 7 mb; between 10500 and 10620 s, it increases by another 8.3 mb. The occlusion downdraft penetrates to the surface on the northern side of the vortex (Fig. 4.4.2c), with the strongest updraft on the southern side. The vortex has a surface pressure deficit of 27.5 mb, with ground-relative wind-speeds of 49 m s^{-1} and peak vertical vorticity of 0.40 s^{-1} .

After 10620 s, updrafts begin to weaken (Fig. 4.4.3) and downdrafts between 0.5 and 2.5 km intensify (Fig. 4.4.4). By 10740 s, the tornadic vortex has become surrounded by downdraft and its maximum pressure deficit has decreased to 11 mb, while vertical vorticity has decreased to 0.22 s^{-1} . By 10800 s, we conclude that the tornadic vortex has dissipated, leaving behind a strong occluded near-ground circulation. At the surface, the downdrafts which eventually surround the tornado also quickly warm the local environment (Fig. 4.4.8), with θ_e values increasing by up to 10 K (due to turbulent mixing) during the 8 minutes since tornadogenesis.

At 11160 s (Fig. 4.4.9), the near-ground mesocyclone has strongly occluded and the storm is at a point similar to stage 4 of the conceptual model. At the surface (Fig. 4.4.9c,d,f) the circulation is completely wrapped in heavy precipitation, with a

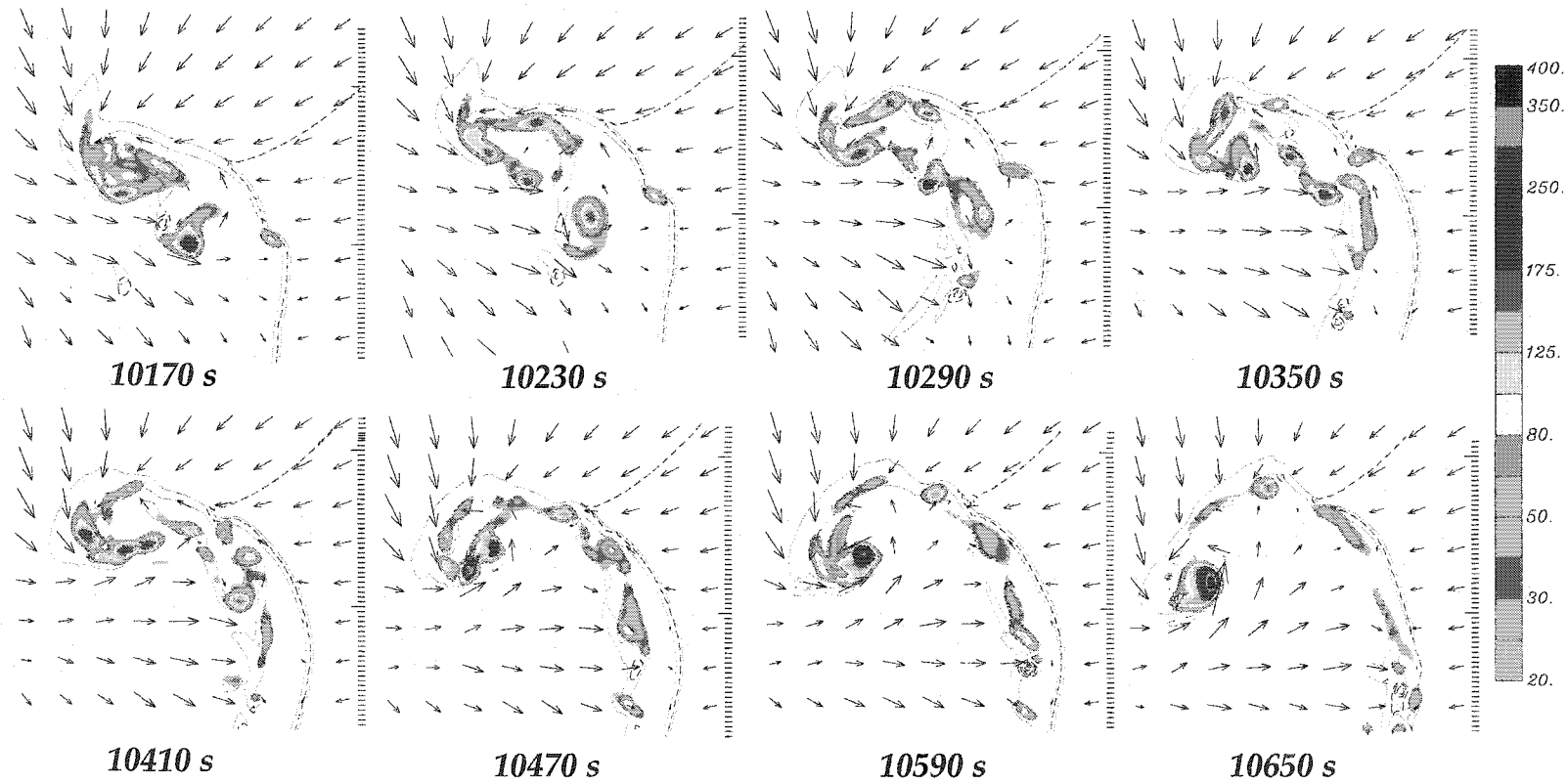


Figure 4.4.7: Horizontal cross-sections of vertical vorticity ($\times 10^{-3} \text{ s}^{-1}$) at $z = 35 \text{ m}$ during tornadogenesis in cycle "C".

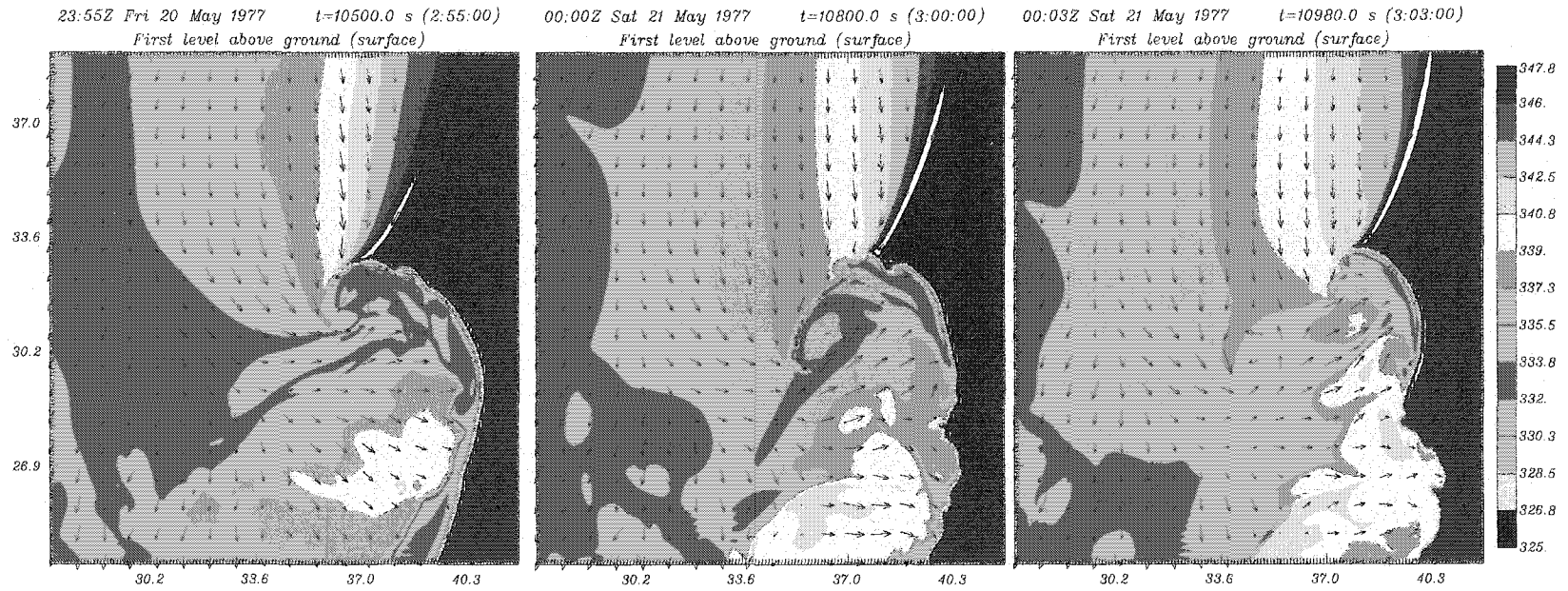


Figure 4.4.8: Horizontal cross-sections at $z = 30$ m of equivalent potential temperature (K) at 10500, 10800, and 10980 s, during the tornadic and post-tornadic phases of cycle "C".

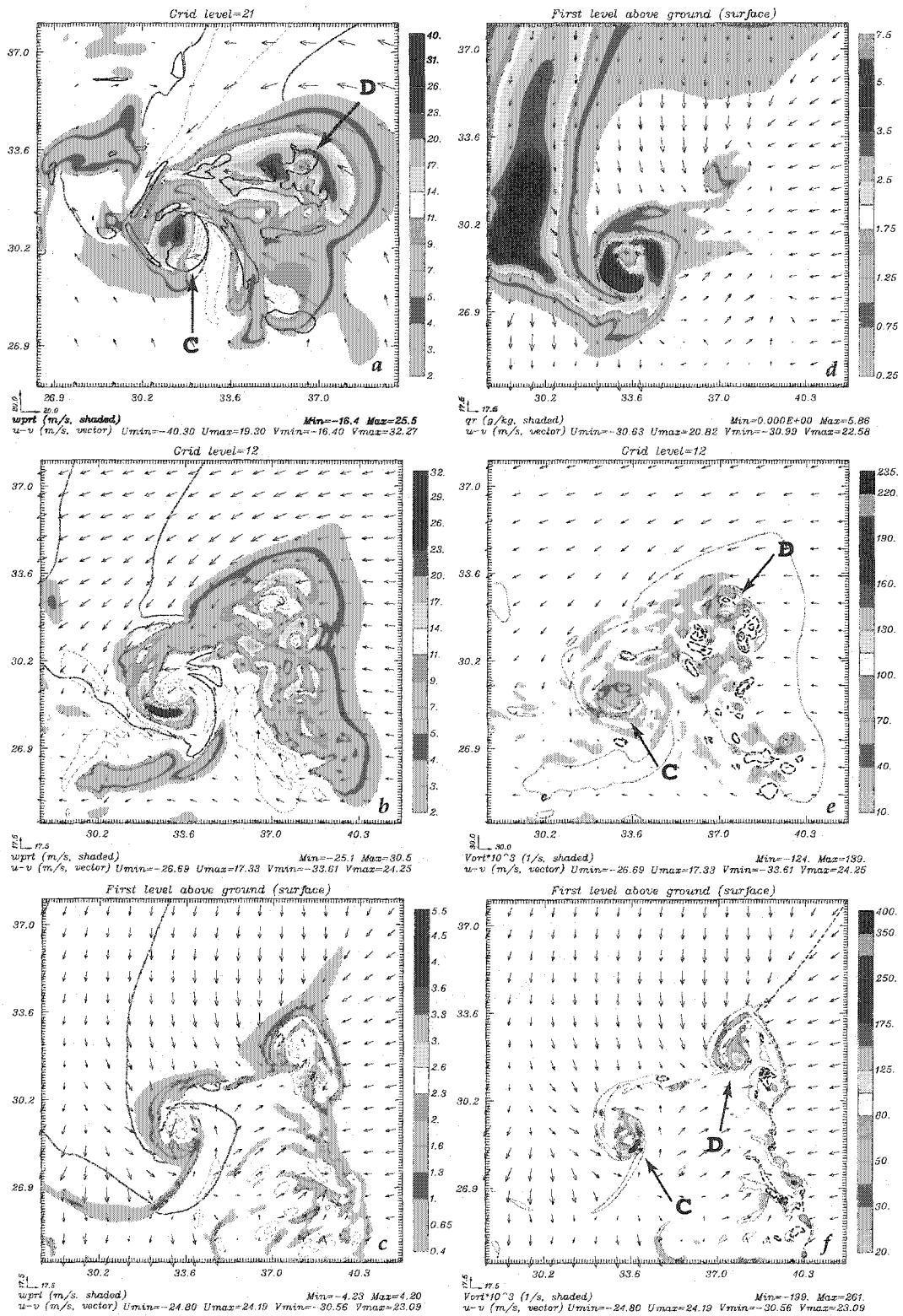


Figure 4.4.9: Same as in Fig. 4.4.1, except for $t = 11160$ s.

characteristic “donut-hole” signature in the center (e.g., Fujita and Wakimoto 1982), approximately where the strongest part of the occlusion downdraft is located. The occluding surface-based updraft also has begun to break away from the rest of the gust front, farther to the northeast.

Similarly, at 1 and 3 km (Fig. 4.4.9a,b), the occluding updraft has nearly separated from the newer portions of the storm developing to the east (what will become cycle “D”). The occluded updraft remains remarkably strong (30.5 m s^{-1} at 1 km) despite the fact that its surface roots are completely cut off (Fig. 4.4.9.c) from the potentially buoyant inflow air to the east. The updraft is driven by strong vertical pressure gradient forces of up to 1.63 m s^{-2} at $z = 1 \text{ km}$ which counteract the presence of weaker negative buoyancy (-0.11 m s^{-2}) in the updraft at this height. However, strong downdrafts ($> 20 \text{ m s}^{-1}$) immediately adjacent to the occluded updraft (driven by strong downward vertical pressure gradients of up to -1.0 m s^{-2} , Fig. 4.4.4) will quickly diminish its size and intensity within the next 500 s.

At the surface (Fig. 4.4.9c,d,f), a new mesocyclone has already started forming approximately 3 km to the northeast of the occluded one. A second hook is already developing in the surface rainwater field. At 1 km and above (Fig. 4.4.9 a,b,e), the new updraft and mesocyclone remain somewhat disorganized.

By 11640 s, the new mesocyclone and associated updraft have become better organized and the storm corresponds to stage 5 of the conceptual model. At the surface (Fig. 4.4.10c,d,f), the occluded circulation of cycle “C” is still visible as a small hook with a persistent vorticity maximum, despite the fact that it is located in an area of mostly divergent outflow. A new hook already has formed around the intensifying mesocyclone of cycle “D”, which has a vorticity maximum of 0.25 s^{-1} at the surface. At 1 km, the mesocyclone is now clearly visible (Fig. 4.4.10e), although the updraft above this level still contains multiple maxima (Fig 4.4.10a). Unlike the

previous cycle, at this point the RFD remains quite weak and no strong associated downdrafts are visible at 1 km. The circulation associated with cycle "D" later intensifies (see Sec. 4.3) but remains non-tornadic and is one of the shortest cycles of the simulation.

4.4.3 Transitions in Other Occlusion Cycles

In the transition from occlusion cycle "C" to "D", the storm undergoes a process that is roughly similar to that described by the conceptual model of cyclic mesocyclogenesis in Adlerman et al. (1999). However, besides the obvious differences in the scale of resolved features, the evolution of this cycle differs from the one described in Adlerman et al. (1999) and Adlerman and Droegemeier (2002) in the *discreteness* of the transition. Previous simulations, which were conducted at 500 m horizontal grid spacing, showed an updraft above the surface (between 1-4 km) that was clearly composed of two distinct maxima separated by up to 4 km (e.g. see Fig. 1b of Adlerman and Droegemeier 2002, or Fig. 22-23 of Adlerman et al. 1999). At the surface, this separation was reflected in a gust front which surged farther ahead of the occluding mesocyclone and old updraft, resembling a storm which has "gusted-out."

In our current simulation, the evolution of the updraft suggests a more continuous process than previously described. Although two updraft and vorticity maxima are evident in cycle "C", animations suggest a process that resembles the "shedding" of an occluding updraft from the developing updraft to its east. This is similar to what Dowell and Bluestein (2002a) describe in their radar study of cyclic tornadogenesis. At the surface, the storm no longer appears to "gust-out", as the transition between near-ground mesocyclones is quite rapid, with one hook oftentimes connected to the new hook (e.g., Fig. 4.4.9d). Because we are using the

same initial sounding and essentially the same numerical model as in our previous work, these differences most likely result from the use of finer grid spacing.

The other four transitions between cycles display significant variations in their discreteness (i.e., the degree to which the occluding updraft and mesocyclone are clearly separate and distinct from those of the next cycle). Figure 4.4.11 shows the transition between non-tornadic cycle "A" and tornadic cycle "B." Cycle "A" is one of the weakest cycles (e.g., Figs. 4.3.2, 4.3.4, 4.3.5) with relatively small maxima in vertical velocity and vorticity. During the initial occlusion period at 5400 s (Fig. 4.4.11), the updraft at 3 km appears unicellular with three embedded maxima. The updraft and mesocyclone associated with cycle "A" is somewhat indistinct, noted mostly by a small area of downdraft, surrounded by updraft, and centered on a persistent small (but traceable) area of rotation. Between 5880 and 6510 s, the small updraft and vorticity features associated with mesocyclone "A" weaken and move westward, while the developing updraft and mesocyclone "B" become quite prominent to the east. At the surface, mesocyclone "A" is rapidly pushed southward and decays, while "B" forms from the congealing of two separate areas of vorticity farther northeast along the gust front. In this case (and most of the others), we note that the near-ground mesocyclone and its associated updraft decouple from the updraft aloft during the occlusion process. This allows the occluded surface features to dissipate far sooner than the occluding updraft aloft (e.g., compare Fig. 4.4.11 at 5880 and 6510 s). In a typical radar analysis, the evolution of "A" at 3 km would most likely be smoothed out and not noticed.

Figure 4.4.12 displays the transition between tornadic cycle "B" and tornadic cycle "C." Unlike the previous example, at 8190 s the updraft at 3 km clearly contains two distinct maxima, separated by a maximum distance of approximately 1 km. As the occlusion progresses through 8970 s, the occluding updraft "B" narrows

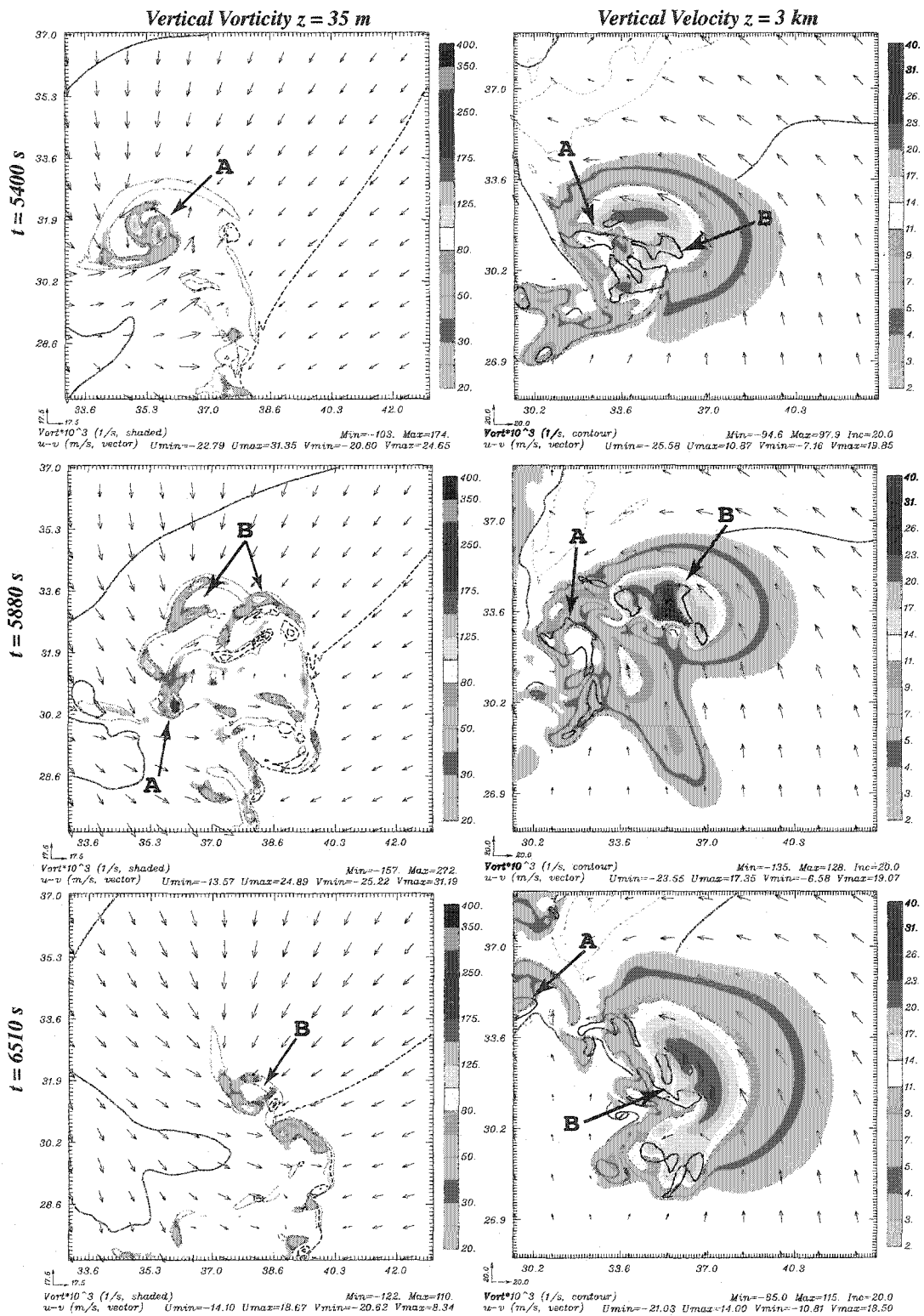


Figure 4.4.11: Horizontal cross-sections of vertical vorticity at $z = 35$ m (left) and vertical velocity at $z = 1$ km (right) during the transition between cycles one and two. Single blue contour indicates q_r isoline of 1 g kg^{-1} . All other notations are the same as in Figure 4.4.1 (a) and (f).

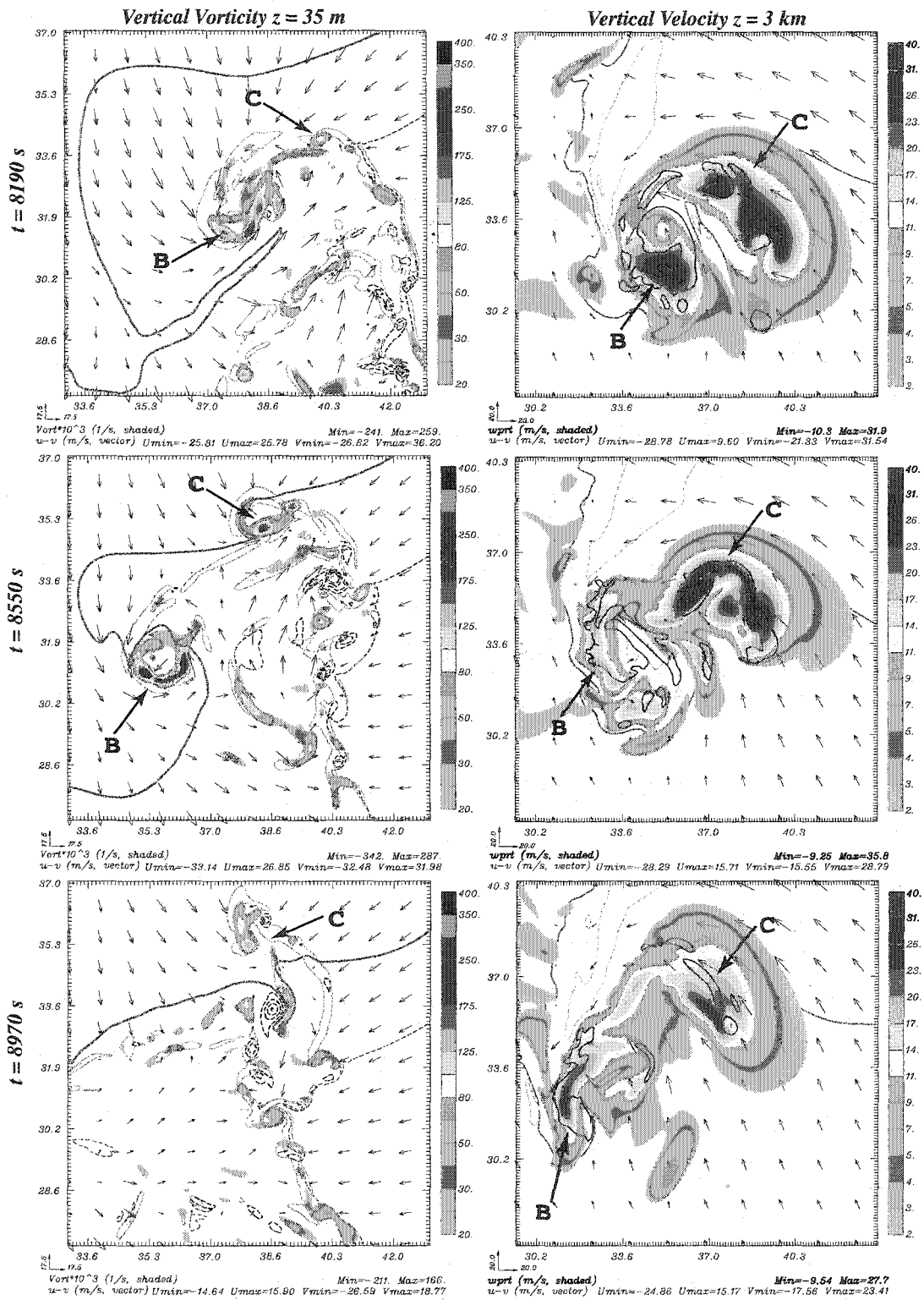


Figure 4.4.12: Horizontal cross-sections of vertical vorticity at $z = 35$ m (left) and vertical velocity at $z = 1$ km (right) during the transition between cycles two and three. Single blue contour indicates q_r isoline of 1 g kg^{-1} . All other notations are the same as in Figure 4.4.1 (a) and (f).

and moves off to the southwest, but remains distinct and intense, even after the formerly tornadic near-ground circulation has dissipated.

The transition from non-tornadic cycle "D" to tornadic cyclic "E" is displayed in Figure 4.4.13. At the beginning of the occlusion process at 12300 s, the updraft at 3 km appears somewhat unicellular, but with two maxima surrounding a central minimum. The updraft maximum on the southwest side is occluding and is correlated with the near-ground updraft and circulation "D" in the decaying hook echo. As this occlusion progresses through 13140 s, the circulation at 3 km associated with "D" is shed as a small, rapidly rotating updraft approximately 1.5 km in diameter. By 13140 s, an organized near-ground mesocyclone is already visible and the updraft associated with cycle "E" has already taken on a dual-maxima appearance.

The last transition from tornadic cycle "E" to non-tornadic cycle "F" is shown in Figure 4.4.14. At this point in the simulation, some elevated convection begins to form south of the main storm and interact with it (Fig. 4.3.1c, 14400-15600 s). At the beginning of the occlusion at 13800 s, the updraft structure at 3 km is quite complex, with two large maxima surrounding a smaller area of downdraft. The occluding mesocyclone and updraft ("E") are embedded on the western side and consist of a smaller updraft maxima and a downdraft, delineated approximately by the single vertical vorticity contour surrounding both (as discussed previously, this is most easily seen by watching animations of the 30 s data). As the occlusion progresses from 14250 to 14640 s, the occluding updraft at 3 km is shed from the main storm and moves off to the southwest. At the surface, the new mesocyclone "F" rapidly forms approximately 4.5 km to the northeast of "E" around 14250 s. A new hook begins to approach the developing near-ground circulation "F" at 14640 s, while the

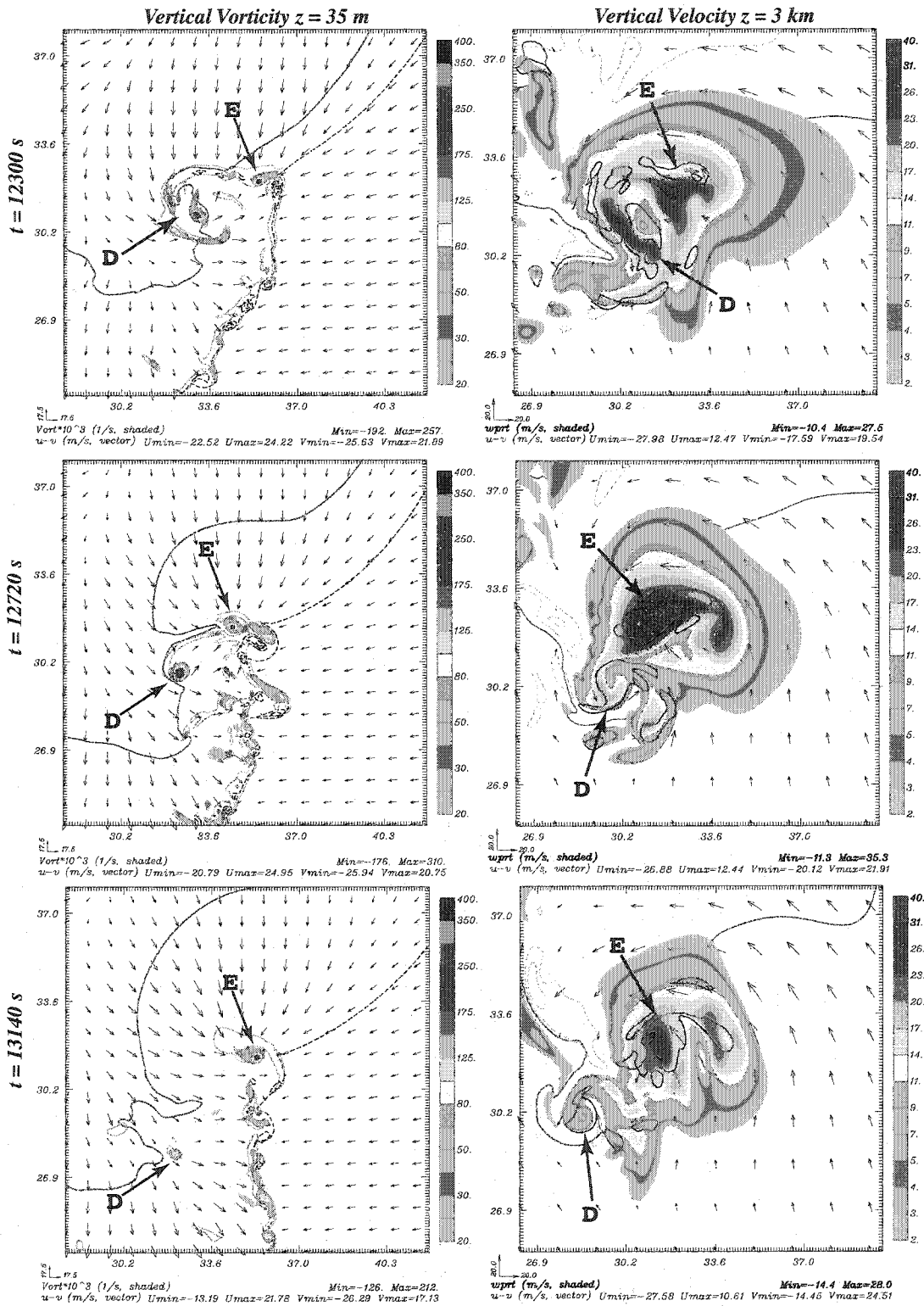


Figure 4.4.13: Horizontal cross-sections of vertical vorticity at $z = 35$ m (left) and vertical velocity at $z = 1$ km (right) during the transition between cycles four and five. Single blue contour indicates q_r isoline of 1 g kg^{-1} . All other notations are the same as in Figure 4.4.1 (a) and (f).

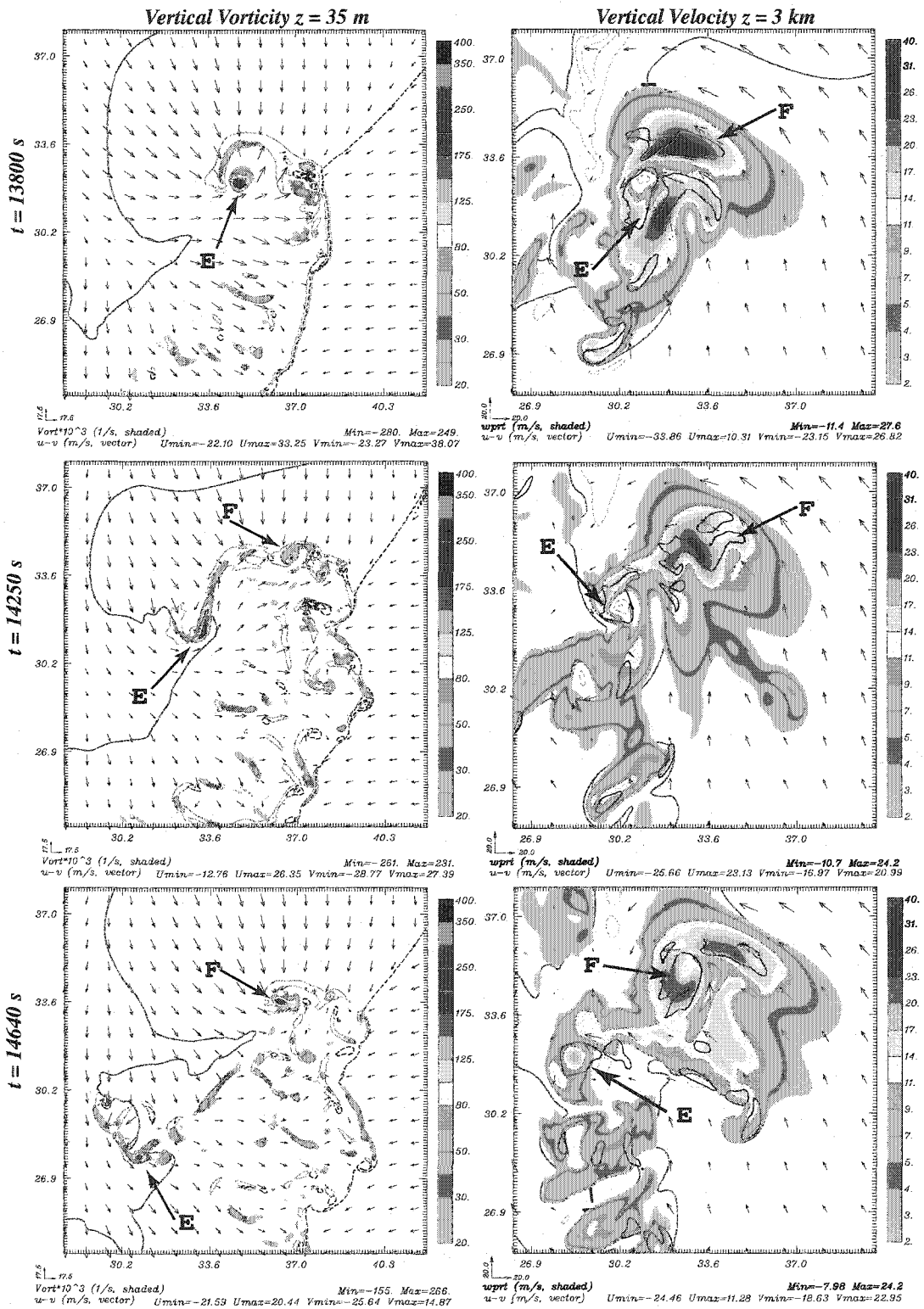


Figure 4.4.14: Horizontal cross-sections of vertical vorticity at $z = 35$ m (left) and vertical velocity at $z = 1$ km (right) during the transition between cycles five and six. Single blue contour indicates q_r isoline of 1 g kg^{-1} . All other notations are the same as in Figure 4.4.1 (a) and (f).

decaying hook and associated circulation “E” are located about 9 km to its southwest.

In summary, even within a single storm there are large variations in the morphology of cyclic mesocyclogenesis, especially above the surface. Although the conceptual model describes a “dual updraft” as a key feature, this may not always be true. Consistent with some observations (Dowell and Bluestein 2002a,b), the occluding updraft may first present itself as a secondary maximum within what appears to be a unicellular storm (Figs. 4.4.11, 4.4.13). At other times in its evolution, the occluding updraft may be identified by a small updraft/ downdraft couplet that sheds from the main updraft (Figs. 4.4.11, 4.4.13, 4.4.14), or it may take on the more identifiable appearance of one distinct updraft separated by a narrow downdraft from another updraft on the inflow side of the storm (Figs. 4.4.5, 4.4.12; Klemp et al. 1981; Ray et al. 1981; Adlerman et al. 1999; Adlerman and Droegemeier 2002).

Adlerman and Droegemeier (2000) speculated that the character of the occlusion process aloft might be a function of the separation between the new and occluding near-ground mesocyclones. Although this is probably true to some extent, in the present simulations a better correlation is evident with the strength of the occluding updraft and mesocyclone. When the occluding updraft and mesocyclone are tornadic (Figs. 4.4.5; 4.4.12), there is a greater tendency for a clearly dual updraft. With a weaker tornadic cycle or a non-tornadic cycle (Figs. 4.4.11, 4.4.13, 4.4.14), the transition is more subtle. In this particular simulation, this difference results from two effects: 1) the extent to which downdrafts below 1 km penetrate upward through the storm and 2) the size of the occluding updraft. In the tornadic cases, the rotationally-driven dynamic pressure gradients must clearly be larger than in the non-tornadic cases, and give rise to both stronger updrafts and downdrafts (Figs. 4.3.2, 4.3.3). The stronger occlusion downdrafts build upward

near the circulation center, and cause a clearly divided or dual updraft aloft. The stronger updrafts allow the occluding mesocyclone to persist longer after it has become separated from its surface roots, thus making the transition seem more discrete (i.e., the updraft does not immediately begin to decay as it moves away from the inflow side of the storm)

4.5 Trajectory Results

4.5.1 Introduction

In order to determine the origins of low-level rotation, it is useful to calculate the Lagrangian vorticity equation forcing terms in semi-natural coordinates, where $(\mathbf{s}, \mathbf{n}, \mathbf{k})$ represent orthonormal basis vectors for the semi-streamwise, semi-crosswise and vertical directions (Lilly 1982) and the vector wind $\mathbf{V} = (V_H, 0, w)$. The inviscid Boussinesq equations (neglecting turbulent mixing) for the vertical (ζ), semi-streamwise (ω_s), and semi-crosswise (ω_n) vorticity are

$$\frac{d\zeta}{dt} = \bar{\omega}_h \cdot \nabla w + \zeta \frac{\partial w}{\partial z} \quad (1)$$

$$\frac{d\omega_s}{dt} = \omega_n \frac{d\psi}{dt} + \bar{\omega} \cdot \nabla V_H + \frac{\partial B}{\partial n} \quad (2)$$

$$\frac{d\omega_n}{dt} = -\omega_s \frac{d\psi}{dt} + \bar{\omega} \cdot (V_H \nabla \psi) - \frac{\partial B}{\partial s} \quad (3)$$

where the horizontal direction of a parcel is defined as $\psi = \tan^{-1}(v/u)$, and B represents buoyancy. We use the notation of *semi-streamwise* and *semi-crosswise* to distinguish our vorticity components from those used in natural coordinates, i.e., where the orthonormal basis vectors $(\mathbf{s}, \mathbf{n}, \mathbf{b})$ are defined for the streamwise, normal, and binormal directions and the vector wind $\mathbf{V} = (V, 0, 0)$ (Scorer 1978). The first

terms on the right hand side of (2) and (3) represent the exchange between semi-streamwise and semi-crosswise vorticity as parcels change direction in the horizontal plane (Scorer 1978). Although these terms do not alter the magnitude of vorticity, they are not equal and opposite. The second and third term on the right hand side of (2) and (3) represent the rate of change of semi-streamwise and semi-crosswise vorticity from the stretching and tilting of vortex tubes, and baroclinic vorticity generation, respectively.

These equations can provide more insight into the evolution of rotation than the traditional Cartesian framework, and were evaluated by Adlerman et al. (1999) in the context of near-ground mesocyclogenesis. The calculations in this section are performed similarly, except for some differences in the integration technique (see Appendix A). All trajectory calculations presented are produced from 30 s model data using a 4th-order Runge-Kutta integration technique (e.g. Abramowitz and Stegun 1972) with a time-step of 1 s (in tests, a time-step of 0.5 s showed minimal differences). Parcel quantities (i.e., model variables) are calculated from linear spatial and temporal interpolation of the original three-dimensional history data at scalar points. Derived quantities (e.g., vorticity or the vorticity tendency terms) are first calculated on the Cartesian model grid at scalar points, then linearly interpolated in space and time to the parcel locations. The only exceptions are the exchange terms which must be calculated along trajectories. In all cases, the trajectory calculations are performed with ground-relative winds. Because domain movement was adjusted during the simulation to keep ground-relative storm motion minimal and integration times are short, *these trajectory calculations are approximately storm relative*. In addition, specifying a separate storm motion for each trajectory calculation is somewhat ill-defined for these simulations, since the

occluding mesocyclone and updraft often move in a different direction than those of the next cycle.

Although the integrated three-dimensional trajectories are quite smooth for all of the examples presented, the decomposition into horizontal forcing terms (i.e., semi-crosswise and semi-streamwise) became quite error prone for trajectories originating in the tornado cyclone, especially in the early parts of the integration. This is not entirely unexpected, since in strongly curved flow the streamwise and crosswise directions can become ill-defined (e.g., near a stagnation point) and errors are easily introduced in horizontal derivatives, especially changes in Ψ . This problem is magnified in a high-resolution simulation, as areas of maxima and minima in vorticity forcing terms are often 300-500 m in diameter. Indeed, even the horizontal forcing terms in trajectories from the mesocyclone were far noisier and error prone than in the previous coarser resolution simulations of Adlerman et al. (1999). This was not as much of a problem for the vertical decomposition, since the two vertical forcing terms near a lower boundary are usually trivial (i.e., as a parcel moves into a strong updraft, tilting initially dominates; as the parcel trajectory becomes more vertical, stretching dominates).

Although more accurate integration and interpolation techniques were attempted (see Appendix A) no significant improvement was noted. The most likely technique to improve the results would be the use of history files with higher time resolution, probably on the order of 5 s or less (unfortunately, this would necessitate a minimum four-fold increase in the size of the dataset). In light of these limitations, backward parcel trajectories for the *tornado cyclones* will focus on the source and evolution of parcels, rather than on the semi-streamwise and semi-crosswise forcing terms. In all cases, multiple examples of the trajectory integration are shown to demonstrate sensitivities to initial parcel location.

4.5.2 Mesocyclogenesis Trajectories

Because a detailed description of the stages of cycle "C" is presented in Section 4.4, we first examine mesocyclogenesis for this cycle. Figure 4.5.1 displays two-dimensional horizontal projections of a rectangular group of parcels integrated backward from a location centered on the initial mesocyclone of cycle "C." Parcels are started at 9600 s from a height of 200 m, are spaced 100 m apart, and are integrated backward for 10 minutes. Ten squares of diameter 0.8 through 2.6 km are used, four of which are shown. Parcels are color-coded such that the eastern, northern, western and southern parcels are designated by yellow, red, green, and blue, respectively.

Figure 4.5.1 shows two main source regions for parcels entering the near-ground mesocyclone. A three-dimensional perspective of these trajectories is shown in Figure 4.5.2. The first source region is centered to the northwest of the mesocyclone, consisting of parcels that descend toward the surface through the developing RFD (Fig. 4.4.1) from heights of 200-700 m, and then rise back up into the developing mesocyclone. The second major region consists of parcels from the east and northeast which start out between 0-150 m above the ground and travel nearly horizontally before rising into the mesocyclone. A less significant third source region exists, consisting of parcels which travel near the surface within the RFD, east of the strongest rainwater values, then rise up into the mesocyclone (Fig. 4.5.2, red, yellow, and blue parcels farthest to the southwest). In the smaller initial trajectory boxes (Fig.4.5.2, left, green and red), there also are a few parcels which travel within small-scale downdrafts behind the gust-front and are recirculated into the mesocyclone.

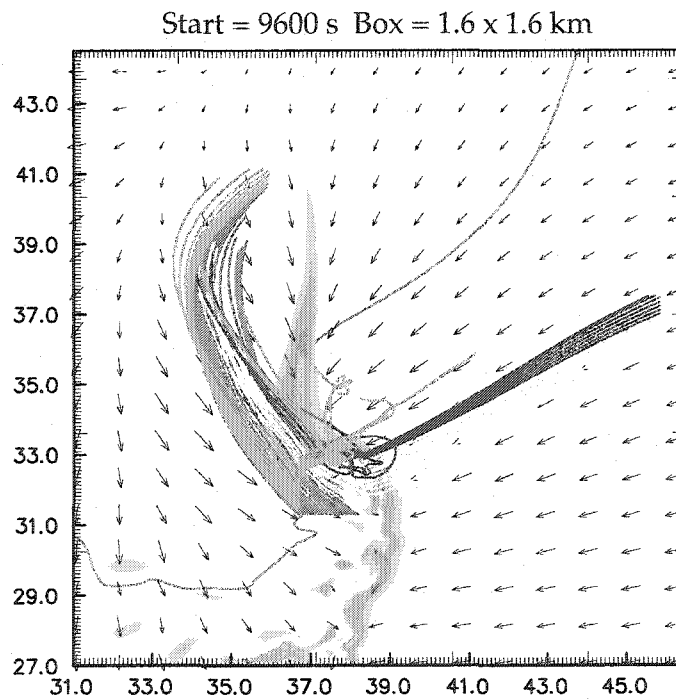
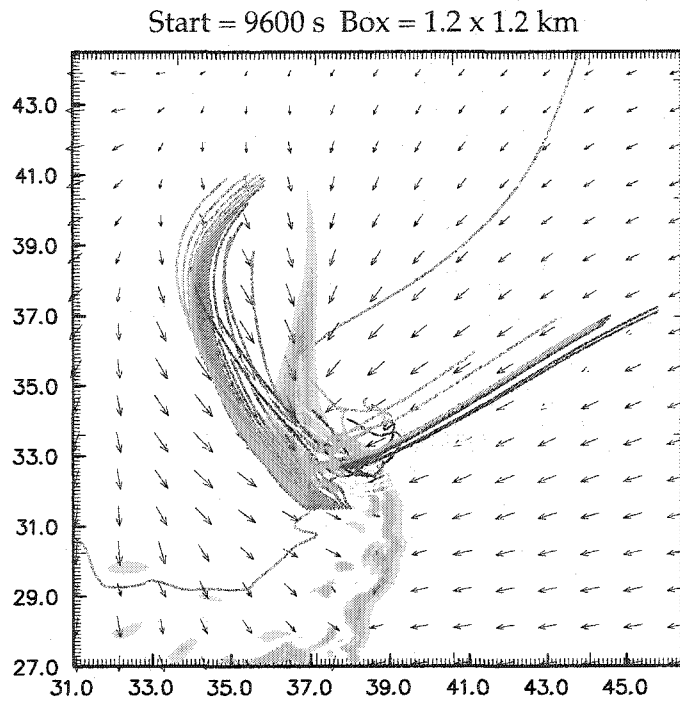
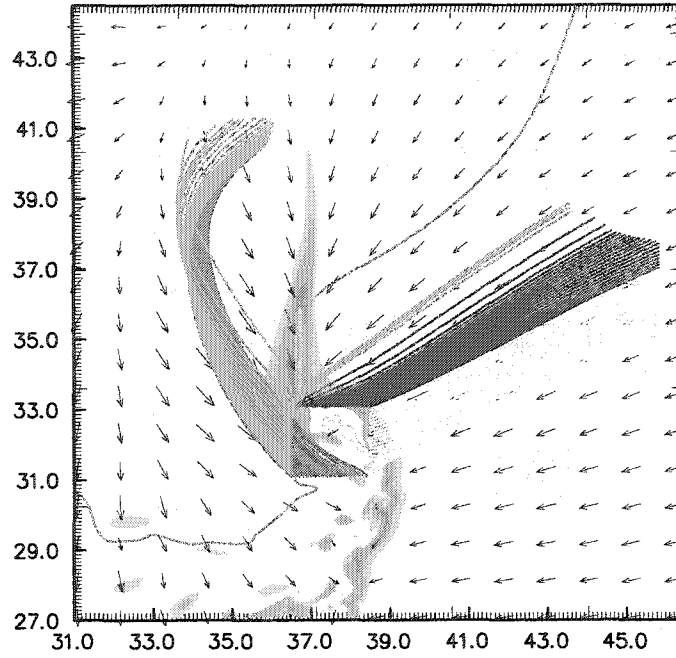


Figure 4.5.1a: Projection of three-dimensional backward trajectories toward the new near-ground mesocyclone of cycle "C". Parcels started from $z = 200$ m and were integrated from $t = 9600$ to 9000 s, initially spaced 100 m apart. Initial diameter of box indicated on each plot. Background depicts vertical velocity and 1 g kg^{-1} rainwater contour at $z = 30$ m at 9600 .

Start = 9600 s Box = 2.0 x 2.0 km



Start = 9600 s Box = 2.6 x 2.6 km

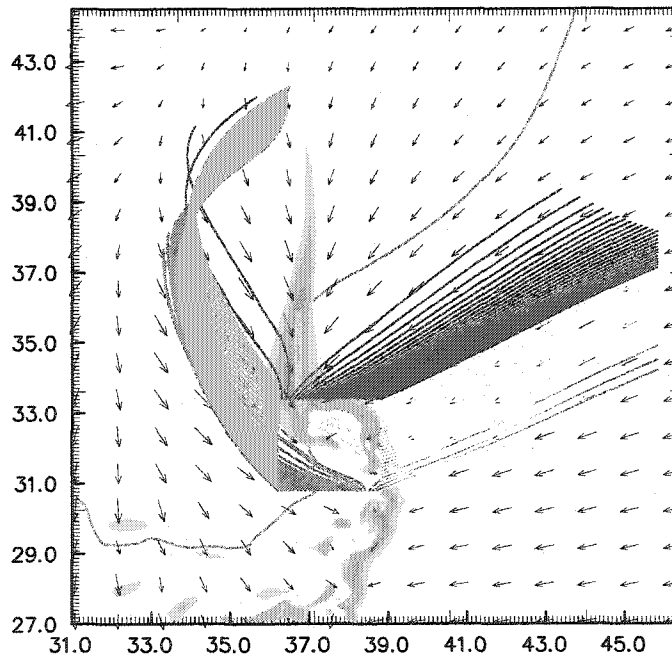


Figure 4.5.1b: As in 4.5.1a, except for box sizes of width 2.0 and 2.6 km.

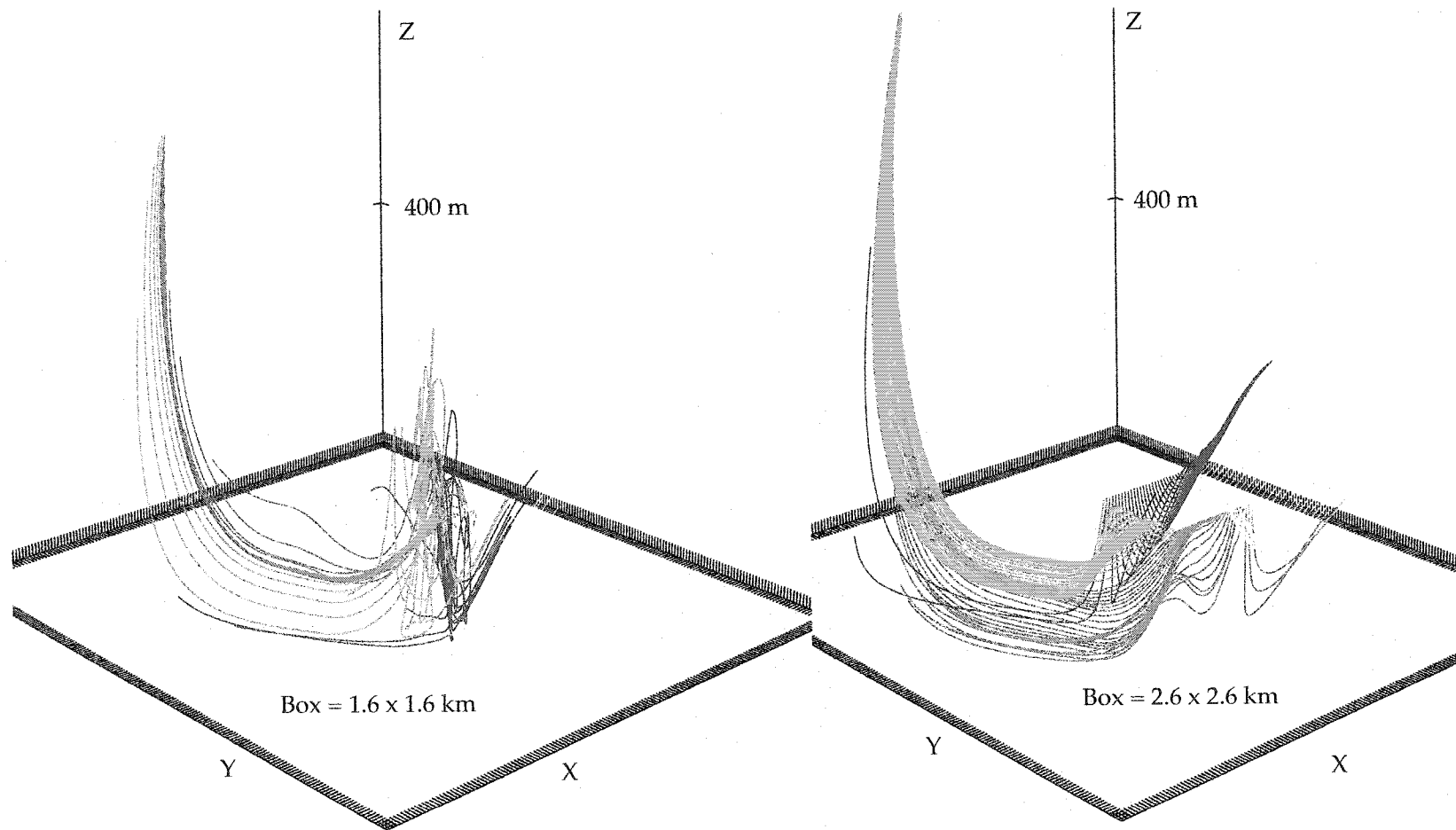


Figure 4.5.2: Three-dimensional perspective of the backward trajectories shown in Figure 4.5.1, toward the near-ground mesocyclone of cycle "C". Parcels were started from $z = 200$ m and were integrated from $t = 10620$ to 10140 s, initially spaced 50 m apart.

We first examine two parcels from the green source region of the 2.6 km diameter square (Fig. 4.5.1b). Most of the blue parcels have similar histories, usually descending from a slightly lower height. Figure 4.5.3 shows the history of a parcel on the southwest outer periphery of the mesocyclone. The parcel descends for approximately 300 s, during which time the vertical vorticity initially decreases as environmental vortex lines are tilted downward, but then increases slightly as the parcel reaches its nadir. The parcel then travels horizontally for about 125 s, after which it rises into the mesocyclone with increasing vertical vorticity. A parcel from the northwest corner of the mesocyclone behaves similarly (Fig. 4.5.4), although the decrease and subsequent increase of vertical vorticity during descent is less obvious as a result of the larger values of vorticity present. This increase of vertical vorticity during parcel descent was observed in several other studies (Davies-Jones and Brooks 1993; Adlerman et al. 1999) and suggests that vortex lines are being turned upward during descent from a combination of tilting and baroclinic generation (Davies-Jones and Brooks 1993; Davies-Jones et al. 2001). However, compared with the trajectories shown in Adlerman et al. (1999, Fig. 9), this effect is not as prominent. The other descending trajectories show similar tendencies.

The evolution of the three components of vorticity and its total magnitude are shown in Figure 4.5.5 for the same two parcels described above. At the beginning of the descent, both parcels have most of their total vorticity contained in the semi-streamwise and semi-crosswise components. In both parcels, semi-streamwise vorticity increases during the entire descent and becomes the dominant component, while semi-crosswise vorticity decreases before the parcel reaches its nadir. Therefore, during descent, the vortex lines become increasingly parallel to the direction of parcel motion.

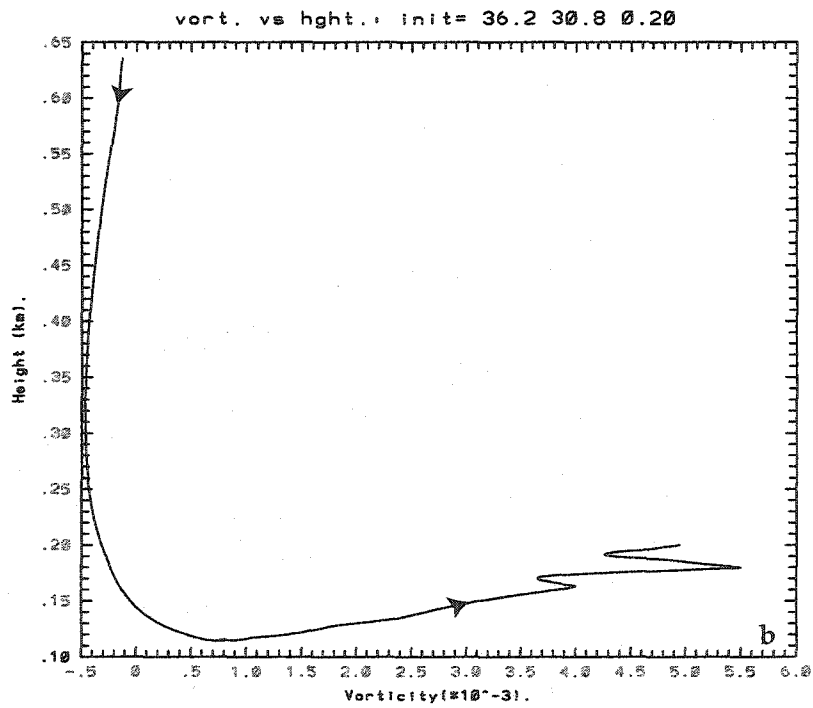
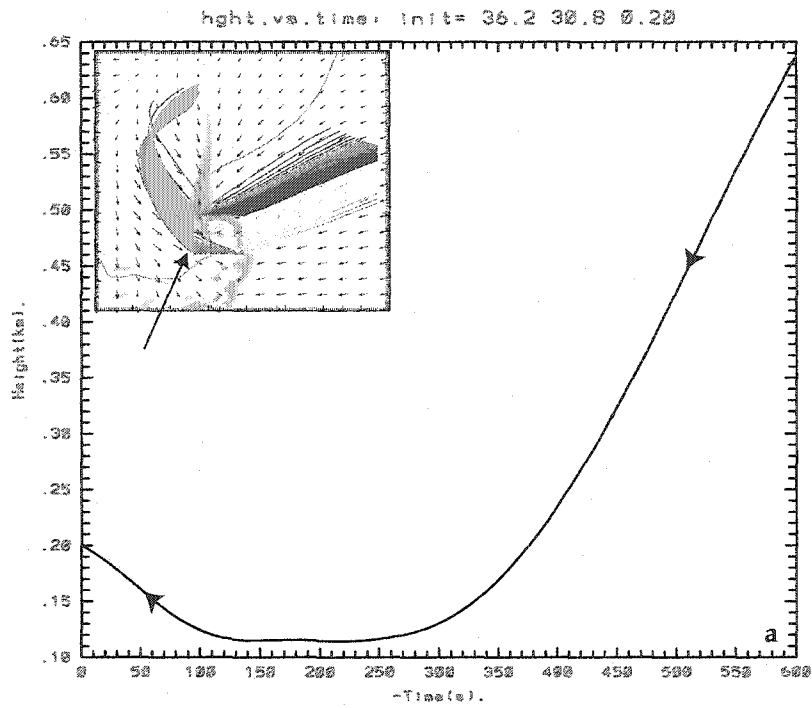


Figure 4.5.3: a) Time (s) vs. height (km) plot of a parcel originating at the SW-corner of the initial trajectory rectangle in Fig. 4.5.1b (bottom). b) Vertical vorticity ($\times 10^{-3} \text{ s}^{-1}$) vs. height plot of the same parcel as in (a).

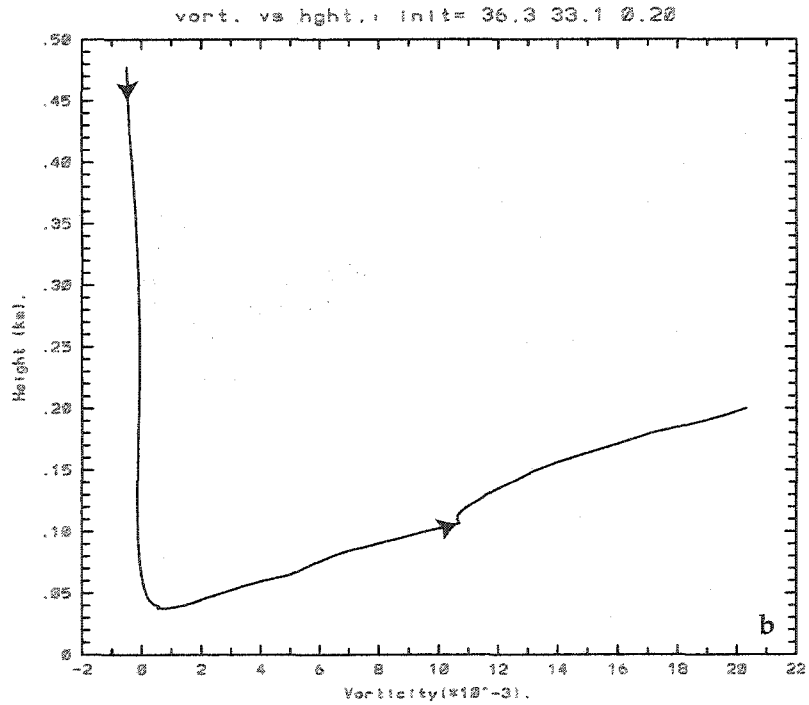
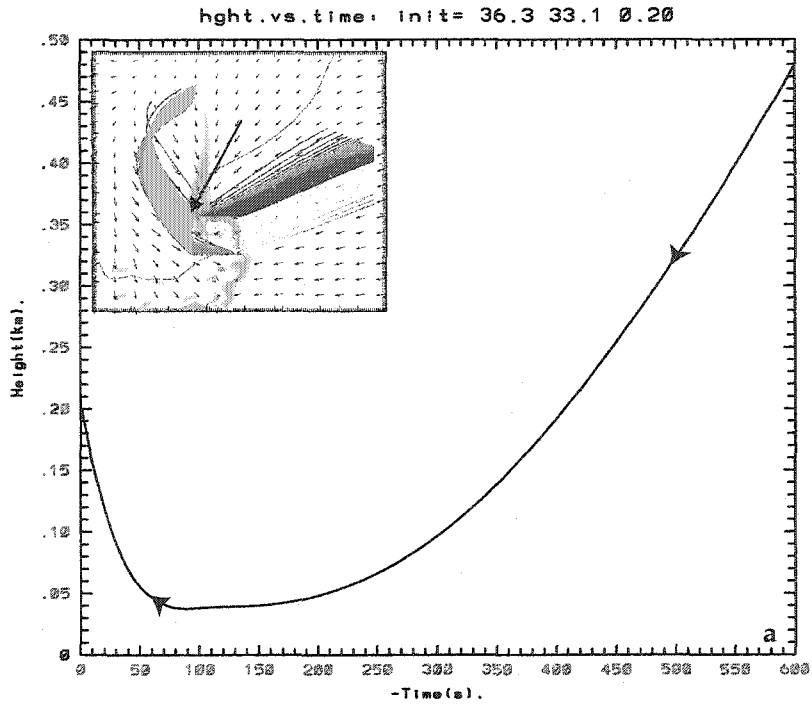


Figure 4.5.4: a) Time (s) vs. height (km) plot of a parcel originating at the NW-corner of the initial trajectory rectangle in Fig. 4.5.1b (bottom). b) Vertical vorticity ($\times 10^{-3} \text{ s}^{-1}$) vs. height plot of the same parcel as in (a).

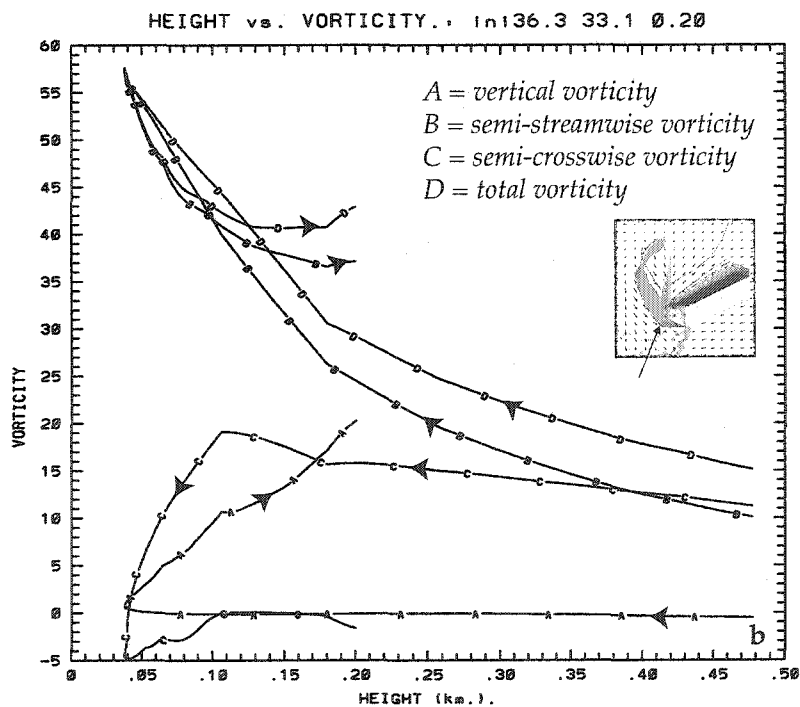
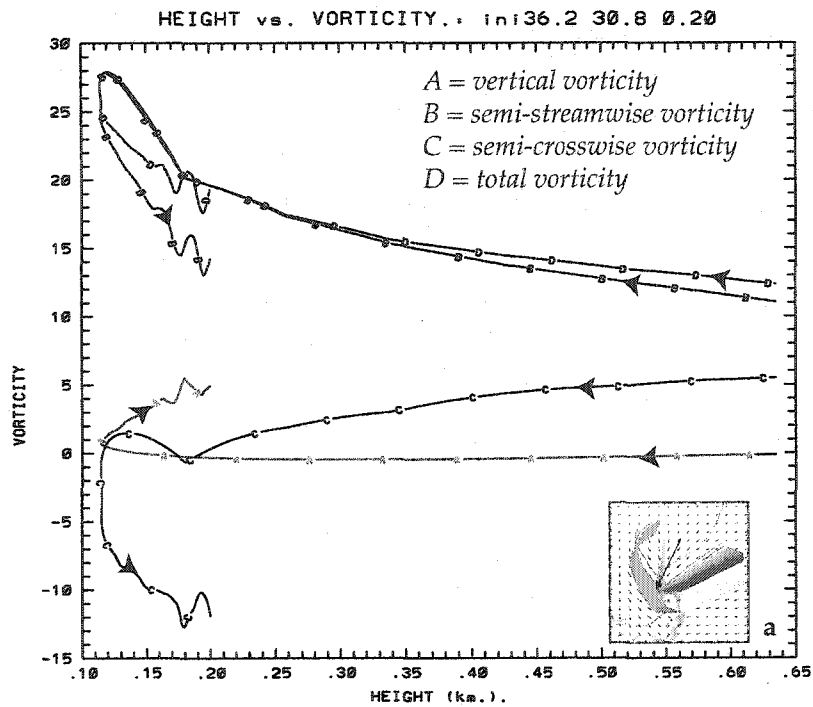


Figure 4.5.5: a) Vorticity ($\times 10^{-3} \text{ s}^{-1}$) vs. height (km) plot of the same parcel as in Fig. 4.5.3 b) Same as (a), except for the parcel in Fig. 4.5.4.

During the final part of the descent, vertical tilting of horizontal vorticity (not shown) increases from near zero to approximately $1 \times 10^{-5} \text{ s}^{-2}$, and vertical vorticity begins to increase slightly (Fig. 4.5.5). Once the parcel passes its nadir, vertical stretching dominates as it begins to rise into the mesocyclone. The main difference in the final values of vertical vorticity achieved by the parcels is a result of small-scale variations in the stretching term within the mesocyclone, which ranges from $2.0 \times 10^{-5} \text{ s}^{-2}$ for the parcel from the southwest corner to $52 \times 10^{-5} \text{ s}^{-2}$ for the parcel from the northwest corner.

In order to determine the source of horizontal vorticity that eventually is tilted and stretched into the vertical, we consider the forcing terms in the semi-streamwise and semi-crosswise equations (Eqns. 2-3) for the parcel from the northwest corner (Fig. 4.5.6). Initially (from 0.64-0.35 km, ~ 150 s), the semi-streamwise exchange and baroclinic generation terms dominate the semi-streamwise component, while semi-crosswise exchange dominates the semi-crosswise component, with tilting and baroclinic generation playing a smaller role. Thus, as the parcel begins its descent, most of the semi-streamwise vorticity is generated by baroclinity and by the exchange from the semi-crosswise component as the parcel curves cyclonically through the downdraft. Stretching in the semi-crosswise direction (i.e. toward the updraft) also helps to generate vorticity that can be exchanged.

As the parcel descends farther (0.35-0.10 km), semi-streamwise exchange decreases as the trajectory becomes less curved (Fig. 4.5.6). Semi-streamwise baroclinic generation remains steady, while semi-crosswise baroclinic generation becomes negative, suggesting that the trajectories now cross a buoyancy gradient toward higher values (i.e., eastward, pointing toward the updraft and away from the

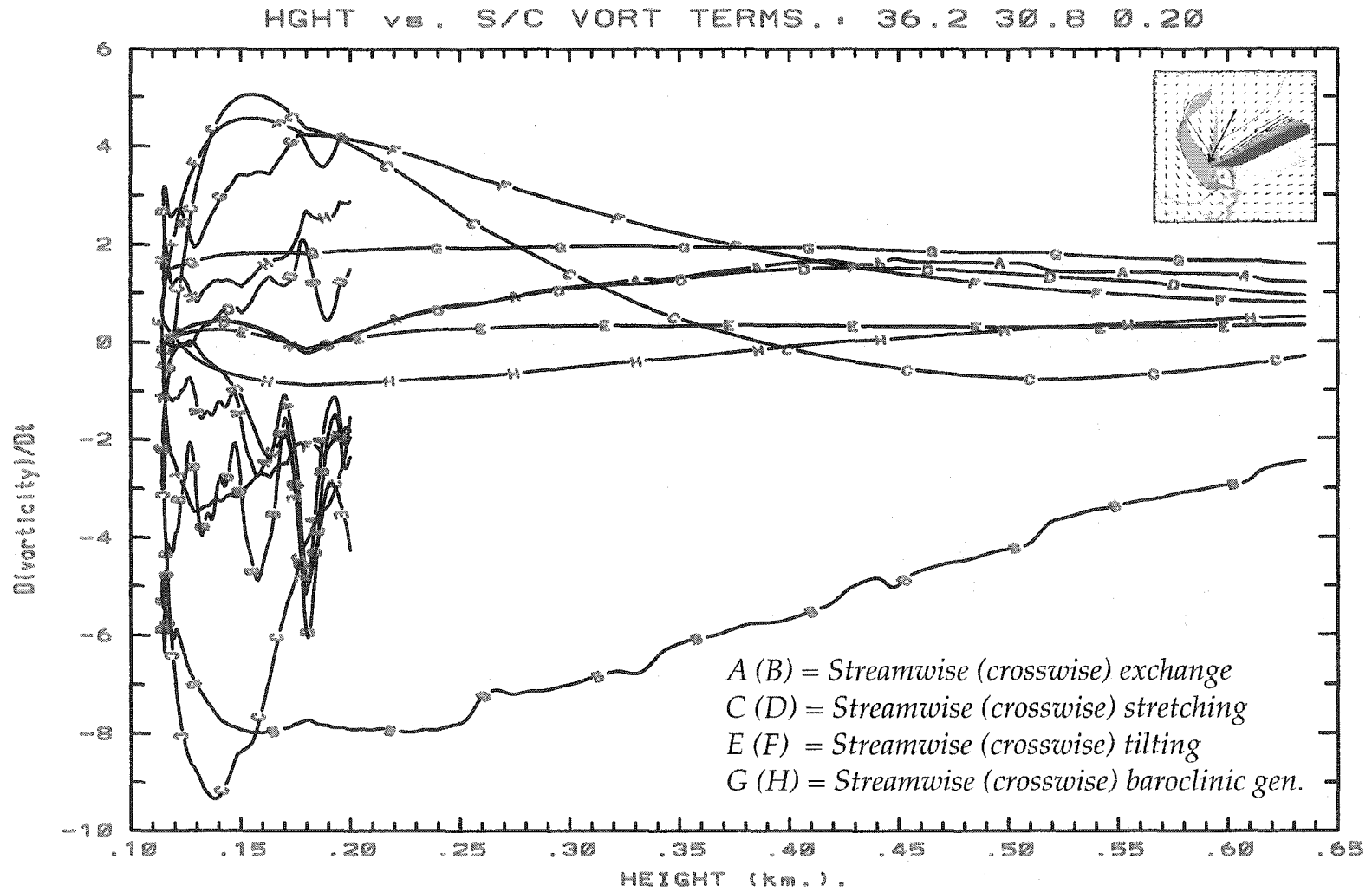


Figure 4.5.6: a) Terms in the semi-streamwise and semi-crossorticity vorticity equations ($\times 10^{-5} \text{ s}^{-2}$) vs. height (km) for the same parcel as in Fig. 4.5.3.

cooler downdraft) rather than the opposite. At this time, stretching in the semi-streamwise direction becomes the dominant effect before the parcel reaches its nadir.

In summary, for parcels which descend into the mesocyclone on its western and southern side, most of the semi-streamwise vorticity that is tilted and stretched into the vertical arises from three sources: exchange from the semi-crosswise direction, baroclinic generation, and stretching in the semi-streamwise direction as the parcel accelerates into the mesocyclone. There exists quite a bit of variation among parcels in the magnitude of the exchange terms as a result of differently curved trajectories, but in all cases, *baroclinic generation is present throughout most of the descent and semi-streamwise stretching eventually dominates*. Although there exist some small differences, this result is quite similar to that described in Adlerman et al. (1999).

Most parcels from the eastern source regions have relatively similar trajectories, usually moving nearly horizontally before they rise into the mesocyclone. Those on the northern border (red) would seem to be more important because they contribute to positive circulation around the square in the domain's reference frame, while those on the eastern side (yellow) contribute to negative circulation. One such parcel from the northwest corner is shown in Figure 4.5.7. For most of the trajectory (before the parcel begins its upward motion), vertical vorticity remains near zero (Fig. 4.5.7a). Initially, most of the horizontal vorticity is split evenly between the semi-crosswise and semi-streamwise components (Fig. 4.5.7c). Thus, the horizontal vorticity lies approximately 45 degrees to the left of the initial parcel motion. As the parcel approaches the mesocyclone, semi-streamwise vorticity increases until the vorticity is tilted into the vertical and then stretched. Decomposition of the horizontal forcing terms shows that most of this increase is a result of semi-streamwise baroclinic generation along the weak forward-flank

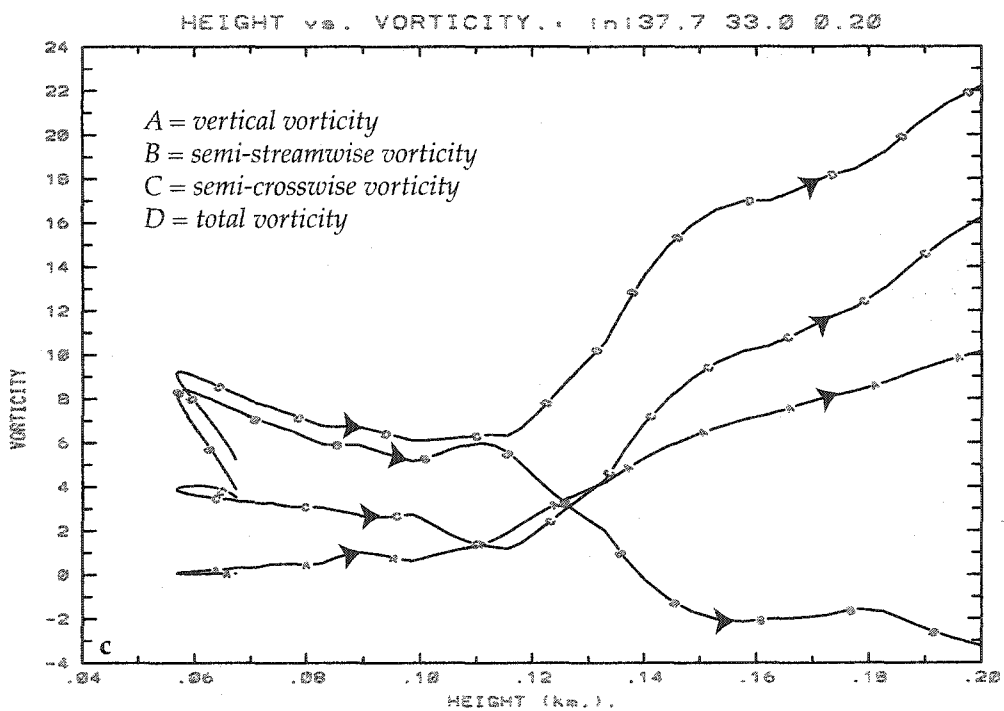
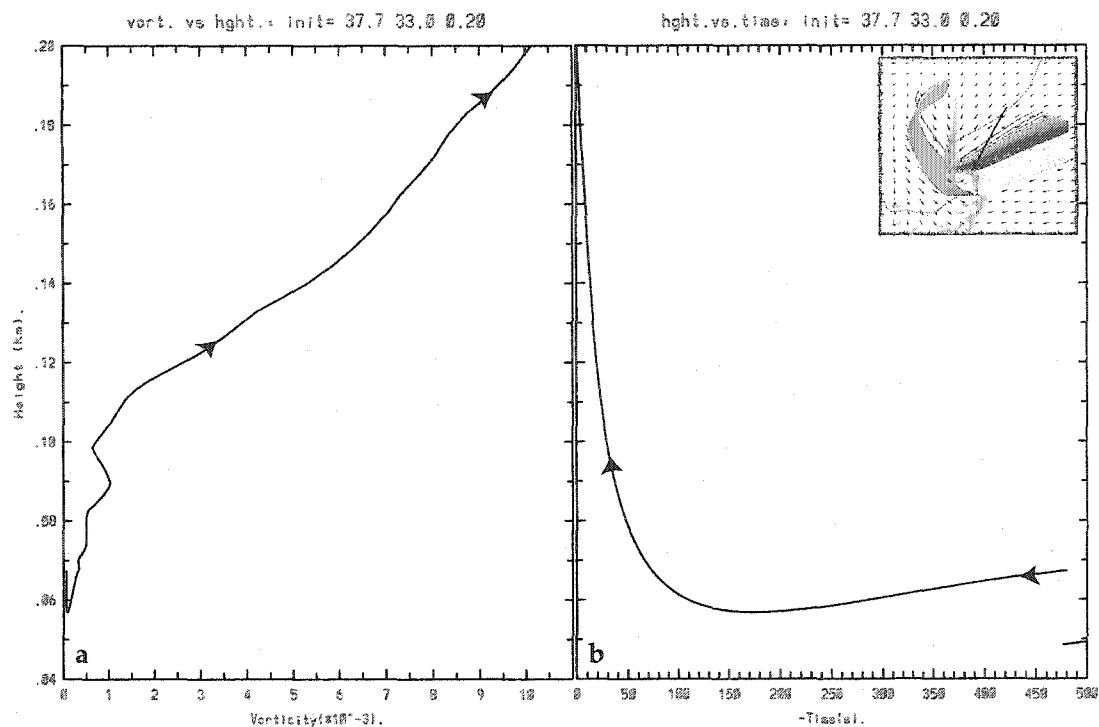


Figure 4.5.7: a) Vertical vorticity ($\times 10^{-3} \text{ s}^{-1}$) vs. height (km) plot of a parcel originating at the NE-corner of the initial trajectory rectangle in Fig. 4.5.1b (bottom). b) Time (s) vs. height (km) of the same parcel as in (a). c) Vorticity ($\times 10^{-3} \text{ s}^{-1}$) vs. height (km) plot of the same parcel as in (a).

precipitation gradient (Fig. 4.4.1d) to the northeast of the mesocyclone. Stretching in the semi-streamwise direction plays a secondary role. Parcels on the eastern side of the mesocyclone (yellow) have very similar trajectories to those of the north (red), except that baroclinic generation is usually smaller due to the absence of buoyancy gradients ahead of the storm. Most of the initial vorticity is semi-streamwise and appears to be environmental.

Although the evolution of the northern (red) parcels is similar to that described in Adlerman et al. (1999), the evolution of the eastern (yellow) parcels is different because most of the initial vorticity appears to be environmental and semi-streamwise. This results from a cold pool and associated gust front, the latter of which was oriented differently compared to that in the current simulation. Specifically, in Adlerman et al. (1999), the initial storm was more outflow-dominant and the gust front extended farther northeast from the developing mesocyclone (see Figure 8). Therefore, parcels that approached from the east passed through an environment in which the local vertical wind structure was altered and most of the vorticity was semi-crosswise.

Having described in detail the mesocyclogenesis mechanism for cycle "C", we now briefly examine mesocyclogenesis trajectories for the following cycle "D." Figure 4.5.8 displays the two-dimensional horizontal projections of a rectangular group of parcels integrated backward from a location centered on the initial mesocyclone of cycle "D." Parcels are started at 10980 s from a height of 200 m, are spaced 100 m apart, and are integrated backward for 8 minutes. Ten squares of diameter 0.6 through 2.4 km are used, four of which are shown. A three-dimensional perspective is given in Figure 4.5.9.

Because the development of the near-ground mesocyclone associated with cycle "D" occurs while the near-ground mesocyclone of cycle "C" is approximately 5

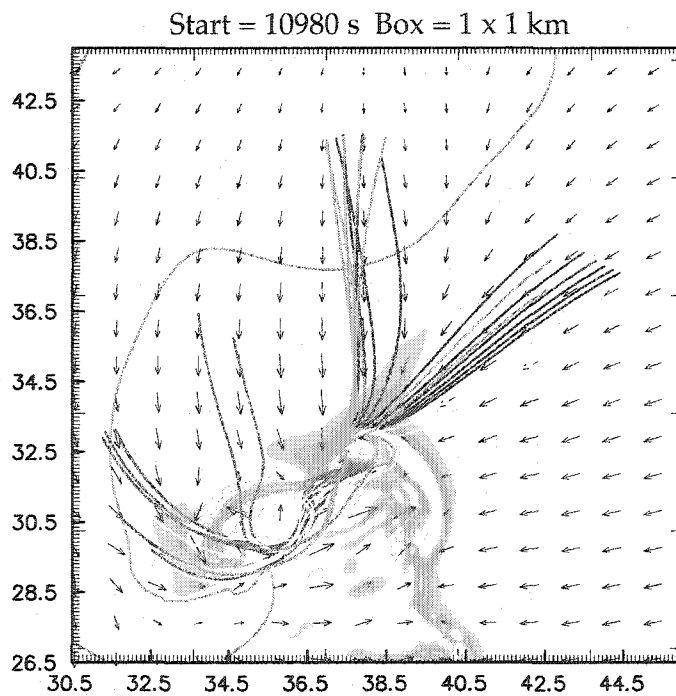
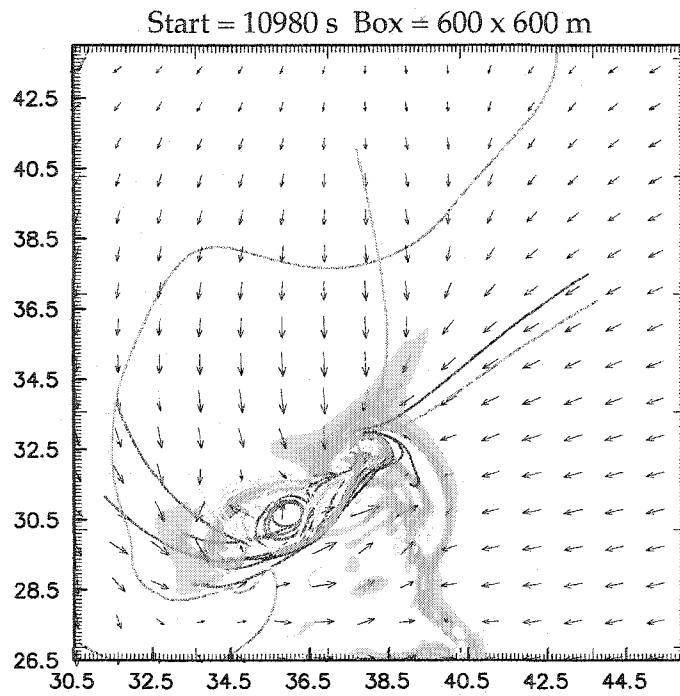


Figure 4.5.8a: Projection of three-dimensional backward trajectories toward the new near-ground mesocyclone of cycle "D". Parcels started from $z = 200$ m and were integrated from $t = 10980$ to 10500 s, initially spaced 100 m apart. Initial diameter of box indicated on each plot. Background depicts vertical velocity and 1 g kg^{-1} rainwater contour at $z = 30$ m at 10980.

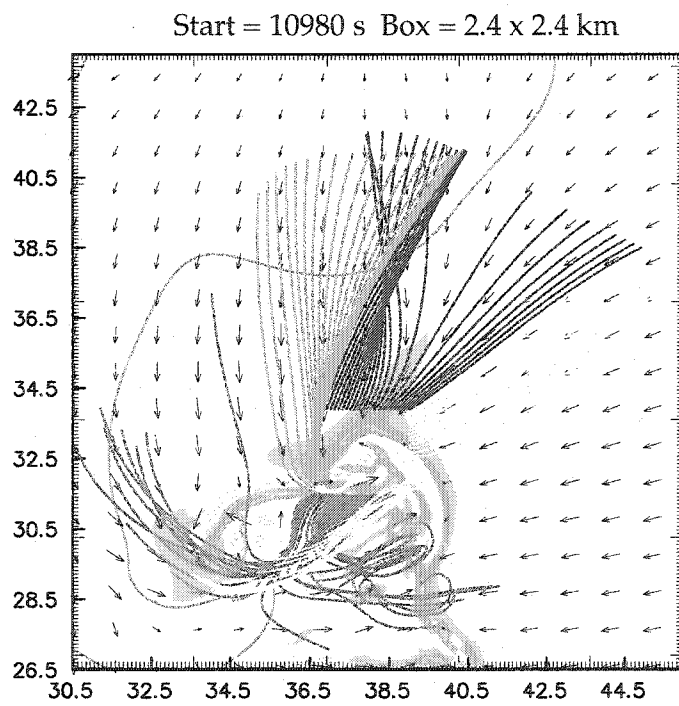
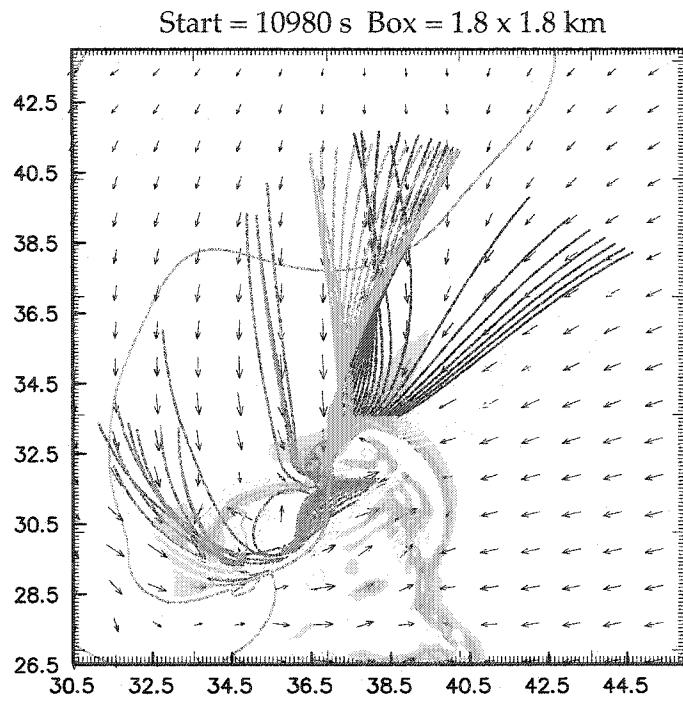


Figure 4.5.8b: As in 4.5.8a, except for box sizes of width 1.8 and 2.4 km.

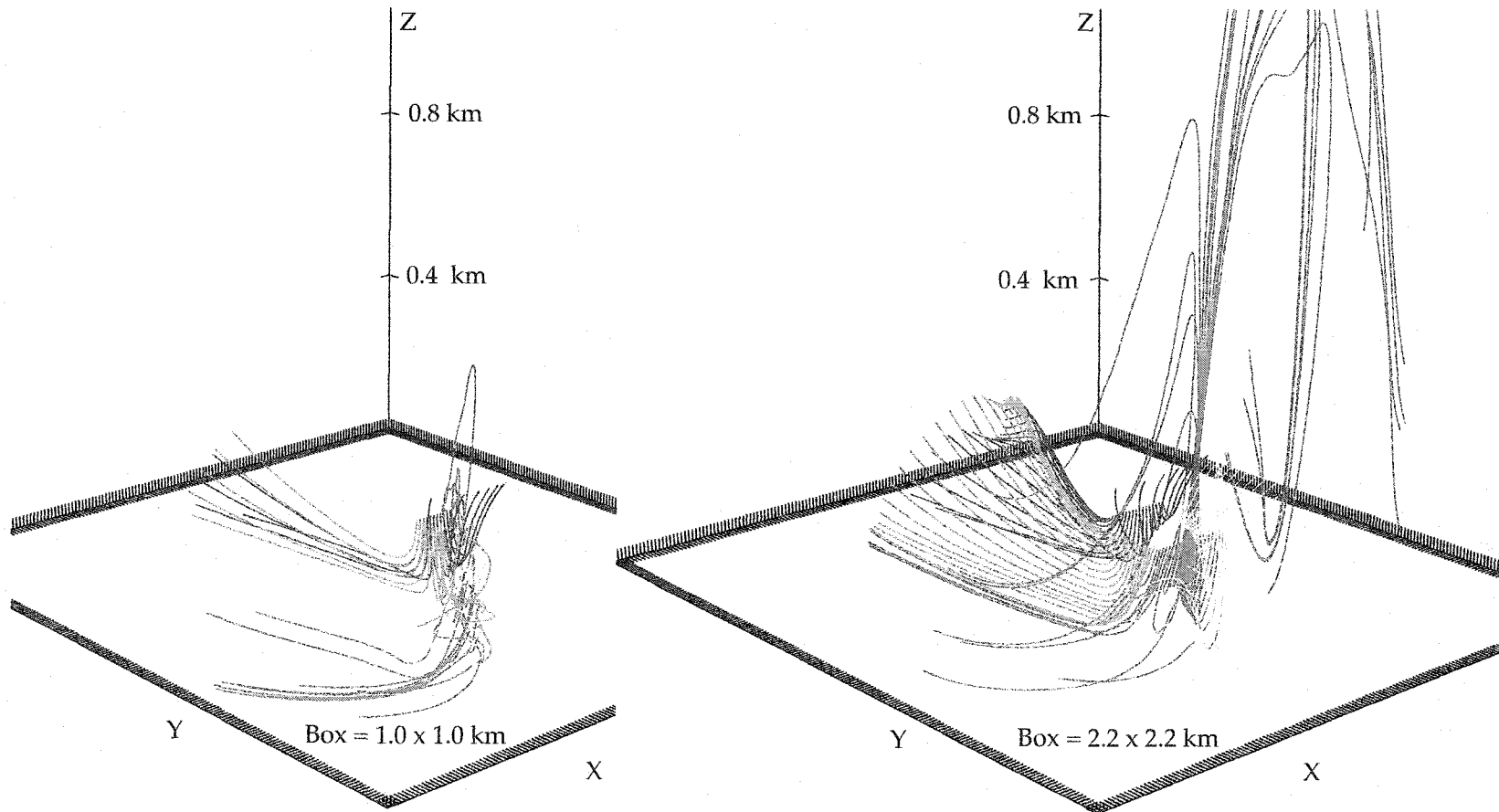


Figure 4.5.9: Three-dimensional perspective of the backward trajectories shown in Figure 4.5.8, toward the new near-ground mesocyclone of cycle "D". Parcels were started from $z = 200$ m and were integrated from $t = 10980$ to 10500 s, initially spaced 100 m apart.

km to the southwest, the parcel histories are quite different from those of the previous cycle. We can roughly divide the source regions into three areas. First are parcels which originate to the northeast of the developing mesocyclone (yellow and red). They start out between 10-100 m above the surface and move nearly horizontally before rising into the developing mesocyclone. Their dynamics are very similar to those of the northern and eastern parcels described for cycle "C", including travel through a zone of enhanced baroclinic generation to the northeast.

The second source region for parcels in cycle "D" is to the north (green and red) of the developing mesocyclone (Fig. 4.5.8). Those with more cyclonically curved trajectories originate at levels between 100-300 m and descend toward the ground before they rise back up into the mesocyclone. Those parcels whose trajectories are nearly straight, or have a slight anticyclonic curvature, tend to originate below 100 m and travel nearly horizontally before they rise into the new mesocyclone. Many of these parcels have most of their vorticity in the semi-streamwise component. Depending on their history and amount of curvature, either the semi-streamwise exchange and baroclinic generation terms dominate, or the semi-streamwise exchange and stretching terms dominate. In general, the history of these parcels is fairly similar to that of the western and southern (green and blue) parcels in the previous cycle.

Parcels from the third region include those from the southwest and south (yellow and blue), and they have the most complex evolution. Those from the southwest tend to originate at heights of between 0-300 m and travel through the occluding circulation of cycle "C", especially those which are started from the centermost part of the developing mesocyclone (Fig. 4.5.8a). Parcels that move from the south (mostly blue, Fig. 4.5.b) tend to originate at higher levels, from 300-900 m, and descend through the strong occlusion downdraft and RFD of the previous cycle.

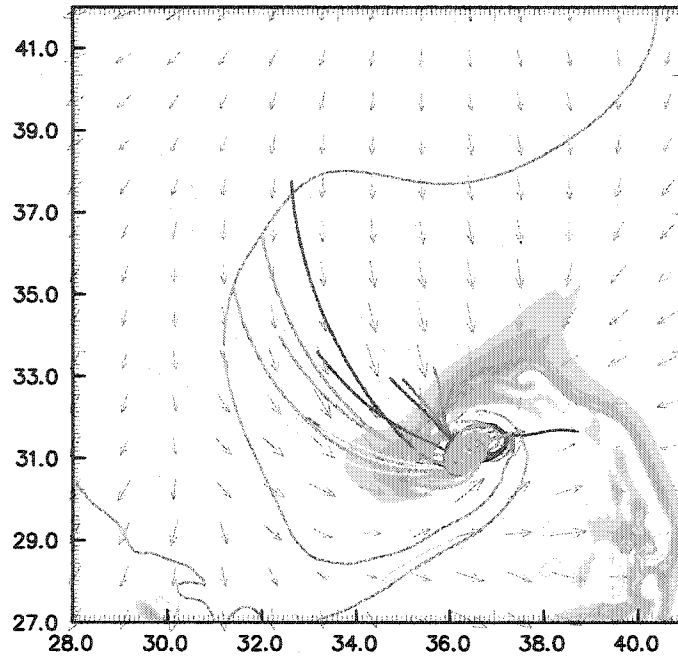
In essence, both sets of parcels are “recycled” through the old occlusion into the new. Their parcel histories cannot be generalized other than to say that they tend to contain substantial quantities of both positive and negative vorticity. It is interesting to note that in this case, more than 75% of the parcels appear to contribute to positive circulation around the square (Fig. 4.5.8b), slightly more than in the previous cycle (Fig. 4.5.1b).

In summary, the trajectories suggest that the mode of mesocyclogenesis depends upon the position of the new mesocyclone with respect to that of the previous cycle. When the new mesocyclone is fairly isolated and the storm structure resembles that of “young” supercell (i.e., in its first cycle, with a surface pattern similar to Fig. 4.4.1), mesocyclogenesis proceeds in a fashion similar to that described in Adlerman et al. (1999). When the new mesocyclone develops quickly after the previous cycle and the surface pattern reflects this (i.e., the presence of two hooks, two strong near-ground circulations along the gust front), the evolution will be more complex, with the occluding mesocyclone most likely contributing to the formation of the next cycle.

4.5.3 Tornadogenesis Trajectories

Having examined two examples of trajectories integrated backward from the mesocyclone, we now briefly examine the trajectories associated with two instances of tornadogenesis in cycles “C” and “B.” Figure 4.5.10 displays the two-dimensional horizontal projections of a rectangular group of parcels integrated backward from a location centered on the tornado of cycle “C” at its peak intensity (corresponding with Figure 4.4.5). Parcels are started at 10620 s from a height of 200 m, are spaced 50 m apart, and are integrated backward for 8 minutes. Ten squares of diameter 0.2 through 2.0 km are used, four of which are shown. A three-dimensional projection

Start = 10620 s Box = 200 x 200 m



Start = 10620 s Box = 600 x 600 m

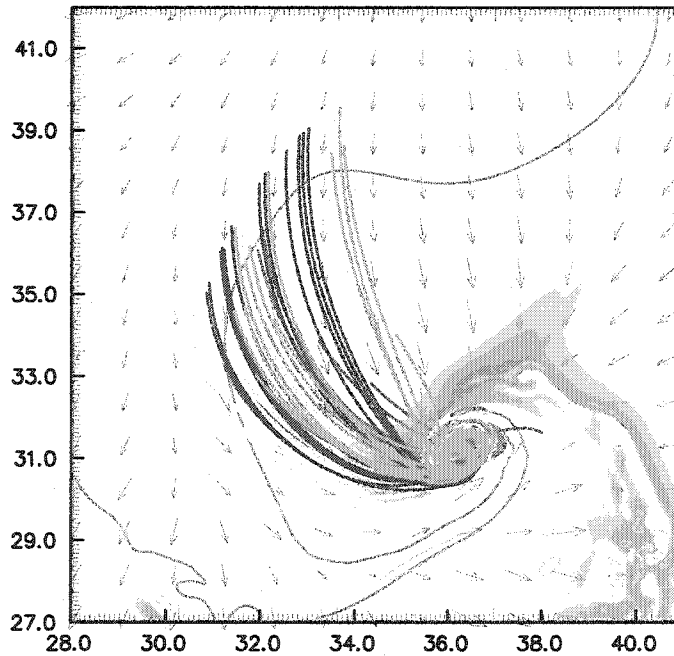
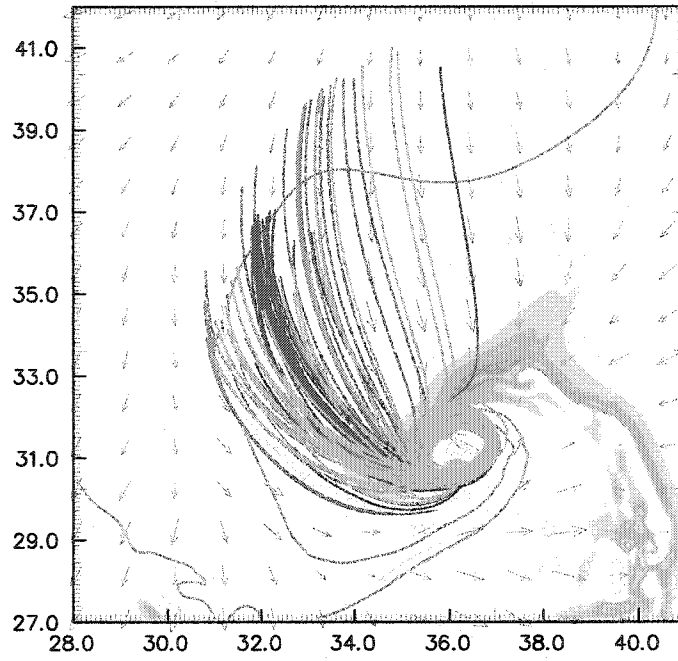


Figure 4.5.10a: Projection of three-dimensional backward trajectories toward the tornado cyclone of cycle "C". Parcels started from $z = 200$ m and were integrated from $t = 10620$ to 10140 s, initially spaced 50 m apart. Initial diameter of box indicated on each plot. Background depicts vertical velocity and 1 g kg^{-1} rainwater contour at $z = 30$ m at 10620.

Start = 10620 s Box = 1.4 x 1.4 km



Start = 10620 s Box = 2.0 x 2.0 km

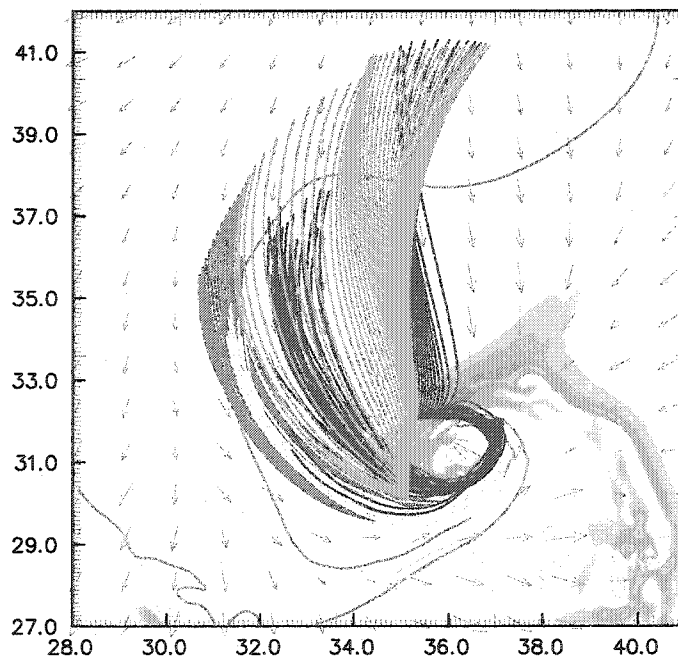


Figure 4.5.10b: As in 4.5.10a, except for box sizes of width 1.4 and 2.0 km.

of the trajectories is shown in Figure 4.5.11 and some cross-sections at the initial time are shown in Figure 4.5.12.

Although the parcels all appear to come from similar source regions (Figs. 4.5.10a,b), the three-dimensional plot (Fig. 4.5.11) shows that large differences are evident based upon the initial size of the square. Parcels started within and close to the tornado cyclone itself (Fig. 4.5.10a, 4.5.11 left) originate from very low levels, usually below 75 m, while those closest to the center (the 200 x 200 m square) originate below 30 m.

The history of one such center parcel is shown in Figure 4.5.13. This parcel is located on the eastern side of the tornado cyclone (yellow) on the 300 x 300 m trajectory box, and it originates near coordinates $x = 32.0$, $y = 33.0$. As the parcel travels horizontally toward the developing tornado, all of its vorticity is in the semi-streamwise component and already is quite large ($50 \times 10^{-3} \text{ s}^{-1}$). The parcel moves through an area of semi-streamwise baroclinic generation between $2\text{-}5 \times 10^{-5} \text{ s}^{-2}$, and a small increase in semi-streamwise vorticity ($10 \times 10^{-3} \text{ s}^{-1}$) occurs. As soon as the parcel begins to rise upward, vertical stretching of up to 0.015 s^{-2} at $z = 35 \text{ m}$ rapidly increases vertical vorticity to values above 0.2 s^{-1} . At the end of the trajectory, the parcel spirals around the tornado cyclone and undergoes some oscillations in height as it travels near portions of the occlusion downdraft.

As one moves to the outer edges of the tornado cyclone and into the larger overall mesocyclone circulation, two behaviors are evident (Fig. 4.5.11). First, some parcels descend toward the surface from heights of between 50-300 m as they move cyclonically through the intense RFD which has surrounded the mesocyclone. These parcels are very similar to the cyclonically curving parcels which travel through the RFD in previous instances of mesocyclogenesis. A second group of parcels rises quickly into the updraft on the northern and western sides of the tornadic

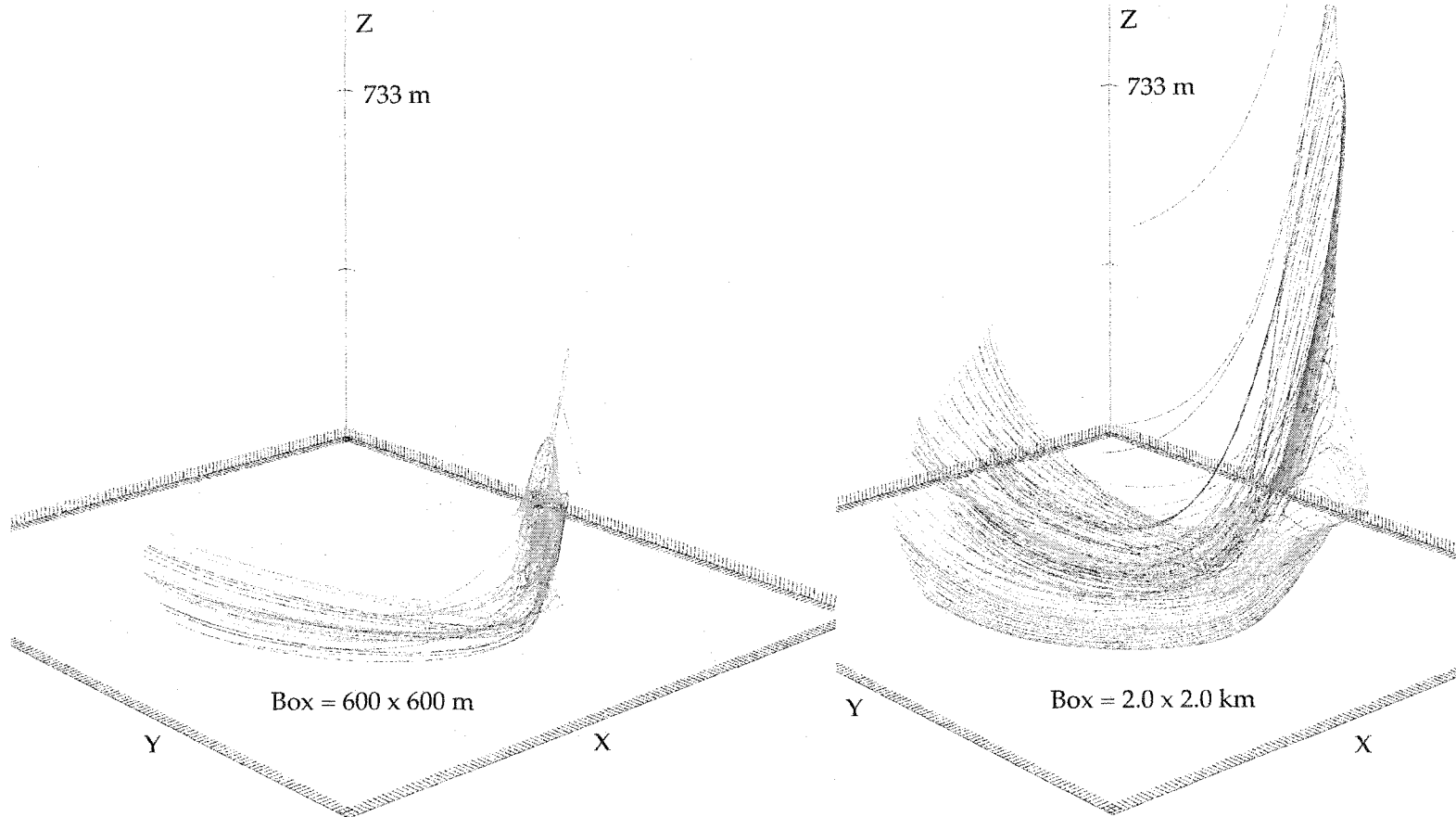


Figure 4.5.11: Three-dimensional perspective of the backward trajectories shown in Figure 4.5.10, toward the tornado cyclone of cycle "C". Parcels were started from $z = 200$ m and were integrated from $t = 10620$ to 10140 s, initially spaced 50 m apart.

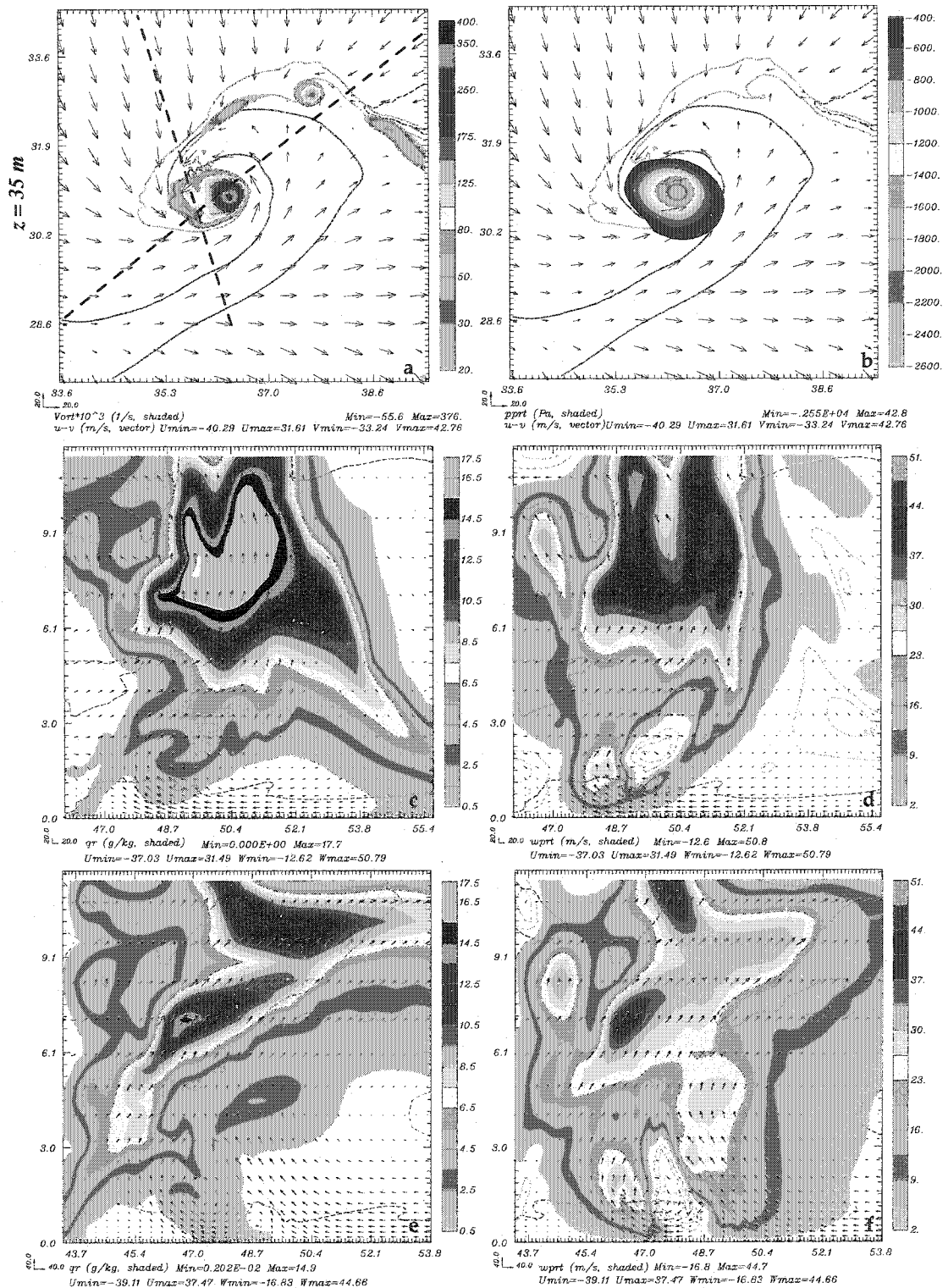


Figure 4.5.12: Horizontal cross-sections at $z = 35$ m of (a) vertical vorticity and (b) perturbation pressure at $t = 10620$ s. Vertical cross-sections of (c) rainwater mixing ratio and (d) vertical velocity on the SE-NW oriented line in (a). Vertical cross-sections of (e) rainwater mixing ratio and (f) vertical velocity on the SW-NE oriented line in (a).

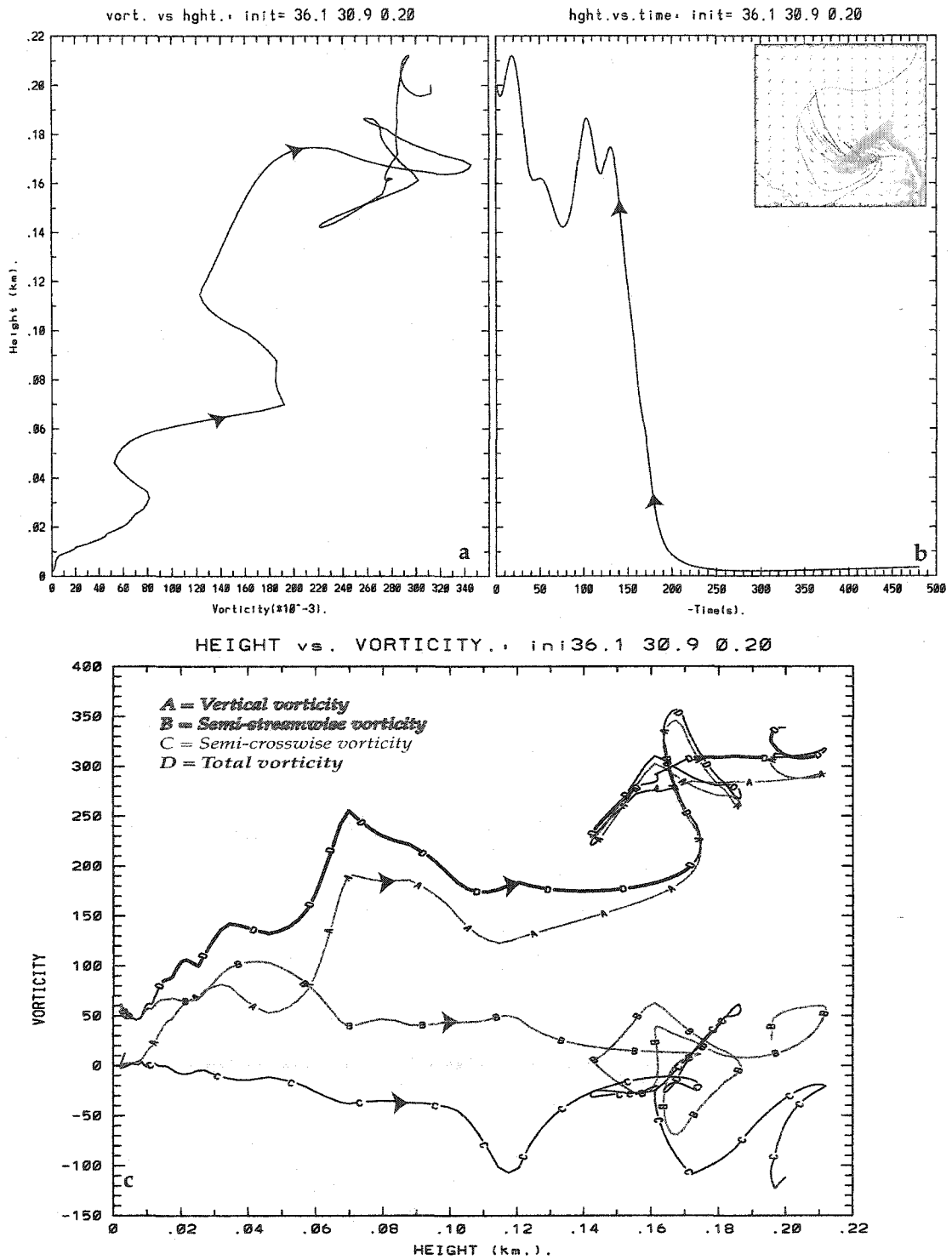


Figure 4.5.13: a) Vertical vorticity ($\times 10^{-3} \text{ s}^{-1}$) vs. height (km) plot of a parcel originating within the tornado circulation in Fig. 4.5.10a (top). b) Time (s) vs. height (km) of the same parcel as in (a). c) Vorticity ($\times 10^{-3} \text{ s}^{-1}$) vs. height (km) plot of the same parcel as in (a).

mesocyclone from levels between 0-900 m up to a maximum of approximately 1.2 km, whereupon they are recirculated back into the occlusion downdraft. Most of these parcels still contain a small amount ($< 0.02 \text{ s}^{-1}$) of positive vertical vorticity when they reach their point of origin at 200 m.

These tornado trajectories are quite different from those described by Wicker and Wilhelmson (1995). In our case, none of the tornado cyclone trajectories come from areas east of the gust front or descend from above 1 km. We do find descending trajectories in the tornadic mesocyclone circulation, but they tend to be recirculated parcels, rather than those of pure descent. However, our trajectories do show a surface baroclinic source region to the northwest of the tornado, similar to that in Wicker and Wilhelmson (1995).

A slightly more complex example of tornadogenesis is exhibited in cycle "B." This tornado forms rapidly at approximately 8340 s in a strongly occluded mesocyclone (Fig. 4.3.1a). Figure 4.5.14 displays the two-dimensional horizontal projections of a rectangular group of parcels integrated backward from a location centered on the tornado at its peak intensity. Parcels are started at 8400 s from a height of 200 m, are spaced 50 m apart, and are integrated backward for 8 minutes. Ten squares of diameter 0.2 through 2.0 km are used, four of which are shown. A three-dimensional projection of the trajectories is shown in Figure 4.5.15.

Parcels started from within the tornado cyclone (Fig. 4.5.14a, top) behave very similarly to those in the tornado of cycle "C." They travel approximately horizontally through a baroclinic zone, starting at heights between 30-70 m. However, unlike the other tornado trajectories, a few parcels within the tornado cyclone (from boxes 200-300 m in diameter) descend in the occlusion downdraft from heights of 650-750 m.

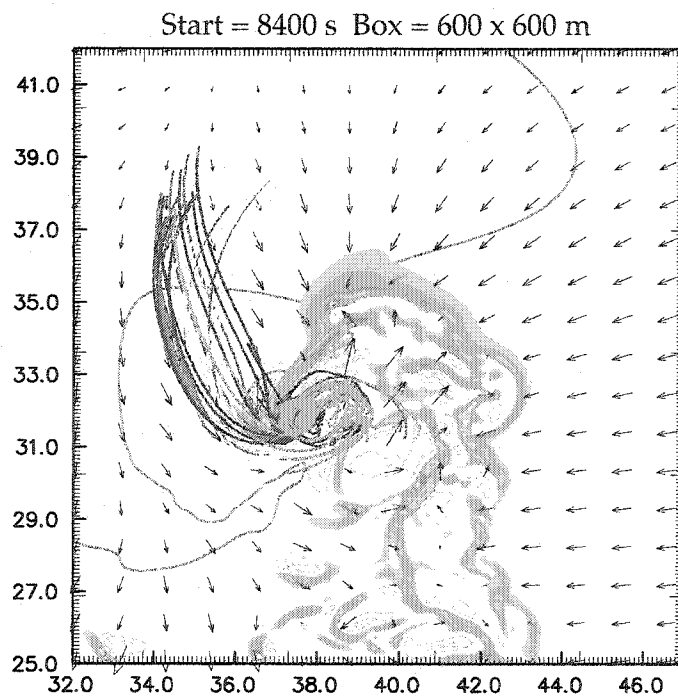
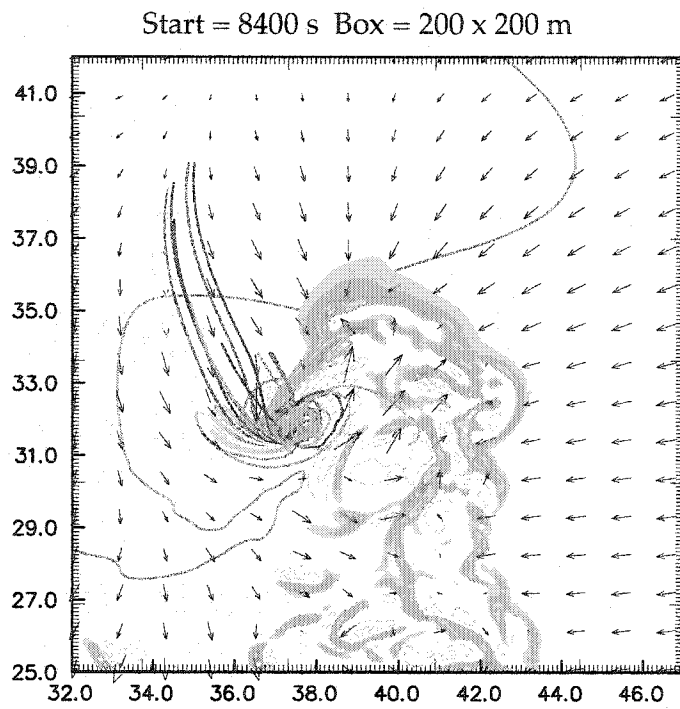
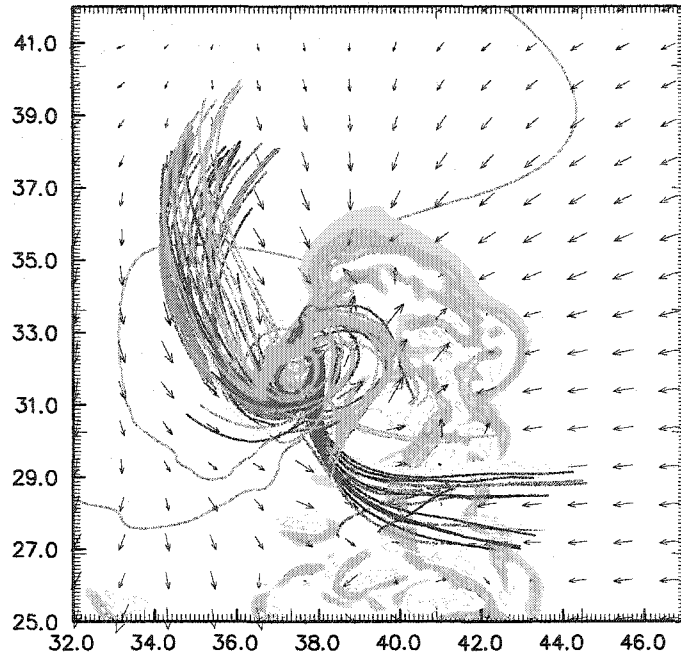


Figure 4.5.14a: Projection of three-dimensional backward trajectories toward the tornado cyclone of cycle "B". Parcels started from $z = 200$ m and were integrated from $t = 8400$ to 7920 s, initially spaced 50 m apart. Initial diameter of box indicated on each plot. Background depicts vertical velocity and 1 g kg^{-1} rainwater contour at $z = 30$ m at 8400 .

Start = 8400 s Box = 1.4 x 1.4 km



Start = 8400 s Box = 2.0 x 2.0 km

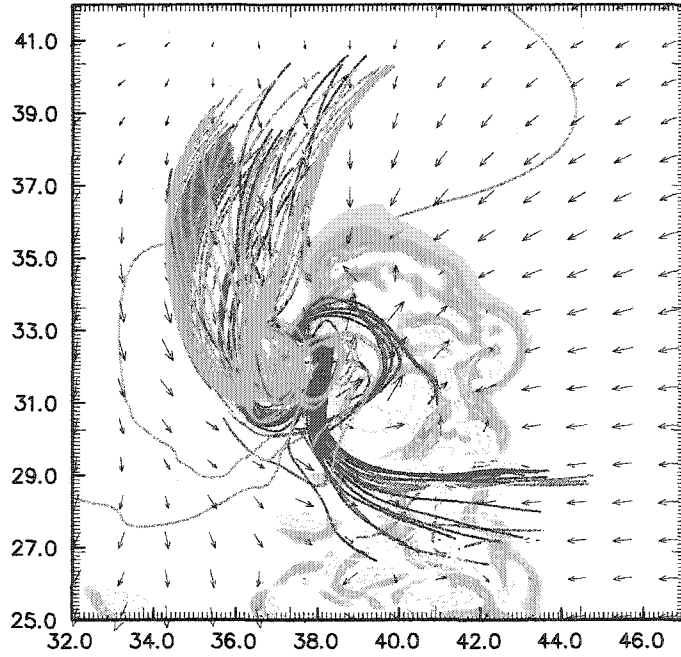


Figure 4.5.14b: As in 4.5.14a, except for box sizes of width 1.4 and 2.0 km.

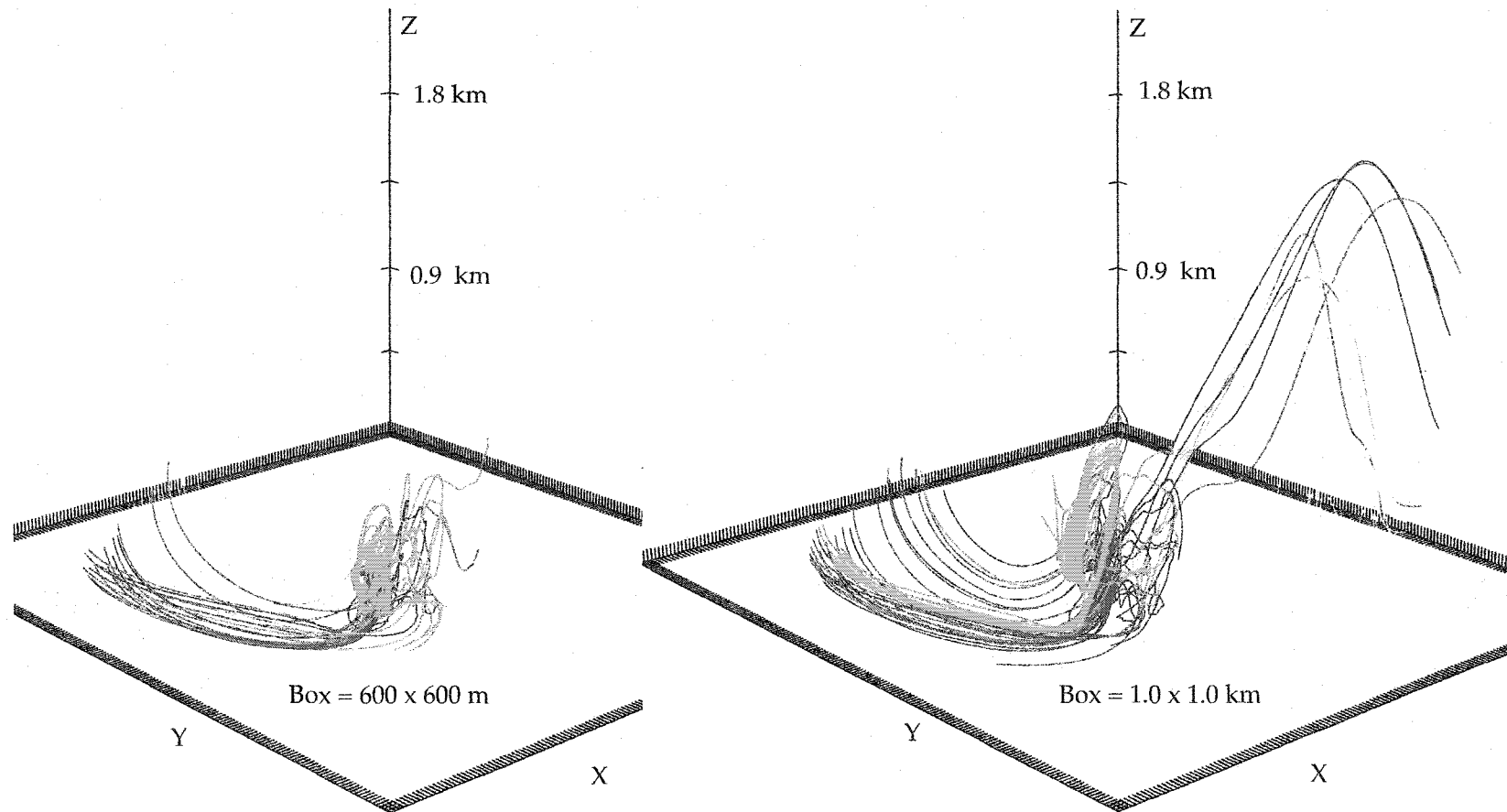


Figure 4.5.15: Three-dimensional perspective of the backward trajectories shown in Figure 4.5.14, toward the second tornado cyclone of cycle "B". Parcels were started from $z = 200$ m and were integrated from $t = 8400$ to 7920 s, initially spaced 50 m apart.

As we move outward from the tornado cyclone into the circulation of the tornadic mesocyclone, trajectories vary greatly but can be roughly divided into two source areas. The first is the new source region evident along and east of the gust front and southeast of the tornado (yellow, red, blue; Fig. 4.5.14b, 4.5.15 right). Parcels from this region travel up and over the gust front in a region well south of the main updraft, and originate at levels between 0.1 and 2.0 km. They then descend through downdrafts on the southern edge of the hook and are absorbed into the RFD and occlusion downdraft on the northern and eastern sides of the tornadic mesocyclone. The second group of mesocyclone trajectories (Fig. 4.5.14b) descends cyclonically from 200-500 m from a region north and northwest of the tornado. These are again similar to the descending trajectories observed in the mesocyclogenesis stages of cycles "C" and "D."

These trajectories are again quite different from those simulated by Wicker and Wilhelmson (1995). The tornadic parcels come mainly from a surface baroclinic region to the northwest of the mesocyclone, although in this case there exists some evidence for parcels descending from aloft through the occlusion downdraft. There also exists evidence for parcels originating east of the gust-front, although they only reach the mesocyclone rather than the tornado cyclone.

4.6 Summary and Discussion

As shown in the previous sections, the general evolution of the mesocyclone occlusion process using fine grid spacing remains similar to that in previous studies that used coarser spacings. Mesocyclone occlusion stages analogous to those of Adlerman et al. (1999) can be identified within each cycle. However, the overall evolution appears to be accelerated, with five mesocyclone occlusions occurring over the first four hours, in contrast with the two occlusions noted in identical coarser-

resolution simulations (Adlerman et al. 1999; Adlerman and Droegemeier 2002). A tendency exists for the length of the cycles to decrease with time, although after the fifth occlusion the storm remains fairly steady until the end of the simulation. This most likely results from the interference of precipitation that develops to the south of the main updraft.

Only three of the six mesocyclone cycles contain short-lived tornadoes ("B", "C", and "E"), with one of the cycles ("B") containing two. When a particular mesocyclone cycle is tornadic, updrafts, downdrafts, and pressure perturbations are larger. However, *the general evolution outlined in the conceptual model remains the same.* All but the second tornado in "B" occur at the point in the middle of the mesocyclone occlusion cycle when updrafts begin to increase and a well-developed hook wraps westward. In contrast, the second tornado in "B" occurs at a later time when the near-ground mesocyclone is already strongly occluded and the hook has wrapped back to just east of the rain core.

The details of the mesocyclone occlusion process vary significantly, especially with respect to the updraft above the surface. The occluding updraft can manifest itself as a secondary maximum within a unicellular updraft, as a small updraft/downdraft couplet, or as a distinct updraft separated from another farther downshear. The latter case is analogous to the dual updraft of the conceptual model (Adlerman et al. 1999), and it tends to be present in the stronger tornadic cycles.

Backward trajectories through the developing mesocyclone show that the mode of mesocyclogenesis is dictated by the details of the previous cycle. If the developing mesocyclone remains isolated, mesocyclogenesis is similar to that described in Adlerman et al. (1999). However, when the developing mesocyclone is adjacent to the occluding circulation, parcels from the old mesocyclone may be recirculated back into the mesocyclone of the next cycle (Davies-Jones 1982, p.186).

Backward trajectories through two of the four tornadoes demonstrate that parcels entering the tornado cyclone itself take quite similar paths, usually traveling near the surface through the RFD before rising into the tornadic circulation. However, parcels entering the outer periphery of the tornadic mesocyclone vary depending on the details of a particular cycle, though they usually contain some parcels that descend through the RFD and others that are recirculated through the occlusion downdraft.

Adlerman et al. (1999) suggested that previous cycles set the stage for more rapid development of subsequent cycles through the fortuitous orientation of surface buoyancy gradients. This still appears true in this simulation, as the mesocyclone trajectories suggest. However, our results also show that the occluding mesocyclone may contribute directly to the development of the next cycle through the ingestion of recirculated parcels. Figures 4.6.1 and 4.6.2 show horizontal cross-sections of surface semi-streamwise baroclinic generation during the transitions from cycles "C" to "D" and "D" to "E." Similar to Adlerman et al. (1999, see Fig. 24), a prominent area of baroclinic generation near the RFD moves east during the occlusion period and is ingested by the developing mesocyclone. However, another area that appears important in our mesocyclone trajectories extends northeast along the forward-flank gust-front.

Overall, one of most striking features of the simulation is the prominence of fine-scale structure. Even when an updraft appears unicellular, multiple small, but well-resolved (~500 m) maxima and minima are present. A single mesocyclone is no longer evident in the vorticity field, but instead there exists a broad circulation with several smaller scale areas of rotation embedded within. Some of the vorticity maxima are very transient (durations of 60-120 s) and likely are associated with small-scale updraft pulses, while others may be identified with the occluding and

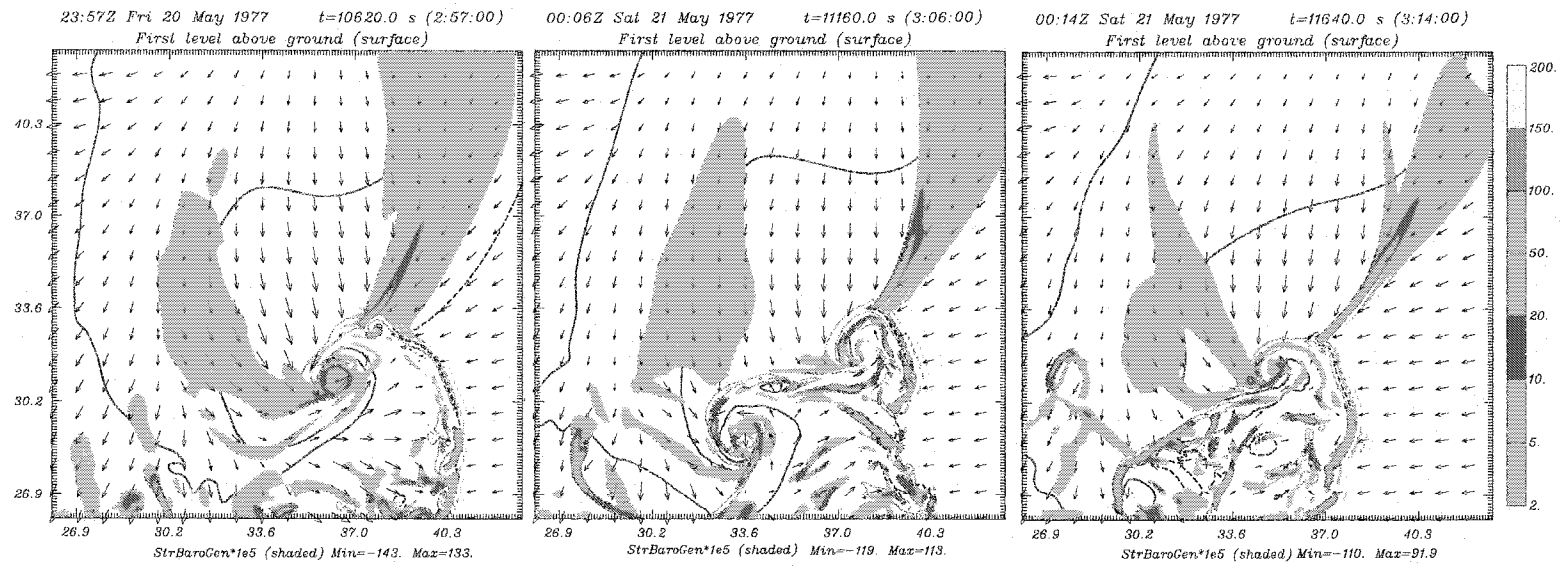


Figure 4.6.1: Horizontal cross-sections at $z = 30$ m of semi-streamwise baroclinic generation ($\times 10^{-5} \text{ s}^{-2}$) at 10620, 11160, and 11640 s, during the transition from tornadic cycle "C" to non-tornadic cycle "D".

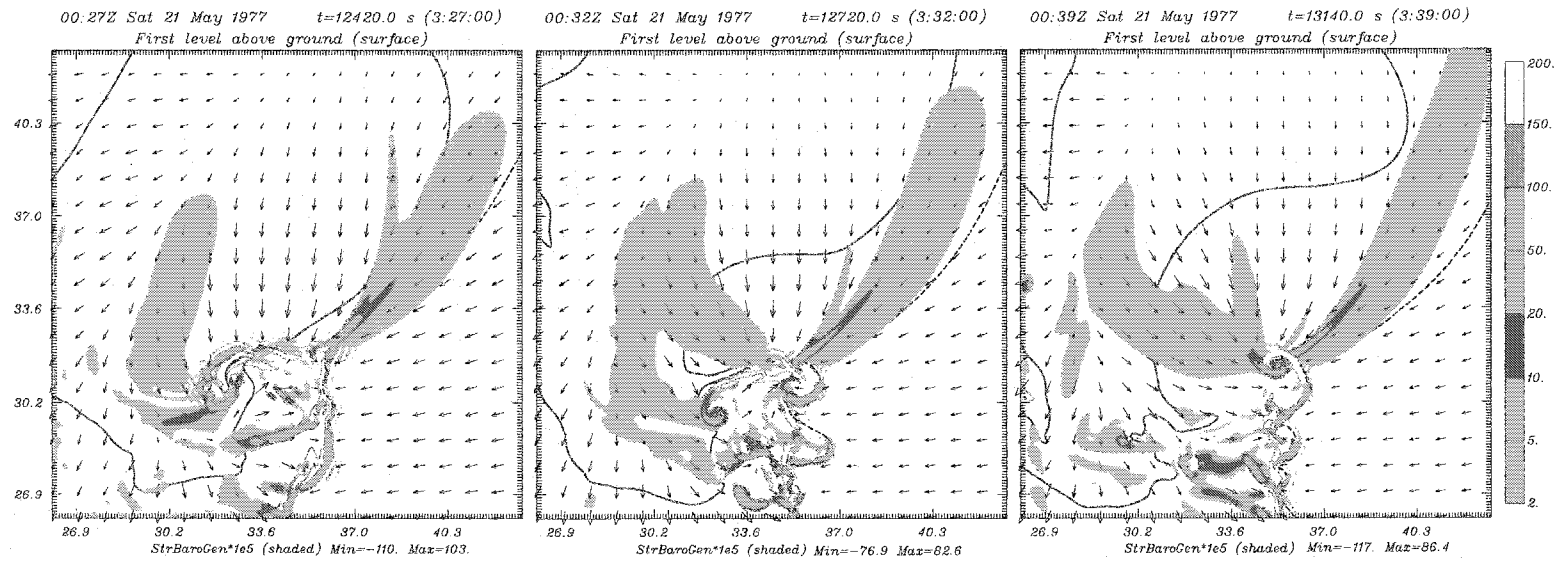


Figure 4.6.2: Horizontal cross-sections at $z = 35$ m of semi-streamwise baroclinic generation ($\times 10^{-5} \text{ s}^{-2}$) at 12420, 12720, and 13140 s, during the transition from non-tornadic cycle "D" to tornadic cycle "E".

newly developing mesocyclones. At these fine scales, vorticity becomes a problematic quantity in mesocyclone identification. As higher-resolution radars become available, the real-time identification and tracking of mesocyclones within a storm will be quite challenging. *Animations of this simulation suggest that the easiest way to identify and follow a particular mesocyclone is through the evolution of its updraft or updraft/downdraft couplet, either of which usually appears more coherent and less transient than its vorticity. Therefore, in the future, real-time dual-Doppler analysis may be necessary for accurate mesocyclone identification.*

CHAPTER 5

SUMMARY, CONCLUSIONS, AND OUTLOOK

This purpose of this study was to use idealized numerical simulations to investigate the cyclic redevelopment of vertical vortices in supercell storms. Building upon previous work that examined the dynamics and model sensitivity of cyclic mesocyclogenesis, this study was comprised of two separate but related parts. First, we examined the environmental parameter space that delineated between the timing and modes of mesocyclone occlusions. Second, we used a high-resolution numerical simulation to examine the dynamics of cyclic tornadogenesis.

The environmental sensitivity study examined variations in hodograph shape, shear magnitude, and shear distribution. A limited number of CAPE variations also were examined. In contrast to many other parameter studies, we used the 20 May 1977 Del City sounding rather than an analytic profile. Hodograph shapes included straight, quarter-circle (with and without a tail), half-circle, three-quarter circle, and circular (both 360 and 720 degrees of turning). All of our simulated storms could be categorized as supercellular, but in order to more fully cover the parameter space the range of shears used extended above that which normally might be observed in the atmosphere.

These simulations not only produced storms whose behavior ranged from steady-state to varying degrees of occluding cyclic mesocyclogenesis (as in previous simulations), but also demonstrated that a distinct mode of *non-occluding* cyclic mesocyclogenesis may occur in certain environments. The preferred mode of cyclic mesocyclogenesis appeared to be strongly related to both the hodograph shape and the strength of the shear.

Straight-hodographs produced *only* non-occluding cyclic mesocyclogenesis. After introducing some curvature with the quarter-circle hodograph, steady, non-occluding and occluding modes were observed. In general, steady state and occluding modes were prevalent at low shears, while the non-occluding mode appeared at intermediate and higher shears.

When a higher degree of curvature was introduced within the half-circle and three-quarter hodographs, the tendency for non-occluding cyclic mesocyclogenesis was diminished. At very low and very high shears, steady behavior was apparent, with occluding modes occurring at intermediate shears.

None of the full-circle hodographs exhibited cycling during the 4-hour simulation period. However, these were also not the most steady-state of the simulations, as might have been expected from drawing a parallel with that of an analytic Beltrami flow (i.e., where the environmental vorticity is entirely streamwise and the motions are steady-state). Indeed, when the simulations were extended out to 5 hours, one of the full-circle simulations did undergo an occlusion cycle. The influence of falling precipitation and its associated cold-pool strongly disrupted the idealized nature of a full-circle simulation. This is not surprising, as Davies-Jones (2000b) demonstrated that even in an axisymmetric model without buoyancy, falling precipitation was able to upset a Beltrami flow.

However, we can still draw a few parallels between the behavior of a Beltrami model and our results. The steady-state Beltrami model assumes zero CAPE (i.e., no buoyancy and a BRN of zero) and a circular hodograph over the entire domain depth. In general, our simulations exhibited less tendency to cycle as hodograph curvature increased over a deep depth and moved toward a more circular wind profile. In addition, our simulations demonstrated that cycling slowed as CAPE and hence BRN were decreased.

The ability to predict the mode and periodicity of storm cycling 'a priori' remains a difficult problem. Our results suggest that some general inferences can be made based upon hodograph shape and an average shear, but that standard indices such as helicity or BRN do not contain much predictive value. However, for discriminating only between occluding versus non-occluding cyclic modes, a stronger signal was apparent. We showed that non-occluding cyclic behavior tends to dominate when the initial sounding has a higher SRH, lower BRN, and a larger storm-relative inflow.

Before any operational prediction of cycling characteristics can be made, much more work needs to be done in several areas. First, a fuller exploration of the influence of the temperature and moisture profile upon cycling would need to be performed, similar to the work of McCaul and Cohen (2000) and McCaul and Weisman (2001). In addition, the effect of various ice physics parameterizations instead of warm rain microphysics would need to be addressed. These are not trivial tasks, as ideally one would like to repeat the thermodynamic alterations for most of the hodograph variations. This would result in several hundred simulations, each of which must be subjectively analyzed.

Secondly, a comparison of the numerical simulations with radar observations is necessary to understand the prevalence of each type of cycling mode and whether the simulated storms correctly correspond with the observed environmental conditions. Because some of the most easily distinguishable characteristics of occluding versus non-occluding modes occur near the surface, the classification process may be rather difficult unless the storm is within close range of current fixed radars. This comparison also would need to address the level of complexity required in the simulations to be comparable with observed modes of cycling. The role of surface friction, realistic initialization techniques, and more sophisticated

microphysics would inevitably be important for assessing the predictability of cyclic modes and timings.

In the cyclic tornadogenesis study, we simulated a storm that underwent six mesocyclone cycles (i.e., five occlusions) during a five-hour simulation in the Del City environment. Three of the mesocyclone cycles were tornadic, with one cycle containing two instances of tornadogenesis. The evolution of each occlusion cycle was similar to the conceptual model described in Adlerman et al. (1999), although the overall evolution was accelerated.

The details of transition between each cycle varied significantly. Above the surface, the occluded updraft took on several forms. In the stronger tornadic case, the updraft tended to have dual maxima with a downdraft separating the occluding mesocyclone from the mesocyclone of the next cycle. In the non-tornadic and weaker tornadic cases, the occluding updraft took on the form of a small updraft/downdraft couplet or a secondary maximum within a larger unicellular updraft. The differences could be attributed to the strength of a particular mesocyclone and the corresponding intensity of the occlusion downdraft.

Backward trajectories through the mesocyclone demonstrated that each cycle of mesocyclogenesis is influenced by the previous cycle. Trajectories comparable to those of Adlerman et al. (1999) were found when the mesocyclone was developing in an environment relatively free of influence from the previous cycle. The parcels generally descended through the RFD or ascended from east and northeast of the gust front. Semi-streamwise exchange, baroclinic generation, and stretching were all found to be important vorticity intensification mechanisms.

When the mesocyclone of a new cycle was developing in close proximity to that of an occlusion, trajectories were significantly altered. Similar the mode noted above, parcels were found to ascend into the developing mesocyclone from an area

northeast of the gust front. Parcels to the north and northwest were found to descend or travel nearly horizontally through baroclinic zones, again like the descending parcels of the previous mode. However, parcels from a third southern source region were found to travel near the surface through the occluding mesocyclone or descend through the occlusion downdraft and RFD.

Backward trajectories through the strongest tornado cyclone demonstrated that parcels entering the tornadic mesocyclone have a different history from those which originated closer to the center of rotation. The tornado cyclone parcels tended to travel near the ground through a baroclinic zone northwest of the circulation, whereas parcels closer to the periphery of the mesocyclone tended to come from the same area but originated at higher levels. The latter were found to either descend through the RFD or ascend through the updraft and then recirculate through the occlusion downdraft before entering the tornadic mesocyclone.

Backward trajectories through the tornado cyclone of an earlier cycle again demonstrated that each cycle has slightly different parcel histories. Although the tornado cyclone parcels were very similar to those of previous example, the tornadic *mesocyclone* now included parcels that originated east of the gust front and well south of the main updraft.

Our cyclic tornadogenesis simulation suggests several directions for future research. First, the fine-scale structure apparent throughout the simulation deserves further attention. At the surface, the gust front was found to act as a vortex sheet that shed discrete vortices under the influence of the RFD. One instance of tornadogenesis occurred when these shed vortices coalesced under the influence of convergent surface flow. Although the action of a vortex sheet in non-supercell tornadogenesis has been fairly well documented (Lee and Wilhelmson 1997a, 1997b, 2000), comparable vortex instabilities and motions in supercell tornadogenesis

remain mostly speculative and have only recently been documented (Bluestein et al. 2003). Further simulations and/or rapid-scan (< 60 s) high-resolution radar data will be necessary to understand the evolution of these small-scale vortices.

Aloft, the fine-scale structure also merits further attention. Past conceptual models, radar observations and coarse-grid simulations have given the impression that the mesocyclone is a single traceable area of vorticity. Such is not the case here. As finer grid spacing is used and vorticity maxima become large, it may be more useful to redefine the mesocyclone as an area of positive circulation correlated with an updraft maxima or updraft/downdraft couplet. As higher-resolution radars become available, conventional severe-storm algorithms will have to become more sophisticated to deal with the inherent complexity of this finer detail/structure (e.g., Bluestein et al. 2003).

Our simulations also suggest that tornadogenesis and near-ground mesocyclogenesis have multiple similar but distinct modes, as many radar studies have noted (e.g., Ziegler et al. 2001; Dowell and Bluestein 2002a,b). Most likely, every instance of tornadogenesis will be unique, with trajectories that vary based upon the influence of the local surface environment. As computing limits grow rapidly and non-nested high-resolution simulations with grid spacings on the order of 100 m become commonplace, tornadogenesis ensembles will be useful for assessing the significance of the differences among each mode. Data at intervals on the order of 1 s should be used to maximize the accuracy of trajectories for analysis. Before that time, considerable effort should be made to improve the treatment of surface friction and microphysics within storm-scale models, as these two factors persist as the most limiting aspects of our current efforts.

BIBLIOGRAPHY

- Abramowitz, M., and I. A. Stegun, eds., 1972: Handbook of Mathematical Functions with Formulas, Graphs, and Mathematical Tables. Dover Publications, 1046 pp.
- Adlerman, E. J., and K. K. Droegemeier, 2000: A numerical simulation of cyclic tornadogenesis. Preprints, 20th Conf. Severe Local Storms, Orlando, FL, Amer. Meteor. Soc., 591-594.
- Adlerman, E. J., and K. K. Droegemeier, 2002: The sensitivity of numerically simulated cyclic mesocyclogenesis to variations in physical and computational parameters. *Mon. Wea. Rev.*, **130**, 2671-2691.
- Adlerman, E. J., K. K. Droegemeier, and R. P. Davies-Jones, 1999: A numerical simulation of cyclic mesocyclogenesis. *J. Atmos. Sci.*, **56**, 2045-2069.
- Adrian, R. J., 1981: Comment on "A note on Poisson's equation for pressure in a turbulent flow." *Phys. Fluids*, **25**, 577.
- Agee, E.M., J.T. Snow, and P. Clare, 1976: Multiple vortex features in the tornado cyclone and the occurrence of tornado families. *Mon. Wea. Rev.*, **104**, 552-563.
- Andre, J. C., and M. Lesieur, 1977: Influence of helicity on the evolution of isotropic turbulence at high Reynolds number. *J. Fluid. Mech.*, **88**, 187-207.
- Atkins, N. T., M. L. Weisman, and L. J. Wicker, 1999: The influence of pre-existing boundaries on supercell evolution. *Mon. Wea. Rev.*, **127**, 2910-2927.
- Barnes, S.L., 1968: On the source of thunderstorm rotation, ESSA Tech Memo. ERLTM-NSSL38, National Severe Storms Laboratory, 28pp.
- Barnes, S.L., 1970: Some aspects of a severe, right-moving thunderstorm deduced from mesonet network rawinsonde observations. *J. Atmos. Sci.*, **27**, 634-648.
- Berger, M., and J. Olinger, 1984: Adaptive mesh refinement for hyperbolic partial differential equations. *J. Comput. Phys.*, **79**, 484-512.
- Bluestein, H. B., C. C. Weiss, and A. L. Pazmany, 2003: Mobile Doppler radar observations of a tornado in a supercell near Bassett, Nebraska, on 5 June 1999. Part I: tornadogenesis. *Mon. Wea. Rev.*, **131**, 2954-2967.
- Bradshaw, P., and Y. M. Koh, 1981: A note on Poisson's equation in a turbulent flow. *Phys. Fluids.*, **24**, 777.

- Brandes, E. A., 1984: Vertical vorticity generation and mesocyclone sustenance in tornadic thunderstorms: the observational evidence. *Mon. Wea. Rev.*, **112**, 2253-2269.
- Brandes, E. A., 1993: Tornadic thunderstorm characteristics determined with Doppler radar. *The Tornado: Its Structure, Dynamics, Prediction, and Hazards*, Geophys. Monogr., No.79 Amer. Geophys. Union Press, 143-159.
- Brooks, H. E., and R. B. Wilhelmson, 1993: Hodograph curvature and updraft intensity in numerically modeled supercells. *J. Atmos. Sci.*, **50**, 1824-1833.
- Brooks, H. E., and J. P. Craven, 2002: Database of proximity soundings for significant severe thunderstorms, 1957-1993. *21st Conf. on Severe Local Storms.*, San Antonio, TX, Amer. Meteor. Soc., 639-642.
- Brooks, H. E., C. A. Doswell III, and R. P. Davies-Jones, 1993: Environmental helicity and the maintenance and evolution of low-level mesocyclones. *The Tornado: Its Structure, Dynamics, Prediction, and Hazards*, Geophys. Monogr., No. 79., Amer. Geophys. Union Press, 97-104.
- Brooks, H. E., C. A. Doswell III, and R. B. Wilhelmson, 1994: On the role of midtropospheric winds in the evolution and maintenance of low-level mesocyclones. *Mon. Wea. Rev.*, **122**, 126-136.
- Brown, J. M., and K. R. Knupp, 1980: The Iowa cyclonic-anticyclonic tornado pair and its parent thunderstorm. *Mon. Wea. Rev.*, **108**, 1626-1646.
- Brown, R. A., D. W. Burgess, and K. C. Crawford, 1973: Twin tornado cyclones within a severe thunderstorm: Single Doppler radar observations. *Weatherwise*, **26**, 63-71.
- Browning, K. A., 1962: Cellular structure of convective storms. *Meteor. Mag.*, **91**, 341-350.
- Browning, K. A., 1964: Airflow and precipitation trajectories within severe local storms which travel to the right of the winds. *J. Atmos. Sci.*, **21**, 634-639.
- Browning, K. A., and R. J. Donaldson, 1963: Airflow and structure of a tornadic storm. *J. Atmos. Sci.*, **20**, 533-545.
- Browning, K. A., and F. H. Ludlam, 1962, Airflow in convective storms. *Quart. J. Roy. Meteor. Soc.*, **8**, 117-135.
- Browning, K. A., and C. R. Landry, 1963, Airflow within a tornadic thunderstorm. Preprints, *10th Weather Radar Conference*, Boston, MA, Amer. Meteor. Soc., 116-122.

- Bryan, G. H., J. C. Wyngaard, and J. M. Fritsch, 2003: Resolution requirements for the simulation of deep moist convection. *Mon. Wea. Rev.*, **131**, 2394-2416.
- Burgers, J. M., 1948: A mathematical model illustrating the theory of turbulence. *Adv. Appl. Mech.*, **1**, 197-199.
- Burgess, D. W., and R. P. Davies-Jones, 1979: Unusual tornadic storms in eastern Oklahoma on 5 December 1975. *Mon. Wea. Rev.*, **107**, 451-457.
- Burgess, D. W., and M. A. Magsig, 1998: Recent observations of tornado development at near range to WSR-88D radars. Preprints, *19th Conf. on Severe Local Storms*, Minneapolis, MN, Amer. Meteor. Soc., 756-759.
- Burgess, D. W., V. T. Wood, and R. A. Brown, 1982: Mesocyclone evolution statistics. Preprints, *12th Conf. on Severe Local Storms*, Boston, MA, Amer. Meteor. Soc., 422-424.
- Burgess, D. W., R. J. Donaldson Jr., and P. R. Desrochers, 1993: Tornado detection and warning by radar. *The Tornado: Its Structure, Dynamics, Prediction, and Hazards*, Geophys. Monogr., No. 79, Amer. Geophys. Union Press, 143-159.
- Byers, H. R. 1942: *The Thunderstorm*. Washington DC, Government Printing Office, 287pp.
- Chisholm, A. J., and J. H. Renick, 1972: The kinematics of multicell and supercell Alberta hailstorms. Alberta Hail Studies, 1972, Research Council of Alberta Hail Studies Rep. 72-2, 24-31.
- Craven, J. P., H. E. Brooks, and J. A. Hart, 2002: Baseline climatology of sounding derived parameters associated with deep moist convection. *21st Conf. on Severe Local Storms.*, San Antonio, TX, Amer. Meteor. Soc., 643-646.
- Darkow, G. L., 1971: Periodic tornado production by long-lived parent thunderstorms. Preprints, *7th Conf. on Severe Local Storms.*, Kansas City, MO, Amer. Meteor. Soc., 214-217.
- Darkow, G. L., and J. C. Roos, 1970: Multiple tornado producing thunderstorms and their apparent cyclic variations in intensity. Preprints, *14th Conf. Radar Meteor.*, Tucson, AZ, Amer. Meteor. Soc., 305-308.
- Davies, J. M., 1993: Small tornadic supercells in the central plains. Preprints, *17th Conf. on Severe Local Storms.*, St. Louis, MO, Amer. Meteor. Soc., 305-309.

- Davies, J. M., 2002: On low-level thermodynamic parameters associated with tornadic and nontornadic supercells. *21st Conf. on Severe Local Storms.*, San Antonio, TX, Amer. Meteor. Soc., 603-606.
- Davies-Jones, R. P., 1982: Observational and theoretical aspects of tornadogenesis. *Intense Atmospheric Vortices*, L. Bengtsson and J. Lighthill, Eds., Springer-Verlag, 175-189.
- Davies-Jones, R. P., 1984: Streamwise vorticity: The origin of updraft rotation in supercell storms. *J. Atmos. Sci.*, **41**, 2991-3006.
- Davies-Jones, R. P., 1985: Dynamical interaction between an isolated convective cell and a veering environmental wind. Preprints, *14th Conf. on Severe Local Storms.*, Indianapolis, IN, Amer. Meteor. Soc., 216-219.
- Davies-Jones, R. P., 1996a: Inclusion of boundary conditions on pressure in conceptual models of updraft-environment interaction. Preprints, *18th Conf. on Severe Local Storms.*, San Francisco, CA, Amer. Meteor. Soc., 713-717.
- Davies-Jones, R. P., 1996b: Formulas for the barotropic and baroclinic components of vorticity with applications to vortex formation near the ground. Preprints, *7th Conf. Mesoscale Processes*, Reading, UK, Amer. Meteor. Soc., 14-16.
- Davies-Jones, R. P., 2000a: A Lagrangian model for baroclinic genesis of mesoscale vortices. Part I: Theory. *J. Atmos. Sci.*, **57**, 715-736.
- Davies-Jones, R. P., 2000b: Can the hook echo instigate tornadogenesis barotropically? Preprints, *20th Conf. on Severe Local Storms.*, Orlando, FL, Amer. Meteor. Soc., 269-272.
- Davies-Jones, R. P., 2002: Linear and nonlinear propagation of supercell storms. *J. Atmos. Sci.*, **59**, 3178-3205.
- Davies-Jones, R. P., 2003: Reply to Comment on "Linear and nonlinear propagation of supercell storms". *J. Atmos. Sci.*, **60**, 2420-2426.
- Davies-Jones, R. P., D. Burgess, and M. Foster, 1990: Test of helicity as a tornado forecast parameter. Preprints, *16th Conf. on Severe Local Storms*, Kananaskis Park, Alberta, Canada, Amer. Meteor. Soc., 588-592.
- Davies-Jones, R. P., and H. E. Brooks, 1993: Mesocyclogenesis from a theoretical perspective. *The Tornado: Its Structure, Dynamics, Prediction, and Hazards, Geophy. Monogr.*, No. 79, Amer. Geophys. Union, 105-114.

- Davies-Jones, R. P., R. J. Trapp, and H. B. Bluestein, 2001: Tornadoes and tornadic storms. *Severe Convective Storms, Meteor. Monogr.*, No. 50, Amer. Meteor. Soc., 167-221.
- Doswell, C. A. III, and D. W. Burgess, 1993: Tornadoes and tornadic storms: A review of conceptual models. *The Tornado: Its Structure, Dynamics, Prediction, and Hazards, Geophys. Monogr.*, No. 79, Amer. Geophys. Union, 161-172.
- Doswell, C. A. III, and J. S. Evans, 2003: Proximity sounding analysis for derechos and supercells. *Atmos. Research*, submitted.
- Dowell, D. C., 2000: *A pseudo-dual-Doppler analysis of cyclic tornadogenesis*. Ph.D. Dissertation, School of Meteorology, University of Oklahoma, 227pp. [Available from School of Meteorology, University of Oklahoma, 100 East Boyd, Suite 1310, Norman, OK, 73019.]
- Dowell, D. C., H. B. Bluestein, and D. P. Jorgensen, 1997: Airborne Doppler radar analysis of supercells during COPS-91. *Mon. Wea. Rev.*, **125**, 365-383.
- Dowell, D. C., and H. B. Bluestein, 2000: Conceptual models of cyclic supercell tornadogenesis. Preprints, *20th Conf. on Severe Local Storms*, Orlando, FL, Amer. Meteor. Soc., 259-262.
- Dowell, D. C., and H. B. Bluestein, 2002a: The 8 June 1995 McLean, Texas storm. Part I: Observations of cyclic tornadogenesis. *Mon. Wea. Rev.*, **130**, 2626-2648.
- Dowell, D. C., and H. B. Bluestein, 2002b: The 8 June 1995 McLean, Texas storm. Part II: Cyclic tornado formation, maintenance, and dissipation. *Mon. Wea. Rev.*, **130**, 2649-2670.
- Droegemeier, K. K., S. M. Lazarus, and R. P. Davies-Jones, 1993: The influence of helicity on numerically simulated convective storms. *Mon. Wea. Rev.*, **121**, 2005-2029.
- Edwards, R., and R. L. Thompson, 2000: RUC-2 supercell proximity soundings, Part II: An independent assessment of supercell forecast parameters. Preprints, *20th Conf. on Severe Local Storms*, Orlando, FL, Amer. Meteor. Soc., 435-438.
- Emanuel, K. A., 1994: *Atmospheric Convection*. Oxford University Press, 580pp.
- Fiedler, B. H., 1995: On modeling tornadoes in isolation from the parent storm. *Atmosphere Ocean*, **33**, 501-512.
- Finley, C. A., W. R. Cotton, and R. A. Pielke, 1998a: Numerical simulation of two tornadoes produced by a high-precipitation supercell. Preprints, *19th*

- Conf. on Severe Local Storms*, Minneapolis, MN, Amer. Meteor. Soc., 206-209.
- Finley, C. A., W. R. Cotton, and R. A. Pielke, 1998b: Secondary vortex development in a tornado vortex produced by a simulated supercell thunderstorm. Preprints, *19th Conf. on Severe Local Storms*, Minneapolis, MN, Amer. Meteor. Soc., 359-362.
- Finley, C. A., W. R. Cotton, and R. A. Pielke, 2001: Numerical simulation of tornadogenesis in a high-precipitation supercell. Part 1: Storm evolution and transition into a bow echo. *J. Atmos. Sci.*, **58**, 1597-1629.
- Finley, C. A., W. R. Cotton, and R. A. Pielke, 2002: Tornadogenesis in a simulated HP supercell. Preprints, *21st Conf. on Severe Local Storms*, San Antonio, TX, Amer. Meteor. Soc., 531-534.
- Foote, G. B., and H. W., Frank, 1983: Case study of a hailstorm in Colorado. Part III: Airflow from triple-Doppler measurements. *J. Atmos. Sci.*, **40**, 686-707.
- Forbes, G. S., 1975: Relationship between tornadoes and hook echoes associated with left-turn tornado families. Preprints, *9th Conf. on Severe Local Storms*, Norman, OK, Amer. Meteor. Soc., 280-285.
- Forbes, G. S., 1977: Thunderstorm-scale variations of echoes associated with left-turn tornado families. Preprints, *10th Conf. on Severe Local Storms*, Omaha, NE, Amer. Meteor. Soc., 321-326.
- Foster, M. P., A. R. Moller, L. J. Wicker, and L. Cantrell, 1994: The rapid evolution of a tornadic small supercell: observations and simulation. Preprints, *14th Conf. Weather Analysis and Forecasting*, Dallas, TX, Amer. Meteor. Soc., 323-328.
- Fujita, T. T., 1958: Mesoanalysis of the Illinois tornadoes of 9 April 1953, *J. Meteor.*, **15**, 228-296.
- Fujita, T. T., 1975: New evidence from April 3-4, 1974 Tornadoes. Preprints, *9th Conf. on Severe Local Storms*, Norman, OK, Amer. Meteor. Soc., 248-255.
- Fujita, T. T., and H. Grandoso, 1968: Split of a thunderstorm into anticyclonic and cyclonic storms and their motions as determined from numerical model experiments. *J. Atmos. Sci.* **25**, 416-439.
- Fujita, T. T., and R. M. Wakimoto, 1982: Anticyclonic tornadoes in 1980 and 1981. Preprints, *12th Conf. on Severe Local Storms*, San Antonio, TX, Amer. Meteor. Soc., 213-216.

- Fujita, T. T., D. L. Bradbury, and C. F. Van Thullenar, 1970: Palm Sunday tornadoes of April 11, 1965. *Mon. Wea. Rev.*, **98**, 26-69.
- Gaudet, B. J., and W. R. Cotton, 2003: Low-level mesocyclonic concentration by non-axisymmetric processes. Part I: Supercell and mesocyclone evolution, *J. Atmos. Sci.*, submitted.
- Gilmore, M. S., and L. J. Wicker, 1998: The influence of midtropospheric dryness on supercell morphology and evolution. *Mon. Wea. Rev.*, **126**, 943-958.
- Grasso, L. D., and W. R. Cotton, 1995: Numerical simulation of a tornado vortex. *J. Atmos. Sci.*, **52**, 1192-1203.
- Hart, J., and J. Korotky, 1991: The SHARP workstation v1.50, A skew-T/hodograph analysis and research program for the IBM and compatible PC, user's manual. National Weather Service, National Oceanic and Atmospheric Administration, U.S. Department of Commerce, 62 pp.
- Hitschfeld, W. 1960: The motion and erosion of convective storms in severe vertical wind shear. *J. Meteor.*, **17**, 270-282.
- Hoecker, W. H., 1959: History and measurement of two major Scottsbluff tornadoes of 27 June 1955. *Bull. Amer. Meteor. Soc.*, **40**, 117-133.
- Hou, D., E. Kalnay, and K. K. Droegemeier, 2001: Objective verification of the SAMEX '98 Ensemble Forecasts. *Mon. Wea. Rev.*, **129**, 73-91.
- Jahn, D. E., 1995: Simulation of convective storms in environments with independently varying bulk Richardson number shear and storm-relative helicity. MS thesis, School of Meteorology, University of Oklahoma, 124pp. [Available from School of Meteorology, University of Oklahoma, 100 East Boyd, Suite 1310, Norman, OK, 73019.]
- Jensen, B., E. N. Rasmussen, T. P. Marshall, and M. A. Mabey, 1983: Storm scale structure of the Pampa storm. Preprints, *13th Conf. on Severe Local Storms*, Tulsa, OK, Amer. Meteor. Soc., 85-88.
- Johnson, K. W., P. S. Ray, B. C. Johnson and R. P. Davies-Jones, 1987: Observations related to the rotational dynamics of the 20 May 1977 tornadic storms. *Mon. Wea. Rev.*, **115**, 2463-2478.
- Joukowski, N., 1910: On the shape of the lifting surfaces of kites (German). *Z. Flugtech. Motorluftschiffahrt*, **1**, 281.
- Kessler, E., 1969: On the distribution and continuity of water substance in atmospheric circulation. *Meteor. Monog.*, **10**, No. 32, Amer. Meteor. Soc., 84pp.

- Kennedy, P. C., N. E. Westcott, and R. W. Scott, 1993: Single-Doppler radar observations of a mini-supercell tornadic thunderstorm. *Mon. Wea. Rev.*, **121**, 1860-1870.
- Klemp, J. B., 1987: Dynamics of tornadic thunderstorms. *Ann. Rev. Fluid. Mech.*, **19**, 369-402.
- Klemp, J. B. and R. B. Wilhelmson, 1978a: The simulation of three-dimensional convective storm dynamics. *J. Atmos. Sci.*, **35**, 1070-1096.
- Klemp, J. B. and R. B. Wilhelmson, 1978b: Simulation of right and left moving storms produced through storm splitting. *J. Atmos. Sci.*, **35**, 1097-1119.
- Klemp, J. B., and R. Rotunno, 1983: A study of the tornadic region within a supercell thunderstorm. *J. Atmos. Sci.*, **40**, 359-377.
- Klemp, J. B., and M. L. Weisman, 1983: The dependence of convective precipitation patterns on vertical wind shear. Preprints, *21st Conf. on Radar Meteor.*, Edmonton, Canada, Amer. Meteor. Soc., 44-49.
- Klemp, J. B., R. B. Wilhelmson, and P. S. Ray, 1981: Observed and numerically simulated structure of a mature supercell thunderstorm. *J. Atmos. Sci.*, **38**, 1558-1580.
- Kraichnan, R. H., 1973: Helical turbulence and absolute equilibrium. *J. Fluid. Mech.*, **59**, 745-752.
- Kulie, M. S., and Y. Lin 1998: The structure and evolution of a numerically simulated high precipitation supercell thunderstorm. *Mon. Wea. Rev.*, **126**, 2090-2116.
- Kutta, W., 1902: Lift forces in flowing fluids (German). *Ill. aeronaut. Mitt.*
- Lee, B. D. and R. B. Wilhelmson, 1997a: The numerical simulation of non-supercell tornadogenesis. Part I: Initiation and evolution of pre-tornadic misocyclone circulations along a dry outflow boundary. *J. Atmos. Sci.*, **54**, 32-60.
- Lee, B. D. and R. B. Wilhelmson, 1997b: The numerical simulation of non-supercell tornadogenesis. Part II: Evolution of a family of tornadoes along a weak outflow boundary. *J. Atmos. Sci.*, **54**, 2387-2415.
- Lee, B. D. and R. B. Wilhelmson, 2000: The numerical simulation of non-supercell tornadogenesis. Part III: Parameter tests investigating the role of CAPE, vortex sheet strength and boundary layer vertical shear. *J. Atmos. Sci.*, **57**, 2246-2261.

- Lemon, L. R., and C. A. Doswell III, 1979: Severe thunderstorm evolution and mesocyclone structure as related to tornadogenesis. *Mon. Wea. Rev.*, **107**, 1184-1197.
- Leslie, L. M., 1971: The development of concentrated vortices: a numerical study. *J. Fluid Mech.*, **48**, 1-21.
- Levit, N. L., K. K. Droegemeier, and F. Kong, 2004: High-resolution storm-scale ensemble forecasts of the 28 March 2000 Fort Worth tornadic storms. Preprints, 20th Conf. on Wea. Analysis and Forecasting/16th Conf. on Num. Wea. Prediction, Seattle, WA, Amer. Meteor. Soc.
- Lewellen, W. S., D. C. Lewellen, and R. I. Sykes, 1997: Large-eddy simulation of a tornado's interaction with the surface. *J. Atmos. Sci.*, **54**, 581-605.
- Lilly, D. K., 1982: The development and maintenance of rotation in convective storms. *Intense Atmospheric Vortices*, L. Bengtsson and J. Lighthill, Eds., Springer-Verlag, 149-160.
- Lilly, D. K., 1983: Dynamics of rotating thunderstorms. *Mesoscale Meteorology, Theories, Observations, Models*. D.K. Lilly and T. Gal-Chen, Eds., Reidel, 531-544.
- Lilly, D. K., 1986a: The structure, energetics, and propagation of rotating convective storms. Part I: Energy exchange with the mean flow. *J. Atmos. Sci.*, **43**, 113-125.
- Lilly, D. K., 1986b: The structure, energetics, and propagation of rotating convective storms. Part II: Helicity and storm stabilization. *J. Atmos. Sci.*, **43**, 126-140.
- Lilly, D. K., 1990: Numerical prediction of thunderstorms – has its time come? *Q. J. R. Meteorol. Soc.*, **116**, 779-798.
- Markowski, P. M., 2002: Hook echoes and rear-flank downdrafts: A review. *Mon. Wea. Rev.*, **130**, 852-876.
- Markowski, P. M., J. M. Straka, and E. N. Rasmussen, 1998: A preliminary investigation of the importance of helicity location in the hodograph. *19th Conf. on Severe Local Storms*, Minneapolis, MN, Amer. Meteor. Soc., 230-233.
- Markowski, P. M., J. M. Straka, and E. N. Rasmussen, 2003: Tornadogenesis resulting from the transport of circulation by a downdraft: idealized numerical simulations. *J. Atmos. Sci.*, **60**, 795-823.

- Marwitz, J. D., 1972: The structure and motion of severe hailstorms. Part III: Severely sheared storms. *J. Appl. Meteor.*, **11**, 189-201.
- McCaul, E. W., Jr., 1987: Observations of the Hurricane Danny tornado outbreak of 16 August 1985. *Mon. Wea. Rev.*, **115**, 1206-1223.
- McCaul, E. W., Jr., 1991: Buoyancy and shear characteristics of hurricane-tornado environments. *Mon. Wea. Rev.*, **119**, 1954-1978.
- McCaul, E. W., Jr., 1993: Observations and simulations of hurricane-spawned tornadic storms. *The Tornado: Its Structure, Dynamics, Prediction, and Hazards*, C.R. Church, Ed., Amer. Geophys. Union Press, 119-142.
- McCaul, E. W., Jr., and M. L. Weisman, 1996: Simulations of shallow supercell storms in landfalling hurricane environments. *Mon. Wea. Rev.*, **124**, 408-429.
- McCaul, E. W., Jr., and C. Cohen, 2000: The sensitivity of simulated storm structure and intensity to the lifted condensation level and the level of free convection. Preprints, 20th Conf. Severe Local Storms, Orlando, FL, Amer. Meteor. Soc., 595-598.
- McCaul, E. W., Jr., and M. L. Weisman, 2001: The sensitivity of simulated supercell structure and intensity to variations in the shapes of environmental buoyancy and shear profiles. *Mon. Wea. Rev.*, **129**, 664-687.
- Moller, A. R., and C. A. Doswell III, 1988: A proposed advanced storm spotter's training program. Preprints, 15th Conference on Severe Local Storms, Baltimore, MD, Amer. Meteor. Soc. 173-177.
- Moller, A. R., C. A. Doswell III, M. P. Foster, and G. R. Woodall, 1994: The operational recognition of supercell thunderstorm environments and storm structures. *Wea. Forecasting*, **9**, 327-347.
- Monteverdi, J.P., and J. Quadros, 1994: Convective and rotational parameters associated with three tornado episodes in northern and central California. *Wea. Forecasting*, **9**, 285-300.
- Nelson, S. P., 1987: The hybrid multicellular-supercellular storm - an efficient hail-producer. Part II: General characteristics and implications for hail-growth. *J. Atmos. Sci.*, **44**, 2060-2073.
- Newton, C. W., and S. Katz, 1958: Movement of large convective rain storms in relation to winds aloft. *Bull. Am. Meteor. Soc.*, **32**, 129-136.
- Newton, C. W., and H. R. Newton, 1959: Dynamical interactions between large convective clouds and environmental vertical shear. *J. Meteor.*, **16**, 483-496.

- Novlan, D. J., and W. M. Gray, 1974: Hurricane-spawned tornadoes. *Mon. Wea. Rev.*, **102**, 476-488.
- Rasmussen, E. N. 2003: Refined supercell and tornado forecast parameters. *Wea. Forecasting*, **18**, 530-535.
- Rasmussen, E. N., and R. B. Wilhelmson, 1983: Relationships between storm characteristics and 1200 GMT hodographs, low-level shear, and stability. Preprints, *13th Conf. on Severe Local Storms*, Tulsa, OK, Amer. Meteor. Soc., J5-J8.
- Rasmussen, E. N., and D. O. Blanchard, 1998: A baseline climatology of sounding-derived supercell and tornado forecast parameters. *Wea. Forecasting.*, **13**, 1148-1164.
- Rasmussen, E. N., and J. M. Straka, 1998: Supercell morphology variations. Part I. Observations of upper-level storm-relative flow. *Mon. Wea. Rev.*, **126**, 2406-2421.
- Rasmussen, E. N., R. E. Peterson, J. E. Minor, and B. D. Campbell, 1982: Evolutionary characteristics and photogrammetric determination of wind speeds within the Tulia outbreak tornadoes 28 May 1980. Preprints, *12th Conf. on Severe Local Storms*, San Antonio, TX, Amer. Meteor. Soc., 301-304.
- Ray, P. S., B. C. Johnson, K. W. Johnson, J. S. Bradberry, J. J. Stephens, K. K. Wagner, R. B. Wilhelmson, and J. B. Klemp, 1981: The morphology of several tornadic storms on 20 May 1977. *J. Atmos. Sci.*, **38**, 1643-1663.
- Richardson, Y. P., 1999: *The influence of horizontally-varying shear and CAPE on numerically simulated convective storms*. Ph.D. Dissertation, School of Meteorology, University of Oklahoma, 236pp. [Available from School of Meteorology, University of Oklahoma, 100 East Boyd, Suite 1310, Norman, OK, 73019.]
- Richardson, Y. P., and K. K. Droegemeier, 1996: An investigation of the dynamics governing organized multicell rotation and transition. Preprints, *18th Conf. on Severe Local Storms*, San Francisco, CA, Amer. Meteor. Soc., 195-199.
- Richardson, Y. P., and K. K. Droegemeier, 1998: A study of the influence of horizontally-varying vertical shear and CAPE on numerically simulated convective storms. Preprints, *19th Conf. on Severe Local Storms*, Minneapolis, MN, Amer. Meteor. Soc., 249-251.

- Rotunno, R. 1981: On the evolution of thunderstorm rotation. *Mon. Wea. Rev.*, **109**, 577-586.
- Rotunno, R. 1984: An investigation of a three-dimensional asymmetric vortex. *J. Atmos. Sci.*, **41**, 283-298.
- Rotunno, R. 1986: Tornadoes and tornadogenesis. *Mesoscale Meteorology and Forecasting*. P. S. Ray, Ed., Amer. Meteor. Soc., 414-436.
- Rotunno, R., and J. B. Klemp, 1982: The influence of the shear-induced pressure gradient on thunderstorm motion. *Mon. Wea. Rev.*, **110**, 136-151.
- Rotunno, R. and J. B. Klemp, 1985: On the rotation and propagation of numerically simulated supercell thunderstorms. *J. Atmos. Sci.*, **42**, 271-292.
- Scorer, R. S., 1978: *Environmental Aerodynamics*. Ellis Horwood, 488pp.
- Simpson, J. E., 1972: The effect of the lower boundary on the head of a gravity current. *J. Fluid Mech.*, **53**, 759-768.
- Skamarock, W. C. and J. B. Klemp 1993: Adaptive grid refinement for 2D and 3D nonhydrostatic atmospheric flow. *Mon. Wea. Rev.*, **121**, 788-804.
- Snow, J. T., and E. M. Agee, 1975: Vortex splitting in the mesocyclone and the occurrence of tornado families. Preprints, *9th Conf. on Severe Local Storms*, Norman, OK, Amer. Meteor. Soc., 270-277.
- Tapp, M. C., and P. W. White, 1976: A non-hydrostatic mesoscale model. *Quart. J. Roy. Meteor. Soc.*, **102**, 277-296.
- Thompson, R. L., R. Edwards, and J. A. Hart, 2002a: Evaluation and interpretation of the supercell composite and significant tornado parameters at the Storm Prediction Center. Preprints, *21st Conf. on Severe Local Storms*, San Antonio, TX, Amer. Meteor. Soc., J11-J14.
- Thompson, R. L., R. Edwards, and J. A. Hart, 2002b: An assessment of supercell and tornado forecast parameters with RUC-2 model close proximity soundings. Preprints, *21st Conf. on Severe Local Storms*, San Antonio, TX, Amer. Meteor. Soc., 595-598
- Trapp, R. J., 1999: Observations of nontornadic low-level mesocyclones and attendant tornadogenesis failure during VORTEX 95. *Mon. Wea. Rev.*, **127**, 1693-1705.
- Trapp, R. J. and R. P. Davies-Jones, 1997: Tornadogenesis with and without a dynamic pipe effect. *J. Atmos. Sci.*, **54**, 113-133.

- Vasiloff, S. V., E. A. Brandes, R. P. Davies-Jones, and P. S. Ray, 1986: An investigation of the transition from multicell to supercell storms. *J. Clim. Appl. Meteor.*, **25**, 1022-1036.
- Wakimoto, R. M., H. V. Murphey, D. C. Dowell, and H. B. Bluestein, 2003: The Kellerville tornado during VORTEX: Damage survey and Doppler radar analysis. *Mon. Wea. Rev.*, **131**, 2197-2221.
- Walko, R. L., 1993: Tornado spin-up beneath a convective cell. *The Tornado: Its Structure, Dynamics, Prediction, and Hazards, Geophys. Monogr.*, No. 79, Amer. Geophys. Union, 89-95.
- Weisman, M. L., and J. B. Klemp, 1982: The dependence of numerically simulated convective storms on vertical wind shear and buoyancy. *Mon. Wea. Rev.*, **110**, 504-520.
- Weisman, M. L., and J. B. Klemp, 1984: The structure and classification of numerically simulated convective storms in directionally varying wind shears. *Mon. Wea. Rev.*, **112**, 2479-2498.
- Weisman, M. L., and J. B. Klemp, 1986: Characteristics of isolated convective storms. *Mesoscale Meteorology and Forecasting*. P. S. Ray, Ed., Amer. Meteor. Soc., 331-358.
- Weisman, M. L., and R. Rotunno, 2000: The use of vertical wind shear versus helicity in interpreting supercell dynamics. *J. Atmos. Sci.*, **57**, 1452-1472.
- Wicker, L. J., 1990: A numerical simulation of a tornado-scale vortex in a three-dimensional cloud model. Ph.D. thesis, University of Illinois, 264 pp.
- Wicker, L. J., and R. B. Wilhelmson, 1993: Numerical simulation of tornadogenesis within a supercell thunderstorm. *The Tornado: Its Structure, Dynamics, Prediction, and Hazards, Geophys. Monogr.*, No. 79, Amer. Geophys. Union, 75-88.
- Wicker, L. J., and R. B. Wilhelmson, 1995: Simulation and analysis of tornado development and decay within a three-dimensional supercell thunderstorm. *J. Atmos. Sci.*, **52**, 2675-2703.
- Wicker, L. J., and L. Cantrell, 1996: The role of vertical buoyancy distribution in miniature supercells. *Preprints, 18th Conf. on Severe Local Storms*, San Francisco, CA, Amer. Meteor. Soc., 225-229.
- Wilhelmson, R. B., and J. B. Klemp, 1978: A three-dimensional numerical simulation of splitting that leads to long-lived storms. *J. Atmos. Sci.*, **35**, 1037-1063.

- Wilhelmson, R. B., and J. B. Klemp, 1981: A three-dimensional numerical simulation of splitting severe storms on 3 April 1964. *J. Atmos. Sci.*, **38**, 1581-1600.
- Wilhelmson, R. B., and L. J. Wicker, 2001: Numerical modeling of severe local storms. *Severe Convective Storms, Meteor. Monogr.*, No. 50, Amer. Meteor. Soc., 123-166.
- Xue, M., K. K. Droegemeier, V. Wong, A. Shapiro, and K. Brewster, 1995: ARPS Version 4.0 User's Guide. Center for Analysis and Prediction of Storms. University of Oklahoma, 380pp. [Available from Center for Analysis and Prediction of Storms, University of Oklahoma, 100 E. Boyd. St., Rm. 1110, Norman, OK 73019]
- Xue, M., K. K. Droegemeier, and V. Wong, 2000: The Advanced Regional Prediction System (ARPS) - A multiscale nonhydrostatic atmospheric simulation and prediction tool. Part I: Model dynamics and verification. *Meteor. Atmos. Physics.*, **75**, 161-193.
- Xue, M., K. K. Droegemeier, V. Wong, A. Shapiro, K. Brewster, F. Carr, D. Weber, Y. Liu, and D. H. Wang, 2001: The Advanced Regional Prediction System (ARPS) - A multiscale nonhydrostatic atmospheric simulation and prediction tool. Part II: model physics and applications. *Meteor. Atmos. Physics.*, **76**, 143-165.
- Xue, M., D.-H. Wang, J.-D. Gao, K. Brewster, and K. K. Droegemeier, 2003: The Advanced Regional Prediction System (ARPS), storm-scale numerical weather prediction and data assimilation. *Meteor. and Atmos. Physics.*, **82**, 139-170
- Ziegler, C. L., E. N. Rasmussen, T. R. Shepherd, A. I. Watson, and J. M. Straka, 2001: The evolution of low-level rotation in the 29 May 1994 Newcastle -Graham, Texas, storm complex during VORTEX. *Mon. Wea. Rev.*, **129**, 1339-1368.

APPENDIX A

Trajectory Code Description

The trajectory code originally used in Adlerman et al. (1999) underwent many revisions and alterations for this study. First, initial tests using the high-resolution tornadogenesis data showed that changes on the order of 250 m could radically alter the history of parcels. Therefore, doing single trajectories or a box of trajectories might give results that were arbitrary and possibly misleading. Therefore, we developed what we call "trajectory ensembles". Instead of following a single box of points backward in time, we now specify an initial box diameter (D) and an initial "ensemble spacing" (DX), i.e., a change in the diameter of the box. The trajectories are calculated first for a box of diameter D , then for a box of $D + DX$, then for a box of $D + 2DX$, and onward for an arbitrary number of boxes (usually 10). Therefore, in a single calculation on the order of 1000 parcels are usually followed. This also allows us to center the box upon a location of "tornadogenesis" and observe the changes as the box is expanded to cover a larger region of tornadic "mesocyclogenesis".

The initial integration technique used in Adlerman et al. (1999) was a three-step predictor-corrector method, of first-order accuracy. For this work, we implemented a fourth-order Runge-Kutta scheme (Abramowitz and Stegun 1972). Although the actual differences in the trajectories were not large, this higher-order scheme was used for all calculations in this work.

A trilinear interpolation scheme was utilized in Adlerman et al. (1999). In an attempt to improve accuracy, Everett's interpolation formula (Abramowitz and Stegun 1972) was implemented in the horizontal direction. Despite a much higher computational cost and associated slowdown in calculations, changes in the

trajectories were extremely minimal. Therefore, the trilinear formula was used for all calculations in this work. Both the changes in integration technique and interpolation scheme suggest that the limiting factor in trajectory accuracy is the finite time spacing of the history files, rather than the methods of computation.

APPENDIX B

Magnitude of the Numerical Diffusion Term in ARPS

Consider the one-dimensional momentum equation, neglecting all terms except the local time derivative and the numerical diffusion term. We use the 4th-order formulation, resulting in the equation $u_t = -K_4 u_{xxxx}$, where K_4 is the 4th-order mixing coefficient. If one assumes a traveling wave solution of the form $e^{i(kx - \omega t)}$, we can derive a dispersion relationship $\omega = K_4 k^4$. In terms of wavelength λ and period T , this is equivalent to $T = \lambda^4 / (8\pi^3 K_4)$. [In our simulations, we use the 4th-order formulation in the horizontal direction. In the vertical direction, we use a 2nd-order formulation to more strongly damp noise because it is potentially more disruptive as a result of the buoyancy term. A similar dispersion relationship can be derived for 2nd-order numerical diffusion.]

In the context of our tornadogenesis simulation, the smallest resolvable horizontal wavelength is 210 m and the mixing coefficient is $2.65 \times 10^8 \text{ m}^4 \text{ s}^{-1}$, giving a damping timescale T of 0.03 s. For larger horizontal wavelengths of 420 m and 1050 m, the respective damping timescales are approximately 0.5 and 19 s. This suggests that $4\Delta X$ waves are being damped in a *single timestep*, which obviously is not happening in the simulation.

An explanation for this is found by comparing the scale of the numerical diffusion term with the scale of the other terms in the horizontal momentum equation. Consider the approximate scales for a convective simulation. We assume a length scale L of 10 km, a velocity scale U of 10 m s^{-1} , and a pressure scale P of 100 Pa. Taking density as 1 kg m^{-3} and using the momentum equation in the x -direction, the numerical diffusion term is proportional to $K_4 (U/L^4)$ or 10^{-7} , the pressure gradient term is proportional to (P/L) or 10^{-2} , and the advection terms are

proportional to (U^2/L) or 10^{-2} . Thus, the numerical diffusion terms are effectively several orders of magnitude smaller than the advection and pressure gradient terms.